Julian Kahlbow

The low-Z Shore of the Island of Inversion: Invariant-mass Spectroscopy of the heavy Fluorine Isotopes $^{29}F^{*}$ & ^{30}F at SAMURAI with NeuLAND

TECHNISCHE
UNIVERSITÄT
DARMSTADT

2019

TECHNISCHE
UNIVERSITÄT
DARMSTADT

The low-*Z* Shore of the Island of Inversion: Invariant-mass Spectroscopy of the heavy Fluorine Isotopes ^{29}F* & ^{30}F at SAMURAI with NeuLAND

Die Grenzen der „Insel der Inversion“: Spektroskopie der schweren Fluor-Isotope ^{29}F* & ^{30}F an SAMURAI mit NeuLAND

Vom Fachbereich Physik
der Technischen Universität Darmstadt

zur Erlangung des Grades
eines Doktors der Naturwissenschaften (Dr. rer. nat.)

genehmigte Dissertation von
Julian Kahlbow, M.Sc.

Referent
Prof. Dr. Thomas Aumann
Korreferent
Prof. Dr. Thorsten Kröll

Darmstadt 2019
D17

Julian Kahlbow
The low-*Z* Shore of the Island of Inversion: Invariant-mass Spectroscopy of the heavy Fluorine Isotopes ^{29}F* & ^{30}F at SAMURAI with NeuLAND

Die Grenzen der „Insel der Inversion“: Spektroskopie der schweren Fluor-Isotope ^{29}F* & ^{30}F an SAMURAI mit NeuLAND

Darmstadt, Technische Universität Darmstadt
Tag der Einreichung: 11.06.2019
Tag der mündlichen Prüfung: 08.07.2019

Jahr der Veröffentlichung der Dissertation auf TUprints: 2021
Bitte zitieren Sie dieses Dokument als / Please cite as:
URN: urn:nbn:de:tuda-tuprints-91920
URL: https://tuprints.ulb.tu-darmstadt.de/id/eprint/9192

Abstract

The island of inversion is the region in the chart of nuclides at $Z \sim 11$ and $N \sim 20$ where the $N = 20$ shell gap is quenched and intruder configurations are already dominant in the ground-state wave function. First experimental evidence for shell-structure changes compared to the naive shell model was found already in the 1970's. This thesis studies the neutron-rich fluorine isotopes ^{30}F and ^{29}F that are located just at the predicted lower proton-number boundary of the island of inversion.

The experiment was carried out in inverse kinematics at the SAMURAI setup at the Radioactive Ion Beam Factory (RIKEN Nishina Center, Tokyo/Japan). The nuclei of interest are populated in quasi-free proton- and neutron-knockout reactions at $\sim 250\,\mathrm{MeV/u}$ on the $15\,\mathrm{cm}$ LH_2 target of the MINOS device. The scattered charged nucleons are tracked in the MINOS TPC, while the heavy charged fragment is analyzed by the large-acceptance dipole magnet SAMURAI. The NeuLAND demonstrator and the NEBULA neutron detectors measure coincidentally neutrons in forward direction. The DALI2 array detects γ-rays around the target region.

The NeuLAND demonstrator, part of the R^{3}B experiment at GSI/FAIR (Germany), was added to the SAMURAI setup for a two-year experimental program. The detector was commissioned in a particular experiment where the one-neutron detection efficiency is determined at $110\,\mathrm{MeV}$ and $250\,\mathrm{MeV}$. Therefore, a quasi-monoenergetic neutron beam is produced in the p(^{7}Li,^{7}Be)n reaction. The one-neutron detection efficiency is determined to be $31.0(13)\,\%$ and $27.4(10)\,\%$ (for $\Delta E > 5\,\mathrm{MeV}$) at $110\,\mathrm{MeV}$ and $250\,\mathrm{MeV}$, respectively. The results agree with the simulations.

The SAMURAI setup allows to perform the complete spectroscopy of neutron-unbound nuclei. The first spectroscopic information for ^{30}F is here obtained in the ^{31}Ne$(p,2p)^{29}$F$+n$ reaction. By applying the invariant-mass method, the relative energy is calculated from the momentum measurement of the fragment and decay neutron. The ground-state resonance is determined to be at $583(85)\,\mathrm{keV}$ with a width of $\Gamma = 730(151)\,\mathrm{keV}$. In the single-particle limit for a Breit-Wigner resonance the value of the width indicates a significant contribution from a valence neutron in the $2p$ orbital. This is a signature as found for nuclei in the island of inversion.

Bound and neutron-unbound states are studied for ^{29}F. The excited states are populated in the ^{30}Ne$(p,2p)^{29}$F* reaction. A known bound excited state at $1063(7)\,\mathrm{keV}$ is confirmed in this experiment and a new one with transition energy of $287\,\mathrm{keV}$ is found. Above the separation threshold ^{29}F decays into ^{27}F$+n+n$, the relative energy of the three particles is reconstructed and

analyzed. Five more excited states are identified. The correlation analysis of this three-body decay in Jacobi coordinates shows that ^{29}F* decays dominantly in sequential-decay mode via resonances in ^{28}F. ^{28}F is also separately investigated in the ^{29}F(p,pn) reaction. The Breit-Wigner line shapes for sequential decay are introduced to determine the three-body resonance energies. The level and decay schemes are obtained.

Eventually, the comparison to a shell-model calculation with the SDPF-M interaction and a *ab-initio* Self-consistent Green's function theory using a N^{2}LO$_{\rm sat}$+N^{3}LO(lnl) interaction is shown. It is concluded that the $N = 20$ shell-gap quenching persists at $Z = 9$ ($N \sim 20$) and intruder configurations are crucial in the description. The studied neutron-rich fluorine isotopes show characteristics as found in the island of inversion.

Zusammenfassung

Die sogenannte Insel der Inversion bei Atomkernen mit $Z \sim 11$ und $N \sim 20$ zeichnet sich durch eine Verkleinerung des Schalenabstands bei $N = 20$ sowie durch Intruderkonfigurationen von höheren Orbitalen in der Wellenfunktion aus. Erste experimentelle Hinweise auf die Veränderung der Schalenstruktur im Vergleich zum einfachen Schalenmodell gab es bereits in den 1970er Jahren. Diese Arbeit untersucht die Fluor-Isotope ^{30}F und ^{29}F, die sich an der vorhergesagten unteren Grenze für die Kernladungszahl der Insel der Inversion befinden.

Das Experiment wurde am SAMURAI-Setup der Radioactive Ion Beam Factory (RIKEN Nishina Center, Tokio/Japan) durchgeführt. Die zu untersuchenden Atomkerne werden in quasifreien Proton- und Neutron-Knockout-Reaktionen an dem $15\,\mathrm{cm}$ langen MINOS LH_2-Target bei $\sim 250\,\mathrm{MeV/u}$ produziert. Die Spuren der gestreuten leichten, geladenen Nukleonen werden in der MINOS TPC gemessen. Die schweren, geladenen Reaktionsfragmente werden hingegen mit dem SAMURAI Dipol-Magneten analysiert. Die Neutronendetektoren NeuLAND Demonstrator und NEBULA messen koinzident Neutronen unter Vorwärtsrichtung. Der DALI2-Detektor misst γ-Strahlung in der Target-Region.

Der NeuLAND Demonstrator ist ein Detektor am R^{3}B-Experiment bei GSI/FAIR (Deutschland), wurde aber für eine zweijährige Experimentierkampagne am SAMURAI-Setup eingesetzt. Mit einem separaten Experiment, bei dem die 1-Neutronen-Nachweiseffizienz bei den Energien $110\,\mathrm{MeV}$ und $250\,\mathrm{MeV}$ bestimmt werden sollte, wurde der Detektor charakterisiert. Dazu wurde ein nahezu monoenergetischer Neutronenstrahl in der p(^{7}Li,^{7}Be)n Reaktion produziert. Die 1-Neutronen-Nachweiseffizienz wurde zu $31.0(13)\,\%$ bei $110\,\mathrm{MeV}$ und zu $27.4(10)\,\%$ bei $250\,\mathrm{MeV}$ (für $\Delta E > 5\,\mathrm{MeV}$) bestimmt. Diese Ergebnisse stimmen mit Resultaten aus Simulationen überein.

Das SAMURAI-Setup ermöglicht die vollständige Spektroskopie neutronen-ungebundener Atomkerne. Erstmalig wird hier ^{30}F analysiert, dafür wird die Reaktion ^{31}Ne$(p, 2p)^{29}$F$+n$ untersucht. Unter Anwendung der Invarianten-Masse-Methode wird die Relativenergie aus der Impulsmessung von Fragment und Neutron berechnet. Die Grundzustandsenergie liegt bei $583(85)\,\mathrm{keV}$ bei einer Resonanzbreite von $\Gamma = 730(151)\,\mathrm{keV}$. Dieses Ergebnis deutet im Einteilchenlimit für die Breite einer Breit-Wigner-Resonanz auf einen deutlichen Beitrag des Valenzneutrons im $2p$-Orbital hin. Diese Konfiguration entspricht einer typischen Signatur, wie sie bei Kernen in der Insel der Inversion zu finden ist.

Im Fall von ^{29}F werden gebundene und neutronen-ungebundene Zustände analysiert. Die-

se angeregten Zustände werden bei der ^{30}Ne$(p, 2p)^{29}$F* Reaktion erzeugt. Die Messung bestätigt einen bereits bekannten, gebundenen angeregten Zustand bei $1063(7)\,\mathrm{keV}$. Außerdem wurde ein neuer Zustand mit einer Übergangsenergie von $287\,\mathrm{keV}$ identifiziert. Überhalb der Separationsschwelle zerfällt ^{29}F in ^{27}F$+n+n$, die Relativenergie wird wiederum für die drei Teilchen berechnet und analysiert. Dabei werden fünf weitere Zustände identifiziert. Die Korrelationsanalyse in Jacobi-Koordinaten zeigt, dass ^{29}F* vorwiegend sequentiell über Resonanzen in ^{28}F zerfällt. ^{28}F wird auch separat in der Reaktion ^{29}F(p, pn) untersucht. Die Drei-Körper-Resonanzen werden mit speziellen Breit-Wigner-Distributionen für den sequentiellen Zerfall analysiert.

Die Ergebnisse für ^{29}F werden mit einer Schalenmodell-Rechnung, die die SDPF-M Wechselwirkung verwendet, verglichen, sowie mit der *ab-initio* Self-consistent Green's Function Theorie, die die N^{2}LO$_{\mathrm{sat}}$+N^{3}LO(lnl) Wechselwirkung benutzt. Es wird geschlussfolgert, dass die Verkleinerung des Schalenabstands bei $N = 20$ auch für $Z = 9$ fortbesteht und Intruderkonfigurationen für die Beschreibung der Zustände erforderlich sind. Die neutronenreichen Fluor-Isotope zeigen Charakteristika wie andere Kerne in der Insel der Inversion.

Contents

List of Figures

List of Tables

Chapter 1

Introduction

The atomic nucleus is a quantum-mechanical object of the size of a few femtometer. Its constituents, the neutrons and protons, together called nucleons, interact via the strong interaction.

At the end of the 19th century a new field of physics, namely nuclear physics, emerged with the discovery of radioactivity by A. Henri Becquerel [2, 3] and with the following studies on nuclear decays by Marie Curie and others. In 1911, after his famous gold-foil experiment, Ernest Rutherford formulated a new model of the atom with a small charged nucleus in its center. Together with the discovery of the proton and neutron, this lay the basis for many experimental and theoretical developments [4]. Today, approx. 3000 different stable and unstable nuclei are experimentally found and mapped in the chart of nuclides, see Fig. 1.1.

The basic studies of nuclear abundances and binding energies found discontinuities in the behavior and led W. M. Elsasser claim the existence of "sous-groupes" (engl.: sub-groups) in nuclei in 1934 [5]. Independently, M. Goeppert Mayer [6–8] and O. Haxel, J. H. D. Jensen, and H. E. Suess [9] developed models to describe the structure found in nuclei. They introduced a shell-model picture similarly to that for the electronic structure of atoms, where the particular sub-groups manifest in particular large energy gaps between nuclear shells and they are only reproduced when a spin-orbit term is considered in their nuclear mean-field potential, see Sec. 2.1. The closed shells involve 2, 8, (14), 20, 28, 50, 82, and 126 nucleons [7, 9] – called "magic numbers". Patterns in experimentally determined observables such as separation energy, energy of the first excited state, and angular momentum demonstrate the success of the simple shell-model picture [10]. Neutrons and protons successively fill the shells, the orbits are labeled according to their quantum numbers with level n, orbital-angular momentum $\vec{l}$, spin $\vec{s}$, total angular momentum $\vec{j} = \vec{l} + \vec{s}$, and isospin $\vec{\tau}$.

With the advances in experimental techniques during the last 50 years, nuclei with large asymmetry in the proton-neutron ratio have become accessible like around proton number $Z \approx 10$ and neutron number $N \approx 20$. For instance, mass measurements of the sodium isotopes ^{31,32}Na [11] and the low 2^+-state excitation energy of ^{32}Mg ($885\,\mathrm{keV}$) [12] show inconsistency with theoretical

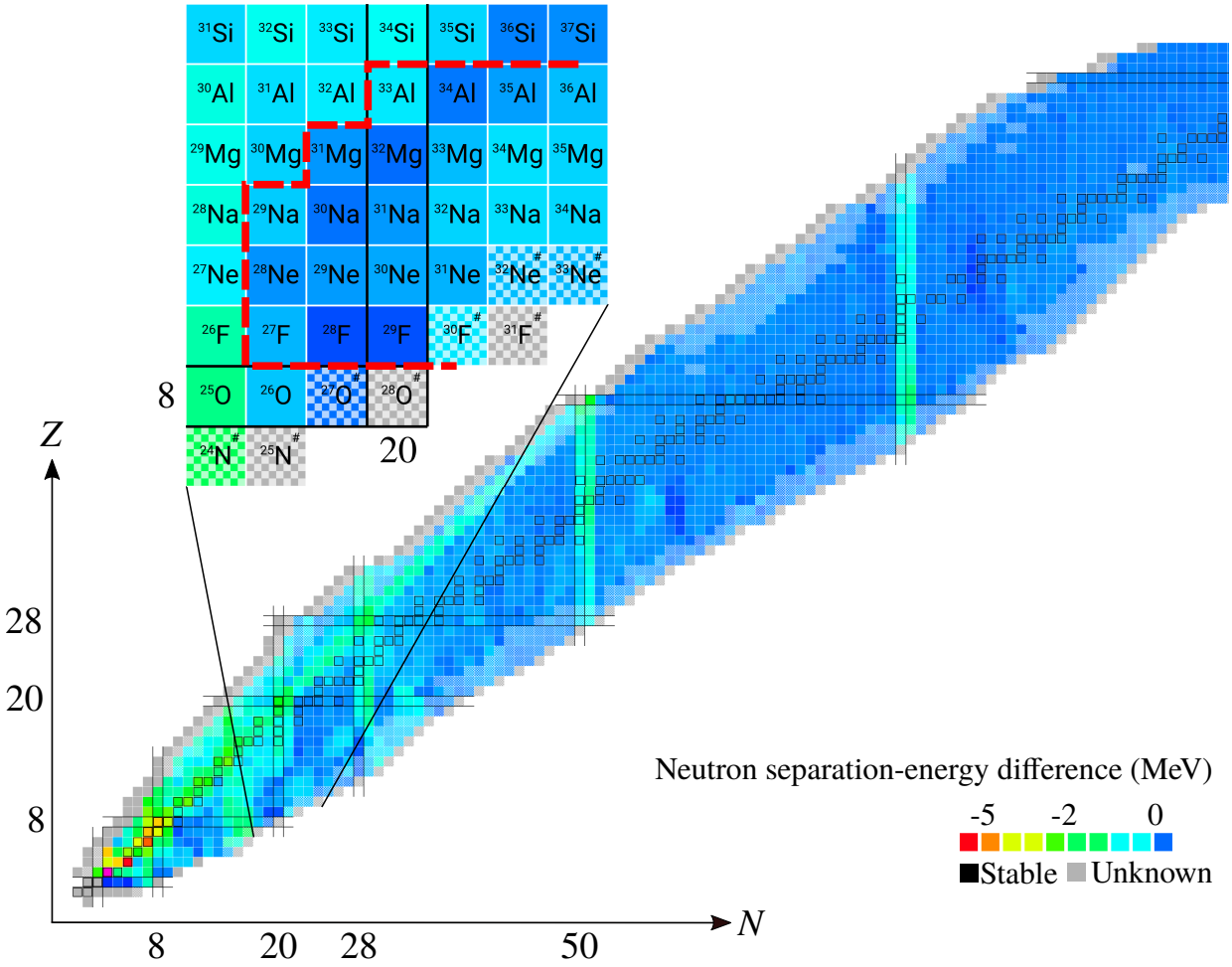

Figure 1.1: Part of the chart of nuclides color-coded according to the one-neutron separation-energy difference between two neighboring isotopes $\Delta S_n = [S_n(Z, N+1) - S_n(Z, N)]/2$, data taken from Ref. [1]. The classical magic numbers are marked with black lines, isotopes marked with a "#" are based on extrapolated values. Areas with particular stability, i. e. large separation energy, describe the neutron magic numbers, whereas the magicity seem to vanish for $N \approx 20$ at $Z \approx 10$, but a new shell closure at $N = 16$ appears. Nuclei within the region that is surrounded by the red line can be considered to belong to the island of inversion (showing fp intruder configurations), the fluorine isotopes are discussed here.

results using the classical shell model and are the first experimental evidence that shell structure evolves and residual interactions which cause e. g. deformation are missing in the shell-model. This region of nuclei later became famous as so-called "island of inversion". Additional nucleon-nucleon interactions that become important for nuclei with increasing isospin asymmetry are the reason for understanding the shell evolution theoretically.

The nuclear-physics community is right in the middle of performing experiments that study the shell structure of such exotic nuclei with new methods. In addition, large efforts are undertaken to understand the nuclear structure theoretically over the whole chart of nuclides. Besides effective shell models, new *ab-initio* approaches try to describe the nucleus from first principles with the nucleons as degrees of freedom and nucleon-nucleon forces [13]. Two fundamental questions that address the limits of nuclear binding and the shell-structure evolution remain the main motivation in nuclear physics: understand the existence and properties of nuclei and the underlying fundamental forces.

Radioactive-ion beam facilities such as the GSI Helmholtz Centre for Heavy-Ion Research (GSI) and the Radioactive Ion Beam Factory (RIBF)/RIKEN or the Isotope Separator On-Line Detector (ISOLDE) at CERN and others produce such short-lived nuclei with large neutron-proton asymmetry at the extremes of nuclear binding. The pioneering works to produce Radioactive Isotope (RI) beams have been done at the Niels Bohr Institute (Copenhagen, Denmark) and with the Bevalac at the Lawrence Berkeley Laboratory (USA) [14]. Experiments at RI-beam facilities identified meanwhile several "islands of shell breaking" [15] where shell-structure inversions are found. For nuclei with large isospin asymmetry around the classical magic neutron numbers $N = 8, 20, 28$, and also 40 (subshell) the shell-gap energy quenches. Besides, new phenomena are found in neutron-rich nuclei such as halo nuclei, di-nucleon correlations, clusters, and for heavier nuclei neutron skins develop. This thesis work focuses on the neutron-rich site of the chart of nuclides.

Halo effects appear at the drip line where the valence neutrons are loosely bound and their exponential wave-function tail extends far beyond the typical nuclear radius of a few femtometer [16]. This can be seen as single nucleons orbiting outside a core. The unexpectedly large interaction cross section of ^{11}Li measured by Tanihata et al. [17] at the Lawrence Berkeley Laboratory led to the interpretation by Hansen and Jonson [18] in terms of halo states. Meanwhile, several such nuclei have been found where (multiple) weakly bound s- or p-wave neutrons (e. g. ^{11}Be, ^{6}He, ^{15}C, ^{31}Ne, ...) or also protons (^{17}Ne) form a halo state [16]. A sensitive probe for neutron halos are momentum distributions after neutron-knockout reaction, that are especially narrow [19], or investigations of the electric-dipole response [20]. The latter is also a tool of choice to investigate excess neutrons that form a neutron skin. A strong low-lying dipole strength is a signature of a decoupled neutron excitation against an isospin-symmetric core [20].

All these experimental findings show that structure and dynamics of nuclei far from the valley of β stability change drastically. The stable nuclei are well bound by about $8\,\mathrm{MeV}$ but adding neutrons shifts the Fermi levels. At the neutron drip line, the neutron-separation energy S_n becomes

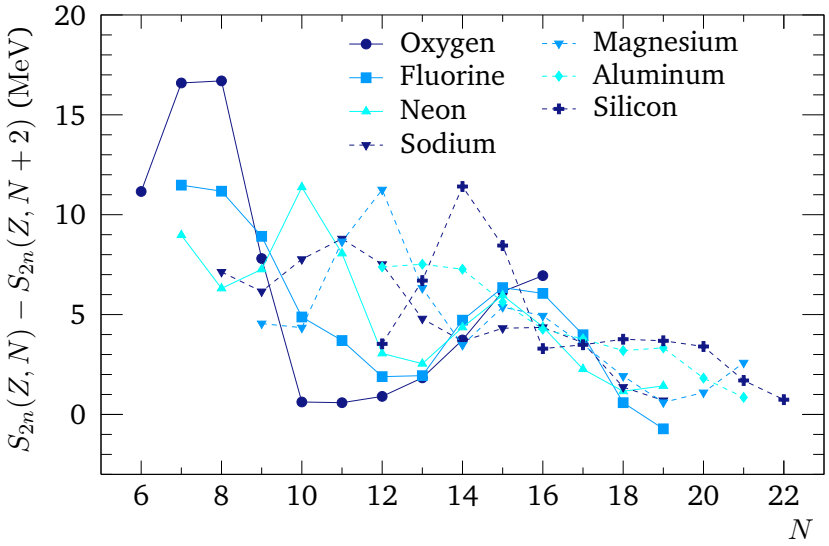

Figure 1.2: Empirical shell gaps associated with ΔS_{2n}. Except for silicon, a new magic number at $N = 16$ appears. Data taken from Ref. [23].

zero but the protons are more deeply bound, the difference can reach $20\,\mathrm{MeV}$ [20].

In a simplified approach, the neutron drip line [21] could be predicted by calculating the separation energy

$$S_n(Z,N) = B(Z,N) - B(Z,N-1), \tag{1.1}$$

using semi-empirical mass models [22] or following trends in the experimentally-determined binding energy B [23]. The larger the neutron-proton asymmetry, the smaller the binding energy.

Looking to the two-neutron separation energies reveals also other effects. Figure 1.2 shows the difference between the two-neutron separation energies, $\Delta S_{2n} = S_{2n}(Z,N) - S_{2n}(Z,N+2)$, which is associated with empirical shell gaps [24], for the (known) oxygen to silicon isotopes using the data from Ref. [23]. For all the isotopes except for silicon a decrease of ΔS_{2n} at $N = 16$ indicates a shell closure at the new magic number $N = 16$ instead of $N = 20$, giving rise to the island of inversion. For silicon the pronounced behavior of $N = 20$ appears where ΔS_{2n} starts falling. For smaller neutron number α-cluster formation becomes apparent at $N = 8, 10, 12$ and 14 for a $4, 5, 6$, and 7 α-clusters in ^{16}O, ^{20}Ne, ^{24}Mg, and ^{28}Si, respectively. The enhancement of ΔS_{2n} for Z close to N for odd-even isotopes of fluorine and sodium reveals the importance of neutron-proton pairing.

Besides neutron-proton pairing, also the neutron-neutron interaction can gain binding as exemplarily seen for the fluorine isotopes. In the fluorine isotopic chain a binding staggering is seen between even and odd isotopes – the odd-odd isotopes ^{28}F and ^{30}F are neutron unbound while ^{29}F & ^{31}F are particle stable. The last bound fluorine isotope is not known though. Experimentally,

the neutron drip line is only established up to oxygen, ^{24}O is the last bound in this chain. The generic mass formula cannot predict precisely the location of the drip line, what becomes obvious for oxygen. In modern calculations, the drip line is correctly predicted only including residual interactions. In case of oxygen, this is a question of three-body forces [25].

In order to study neutron-unbound states and get a better understanding why those nuclei are unbound, new experimental techniques have been developed. The experiment analyzed in this thesis uses proton- and neutron knockout reactions on neutron-rich beams to populate neutron unbound states. The invariant-mass technique is used to obtain spectroscopic information. Since the neutron-unbound states decay immediately into neutron(s) and heavy charged fragment, experimentally the aim is to measure all reaction particles.

A new-generation setup for measurements in inverse and complete kinematics with high-energy RI beams is the SAMURAI stage at the RIBF/RIKEN in Japan [26]. This facility uniquely combines highest-available intensities for RI beams, a high-resolution experimental setup, and a neutron-detection system with high efficiency. This combination allows in the experiment here for the first time ever to study the heavy oxygen isotopes ^{28}O & ^{27}O that decay via four- and three-neutron emission, respectively. The neutrons are coincidentally detected with the NeuLAND demonstrator and NEBULA neutron detectors.

NeuLAND is the new neutron detector developed and foreseen for experiments at the R^{3}B experiment at GSI/FAIR (Germany) [27]. After the first part – the so called NeuLAND demonstrator – had been built as GSI, it was shipped to RIKEN in January 2015 and added to the existing neutron detector at SAMURAI, called NEBULA, to perform experiments there and contribute to the FAIR-Phase-0 research program. Adding NeuLAND almost doubles the one-neutron detection efficiency and increases substantially the multi-neutron tracking efficiency what is necessary to perform the investigation of ^{28}O. This thesis describes in particular an experiment that characterizes the NeuLAND demonstrator at SAMURAI and quantifies its one-neutron detection efficiency applying quasi-monoenergetic neutrons at $250\,\mathrm{MeV}$ and $110\,\mathrm{MeV}$ as a probe, the details are described in Sec. 7.7. NeuLAND could contribute as key detector to several experiments during the campaign at SAMURAI which ended in summer 2017 before the detector was sent back to GSI. Another experiment that is mentioned in a bit more detail is the lifetime measurement of the ^{26}O(g. s.) for that a new method has been developed as part of this thesis work, see Sec. 3.7. The whole campaign with the NeuLAND demonstrator at RIKEN is reviewed in Ref. [28] where in total twelve experiments were conducted.

The focus of this work is the study the heavy fluorine isotopes ^{27}F to ^{30}F at SAMURAI. This project is supported by the Collaborative Research Center 1245 “Nuclei: From Fundamental Interactions to Structure and Stars” at TU Darmstadt. The sub-project A06 focuses on the theoretical and experimental study of “Strong interactions beyond the drip line”, in particular the tetra-neutron system, and the very neutron-rich oxygen and fluorine isotopes. Several theories predict that also those fluorine isotopes are effected by the quenching of the sd-fp shell and intruder con-

tributions have a substantial contribution – thus, showing characteristics as found in the island of inversion and extending it to lower Z number.

Experimentally, little is known about their shell structure. Here, the focus is put to the complete spectroscopy of ^{29}F and ^{30}F including the bound and neutron-unbound states, populated in one-proton-knockout reactions on neon isotopes. The SAMURAI setup allows to do the complete and exclusive spectroscopy of those isotopes where γ-ray spectroscopy is applied to measure bound excited states and the invariant-mass technique to obtain the excitation energy above the neutron-separation threshold. In addition, the large-acceptance setup allows to measure momentum distributions that can be analyzed in quasi-free scattering theory.

The thesis starts with a chapter (Ch. 2) detailing the shell model and the theory of physics of neutron-unbound states. In Ch. 3, the current research around this topic is reviewed focusing on experiments in the island of inversion. Chapters 4 and 5 discuss the experimental and analysis methods, like RI beam production, reaction physics, (multi-) neutron tracking, and the analysis of neutron-unbound states, before the experimental setup is introduced. Following, Ch. 6 and 7 show the experimental-data calibration and analysis. In the end, in Ch. 8, the results are presented for the first spectroscopy of ^{30}F and the Borromean nucleus ^{29}F, where the results are compared to theory predictions.

Chapter 2

Theoretical Background

2.1 The Nuclear Many-Body Problem

The atomic nucleus is a strongly-interacting quantum many-body system. In order to study it theoretically the many-body eigenstate problem needs to be solved:

$$\hat{H}\,|\psi_n\rangle = E_n\,|\psi_n\rangle\,, \tag{2.1}$$

$\hat{H}$ is the many-body Hamiltonian, $|\psi_n\rangle$ a many-body eigenstate and E_n the energy eigenvalue. In the following, it is described how the Hamiltonian and the interaction potential can be formulated and what methods are available to solve the many-body problem.

As of today, it is only possible to study very light systems ($A \leq 2$) in the fundamental theory of Quantum Chromodynamics (QCD) on the lattice. Thus, different phenomenological and microscopic models have been developed to describe nuclei and observables, through to *ab-initio* methods directly based on QCD symmetries.

The many-body Hamiltonian for A nucleons is in general composed of the kinetic-energy operator $\hat{T}$, the two-nucleon $\hat{V}_{NN}$, and further multi-particle interaction terms,

$$\hat{H} = \sum_{i=1}^{A} \hat{T}_i + \sum_{i<j}^{A} \hat{V}_{ij} + \ldots \tag{2.2}$$

The Schrödinger equation can in this case only be solved exactly for few-nucleon systems ($A = 3, 4$) [29].

The many-body state must be antisymmetrized according to space $|nlm_l\rangle$, spin $|sm_s\rangle$, and isospin $|tm_t\rangle$. A particular state for one nucleon can be formulated as

$$|\phi\rangle = |nls(jm_j);tm_t\rangle = \sum_{m_l m_s} C \left(\begin{array}{cc|c} l & s & j \\ m_l & m_s & m_j \end{array} \right) |nlm_l\rangle \otimes |sm_s\rangle \otimes |tm_t\rangle\,, \tag{2.3}$$

where all the possible couplings are expanded in Clebsch-Gordan coefficients C. This becomes already a complex system when only two nucleons couple together with their single-particle quantum numbers and total angular momentum J as $|n_1 l_1 j_1, n_2 l_2 j_2; JT\rangle$, whereas symmetry considerations can help to reduce the problem (like Pauli exclusion principle). A typical single-particle basis are the Harmonic Oscillator (HO) states. An efficient way to formulate the state is to use the second-quantization formalism. A nucleons are combined in all possible configurations and form a complete antisymmetrized basis $\{\phi_i\}$,

$$|\phi_i\rangle = |\beta_1 \beta_2 ... \beta_A\rangle_i \,, \tag{2.4}$$

where the Slater determinants are $|\beta_1 \beta_2 ... \beta_A\rangle = \hat{c}^\dagger_{\beta_1} \hat{c}^\dagger_{\beta_2} ... \hat{c}^\dagger_{\beta_A} |0\rangle$ with the creation operator $\hat{c}^\dagger_\beta$ to create a particle in state β.

2.1.1 The Shell Model

In the mean-field approximation an effective one-body (average) potential U is introduced, rewriting the Hamiltonian in the two-body interaction case (Eq. 2.2) gives

$$\hat{H} = \left[\sum_{i=1}^{A} \left(\hat{T}_i + \hat{U}_i\right)\right] + \left[\sum_{i<j}^{A} \hat{V}_{ij} - \sum_{i=1}^{A} \hat{U}_i\right] = \hat{H}_0 + \hat{H}_{\mathrm{res}}, \tag{2.5}$$

that separates the interaction into a mean-field part $\hat{H}_0$ and the residual interaction $\hat{H}_{\mathrm{res}}$ that is assumed to be small. $\hat{H}_0$ is the single-particle potential that is assumed to be formed by all nucleons which are moving independently in that potential. Suitable mean-field potentials U in this Independent Particle Model (IPM) are typically of harmonic-oscillator or Woods-Saxon shape. Hartree-Fock theory is also used to derive U starting with an effective two-particle interaction [30]. However, the shell structure is only reproduced, including the characteristic energy gaps, by adding a spin-orbit dependent potential acting on orbital angular momentum and spin, $\vec{l} \cdot \vec{s}$, and a term proportional to l^2. The energy-level structure is shown in Fig. 2.1.

Residual Interactions

In the vicinity of the magic numbers and close to β-stable nuclei, this model works well but in particular for the region which is subject of this thesis, the residual interactions are crucial and need to be included. In the picture of an inert core and nucleons above in the valence space, the interactions between valence nucleons have the largest impact on the shift of the energy levels [31], while the nucleon-core interaction can be taken with the average potential. The residual interactions reduces to [31]

$$\hat{H}_{\mathrm{res}} = \hat{V}_{ij}, \tag{2.6}$$

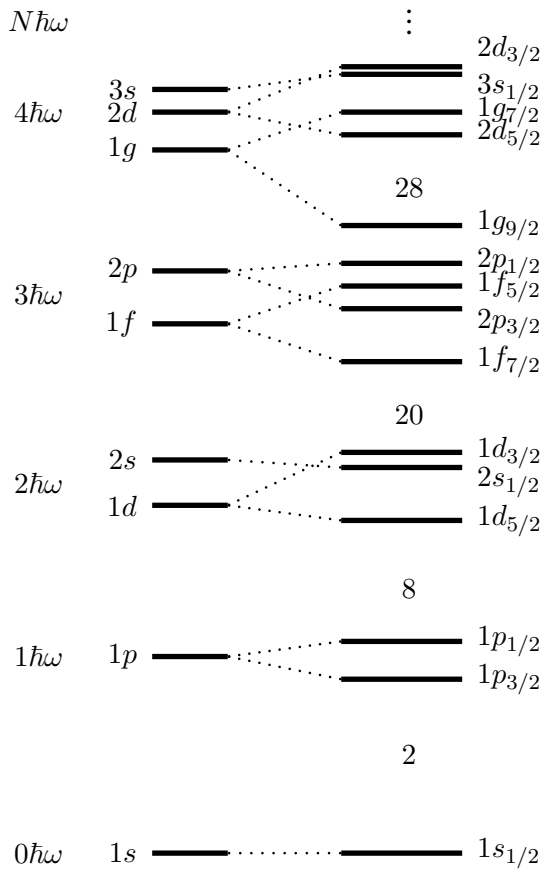

Figure 2.1: Energy levels in single-particle shell model, restricted to four major shells. From left to right the splitting of the major oscillator shells due to the l^2 interaction, and spin-orbit splitting to the right. The levels are labeled with their quantum numbers nlj. The degeneracy of the levels is $2j + 1$, the classical magic numbers are indicated between the shells. The orbital gaps are not to scale.

for the interaction of the valence nucleons ij that is not captured by the mean field.

There are microscopic models to derive the residual interactions from the nucleon-nucleon potential, what is described later, or taking a phenomenological approach. Effective components of the residual interactions are for instance:

- surface δ interaction
- pairing
- spin-orbit coupling

and others leading to configuration mixing.

In the following, the focus is placed on this Shell Model (SM) approach where residual interactions are considered. The mean-field $\hat{H}_0$, that can be modeled by a spherical harmonic oscillator,

is the only contribution to the inert core nucleons. On top of this core, a few valence nucleons interact with each other within a defined model space treated in $\hat{H}_{\mathrm{res}}$. Solving the Schrödinger equation for $\hat{H}_0$ yields the Single Particle Energy (SPE), $\langle\phi_i|\hat{H}_0|\phi_i\rangle$ with the single-nucleon states $|\phi_i\rangle$. The Two-Body Matrix Element (TBME) of the nucleon-nucleon interactions reads in general $\langle\phi_i\phi_j|\hat{H}_{\mathrm{res}}|\phi_k\phi_l\rangle$.

Famous representations for the determination of effective, semi-empirical TBMEs within the sd shell are the USDA/USDB interactions [32, 33], based on the work by Wildenthal [34]. The empirical TBME is obtained e. g. from a comparison between the energy that is calculated using $\hat{H}_0$ and two non-interacting valence nucleons in a defined state $j_1 j_2(J)$, and the same observable determined from experiment. Eventually, this leads to a fit parametrization of the interaction energy [35]. The effective (diagonal) TBME contribution $E_J = \langle\phi_i\phi_j TJ|\hat{H}_{\mathrm{res}}|\phi_i\phi_j TJ\rangle$ (with total angular momentum J) is deduced where the underlying forces are not resolved. The single-particle states $|\phi_i\rangle$ are written in short as j_i including all their quantum numbers. Weighting E_J with the total angular momentum is called the monopole contribution of the TBME

$$V_{j_1 j_2} = \frac{\sum_J (2J+1)\cdot E_J}{\sum_J (2J+1)}. \tag{2.7}$$

The Effective Single Particle Energy (ESPE) is the sum of SPE and TBME and has direct influence on the energy-level spacing. The energy of k nucleons in the valence shell j_2 is for instance

$$E = E_0 + E_{\mathrm{res}} = E_{\mathrm{spe}} + k \cdot V_{j_1 j_2}, \tag{2.8}$$

where the residual energy comes from the interaction between the orbits j_1 and j_2. It is noted that the J-dependent TBMEs contribute to higher multipole orders.

In the just mentioned SM method the residual two-body interaction is modeled in a semi-empirical way but there are also microscopic theories available. The aim of recent research is the understanding of the realistic bare nucleon-nucleon interaction. One approach along this way is the study of the operator structure of the NN potential V_{NN}. The operators are classified into the following components, which are also used to expand the above mentioned monopole interaction,

- central (scalar in spin), e. g. $\sim \hat{\vec{\sigma}}_1 \cdot \hat{\vec{\sigma}}_2$
- spin-orbit (vector in spin), e. g. $\sim (\hat{\vec{\sigma}}_1 + \hat{\vec{\sigma}}_2) \cdot \hat{\vec{L}}$
- tensor (tensor in spin), $\hat{S}_{12}$,

where charge symmetry is presumed, the isospin dependence is either isoscalar or isovector ($\sim \vec{\tau}_1 \cdot \vec{\tau}_2$). The tensor operator $\hat{S}_{12}$ takes in space-coordinate representation the form

$$\hat{S}_{12}(\vec{r}) = \left(\hat{\vec{\sigma}}_1 \cdot \hat{\vec{r}}\right)\left(\hat{\vec{\sigma}}_2 \cdot \hat{\vec{r}}\right) - \frac{r^2}{3}\hat{\vec{\sigma}}_1 \cdot \hat{\vec{\sigma}}_2. \tag{2.9}$$

The other operators which are composed of $\hat{\vec{r}}$, $\hat{\vec{p}}$, and $\hat{\vec{\sigma}}_i$ and which are used to built $\hat{V}_{NN}$ can for example be found in Ref. [30]. Representations for this kind of semi-phenomenological potentials are e. g. the Argonne v_{18}, CD Bonn 2000, or Nijmegen potentials that use experimental phase-shift data and ground-state properties to restrict the parameters in the potential description [36] where some features of three-nucleon forces can already be included. All of them feature a repulsive core and can be described by one-pion exchange in the long-distant region. Those high-precision potentials are e. g. used in the G-matrix approach to calculate TBMEs.

A systematic approach to determine V_{NN} is followed in an Effective Field Theory (EFT), the potential is expanded in powers of $(Q/\Lambda_b)^\nu$ ($\nu \geq 0$) with a typical momentum Q and breakdown scale Λ_b [37]. Given that low-energy nuclear physics acts on momenta in the region of $Q \sim 100\,\mathrm{MeV}/c - 200\,\mathrm{MeV}/c$, a separation of scales is immanent. In this region, nucleons and pions become the effective degrees-of-freedom in a chiral EFT where heavier mesons are not resolved at breakdown scales of $\Lambda_b \sim 500\,\mathrm{MeV}/c$. The dominant contribution comes from the leading-order term $\mathcal{O}((Q/\Lambda_b)^0)$ that includes contact interactions featuring integrated short-range interactions and the interactions from one-pion exchange resolve the long-range interaction. An overview of the hierarchical structure of the nuclear-force diagrams in Weinberg counting can be found e. g. in Ref. [38]. At next-to-next-to-leading order $\mathcal{O}((Q/\Lambda_b)^3)$ non-vanishing three-body forces emerge. Regularization and renormalization issues are not discussed here but are addressed e. g. in Ref. [39]. Besides the chiral EFT other forms like the pion-less EFT or the chiral+Δ EFT, including explicitly Δ-excitation degrees-of-freedom, have been developed.

2.1.2 The Many-Body Problem in *ab-initio* Theory

Above it is discussed how to determine and express the many-body Hamiltonian in a microscopic approach and in particular the nucleon-nucleon potential. There exist approaches to solve the eigenstate problem in Eq. 2.1 with realistic interactions. The eigenstates may be expanded as

$$|\psi_n\rangle = \sum_i c_i \left|\beta_1\beta_2...\beta_A\right\rangle_i . \tag{2.10}$$

In the following, different methods are presented. *Ab-initio* methods start from realistic nucleon-nucleon forces (such as derived in chiral EFT) and can be applied to nuclei up to $A \lesssim 60$. The limit in mass number has been pushed further from $A \sim 12$ in the last decade due to new methods that have been developed. Another approach widely used in the medium-mass region is the SM. Heavier systems are often studied in energy-density-functional theory but it is not further reviewed here.

The number of available *ab-initio* methods show the advances in this field, namely [13]:

- Quantum Monte Carlo (QMC)
- No-Core Shell Model (NCSM)

- Coupled Cluster (CC)
- Self-Consistent Green's Function (SCGF)
- In-Medium Similarity Renormalization Group (IM-SRG)
- Many-Body Perturbation Theory (MBPT) and others.

Two of these methods are chosen to be presented in more detail.

No-Core Shell Model

The *ab-initio* NCSM [40] is a more complex extension of the SM with realistic nuclear forces. Not only a few nucleons are interacting in the valence space but instead all nucleons are active in a truncated model space, therefore there is no inert core. The single-particle basis of choice to describe the many-body state is typically the HO basis. The eigenstates $|\psi_n\rangle$, cf. Eq. 2.1, are expanded in all the possible configurations the nucleons can occupy within a given truncated model space (e. g. as Slater determinants to fulfill anti-symmetrization). The Schrödinger equation is reformulated as matrix eigenvalue problem. The model space is characterized by the maximum number of accessible HO major shells $N_{\max}\hbar\omega$, already for ten neutrons and protons distributed up to the sd-shell the plain number of possible Slater determinants is approx. 3×10^{10}. This dimension puts already a computational limit on solving the many-body problem, especially to have sufficiently large $N_{\max}\hbar\omega$ to reach convergence. Simply speaking, the Hamiltonian with its mixing matrix elements $\langle\psi_i| \hat{H} |\psi_j\rangle$ needs to be diagonalized to solve Eq. 2.1.

One approach is to restrict oneself to relevant basis states before the diagonalization and reject others. This idea is followed in the Importance-Truncated No-Core Shell Model (IT-NCSM) where a weight is put to all basis states by comparison to a reference state from a small model space in first-order perturbation theory. And only those states are considered further that have a sufficient overlap with the reference state [13].

Another method that can extend the mass limit A to approx. 60 in *ab-initio* theory is combining two of these methods, namely the NCSM and IM-SRG. The idea of renormalization is already applied in the EFT approach by the reduction in resolution establishing a low-energy nuclear physics theory [41, 42]. The advantage of the renormalization-group technique is to decouple low from high momentum interactions instead of just truncating the interaction. A renormalization-group method that allows to handle also three-body interactions is the Similarity Renormalization Group (SRG). Figuratively speaking, in the SRG the Hamiltonian matrix is evolved towards a band-diagonal form [43] and the off-diagonal elements, i. e. the coupling of low and high momentum components where multi-particle/multi-hole excitations might be of low contribution, are reduced. A unitary transformation is applied to the Hamiltonian in infinitesimal

steps expressed in a flow equation with flow parameter s [41, 43]

$$\frac{\mathrm{d}}{\mathrm{d}s}\hat{H}(s) = \left[\left[\hat{G}(s), \hat{H}(s)\right], \hat{H}(s)\right], \tag{2.11}$$

with the unitary transformed nuclear Hamiltonian $\hat{H}(s) = \hat{U}(s)\hat{H}\hat{U}(s)^\dagger$ (where $\hat{U}^\dagger\hat{U} = \hat{U}\hat{U}^\dagger = 1$), where the Hermitian operator $\hat{G}(s)$ is chosen to pre-diagonalize $\hat{H}(s)$. It is emphasized that the SRG evolution induces higher many-body forces: starting with nucleon-nucleon interactions also three-body interactions are present. Eventually, the evolved Hamiltonians are used in a NCSM calculation to solve the many-body problem in a smaller space, resulting in ground and excited state energies and their eigenvectors which are used to consistently obtain other observables.

Self-consistent Green's Function Theory

Another theory to solve the many-body problem is based on Green's functions that has recently been applied to nuclear physics and is also capable to address the mass region $A \approx 100$ [44]. The idea of SCGF is to calculate excitations from the ground state or similarly add or remove nucleons to/from it. Therefore, propagators are introduced to move particles. In a basic case, the propagator (or Green's function or correlation function) for a free particle with Hamiltonian $\hat{h}$ – the time evolution of a particle given by state $|\psi(t_0)\rangle$ from time t_0 to t – is calculated like

$$|\psi(t)\rangle = \exp\left\{-\frac{i}{\hbar}\hat{h}(t-t_0)\right\}|\psi(t_0)\rangle\,. \tag{2.12}$$

The Green's function $G(\vec{r}', \vec{r}; t, t_0)$ is defined in space as

$$\begin{aligned}\langle\vec{r}'|\psi(t)\rangle &= \int \langle\vec{r}'|\exp\left\{-\frac{i}{\hbar}\hat{h}(t-t_0)\right\}|\vec{r}\rangle\,\langle\vec{r}|\psi(t_0)\rangle\;\mathrm{d}\vec{r} \\ &= \int G(\vec{r}', \vec{r}; t, t_0)\,\langle\vec{r}|\psi(t_0)\rangle\;\mathrm{d}\vec{r}.\end{aligned} \tag{2.13}$$

Coming back to the many-body problem using the formulation in Eq. 2.1. The creation and annihilation operators are well suited to describe the propagation of a particle, they add or remove a particle at time t and position $\vec{r}$. Instead of evolving the state in time, in the approach by Cipollone et al. [44] as discussed here, the operators are evolved in time what is known as Heisenberg representation. The creation operator $c_\alpha^\dagger$ (similar is the annihilation operator c_α) is evolved like

$$c_\alpha^\dagger(t) = \exp\left\{\frac{i}{\hbar}\hat{h}t\right\}c_\alpha^\dagger\exp\left\{-\frac{i}{\hbar}\hat{h}t\right\}. \tag{2.14}$$

The one-body propagator,

$$g_{\alpha\beta}(t,t') = \langle\psi|\hat{T}\left[c_\alpha(t)c_\beta^\dagger(t')\right]|\psi\rangle\,, \tag{2.15}$$

is adding a particle in single-particle state β at time t' to the system and removes correspondingly a nucleon from state α at time t, representing i. e. the probability amplitude for a nucleon traveling. $\hat{T}[\dots]$ is the time-ordering operator. The approach can be extended in the same way to define e. g. the two-particle/two-hole propagator or other one-/two-body operators (including the nucleon-nucleon potential). Reference [45] makes use of the energy-representation of the propagator, the Fourier transform from t to ω is

$$\begin{aligned} g_{\alpha\beta}(\omega) &= \langle\psi_0|\, c_\alpha \frac{1}{\hbar\omega - \left(\hat{H} - E_0^A\right) + i\eta} c_\beta^\dagger \,|\psi_0\rangle \\ &+ \langle\psi_0|\, c_\beta^\dagger \frac{1}{\hbar\omega + \left(\hat{H} - E_0^A\right) - i\eta} c_\alpha \,|\psi_0\rangle \\ &= g^p_{\alpha\beta}(\omega) + g^h_{\alpha\beta}(\omega), \end{aligned} \tag{2.16}$$

separated into particle and hole propagator, with the ground-state wave function $|\psi_0\rangle$. Solving the Dyson equation [44] obtains finally the correlated propagator

$$g_{\alpha\beta}(\omega) = g^0_{\alpha\beta}(\omega) + g^0_{\alpha\gamma}(\omega)\Sigma^\star_{\gamma\delta}(\omega) g_{\delta\beta}(\omega), \tag{2.17}$$

where $g^0_{\alpha\beta}(\omega)$ refers to the reference state, e. g. Hartree-Fock-Bogoliubov states. The self-energy $\Sigma^\star_{\gamma\delta}(\omega)$ is determined in the iterative, self-consistent way together with the propagator itself. For calculation details it is referred to Refs. [44, 45]. The authors address the computation of the self energy by applying the third-order algebraic construction scheme or for open-shell nuclei the Gorkov formalism, including three-body forces.

Another advantage of the SCGF method is that nucleon spectral functions, which give momentum distributions and spectroscopic-strength distributions, can be calculated directly. The particle spectral functions read

$$S^p_{\alpha\beta}(\vec{p},\omega) = \sum_n \langle\psi_0|c_\alpha|\psi_n^{A+1}\rangle \langle\psi_n^{A+1}|c_\beta^\dagger|\psi_0\rangle \,\delta\left(\hbar\omega - \left(E_n^{A+1} - E_0^A\right)\right), \tag{2.18}$$

while the spectral function for a hole excitation is inferred the same way. Integration of $S^p_{\alpha\beta}(\vec{p},\omega)$ in momentum results in the spectroscopic strength of a certain state ψ_n (with eigenenergies E_n). Adding a proton to ^{28}O results in the spectrum of ^{29}F as being discussed in Sec. 8.2.7.

Continuum Shell Model

The before-mentioned methods struggle to account for states in the continuum. So far, bound states are considered but the nucleus is an open quantum system where the coupling to the continuum causes a residual impact on bound states and lead to resonant states itself, that decay via particle emission.

There can occur resonant states but also non-resonant scattering states in the continuum. The continuum shell model is an approach to account for that, its complex-energy implementation is called Gamow SM [46]. It makes use of the Berggren single-particle basis which combines bound, and resonant, and non-resonant states in the complex-energy plane [13]. The challenge is to isolate the many-body resonant states from scattering eigenstates [46]. The non-resonant continuum is thus discretized but still the number of Slater determinants grows vastly [13].

One approach to efficiently diagonalize the Hamiltonian matrix and to determine the eigenenergies is the density-matrix renormalization group. This method using the Berggren basis in NCSM calculations is under development [13].

2.2 Neutron-unbound States

This section lays the basis for the analysis of the neutron-decay states in ^{29,30}F that are experimentally studied in this thesis. As described in the previous section, the solution of the eigenwert problem in a simple mean-field potential is known from basic quantum mechanics. In the fermionic nuclear many-body system the energy levels are filled successively with nucleons starting from strongest binding up to the Fermi level. For β-stable nuclei the nucleons occupy levels that are strongly bound in the potential well with an average binding energy of $8\,\mathrm{MeV}$ per nucleon. In particular, the neutron-separation energy becomes smaller and the nuclei are more weakly bound for large isospin asymmetry [20]. The bound-state structure is e. g. investigated with scattering experiments, transfer reactions, or nucleon-removal reactions in combination with γ-ray spectroscopy [16].

These measurements are characterized by a significant increase of cross section around and at the particular discrete state – called a resonance. Withal, this is a common behavior exploited in all scattering experiments and in all fields of physics. It is most simple observed for oscillations in classical mechanics where the oscillation amplitude increases dramatically at the eigenfrequency.

Considering a simple Hamiltonian as in Sec. 2.1.1 with a potential of infinitely high walls as the harmonic oscillator, all solutions in terms of energy eigenvalues are negative and thus bound, the spectrum is discrete. On the other hand, in a mean field potential (including residual interactions) that is now of finite depth the solutions are also states with energies larger zero. The spectrum of scattering states, where resonances are embedded, is continuous [47]. Especially, the residual interaction shifts energy levels as outlined before, cf. Sec. 2.1.1, even above the particle-separation threshold such that single-particle resonances are formed. Furthermore, bound and continuum states can be mixed. Theoretical calculations are still difficult, even in a discretized continuum. A recently further developed approach namely the Gamow Shell Model (GSM) addresses a multiconfigurational SM, it is mentioned in Sec. 2.1.2.

A resonance is described by its energy E_r, width Γ ($\sim$ Full Width at Half Maximum (FWHM)), and the decay with angular momentum (J), and parity (π). The study of resonances is obviously

subject of scattering theory where these particular states are populated in a nuclear reaction. The interacting particles are trapped for a short time by a potential barrier, the decay lifetime τ is

$$\tau = \frac{\hbar}{\Gamma}. \tag{2.19}$$

The analysis of the scattering matrix allows to determine the resonance energies. The scattering matrix can be parametrized e. g. in terms of R-matrix or, in a formally equivalent approach [48], can be calculated in a SM approach.

Experimentally, resonances are characterized by their signature in the excitation function, i. e. peaks, dips, or interference patterns in the cross-section curve as function of energy. This is also reflected in the resonance-scattering phase shift δ, that shows a sharp increase at the resonance energy [49],

$$\delta(E) \sim \arctan\left(\frac{\Gamma/2}{E_r - E}\right). \tag{2.20}$$

Coming back to nuclear physics, a striking problem at its time was the analysis of capture reactions of slow neutrons by a nucleus. Breit and Wigner [50] describe this process for the first time in detail and find the formal description of the resonance cross section what is today often referred to as Breit-Wigner line shape. Starting from transition amplitudes, the capture cross section σ_c is derived for resonant absorption to an intermediate state and subsequent γ-ray emission. The result in its original form is [50]

$$\sigma_c = \frac{\Lambda^2}{\pi} S \frac{\Gamma_s \Gamma_r}{(\nu - \nu_0)^2 + \Gamma^2}, \tag{2.21}$$

with the statistical factor S, the de-Broglie wavelength Λ, and the resonance energy ν_0. Γ_i is the width that characterizes the channel i: Γ_s is the entrance channel and Γ is the total width that is dominated by the width of the capture state Γ_r.

Generally speaking, the S-matrix derived for a Breit-Wigner type resonance takes the form [49]

$$S(E) \sim \frac{E - E_r - i\Gamma/2}{E - E_r + i\Gamma/2}. \tag{2.22}$$

The resonance condition is fulfilled at the pole of the denominator, $E = E_r - i\Gamma/2$, in the complex-energy plane. Thus, states and in particular resonances can be defined in a mathematically way by the position of the pole in the complex-energy plane, see Fig. 2.2 [51]:

- $\mathrm{Re}(E) > 0$ & $\mathrm{Im}(E) < 0$: resonance (or unbound state)
- $\mathrm{Re}(E) < 0$ & $\mathrm{Im}(E) = 0$: bound state
- $\mathrm{Re}(E) > 0$ & $\mathrm{Im}(E) = 0$: scattering state

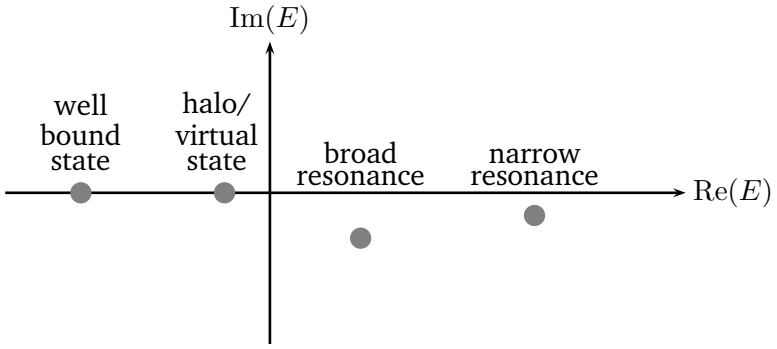

Figure 2.2: Resonant states, indicated by filled circles, in the complex-energy plane as solution of the scattering matrix S. Figure adapted from [51].

A special case occurs when there is no angular barrier present for $l = 0$ neutron scattering – called virtual state ($\Gamma > 4E_r$) [52]. It is not a bound state although the pole is found to be on the negative $\mathrm{Re}(E)$ axis but it is located on the negative $\mathrm{Im}(p)$ axis in the momentum plane ($\mathrm{Re}(p) = 0$) other than a bound state. The pole there is at $p = i/a$ with scattering length a.

In the experiment here, a kind of direct reaction namely a removal reaction is used to populate unbound states. The state of interest is populated through one channel and decays to one of the open channels. The time scale of the population mechanism is much smaller than the interaction time in the resonant state, the width of the incoming channel is negligible and the total width is determined by the decay channel. Thus, a single resonance can here be described by the following simple single-level Breit-Wigner line shape

$$\frac{\mathrm{d}\sigma}{\mathrm{d}E} \propto \frac{\Gamma}{(E - E_r)^2 + \Gamma^2/4}. \tag{2.23}$$

The corrections, coming e. g. from an energy-dependent width, and assumptions applied in the derivation for special decay mechanisms are explained in Sec. 4.5. Other theoretical considerations for scattering other than for a neutral spinless particle or the influence of the potential are described e. g. in Ref. [53].

Additional information can be deduced from the resonance width in terms of the single-particle character of the resonance, i. e. the spectroscopic factor [54, 55]. The spectroscopic factor can be defined as in Ref. [56] as the ratio between the formal reduced width (measured) and the reduced one for a pure single-particle resonance

$$S = \gamma^2/\gamma^2_{\mathrm{sp}}, \tag{2.24}$$

or equivalently $S = \Gamma/\Gamma_{\mathrm{sp}}$, Γ itself depends on the angular momentum l. Formally, it is defined as overlap integral between a single-particle state and the corresponding knockout state (in a removal reaction) [54]. When S approaches unity the fragment-neutron configuration is considered

as a "pure" single-particle neutron state. Thus, it also puts an upper limit to the width for different l and can hint to the angular momentum of the state. However, this limit needs to be treated with caution because Γ_{sp} is model dependent [56]. For the estimation of the single-particle width see Sec. 4.5.

2.3 Neutron Correlations and Decays

As discussed, particle-unbound states are characterized by their resonance energy and width. The decay behavior is a field for nuclear-structure studies and may give insight into few-body physics.

In case of a two-body decay, the decay kinematics is determined by energy and momentum conservation, the energy is shared in a back-to-back emission of the partners. Instead, three-body decays, as for $^{29}\mathrm{F}^{*} \rightarrow ^{27}\mathrm{F}+n+n$, exhibit a wider physics. The relative three-body energy is here called E_{fnn} for the decay into heavy fragment f and two neutrons n. The following decay types are distinguished basically based on resonance energy, width, and possible intermediate states with the one- and two-particle separation thresholds relative to the initial level, D_n and D_{2n}, respectively, cf. Fig. 2.3:

- genuine three-body decay
- di-neutron (di-proton) decay
- sequential decay

The observables in Jacobi coordinates are sensitive to the different types, cf. Sec. 4.6.

2.3.1 Direct Decay

The direct-decay mechanism is often observed for nuclei beyond the drip lines. One kind is a phase-space decay where the kinematic variables of the particles uniformly fill the phase space. It is also characterized by the fact that $D_{2n} < 0$ and $D_n > 0$ of the mother nucleus, the decay particles share their energy without passing an intermediate state, see Fig. 2.3a. The three-body phase-space integral is [58]

$$R_3 = \int \delta^4 \left(P_0 - \sum_{j=1}^{3} P_j \right) \prod_{i=1}^{3} \delta \left(P_i^2 - m_i^2 \right) \, \mathrm{d}^4 P_i, \tag{2.25}$$

with the four-momentum vectors of the mother particle P_0 and the decay particles P_i and their rest masses m_i. Momentum and energy are conserved by having included kinematical factors expressed in δ-distributions. Other conditions are either implicitly included by calculating only known reactions or are left unspecified like restrictions on the angular momentum. The statistical

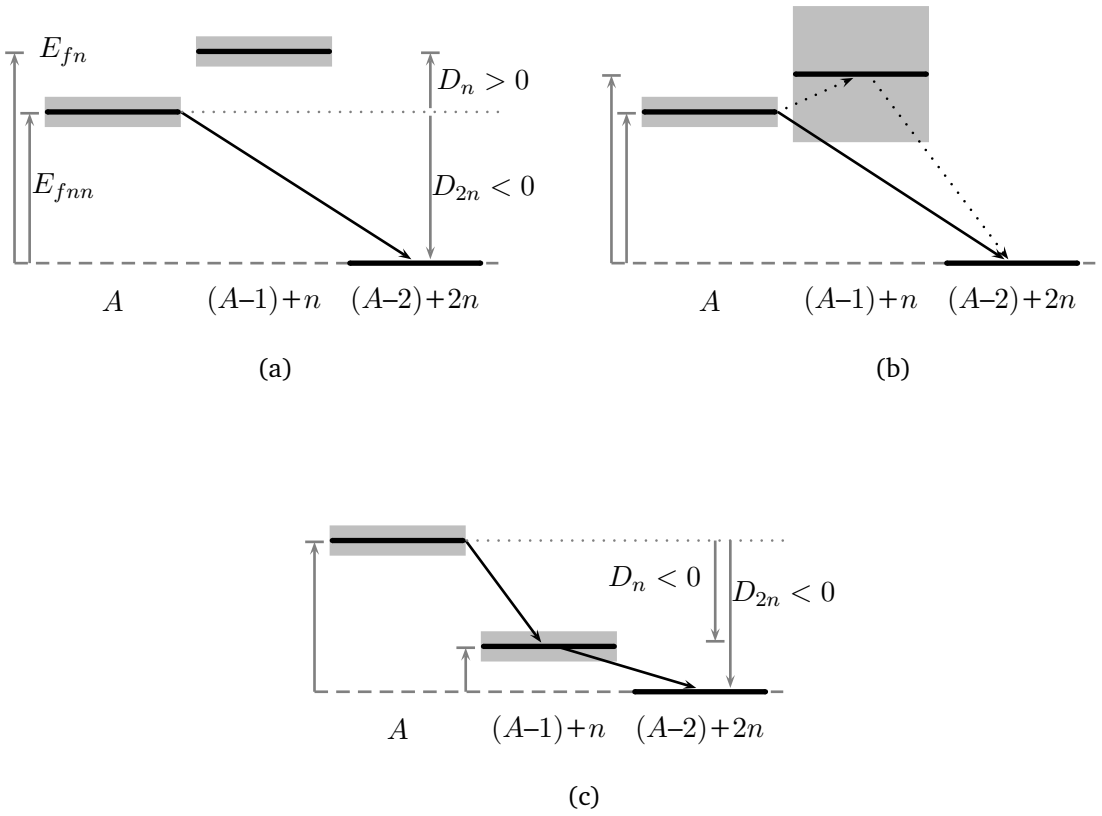

Figure 2.3: Illustration of different two-neutron decay patterns for direct (2.3a, 2.3b) and sequential (2.3c) decay from the mother nucleus (A) via an intermediate ($A-1$) system to the daughter (A-2) nucleus. Figure (2.3a) Genuine three-body (phase-space) decay, (2.3b) phase-space decay directly to daughter nucleus or sequentially to daughter nucleus via broad intermediate resonance. The decay path is denoted with black arrows, where E_{fnn} is the three-body and E_{fn} the two-body intermediate-state energy. The resonance width is shown as gray-shaded area. D_n and D_{2n} denote the one- and two-neutron separation energies relative to the initial state, respectively. The di-neutron decay is not explicitly pictured because it features a special phase-space decay. Figure adapted from Ref. [57].

factor is also accounted for,

$$\delta\left(P_i^2 - m_i^2\right)\,\mathrm{d}^4P_i = \frac{p_i^2}{E_i}\,\mathrm{d}p_i\,\mathrm{d}\cos\theta_i\,\mathrm{d}\phi_i, \tag{2.26}$$

in spherical coordinates with the total three-momentum of the particles p_i. This means, the larger the momentum is, the more states are available to distribute it.

In Jacobi coordinates, the fractional-energy distribution ϵ behaves for a direct decay like [59]

$$\frac{\mathrm{d}\sigma}{\mathrm{d}\epsilon} \sim \sqrt{\epsilon\,(1-\epsilon)}. \tag{2.27}$$

However, the decay is usually not free of Final State Interactions (FSI), especially the nn interaction contributes. Thus, the three-body observables as the fractional-energy distribution gets disturbed. Reference [60] models this effect in terms of a correlation distance between the neutrons (including the scattering length), thus claiming a sensitivity to the spatial distribution of the source nucleus. In the next section this is discussed in terms of the di-neutron decay. Sometimes, an additional category called "democratic decay" is introduced for the decay via a broad resonance [57].

2.3.2 Di-neutron Decay

The di-neutron (or di-proton) decay is a special kind of the direct two-particle decay but not yet studied sufficiently and still debated controversially. However, it is subject of recent efforts in nuclear-structure and -reaction physics on the experimental and theoretical side. Other than in a direct three-body break-up, the decay is seen to proceed through the emission of a di-neutron system that breaks up afterwards [61]. Moreover, the question can be asked whether this di-neutron configuration is present in the initial nucleus.

The pairing interaction may suggest that the neutrons are also spatially localized but Refs. [62] and [59] make very clear that the pairing interaction alone is not a sufficient criteria to create the di-neutron correlation. Again, a di-neutron describes here a compact spatial configuration (e. g. small relative angle) of two neutrons inside the nucleus, others may define it as momentum relation instead.

Hagino and Sagawa [62] state that a coupling of single-particle orbits with opposite parity is essential to form strong di-neutron correlations. This effect is enhanced in weakly-bound or unbound nuclei due to the coupling to continuum states. Still, this does not mean that a pairing di-neutron configuration implies a low-energy enhancement in the two-neutron relative-energy E_{nn} spectrum [59] – it can be mimicked by FSI. According to the uncertainty principle, the short distance translates into a large relative momentum instead.

The FSI is immanent in the decay kinematics and distorts any di-neutron correlation. The neutron-neutron scattering length $a_{nn} = -18.59(40)\,\mathrm{fm}$ (obtained in $\mathrm{D}(\pi^-,\gamma)nn$ reaction) [63]

has impact on the correlation and decay width due to its long range. The FSI can be expressed for nn s-wave interaction as [59]

$$F_{\mathrm{FSI}}(E_{nn}) = \frac{a^2}{1 + 2\mu E_{nn} a_{nn}^2}, \tag{2.28}$$

and is used in the Migdal-Watson approximation [64, 65] as modification of the low-energy relative-energy spectra. It factorizes with the phase-space contribution F_{PS},

$$\frac{\mathrm{d}\sigma}{\mathrm{d}E_{nn}} \sim F_{\mathrm{FSI}}(E_{nn}) F_{\mathrm{PS}}(E_{fnn}, E_{nn}). \tag{2.29}$$

Watson [64] defines the FSI as interaction that modifies the reaction cross section of particles produced in a nuclear reaction. The FSI acts among particles after the reaction ("primary mechanism") but as long as they get away from this mutual force.

Grigorenko et al. [59] conclude that a low-energy enhancement in the E_{nn} spectrum is necessary to discuss a di-neutron emission but not sufficient as said above. The three-body decay needs to be treated in an extensive manner, while the E_{nn} spectrum is sensitive to the structure and spatial distributions in the internal region of the nucleus and thus physics information can be extracted from the di-neutron emission.

Well-suited observables for the studies are fractional energy and angular distributions (with small angle) of binary subsystems in the three-body decay. The system is calculated in Jacobi coordinates, as presented in Sec. 4.6, using the same footing in theory and experiment. Grigorenko et al. [59] show exemplarily how the fractional energy $\epsilon_{nn} = E_{nn}/E_{fnn}$ behaves for spatially correlated neutrons in $(s)^2$, $(p)^2$, or $(d)^2$-wave configuration.

A system that has attracted attention recently is the two-neutron ground-state decay of ^{26}O [59, 62]. This nucleus is suspected to show a di-neutron correlation but has experimentally not been measured yet, also because of its small ground-state energy of $20\,\mathrm{keV}$. An additional observable can be the decay lifetime because the width is also affected by the correlations, see Sec. 3.7.

Other approaches that are used to discuss two-neutron decays can, following the above discussion, called into question. The first observations of the di-neutron emitters ^{16}Be [61] and ^{13}Li [66] apply a theory approach introduced by Volya and Zelevinsky [67]. The advantage is that this theory explicitly treats the continuum degree-of-freedom. The di-neutron decay is modeled as a two-step process where the neutron pair separates from the initial nucleus (with relative energy E_{f-nn}) via a virtual state and immediately afterwards the two neutrons break up (E_{nn}). In this picture, the transition amplitude $A(E_{f-nn}, E_{nn})$ is constructed from two two-body decays as given in Ref. [66].

Initial position correlations and sub-barrier effects are typically not included. However, di-neutron decays need to be treated carefully in a comprehensive theory including structure physics as developed among others in Refs. [59] and [62].

2.3.3 Sequential Decay

When a two-neutron decay proceeds energetically favored through an intermediate state, as depicted in Fig. 2.3c, it is called sequential. It can be seen as a two-step process of two subsequent one-neutron decays with resonance energy and width from the initial nucleus into the $(A-1)$ unbound intermediate-state followed by neutron emission populating the $(A-2)$ final state.

Studies suggest that a sequential decay does not favorable take place as soon as it is energetically possible and quantum-number selection rules allow. The width of the intermediate state plays a crucial role. There are no exact criteria known yet, empirical conditions deduced for proton decay are for instance [68]

$$E_{fnn} > \frac{1}{\epsilon_0} E^r_{fn} \tag{2.30}$$

with $\epsilon_0 \sim 0.3 - 0.84$, or

$$E_{fnn} > E^r_{fn} - \frac{1}{2}\Gamma_{fn}, \tag{2.31}$$

or

$$E_{fnn} > 2E^r_{fn} + \Gamma_{fn}. \tag{2.32}$$

However, the sequential decay cannot necessarily be treated as two independent processes although the time scales involved populating the intermediate state and its decay are so different such that the wave function could be treated undisturbed. The timescale of the intermediate state is determined by its width $\tau = \hbar/\Gamma$ ($\sim 6 \times 10^{-21}\,\mathrm{s}$ for $\Gamma = 100\,\mathrm{keV}$) where the reaction time is approx. two orders of magnitude smaller. The width of the initial three-body resonance, the total width, is not simply described as the sum of the two partial widths when sequential and direct decay are competing or the decay proceeds through the tail of the resonances [69], as depicted in Figs. 2.3c and 2.3b.

The description of a resonance line shape looks in the end very familiar like the usual Breit-Wigner distribution,

$$\frac{\mathrm{d}\sigma}{\mathrm{d}E_{fnn}} \sim \frac{\Gamma_{\mathrm{tot}}(E)}{\left(E^r_{fnn} - E_{fnn}\right)^2 + \Gamma^2_{\mathrm{tot}}/4}, \tag{2.33}$$

where the total width Γ_{tot} includes the width parameters of the intermediate resonance. The detailed description of the line shape and its derivation in R-matrix theory is described in Sec. 4.5. The correlation between the neutrons is mainly absent but after both neutrons are emitted, the nn FSI is present due to the large scattering length and might cause an imprint to the nn subsystem. A possible initial di-neutron correlation is not able to be observed through the decay kinematics.

Chapter 3

Status of Current Research

3.1 Nuclear-Structure Evolution in the Island of Inversion

As discussed in the theory chapter 2, the nucleus obeys shell structure as any finite Fermi system [46]. One shell closure that provides particular stability to the system is at nucleon number 20. Already in the 1970's, with the advances in experimental production techniques reaching out to neutron-rich nuclei, the persistence of the neutron magic number $N = 20$ was questioned. Thibault et al. [11] measured the masses of the sodium isotopes $^{26\text{-}32}$Na ($Z = 11$) with an on-line mass spectrometer at the Conseil Européen pour la Recherche Nucléaire (CERN). The determined masses follow smoothly the trend and agree well with their calculations except for ^{31}Na and ^{32}Na where an abrupt increase is recognized in the two-neutron separation energy S_{2n}. Those isotopes are even stronger bound than expected. This finding is interpreted in their conclusion as feature of a region of sudden deformation what is inconsistent with a shell closure where for the naive shell model filling the valence-shell configuration would be $|^{31}\mathrm{Na(g.s.)}\rangle = |\mathrm{core}\rangle \otimes |\pi(d_{5/2})^3\rangle \otimes |(\nu(d_{3/2})^4\rangle$.

With Hartree-Fock calculations filling freely the negative-parity orbital $1f_{7/2}$ and thus causing deformation, Campi et al. [70] can reproduce the S_{2n} in the sodium-isotopic chain. Also, Wildenthal and Chung [71] show that the experimental results cannot be explained with a shell-model space that is limited to sd-shell interactions.

Another striking result at that time comes from the systematic study of the γ-ray energy of the first 2^+-states in the even magnesium isotopes measured by Détraz et al. [12]. They studied the γ-decay of the $^{22\text{-}32}$Mg ($Z = 12$) isotopes after β decay from sodium isotopes also at ISOLDE/CERN. A sharp drop is seen in γ-energy from ^{30}Mg to ^{32}Mg, its excitation energy is only $885\,\mathrm{keV}$. That is in general an indication of a reduced $sd - fp$ shell gap and excitations across. The conclusions of the authors follow those of Thibault et al. [11] and Campi et al. [70] that a region of deformation starts at around $N = 20$ for sodium and neighboring isotopes.

Following, several other experiments concentrated on the study of those isotopes with different

methods and confirmed the findings. Motobayashi et al. [72] deduced the reduced transition strength $B(E2)$ for the 2^+ state in ^{32}Mg in a Coulomb-excitation experiment at $49.2\,\mathrm{MeV/u}$ at the RIKEN Projectile Fragment Separator (RIPS). The obtained large $B(E2)$ value of $454(78)\,e^2\,\mathrm{fm}^4$ can describe a large deformation and indicates the shell quenching.

In a shell-model calculation, first Poves and Retamosa [73] managed to reproduce the binding for neutron-rich neon, sodium, and magnesium isotopes around $N = 20$ by extending the valence space to the $1f_{7/2}$ and $2p_{3/2}$ orbitals. Because of the gain in correlation energy where $2p2h$ excitations are allowed, a transition to deformed nuclear shape takes place.

Warburton et al. [74] coined the term "Island of Inversion" for this region, where intruder configurations are significant in the ground state. The wave function may be written as

$$|\mathrm{g.s.}\rangle = |\mathrm{core}\rangle \otimes \{\alpha\,|0p0h\rangle + \beta\,|2p2h\rangle + \gamma\,|npnh\rangle\}\,. \tag{3.1}$$

The region of question is centered around ^{32}Na although the boundaries were not known at that time and are still not finally identified. The authors conclude from their shell-model calculations within the $sd - pf$ model space that the reason for the gain in binding is not primarily the weakening of the shell gap but the increase in the monopole proton-neutron and neutron-neutron interaction and in higher order correlation-energy contributions.

3.2 Shell Model and Semi-empirical Residual Interactions

It is obvious that the residual interactions are of utmost importance for understanding the neutron-rich nuclei. This aspect is discussed in more detail in the following. In Sec. 2.1.1 the IPM is discussed where the nucleons act in a mean field and single-particle energies for the different orbits are deduced. However, additional correlations like pairing or quadrupole interactions cause shifts to the ESPE, cf. Eq. 2.8. Those NN residual interactions are now discussed only in terms of effective interactions for TBMEs, in a limited valence space for SM calculations. The TBME is dominated by monopole interactions which might be split into central, and spin-orbit, and tensor part (i.e. non-central). The monopole interaction in case of unlike nucleons [30], i. e. changing the proton occupancy, does shift the two-neutron binding energy. The gap energy can be described as [30] (e. g. for $\nu(d) - \nu(f)$ difference when $\pi(d)$ is filled)

$$\Delta = (2j_{\pi 1} + 1)\left(V^{\pi\nu}_{j_{\pi 1} j_{\nu 2}} - V^{\pi\nu}_{j_{\pi 1} j_{\nu 1}}\right), \tag{3.2}$$

where $V^{NN}_{j_1 j_2}$ is short for the TBME $\langle j_1 j_2 | V^{NN} | j_1 j_2 \rangle$. It turns out that $V^{\pi\nu}_{d_{3/2} d_{5/2}} = -1.88\,\mathrm{MeV}$ is strongest for the $N = 20$ isotones [30]. The monopole strength is especially large compared to heavier nuclei what leads to more abrupt changes in the shell structure as observed in the island of inversion. In contrast, the monopole strength weakens more strongly when interactions with continuum states are involved because the neutron-proton wave functions have smaller overlap –

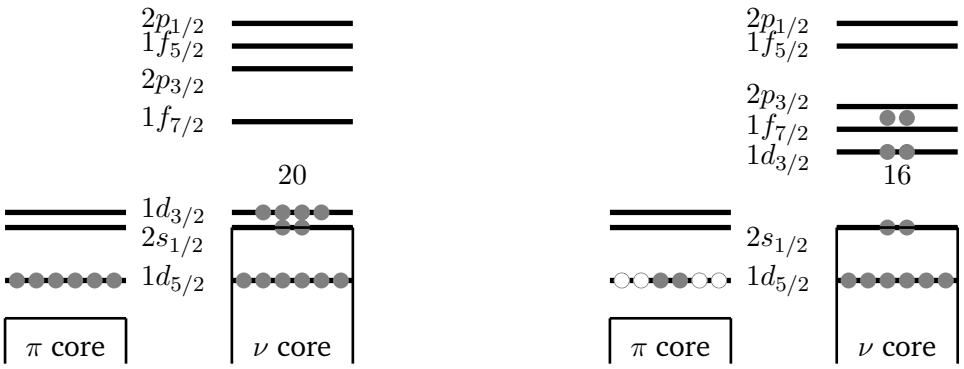

Figure 3.1: Schematic shell-model evolution due to monopole interaction at $N = 20$. Left: fully occupied proton $\pi 1d_{5/2}$ shell and neutron $\nu 1d_{3/2}$ shell. The strongly attractive $V^{\pi\nu}_{d_{5/2}d_{3/2}}$ and repulsive $V^{\pi\nu}_{d_{5/2}f_{7/2}}$ & $V^{\pi\nu}_{d_{5/2}p_{3/2}}$ monopole (mainly) tensor interaction leads to the pronounced shell gap at $N = 20$. Right: Removing protons from the $\pi 1d_{5/2}$ shell, leads to a reduction in the interaction strength. The $\nu 1d_{3/2}$ orbits moves relatively up and the $\nu 1f_{7/2}$ comes down. Thus, reducing the shell gap and a gap at $N = 16$ emerges. Two neutrons are shown as $2p2h$ excitations promoted to the fp shell.

as need to be considered for the study of the fluorine isotopes [30].

A recent experiment at the R^{3}B/LAND setup at GSI addressed this question [75] by investigating neutron-unbound states in ^{25}F and ^{26}F. The results hint to a weakening by $30\,\%$-$40\,\%$ of the effective proton-neutron interaction $\pi d_{5/2} - \nu d_{3/2}$. Thus, continuum degrees of freedom need to be accounted for in the models. The continuum coupling is especially strong in the vicinity of the drip line for such an open quantum system [46].

In case of same-isospin nucleons, that obey the Pauli exclusion principle, the monopole contribution is usually weaker but still significant for the shell-gap size. And for light neutron-rich nuclei charge independence is clearly broken, $V^{\pi\nu} \neq V^{\nu\nu}$. For instance, the gap between $\nu f_{7/2} - \nu p_{3/2}$ becomes smaller while adding neutrons from $N = 20$ to $N = 28$ what might result in the merging of the shell gaps for the magnesium isotopes [76]. The proton $Z = 8$ shell gap remains stable.

3.3 Nuclei in the Island of Inversion

Having presented the basic mechanisms for shell quenching, the consequences for nuclei around $N = 20$ in the island of inversion are discussed. The shell gap develops between $2\hbar\omega$ and $3\hbar\omega$, between the $d_{3/2}$ and $f_{7/2}$ orbitals, it is noted these invoke opposite parities. In the classical shell model, the fluorine isotopes have a proton-particle state in $\pi(d_{5/2})^1$, above the $Z = 8$ shell closure, and the neutrons fill successively the sd shell, with the $\nu d_{3/2}$ orbital for the ^{25}F to ^{29}F isotopes, cf. Fig. 3.1. Heavier fluorine isotopes would cross the $f_{7/2}$ orbital.

Removing four protons from the stable spherical configuration ^{40}Ca, approaching ^{36}S, the shell gap weakens only slightly since the energy difference $V^{\pi\nu}_{d_{3/2}f_{7/2}} - V^{\pi\nu}_{d_{3/2}d_{3/2}}$ is almost constant.

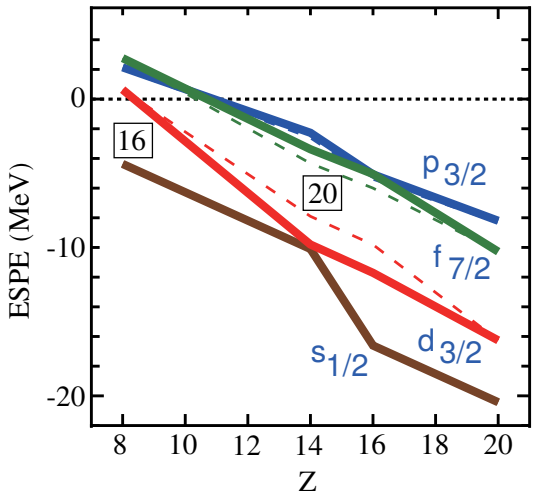

Figure 3.2: Neutron effective single-particle energies calculated with V_{MU} interaction as function of proton number Z for $N = 20$. The solid lines include central and tensor force while the dashed line is only the central force. The $sd - pf$ shell gap decreases for low Z and a gap for $N = 16$ develops. Reprinted figure with permission from Ref. [78], copyright 2019 by the American Physical Society.

Removing two more protons, touching the $\pi d_{5/2}$ shell, the interactions virtually change with tensor interaction $V_{\sigma\tau}$ where $V^{\pi\nu}_{d_{5/2}f_{7/2}} < V^{\pi\nu}_{d_{5/2}d_{3/2}}$ and thus the shell gap reduces to approx. $2\,\mathrm{MeV}$. Formally speaking, the tensor part of the monopole interaction as described by Otsuka et al. [77, 78] can be seen as the origin for this behavior, where spin-flip partners with the same angular momentum in the $\pi\nu$ configuration show an attractive interaction, $j_1 = l \pm 1/2$ and $j_2 = l \mp 1/2$, whereas the parallel-spin interaction is repulsive, $j_1 = l \pm 1/2$ and $j_2 = l \pm 1/2$.

Figure 3.2 illustrates the behavior of the different neutron orbitals with increasing filling of the proton $d_{5/2}$, $s_{1/2}$, and $d_{3/2}$ orbitals (for $N = 20$). The authors use an effective interaction V_{MU} (starting from SDPF-M SPE) including central and tensor force [78]. The shift is more monotonic without tensor interaction and the decrease is slightly stronger for the $1d_{3/2}$ than for $1f_{7/2}$ due to larger wave-function overlap as said above. Below $Z = 14$ the shell gap quenches due to weaker tensor force, the fp orbits become unbound and even invert. This is similar to what Utsuno et al. [79] calculated previously in a Monte-Carlo SM approach.

The reduction of the shell gap around fluorine is predicted with the emergence of the new $N = 16$ magic number. In addition, there is an inversion (or close degeneracy) recognized between the $1f_{7/2}$ and $2p_{3/2}$ (normal-ordered) orbitals that might provoke consequences for the shell structure of the heavy fluorine isotopes as ^{30}F what is also subject of this thesis. These findings manifest in the isotonic chain $N = 20$. For ^{34}Si, the very attractive $\pi d_{5/2} - \nu d_{3/2}$ interaction causes the particular gaps at $Z = 14$ and $N = 20$ what makes it a doubly-magic nucleus. Removing protons from the fully-occupied $\pi d_{5/2}$ orbital the $\nu d_{3/2}$ orbital becomes less bound what eventually leads to the new magic number at $N = 16$ ($s_{1/2} - d_{3/2}$), see Fig. 3.1.

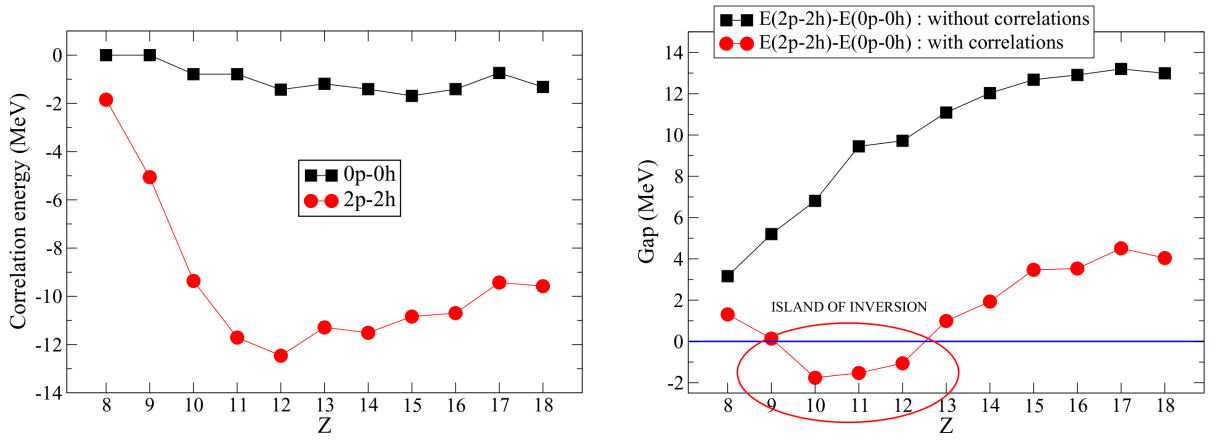

Figure 3.3: Shell model calculations by Caurier et al. [76] with the SDPF-U interactions, comparing effects of interaction energies in the restricted sd valence space or extending it to fp. Left: Correlation energies as function of proton number Z for $N = 20$. $2p2h$ excitations into the fp shell cause a significant gain in energy. Right: Correlation energy included in the $sd - fp$ gap energy calculation. Around $Z = 9 - 12$ the effective gap energy becomes small and intruder configurations are favorable in the ground state – the island of inversion. Reprinted figures with permission from Ref. [76], copyright 2019 by the American Physical Society.

Although the shell gap reduces, it still remains and the orbitals are not degenerate as otherwise e. g. found in ^{11}Be. However, the reason for calling it "inversion" is that the ground-state in this region contains strong admixtures from negative-parity intruder orbitals from fp shell. These configurations become energetically favorable when $2p2h$ (or higher) excitations from sd into fp shell become easily accessible with a reduced gap. This causes eventually a large gain in correlation energy and thus the effective gap vanishes. Caurier et al. [76] show in a shell-model calculation with their developed SDPF-U interaction that the quadrupole-correlation energy can be as large as $12\,\mathrm{MeV}$. In this scheme, quadrupole correlations – usually the second largest contributions after the monopole interaction – are the breaking point for making the island of inversion and may resulting in deformation. Figure 3.3 shows the correlation energy that is strongly changing with proton number Z.

Their calculation predicts the $Z = 9$ ($N = 20$) fluorine isotopes just a the boundary to the island of inversion. Their prediction for ^{29}F is that the $5/2^+$ g. s. is mixed and $60\,\%$ are $0p0h$ contributions [76]. Purpose of this thesis is to help clarify the situation. The ^{29}F ground state could be expanded as

$$\begin{aligned} |^{29}\mathrm{F}(5/2^+, \mathrm{g.s.})\rangle &= |^{28}\mathrm{O}(0^+)\rangle \otimes |\pi(1d_{5/2})^1\rangle \\ &= |^{24}\mathrm{O}(0^+)\rangle \otimes |\pi(1d_{5/2})^1\rangle \\ &\otimes \left\{\alpha\,|\nu(1d_{3/2})^4\rangle + \beta\,|\nu(1d_{3/2})^2\nu(1f_{7/2})^2\rangle + \gamma\,|\nu(1d_{3/2})^2\nu(2p_{3/2})^2\rangle + \ldots\right\}, \end{aligned} \tag{3.3}$$

but many other configurations are possible including higher excitations. The coupling might be

expanded into Clebsch-Gordan coefficients.

A stringent test of the shell-structure features connected with the island of inversion is the study of the shape coexisting 0^+ state in ^{32}Mg by Wimmer et al. [80]. As described already, due to excitations across the $N = 20$ shell gap collective configurations gain energy and become low lying in energy, or even the ground state itself becomes the deformed configuration, thus having different nuclear shapes at similar (excitation) energies. ^{32}Mg is a candidate where the spherical $0p0h$ configuration competes with the $2p2h$ 0^+ configuration which can lead to their coexistence. In the experiment, ^{32}Mg is produced in the two-neutron transfer reaction with a tritium target on ^{30}Mg(t, p). The beam at $1.8\,\mathrm{MeV/u}$ was produced at REX-ISOLDE where the protons from the reaction were detected with the T-REX setup and for coincident γ-ray detection MINIBALL was used. The ground state and an excited state at $1058(2)\,\mathrm{keV}$, that both are of $l = 0$ character as determined from the proton's angular distribution, are identified and thus both are 0^+ states. In comparison to Monte Carlo SM calculations, using the SDPF-M interaction, the ground-state is the dominant $2p2h$ configuration and the excited 0^+_2 state is instead of predominant sd character, it hints to a substantial shape mixing. Also, the $\nu 2p_{3/2}$ contribution is larger than originally predicted by the model in both cases. [80]

3.4 Neutron-rich Fluorine Isotopes

The only experimental-available spectroscopic information for ^{29}F comes from an in-beam γ-measurement at RIBF. Doornenbal et al. [81] measured the excitation-energy spectrum of ^{29}F bound states that are populated in a proton-removal reaction. A ^{30}Ne beam at $228\,\mathrm{MeV/u}$ impinged on a carbon target at the Big RIKEN Projectile Fragment Separator (BigRIPS) beam line, while the fragment ^{29}F is identified in the ZeroDegree Spectrometer (ZDS). The de-excitation γ-rays are measured with the Detector Array for Low Intensity radiation 2 (DALI2) (see Sec. 5.3.2). The authors identified a single state at $1080(18)\,\mathrm{keV}$, the spin and parity could not be assigned experimentally.

Comparing the experimental finding to theory shows a striking difference to USDA/B effective shell-model calculations, cf. Fig. 3.4a. The calculations do not even determine the two-neutron separation energy correctly, the first excited state would be located at approx. $3.5\,\mathrm{MeV}$.

This is a clear indication that the shell gap is too large and interaction energy is missing. In contrast, the calculation with the SDPF-M effective interaction, extending the valence-space interaction to include $\nu(1f_{7/2})$ and $\nu(2p_{3/2})$, as introduced in Refs. [79, 81], produces additional binding and the excitation energy agrees better. In comparison to the calculation the ground state is assigned to $5/2^+$ and the excited state to $1/2^+$. In order to reproduce the experimental result, the gap energy is as small as $1\,\mathrm{MeV}$ with $0p0h$ contributions of only $7.9\,\%$ and $1.0\,\%$ for ground and excited state, respectively. In addition, the authors show a clear correlation to ^{28}O where ^{29}F can be seen as proton-attached state of ^{28}O. ^{29}F$(1/2^+)$ is described as coupling $|^{28}\mathrm{O}(2^+)\rangle \otimes |\pi d_{5/2}\rangle$

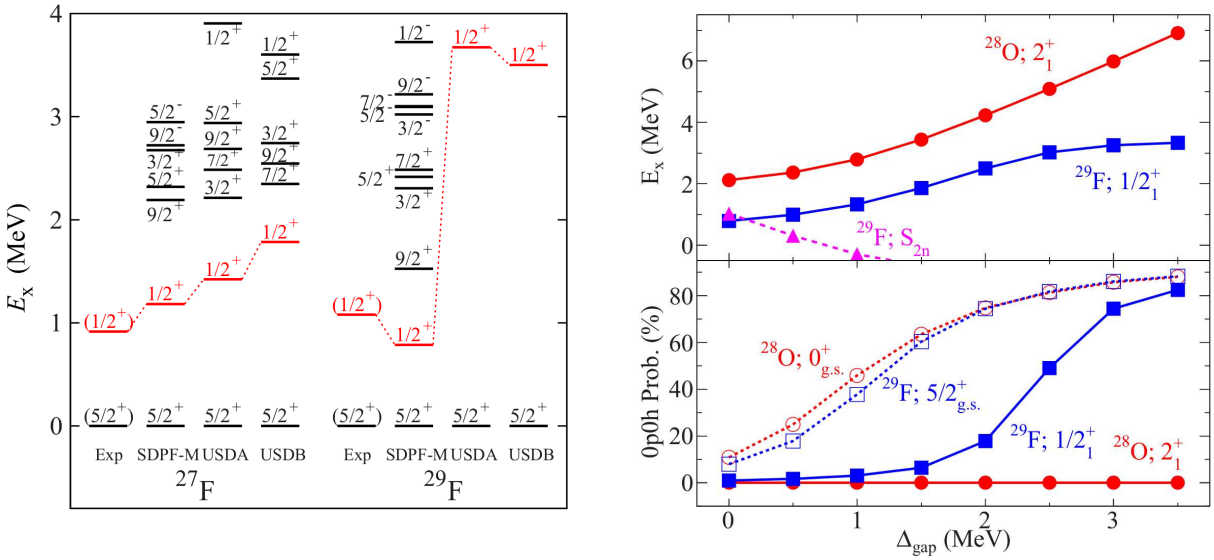

(a) (b)

Figure 3.4: Left: Comparison between experimental results and shell-model calculations of the bound-state spectroscopy of ^{27}F and ^{29}F from RIBF by Doornenbal et al. [81]. The calculations including fp shells in the interactions reproduce the experimental results. Right: Correlation between ^{29}F and ^{28}O as proton-attached calculation for the $0p0h$ probability (bottom) and excitation energy (top). The experimental result is only reproduced with a substantial amount of multi-particle/multi-hole excitations, the same is true for ^{28}O given the calculations. Reprinted figures with permission from Ref. [81], copyright 2019 by the American Physical Society.

and the ground state is the coupling of the ^{28}O(g. s.) and the open-shell proton. The conclusion is that also ^{28}O is affected by intruder configurations and is not a doubly-magic nucleus in a classical SM sense. Besides the spectroscopic information, the mass of ^{29}F was determined by Gaudefroy et al. [82] in a Time-of-Flight (ToF)-based measurement at the Grand Accélérateur National d'Ions Lourds (GANIL). The deduced two-neutron separation energy is $S_{2n} = 1443(436)$ keV.

When talking about the spectroscopy of the fluorine isotopes from a proton-knockout reaction, also the initial nucleus need to be addressed, especially because the neutron-rich neon isotopes themselves are considered to be part of the island of inversion and the spectroscopic strength of the final states depends strongly on the initial structure. Recently, Liu et al. [83] investigated first the intruder configurations in ^{30}Ne by neutron knockout on a carbon target at $228\,\mathrm{MeV/u}$ at RIBF. The γ-decay of the ^{29}Ne fragment was measured as well as longitudinal-momentum distributions, thus the final states in ^{29}Ne are exclusively tagged. The valence-neutron configuration in ^{30}Ne is extracted from the momentum distributions and the spectroscopic strength from the cross sections in comparison to theory. The results show a strong p-wave admixture as well as d-wave contributions whereas f-wave was not found because the involved states are assumed to be unbound at larger excitation energy. The comparison to shell-model calculations suggest that even the $\nu 1f_{5/2}$ and $2p_{1/2}$ orbitals are of importance and contribute as intruder states.

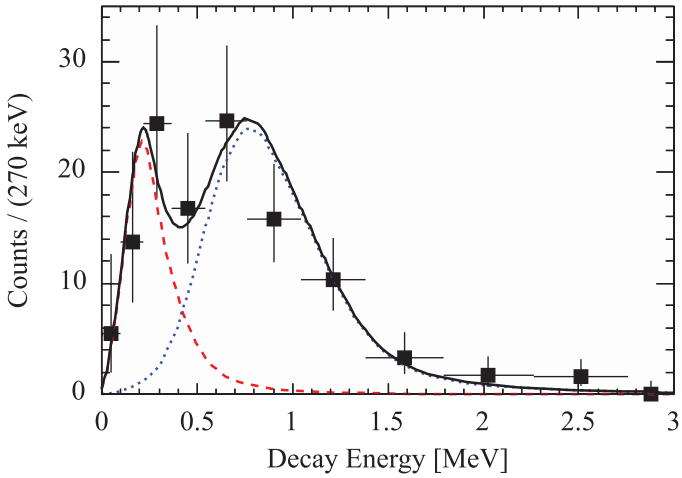

Figure 3.5: Decay-energy spectrum of ^{28}F from ^{29}Ne$(-p)^{27}$F$+n$ measured at NSCL by Christian et al. [86]. Two resonances are identified, the ground state at $220(50)\,\mathrm{keV}$ ($\Gamma = 10\,\mathrm{keV}$) and an excited state at $810\,\mathrm{keV}$ ($\Gamma = 100\,\mathrm{keV}$). More structure is not resolved. Reprinted figure with permission from Ref. [87], copyright 2019 by the American Physical Society.

Another experiment measuring the transition strength of the first-excited 2^+ state in ^{30}Ne obtains a large deformation with quadrupole-deformation parameter $\beta \sim 0.5$ what might be a signature in the island of inversion [84]. The unbound states are accessible in the experiment here, spectroscopic information can also be deduced from the momentum distributions, cf. Ref. [85].

It is known that the very neutron-rich fluorine isotopes show a staggering in binding, the even ones ^{28,30}F are unbound while those with odd mass number ^{27,29,31}F are bound what indicates an energy gain due to neutron pairing and three-body forces. In turn, this means the here investigated excitations of ^{29}F above threshold decay via two-neutron emission into ^{27}F.

The intermediate isotope ^{28}F has so far only been investigated at the National Superconducting Cyclotron Laboratory (NSCL) [86, 87]. In a proton-removal reaction on ^{29}Ne at $62\,\mathrm{MeV/u}$ on a beryllium target, ^{28}F is populated decaying into ^{27}F$+n$. Both reaction products are measured, the neutron is detected in MoNA [87], eventually the invariant mass is determined. The γ-ray array CAESAR was installed to measure coincidentally the de-excitation from bound states in ^{27}F. Besides the ground state, an excited state in ^{28}F, although statistics is low, is found in the decay-energy spectrum, see Fig. 3.5. The location of the ground state is at $220(50)\,\mathrm{keV}$ with decay width $\Gamma = 10\,\mathrm{keV}$, the excited state is at $810\,\mathrm{keV}$, the width is given with $\Gamma = 100\,\mathrm{keV}$. No coincident γ-ray decay is found, but the authors point out explicitly that more resonances could be in the data but are not resolved. With the ground-state energy relative to ^{27}F, the binding energy of ^{28}F is obtained and compared to USDA/B shell-model calculations. The authors conclude from good agreement between theory and experiment that the ^{28}F(g. s.) is dominated by a normal sd-shell configuration. Clearly, more exclusive data are necessary to conclude on the ground-state configuration. The experiment here allows to investigate ^{28}F in neutron- and proton-knockout

reactions on ^{29}F and ^{29}Ne, respectively [60], and comes to a different conclusion. The results show a much richer structure in ^{28}F than has been measured before, as discussed in Sec. 8.2.4.

As in the just-mentioned reaction, and in the ^{30}Ne$(p,2p)^{27}$F$+2n$ reaction investigated here, the possible final states in ^{27}F are of importance to determine the excitation energy. The first direct indication for bound excited states in ^{27}F comes from an inelastic-excitation reaction ^{27}F(p,p') performed at RIPS with the DALI2 array [88]. Two peaks are identified at $504(15)\,\mathrm{keV}$ and $777(19)\,\mathrm{keV}$ but with only 2.4σ and 3.0σ confidence level, respectively. The authors interpret their result as indication for shell-structure apart from sd-shell because only the inclusion of the pf-shell can produce a low bound excited state close to $1\,\mathrm{MeV}$. However, the claimed states are not seen in a recent experiment discussed above where at the same time the γ-decay of ^{29}F is investigated [81]. Instead, a state at $919(12)\,\mathrm{keV}$ is measured that is again best in agreement with the SDPF-M shell model interaction, cf. Fig. 3.4a.

The discussed configuration mixing can gain additional binding and lead to particle stability differently than predicted by sd shell models as it often was a first indication for the onset of the island of inversion. However, only modern accelerators allow to reach out to the drip lines. First, Sakurai et al. [89] found clear evidence for the particle stability of ^{31}F but instability of ^{28}O. In a projectile-fragmentation experiment of ^{40}Ar on a $^{\mathrm{nat}}$Ta target a the RIPS fragment separator the production rates of neutron-rich nitrogen, oxygen, and fluorine isotopes are investigated where particle instability is found namely for ^{24,25}N, ^{27,28}O, and ^{30}F. In contrast, ^{31}F is found to be bound. The results indicate a sudden gain in binding from oxygen to fluorine where adding one proton (in the $1d_{5/2}$ orbital) leads to the binding of at least six more neutrons and may show the doorway into the island of inversion. However, there are no more experimental information available about properties of ^{30}F. Here, the first spectroscopy of ^{30}F is performed. Theory models are still challenged in predicting the neutron drip line. Shell-model calculations with effective interactions clearly see the influence of intruder states, at least the $\nu 1f_{7/2}2p_{3/2}$ shells need to be taken into account [79, 90, 91].

The binding energies are also a good testing ground for *ab-initio* theories along an isotopic chain. Hybrid theories like the NCSM combined with the IM-SRG [92] or combined with perturbation theory [93] can reproduce the oxygen drip line and fluorine binding at the same time. Similar studies can be found in Ref. [44, 45] in the SCGF theory, cf. Sec 2.1.2. In the latter example, the authors address the open-shell nucleus ^{29}F as "particle-attached" calculation of a proton to ^{28}O. In particular, the Dyson equation is solved in the third-order algebraic diagrammatic construction or the Gorkov-SCGF formalism [44] where induced chiral three-body forces are included. A particular advantage of the theory is that the single-particle spectral functions give the spectroscopic strength of the states. The states can become very fragmented, especially for higher excitation energies. Recent SCGF calculations need to be compared to results of the work here.

3.5 Summary to Island of Inversion

The so-called island of inversion is one of the most tested regions in the chart of nuclei. The discussed experiments can only give a brief overview of the experimental efforts to reach the neutron drip line and the techniques like knockout, or transfer, or Coulomb-excitation with γ-ray detection and others to determine nuclear structure information. Conclusive observables are $B(E2)$ values to determine the degree of collectivity, first (2^+) excitation energies and with the invariant-mass and missing-mass technique rather complete energy-level schemes. More details can be found in the reviews Refs. [30] and [94].

However, for the neutron-rich fluorine isotopes experimental information are scarce. In the island of inversion the normal and intruder configurations (like $|\pi(1d_{5/2})\rangle \otimes |\nu(sd)^{-2}\nu(fp)^2\rangle$) are inverted. The reason for competing is vividly the shell quenching and a gain in correlation energy, may leading to deformed configurations [94]. Continuum effects also contribute to the shell evolution what is of particular relevance for the isotopes investigated here. The size of the island of inversion is still an open issue. Following a simple argumentation based on the monopole interaction $\pi(1d_{5/2}) - \nu(1d_{3/2})$ it would range from $Z = 9$ to $Z = 14$ considering the proton number. Indeed, the neutron-rich silicon isotopes do not show a significant collectivity [94], and for the fluorine isotopes more information are needed if those define the onset into the island of inversion, the neon isotopes are definite members. It is more difficult to determine the neutron boundary since basically the whole fp shell can become accessible. The low-N boundary seems to be rather shallow, isotopes with $N \sim 18/19$ show already intruder configurations. Instead, the upper N boundary is not known because the drip lines are not experimentally reachable yet. The red line in Fig. 1.1 indicates the lower N and upper Z boundary of the island of inversion deduced from experimental results [94], whereas the boundary is sometimes still under debate. However, the particular structure and intruder configurations need to be investigated separately for each nucleus. And it is debatable from what percentage of $2p2h$ intruder configurations one calls it island of inversion, ground-state spins might be more conclusive.

Given this survey, it is obvious to look also in other regions of the chart of nuclei for intruder configurations in neutron-rich nuclei around the other ordinary magic numbers. Indeed, there is a group of islands of shell-breaking found [15] associated with the (subshell) magic numbers $N = 8, 14, 20, 28, 40$. Details about the experimental evidence and theoretical explanations can be found in Refs. [30], [94], [95], and references therein.

3.6 Borromean Nuclei

Nuclei are named “Borromean” in analogy to Borromean Rings where three parts are connected and whenever one is disturbed the whole system breaks into the three pieces and no two-body sub-system survives. This phenomenon occurs for nuclei with large isospin asymmetry, known

Borromean nuclei are e. g. ^{8}He, ^{11}Li, ^{14}Be [96], or ^{17}Ne [97] on the neutron-deficient site of the chart of nuclides. This phenomenon might for neutron-rich nuclei be seen as two paired excess nucleons and is thus connected to a halo-nucleus character, but usually needs further investigations and different experimental approaches. It could also be seen as a generalized Ikeda conjecture [98], usually applied to α clusters, where here resonances close to the two-neutron separation threshold may form di-neutron systems. Coulomb-breakup reactions are a sensitive tool to reveal spatial structure in terms of a halo-character [20].

However, the Borromean excited states decay in a three-body decay and thus make a close connection between bound and unbound states and reveal the interactions in an open quantum system, as described in Sec. 3.1. From the decay kinematics itself one can learn about their structure, decays can proceed as genuine three-body, sequential, or di-neutron/proton decay, see Sec. 2.3. It is worth noting, that a di-neutron structure in the initial nucleus is different than in the decay that is governed by FSI. Revel et al. [99] investigate highly-excited states in ^{18}C that are found to be dominated by direct two-neutron emission, but ^{20}O shows a competitive sequential-decay branch. It is the aim of this work to answer such questions also for the Borromean nucleus ^{29}F.

3.7 Lifetime Measurement of the Two-neutron Decay of ^{26}O(g. s.)

Neutron-rich nuclei feature interesting behaviors that are different from the simple shell-model picture. One effect like intruder configurations is described in detail above. Also the limits of binding are re-defined, the neutron drip line in the oxygen isotopes is at the doubly-magic ^{24}O whereas ^{31}F is bound – sometimes referred to as “oxygen anomaly”.

However, ^{26}O is neutron unbound by only $18(5)\,\mathrm{keV}$ as measured by Kondo et al. [100] at SAMURAI with the neutron detector NEBULA. It is speculated by Grigorenko et al. [101, 102] that this low two-neutron separation energy and the presence of $1d_{3/2}$ valence neutrons with $l = 2$ centrifugal barrier leads to an unusually long lifetime of the ground state that is in the order of picoseconds ($1 \times 10^{-12}\,\mathrm{s}$) rather than $\sim 1 \times 10^{-20}\,\mathrm{s}$ as typical for neutron decays [102]. In contrast, recent calculations by the same authors [59] predict a lifetime that is five orders of magnitude smaller than their initial result when introducing their dynamic di-neutron model which considers a semi-realistic structure of ^{26}O with a nucleon-nucleon interaction that governs the emission process.

Experimentally, a lifetime of $\tau = 6.5\,\mathrm{ps}$ is reported from a measurement at NSCL by Kohley et al. [103] which would constitute the first case of a nucleus with radioactive decay via neutron emission. The radioactive decay via proton emission is already firmly investigated, the presence of the Coulomb barrier supports the process and even two-proton correlations are investigated [68]. For ^{26}O there is doubt left because the systematic uncertainties account for $4.3\,\mathrm{ps}$ and the statistic ones for $2.2\,\mathrm{ps}$ in the first measurement.

Part of this thesis work is the development and experimental realization of a new and precise method to measure the lifetime of a nucleus that decays in flight via neutron emission with sensitivity in the picosecond regime. The idea is to produce the neutron-unbound nucleus in a target that at the same time continuously slows down the nucleus and the fragment after (multi-) neutron emission.

The lifetime can be extracted from the velocity-difference spectrum between decay neutron and charged fragment where its shape is characteristic for a certain lifetime. Eventually the shape is compared to simulation studies to extract τ. For decays outside the target, i. e. long lifetimes, there occurs a peak in the spectrum whereas the distribution is flat and broad if the decay happens still inside the target (mainly for short lifetimes) representing the slowing-down process of the fragment but not the decay neutrons.

In order to increase the sensitivity of the method and to have a large energy loss on a short path length the used target needs to have a high stopping power, namely high atomic number and density. The simulations indicate a sensitivity limit of $0.2\,\mathrm{ps}$ of the method. The work on the method and experiment is not described further in this thesis but a detailed description of the method is attached as Ref. [104] to this thesis, App. A.

Meanwhile, the proposed experiment has been carried out at SAMURAI at RIBF for the two-neutron emitter ^{26}O. The target was actually a stack of six targets (4 W + 2 Pt sheets) with a total area density of $14.6\,\mathrm{g/cm^2}$. That is clearly an usually thick target and not suited for spectroscopic measurements but optimized for the experimental conditions and a lifetime region down to $0.5\,\mathrm{ps}$. The arrangement in a stack expands the region of sensitivity such that $0.5\,\mathrm{ps}$ can be identified within $5\,\sigma$ but also longer lifetimes to cover $\tau = 6.5\,\mathrm{ps}$. The investigated reaction channels are the proton removal on ^{27}F and ^{26}F at about $220\,\mathrm{MeV/u}$, where the latter is intended to serve as reference channel in the decay of ^{25}O where no substantial decay lifetime is expected. It is made use of the large acceptance of the SAMURAI setup because the incoming-beam energy spread and the large energy loss in the target result in a wide range of magnetic rigidities. Additional silicon detectors were installed around the target to identify the reaction unambiguously. The experiment was successfully completed in December 2016.

Chapter 4

Experimental and Analysis Methods

This chapter describes the different experimental and analysis methods that are applied to the study of the neutron-rich fluorine isotopes. This includes the production of RI beams, the Quasi-Free Scattering (QFS) reaction mechanism, the invariant-mass technique, and the analysis in terms of Breit-Wigner resonances and three-body coordinates.

4.1 Production of Radioactive-Isotope Beams

Two different approaches exist to produce radioactive ion-beams, namely the Isotope Separation On-Line (ISOL) and inflight-separation technique.

Common to the ISOL method is that a high-intense primary beam, often a proton beam, impinges on a thick production target [14]. The extraction of neutron-rich exotic isotopes depends on the chemical properties of the hot target. The process involves a time scale of at least a few hundred milliseconds. After the different isotopes diffused out of the target, they are separated in an isotope separator, and post accelerated to form the secondary beam, usually at a few tens of MeV only. Facilities making use of this principle exist e. g. at REX-ISOLDE/CERN, at Canada's Particle Accelerator Centre (TRIUMF), or at SPIRAL.

On the contrary, the in-flight separation technique produces the high-energy RI beam directly in nuclear fragmentation or fission reactions to reach out to the drip lines. Accelerator facilities with a coupled fragment separator exist at GSI, or RIBF, and NSCL with beam energies up to $2\,\mathrm{GeV/u}$ and approx. $250\,\mathrm{MeV/u}$, respectively. The fragmentation-type production can be seen as two-step process, called abrasion and ablation [105].

First, a high-energy stable primary beam impinges on a light production target. Considering the typical conditions as available at the RIBF and used to produce neutron-rich fluorine and neon isotopes, a ^{48}Ca beam at $345\,\mathrm{MeV/u}$ impinges on a ^{9}Be target. The abrasion phase is a fast process [105]. Nucleons are ripped off from projectile and target in nucleon-nucleon reactions. This reaction leaves a highly excited pre-fragment which "cools down" by evaporating nucleons

until the Coulomb barrier and other forces hinder the evaporation. The evaporation process can be modeled separately as the ablation phase, the momentum distribution is not much affected anymore.

The momentum distribution of the pre-fragment in the abrasion phase is described by Goldhaber [106]. Assuming, it is the aim to produce ^{30}Ne from the ^{48}Ca beam, the Gaussian width of the momentum distribution of the pre-fragment σ_{pf} is estimated using the Goldhaber formula as following

$$\begin{aligned} \sigma_{\mathrm{pf}}^2 &= \frac{p_F^2}{5} \cdot \frac{\Delta A_{\mathrm{p}} \cdot A_{\mathrm{pf}}}{A_{\mathrm{p}} - 1}, \\ \rightarrow \sigma_{\mathrm{pf}} &\approx \sqrt{\frac{(250\,\mathrm{MeV}/c)^2}{5} \cdot \frac{18 \cdot 30}{47}} = 380\,\mathrm{MeV}/c, \end{aligned} \tag{4.1}$$

with an assumed Fermi momentum of $p_F = 250\,\mathrm{MeV}/c$, and the projectile and pre-fragment mass number A_{p} and A_{pf}, respectively, and their difference ΔA. The necessary momentum acceptance in the laboratory-frame is estimated from the transverse-momentum spread, assumed to be dominated by abrasion, $\sigma(p_\perp) = \sigma_{\mathrm{pf}}$. The angular spread $\Delta\alpha$ can be approximated as

$$\Delta\alpha \approx \frac{\sigma(p_\perp)}{p_p} = \frac{380\,\mathrm{MeV}/c}{42.6 \times 10^3\,\mathrm{MeV}/c} = 9\,\mathrm{mrad}, \tag{4.2}$$

with the total projectile-momentum p_p and transverse momentum $p_\perp$. The fragmentation process defines the technical parameters for the fragment separators, except for the production by fission. The detailed setting of BigRIPS for the experiment is given in Sec. 5.2.

4.2 Quasi-free Scattering Reactions

Direct reactions are a tool to study the structure of nuclei, these include knockout or transfer reactions. Figuratively speaking, single nucleons or configurations are probed and the rest core acts as spectator. The cross section to populate the configurations of interest depends on the overlap between the wave functions of initial and final state. Neutron-rich nuclei are often studied by nucleon-removal reactions, or transfer reactions are also suitable.

Other possible reactions are two-nucleon removals or charge-exchange reactions but typical cross sections are one order of magnitude lower than for single-nucleon removal reactions [107]. However, these reactions can be the reaction of choice to populate very neutron-rich, neutron-unbound nuclei if no other reaction channel is available, as for ^{29}Ne$(p, 3p)^{27}$O. Charge-exchange reactions favor typically a different selectivity to particular final states.

In the experiment discussed here, proton-removal reactions are applied to access nuclei with even larger neutron-proton asymmetry than the initial nucleus. In this case, the proton nuclear configuration is not of primary interest but the populated excited states. However, the proton

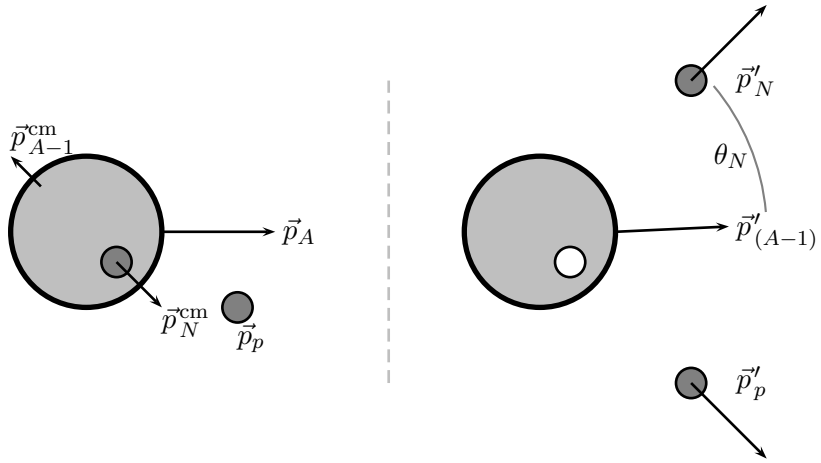

Figure 4.1: Schematic drawing of the quasi-free scattering kinematics in inverse kinematics in the laboratory system (left: before; and right: after the reaction). QFS reaction of nucleus A on a proton target p and knockout of nucleon N.

knockout can provide additional information on the populated configurations as inferred for neutron knockouts.

Hadronic reactions induced on a pure proton target at energies larger than approximately $200\,\mathrm{MeV/u}$ are seen as clean probe to study the nuclear structure. It follows a section about the advantages of quasi-free nucleon-knockout reactions and the spectroscopic information that can be deduced as addressed in detail in Ref. [108].

The QFS reactions in normal kinematics with proton beams and their connection to nuclear structure is discussed theoretically since the 1950's [109] after the shell-model has shown first success. The first experiments were performed at Berkeley Laboratoy [110]. Uniquely, high-energy proton and electron scattering allows to penetrate the nucleus and interact with deeply-bound nucleons. Electron-scattering experiments have famously shown the reduction of single-particle spectroscopic strength what is today associated with e. g. missing short-range interactions in the models [111].

High-energy scattering causes a high-momentum transfer making a localized interaction and emphasizing the single-particle properties. In a qualitative picture, the quasi-free scattering is a reaction where a nucleon knocks another nucleon out of a nucleus and no further FSI takes place. Actually, the mean-free path of the incident proton is in the order of the nuclear radius, the multiple collisions between the reaction particles need to be considered and are theoretically often described with complex optical potentials [108].

Kinematically, the QFS reaction can approximately be seen as a collision between a proton and another nucleon where both nucleons are free particles, sketched in Fig. 4.1. The signature in the non-relativistic case is an opening angle between the two scattered nucleons of $\theta_{NN} = 90°$. As described, a high-energy single proton-nucleon nuclear interaction favors the kinematics of an

almost free scattering reaction. In inverse kinematics in a reaction type $A(p,pN)A-1$, where the target proton is at rest ($\vec{p}_p = 0$), the momentum relation reads in the laboratory system as

$$\vec{p}_A = \vec{p}'_{(A-1)} + \vec{p}'_N + \vec{p}'_p, \tag{4.3}$$

with the proton's and the knocked-out nucleon's momentum, $\vec{p}'_p$ and $\vec{p}'_N$, the fragment momentum $\vec{p}_{A-1}$, and the initial beam momentum $\vec{p}_A$. The momentum transfer $P_q = (E_q, \vec{q})$ is $\vec{q} = \vec{p}'_p$ (or $\vec{p}'_N = \vec{p}_N - \vec{q}$). The sudden approximation is explicitly applied, where the fragment nucleus behaves only as a spectator and is not affected by the reaction, it is assumed:

$$\vec{p}'_{(A-1)} = \vec{p}_{(A-1)}. \tag{4.4}$$

In the sudden approximation, Eq. 4.3 trivially becomes together with the momentum transfer

$$\vec{p}_A = \vec{p}_{A-1} + \vec{p}_N, \tag{4.5}$$

and

$$\vec{p}_N = \vec{p}'_p + \vec{p}'_N. \tag{4.6}$$

Thus, measuring $\vec{p}'_{A-1}$ but not $\vec{p}'_p$ and $\vec{p}'_N$, spectroscopic information of the knocked-out nucleon $\vec{p}_N$ is deduced. Spectroscopic information of the knocked-out nucleon in the initial state can be deduced from the momentum distribution of the spectator [107, 112]. The energy transfer in the reaction is

$$E_q = E_A - \left(E'_{A-1} + E'_p + E'_N\right). \tag{4.7}$$

The excitation energy E_{ex} of the fragment (relative to the Fermi level) is the transferred energy, reduced by the nucleon-separation energy S_N which is necessary to remove the nucleon,

$$E_{\mathrm{ex}} = E_q - S_N. \tag{4.8}$$

Similar calculations can be done for the normal-kinematics case, cf. Ref. [113], but there the $(A-1)$-nucleus is not measured.

The reaction kinematics manifests itself in the angular correlation of the light nucleons after the reaction (p', N') that for large enough momentum transfer leave the target or nucleus. The ideal (free) two-body p-N scattering conditions are mainly modified by relativistic effects, the fact that the scattering partner is bound, and FSI like multiple scattering or absorption. The binding energy reduces the opening angle of the scattered nucleons to less than $\theta < 90^\circ$ [113], the larger S_N the smaller is the opening angle. The azimuthal angle is $\phi = 180^\circ$ in the in-plane scattering.

These two correlations serve as explicit characteristics for the (p, pN) reaction as experimentally shown in Sec. 7.2.

In reaction theory the problem is often treated in an eikonal and Distorted Wave Impulse Approximation (DWIA) approach [114], where the interaction time between the scattered nucleons is small compared to the internal time scale of the moving nucleons – the so called sudden or adiabatic approximation as applied in Eq. 4.4. A recent theory to analyze QFS experiments in inverse kinematics is established by Aumann, Bertulani, and Ryckebusch [115].

FSI are not negligible, absorption e. g. hinders penetrating more deeply-bound nucleons especially for small impact parameters. However, compared to knockout reactions at low energies and with a compound target, QFS reactions (and $(e, e'p)$) probe also the interior of the wave functions and not only the tail region [115]. The theory behind is described in a bit more detail in Sec. 4.3.

4.3 Momentum Distributions

4.3.1 The Four-Momentum Vector

The beam is characterized by its momentum vector $\vec{p}$ and total energy E. These information are combined in the contravariant four-momentum representation $P = (E, \vec{p})^*$. In the laboratory-frame, as the measurement is performed, the total momentum is calculated as

$$p = |\vec{p}| = \beta\gamma m = B\rho \cdot Q, \tag{4.9}$$

with velocity βc, Lorentz factor γ, and rest mass m of the particle or with magnetic rigidity $B\rho$ and charge Q. The energy is

$$E = E_{\text{kin}} + m = \sqrt{p^2 + m^2}, \tag{4.10}$$

with the kinetic energy $E_{\text{kin}} = m(\gamma - 1)$.

The single momentum components $\vec{p} = (p_x, p_y, p_z)$ in a laboratory system are the projection onto the corresponding coordinate-system axes

$$p_x = p \cdot \sin(\theta) \cos(\phi), \tag{4.11}$$

$$p_y = p \cdot \sin(\theta) \sin(\phi), \tag{4.12}$$

and

$$p_z = p \cdot \cos(\theta), \tag{4.13}$$

*in natural units, $c = 1$, throughout the thesis if not mentioned differently

with the polar θ and the azimuthal angle ϕ. The transverse-momentum component $p_\perp$ is

$$p_\perp = \sqrt{p_x^2 + p_y^2}, \tag{4.14}$$

and the longitudinal component is

$$p_\parallel = p_z = \sqrt{p^2 - p_\perp^2}. \tag{4.15}$$

The physics to be studied is generated in the radioactive nucleus that is actually moving with relativistic velocity. This means, the kinematics is boosted into the direction of the velocity vector. The advantage of this Lorentz boost is that e. g. an isotropic neutron decay in the nucleus' rest frame with a relative energy of $1\,\mathrm{MeV}$ is detected here with full acceptance within an acceptance of $80\,\mathrm{mrad}$.

On the other hand, a Lorentz transformation needs to be applied to observe the physics in the rest frame of the nucleus. The following form of the transformation converts the four-momentum P of a system that is moving with velocity βc in z direction back into its rest frame (prime system P'),

$$P'^{\mu} = \Lambda^{\mu}_{\nu} P^{\nu} = \begin{pmatrix} \gamma & 0 & 0 & -\beta\gamma \\ 0 & 1 & 0 & 0 \\ 0 & 0 & 1 & 0 \\ -\beta\gamma & 0 & 0 & \gamma \end{pmatrix} \cdot \begin{pmatrix} E \\ p_x \\ p_y \\ p_z \end{pmatrix}, \tag{4.16}$$

where the transverse direction is not affected.

As described in Sec. 4.2, the transverse and longitudinal components of the momentum distribution of the heavy fragment carry information about the single-particle characteristics of the knocked-out nucleon.

4.3.2 Theoretical Momentum Distributions in a Knockout Process

As shown in Sec. 4.2, the momentum distribution of the reaction residue carries spectroscopic information about the knocked-out nucleon, in particular its angular momentum. First theories that have been developed to quantitatively describe spectroscopy and the momentum distributions are guided by the experiments at low energies where light compound targets such as ^{12}C or ^{9}Be were used. The single-particle cross section σ_{sp} to a given final state is composed of the "knockout" and "continuum" cross section, σ_{ko} and σ_{cont}, respectively,

$$\sigma_{\mathrm{sp}} = \sigma_{\mathrm{ko}} + \sigma_{\mathrm{cont}}, \tag{4.17}$$

where the contribution from Coulomb reaction σ_{C} is neglected for such light targets [107, 116]. The knockout component describes the projectile-nucleon scattering off a target nucleon with

large angle while the target nucleon is not identified. The second term, the "nuclear inelastic scattering into the continuum", also called "diffractive/elastic breakup" (here: continuum), describes the nucleon removal as a dissociation process through the interaction between target nucleus and projectile nucleon. In the nuclear inelastic scattering into the non-resonant or resonant continuum, the nucleon is removed. The removed nucleon is present in forward direction with nearly beam velocity. This contribution is absent in the experiment here because QFS based on a proton target is investigated (see below), and additionally the reaction channel is exclusively identified including the scattered particles, while for low-momentum transfer the proton does not leave the target.

The longitudinal-momentum distributions for the knockout process can be described in an eikonal calculation. The elastic-scattering S-matrices are described in the strong-absorption or "black-disc" model [107]. In the eikonal approximation the single-particle wave function is unchanged except for the interaction region where the absorption takes place, given by a cylinder with "black-disc"/cut radius. The momentum distribution is the one-dimensional Wigner transform of the single-particle wave function ψ_{lm} of the bound nucleon, along the beam z-axis with impact parameter b (and transverse distance $r_\perp$) [107, 117],

$$\frac{\mathrm{d}\sigma}{\mathrm{d}p_z} = \frac{1}{2l+1} \sum_m \int_{b_{\min}}^{\infty} \frac{\mathrm{d}W_{lm}}{\mathrm{d}p_z} \, \mathrm{d}\vec{b}, \tag{4.18}$$

with

$$\frac{\mathrm{d}W_{lm}}{\mathrm{d}p_z} = \frac{1}{2\pi} \iiint \psi^*_{lm}(\vec{r}_\perp, z')\psi_{lm}(\vec{r}_\perp, z) \exp\left\{ip_z(z-z')\right\} \, \mathrm{d}\vec{r}_\perp \mathrm{d}z\mathrm{d}z'. \tag{4.19}$$

Bertulani and Hansen [118] extended the theory by adding more elaborate S-matrices to describe the core-target and nucleon-target interaction. The scattering matrices are associated with optical potentials. The details can be found in Ref. [118]. It was shown that the longitudinal momentum is well-suited to extract information about the angular momentum, while it differs only slightly from the simple "black-disc" model.

The shape of the momentum distribution reflects only the part of the wave function that is sampled. Instead, QFS reactions on a proton target and higher energies, as investigated here, are more sensitive because the reaction is less surface dominated than knockout reactions on a compound target and at low energies, and both nucleons are detected. Reference [115] shows that the quasi-free knockout reactions are more sensitive to the interior of the wave function, thus the momentum distributions are sampled differently – imagine a node in the wave function that is probed and is basically reflected as the Fourier transform in the momentum distribution. Separating the scattering matrix as shown below, the distorted waves are used. Plane waves in the eikonal approximation are distorted with the scattering matrix. The single-particle wave function is calculated in a Woods-Saxon potential with central, surface, and spin-orbit part. The

longitudinal-momentum derived in Ref. [115] reads

$$\frac{\mathrm{d}\sigma}{\mathrm{d}p_z} \sim \frac{1}{2j+1} \sum_m \left\langle \frac{\mathrm{d}\sigma_{pN}}{\mathrm{d}\Omega} \right\rangle_{p_z} \int_0^\infty b \left|\langle S(b)\rangle\right|^2 \mathrm{d}b \left| \int_{-\infty}^{\infty} \exp\left\{-ip_z z\right\} \psi_{jlm}(r_\perp, b, z)\, \mathrm{d}z \right|^2 , \quad (4.20)$$

where $\langle S(b)\rangle$ is the angle-integrated product of the scattering matrices (survival amplitudes) for proton–beam, proton–fragment (core), and nucleon–fragment scattering to incorporate that the particles leave the reaction zone and can be measured,

$$\langle S(b)\rangle = \left\langle S_{pc} S_{p'c} S_{Nc} \right\rangle . \quad (4.21)$$

The proton-nucleon cross section σ_{pN} is taken from the free-scattering cross section [115].

The analysis of momentum distributions is a well-suited tool to extract spectroscopic information of nucleons in a knockout reaction, even if the scattered nucleon is not measured completely but just the fragment. Several reaction-theory models were presented, the latter describes the QFS as studied here and is applied in Sec. 8.2.5. The method is as well applicable to neutron unbound states where the residual momentum is reconstructed from the heavy fragment and the neutron momenta after the decay. Eventually, the experimental cross section for a particular final state can be compared to theoretical single-particle cross sections from the above theories, resulting in spectroscopic factors.

4.4 Invariant-Mass Method

The goal of this thesis is to deduce information about states in the continuum. Experimentally, these resonances cannot be observed directly but only after the decay has happened. This means, information can only be deduced from the incoming particles, prior to the reaction, and the outgoing decay particles after the reaction, while the reaction has just populated the system of interest.

Two methods, namely the missing-mass and invariant-mass method, can be applied to obtain the decay energy of continuum states. To determine the missing mass, all the particles before and those after the reaction that do not compose the system of interest need to be measured with high precision. The missing-mass technique exploits the conservation of energy and momentum between the projectiles P_{in} (beam and target particles) and the particles after the reaction P_f. The missing-mass energy is deduced from

$$\sum_j P^\mu_{in,j} = \sum_i P^\mu_{f,i}. \quad (4.22)$$

Usually, that is limited to the charged particles only. Here, the incoming beam and the scattered protons in the $(p, 2p)$ reaction would need to be measured. The momenta of the protons cannot

be measured with the existing experimental setup.

In contrast, applying the invariant-mass method, all the decay products from the system of interest need to be measured, including (multiple) neutrons. The explicit detection and tracking of neutrons is more challenging than detecting only charged particles but, eventually, the decay-energy resolution is usually better compared to the missing-mass analysis.

Here, the decay energy is inferred from the four-momentum of all the decay particles that formed the resonance. The energy and momentum conservation holds for the initial state and the n decay products,

$$P^{\mu}_{in} = \sum_{i=1}^{n} P^{\mu}_{f,i}. \tag{4.23}$$

The decay energy is a quantity of the decaying system, it is described in the rest frame. As known from special relativity, the rest mass is invariant under any transformation in any reference system, especially in the laboratory system where the quantities are measured. The squared invariant mass M^2 for a n-body decay reads

$$M^2 = \left(\sum_{i=1}^{n} P_{i,\mu}\right) \cdot \left(\sum_{i=1}^{n} P^{\mu}_{i}\right). \tag{4.24}$$

Eventually, the decay or relative energy E_{rel} is

$$E_{\mathrm{rel}} = M - \sum_{i=1}^{n} m_i, \tag{4.25}$$

subtracting the rest masses m_i of the decay particles. Essentially, the momentum information is all that is needed. Rewriting the invariant mass leads to

$$\begin{aligned} M^2 &= \left(\sum_{i}^{n} E_i\right)^2 - \left|\sum_{i}^{n} \vec{p}_i\right|^2 \\ &= \sum_{i}^{n} \left(E_i^2 - |\vec{p}_i|^2\right) + 2\sum_{i<j}^{n} \left(E_i E_j - \vec{p}_i \cdot \vec{p}_j\right). \end{aligned} \tag{4.26}$$

Using the scalar product

$$\vec{p}_i \cdot \vec{p}_j = |\vec{p}_i| \cdot |\vec{p}_j| \cdot \cos(\sphericalangle(\vec{p}_i, \vec{p}_j)), \tag{4.27}$$

together with the mass-energy relation, results in

$$M^2 = \sum_{i}^{n} m_i^2 + 2\sum_{i<j}^{n} \left(E_i E_j - |\vec{p}_i||\vec{p}_j| \cos(\theta_{ij})\right), \tag{4.28}$$

where m_i is the rest mass and θ_{ij} the opening angle between two vectors of the decay particles. The total energy and momentum can be further expanded to $E = \gamma m$ and $|\vec{p}| = \beta\gamma m$, respectively. This formulation illustrates that the opening angle in the laboratory system is the imprint of the relative energy.

In case the heavy fragment is populated in an excited bound state that decays via γ-ray emission with energy E_γ, this energy needs to be considered in addition. The excitation energy is defined as

$$E_{\mathrm{ex}} = E_{\mathrm{rel}} + E_\gamma + S_N, \tag{4.29}$$

with the particle separation energy S_N.

In a three-body decay that is studied for ^{29}F*, the invariant-mass analysis allows to study subsystems, in particular neutron-neutron correlations and the decay behavior, as described in Sec. 4.6.

4.5 Resonance Description in *R*-Matrix Theory

4.5.1 Basic *R*-Matrix Theory

This thesis aims to investigate neutron-unbound states. The resonant states that are populated in a direct reaction decay subsequently into a fragment and at least one neutron. The basic idea is to treat this two-step process as scattering problem on a potential $\hat{V}$. The radial Schrödinger equation, after separation of the angular part, needs to be solved

$$\left(\hat{T} + \hat{V}(r)\right)\psi_l(r) = E\psi_l(r), \tag{4.30}$$

with the scattering solution $\psi_l(r)$ for partial wave l. The kinetic-energy operator is

$$\hat{T} = -\frac{\hbar^2}{2\mu}\left(\frac{\mathrm{d}^2}{\mathrm{d}r^2} - \frac{l(l+1)}{r^2}\right). \tag{4.31}$$

The solution needs to satisfy certain boundary conditions, it is $\psi_l(0) = 0$ and it is continuous at $r = a$ the matching radius – also called channel radius. In R-matrix theory, the channel radius separates the potential into an interior and exterior region. In the exterior region only long-range effects are kept, where the scattering wave function is related to the scattering matrix. The R-matrix method in particular takes care of the orthonormalization of the basis states ψ_{l_n} of ψ_l in the internal region ($r \leq a$) where the resonant states are formed, and fulfill Eq. 4.30 with energy ϵ_n – the details of the R-matrix expansion can be found in Ref. [119]. Mathematically, the R matrix is the inverse of the logarithmic derivative of the wave function at the boundary, while no particular Hamiltonian is assumed. The (phenomenological) R-matrix approach, proposed by Wigner and

Eisenbud [120] and further developed in great detail by Lane and Thomas [121], became a standard method to solve the resonance scattering and which is also applicable to direct-reaction mechanisms.

Here, the calculable approach for the R matrix is described. The diagonal elements of the R matrix, where the same particles in incoming channel and exit channel are considered, take the energy-dependent form (for particular l)

$$R = \sum_{n=1}^{N} \frac{\gamma_n^2}{\epsilon_n - E}, \tag{4.32}$$

with the squared reduced-width amplitude

$$\gamma_n^2 = \frac{\hbar^2}{2\mu a} \psi_n^2(a), \tag{4.33}$$

with the scattering solution $\psi(r)$ (and the basis states ψ_n), sum over the N poles at resonance energies ϵ_n – it is exact for a complete basis. For the complete derivation see Ref. [49]. Dropping the sum over the different resonances in Eq. 4.32 is the R matrix in one-channel scattering as originally proposed by Wigner and Eisenbud [120].

R is uniquely connected to the S matrix [119]. In the following, basic quantities to describe a resonance are introduced, using the basic example of one-channel scattering with one pole. The S matrix knows only one path from populating the resonance and decaying through one particular channel. Using the scattering solutions, the S matrix and phase shift can be determined [53, 119]. One identifies quantities with physical meaning. For neutron resonant-scattering, the positive-energy solutions F and G are the Bessel functions of first and second kind[†], respectively, with the argument $\rho = kr$ [121]. The penetrability,

$$P_l(E) = ka \frac{1}{F_l^2 + G_l^2}, \tag{4.34}$$

and the shift function,

$$S_l(E) = ka \frac{\dot{F}_l F_l + \dot{G}_l G_l}{F_l^2 + G_l^2}, \tag{4.35}$$

are introduced, evaluated at a given scattering energy E with

$$\rho = ka = \frac{\sqrt{2\mu E}}{\hbar c} a, \tag{4.36}$$

its relative momentum k, and the reduced mass μ. The expressions for the partial waves up to $l = 3$ are derived in App. B.1. The penetrability is a measure for the transmission through the

[†] $\dot{F} = \frac{\mathrm{d}}{\mathrm{d}\rho} F(\rho)$

centrifugal barrier [53]. In case of resonance scattering the lifetime is long compared to the time it takes the particle to pass the nucleus.

The S-matrix pole determines the resonance energy E_S and width Γ. The way the components of the (one-pole) R matrix $R = \gamma^2/(\epsilon - E)$ are related is outlined in Refs. [49, 119, 121]. The S matrix can be found in Ref. [122], the resonance parameters for one channel are defined as follows. The partial width is

$$\Gamma = 2P(E) \cdot \gamma^2, \tag{4.37}$$

which reads at the resonance position with the experimentally determined width Γ_r

$$\Gamma(E) = \Gamma_r \frac{P(E)}{P(E_r)}. \tag{4.38}$$

The resonance energy is shifted energy-dependently from ϵ ($= E_r$), shown for fixed l,

$$E_S = \epsilon + \Delta, \tag{4.39}$$

where

$$\Delta = \gamma^2 \left(S(E_r) - S(E) \right). \tag{4.40}$$

The first term is fixed at the resonance-pole energy, while for the second term it is made use of the Thomas approximation and so it is linear in energy. The resonance cross section from the S matrix is proportional to

$$\frac{\mathrm{d}\sigma}{\mathrm{d}E} \sim \frac{\Gamma}{\left(E_r + \Delta - E\right)^2 + \Gamma^2/4}, \tag{4.41}$$

often referred to as single-level energy-dependent Breit-Wigner line shape with the so called "observed" resonance parameters. Close to the threshold the shape becomes asymmetric because the form tends to zero.

This argumentation holds for the kind of reactions investigated here. The (direct) knockout reaction populates the resonance which promptly decays. In the R-matrix formalism this is treated as inelastic scattering from one entrance channel to another exit channel but with one pole. Therefore, two diagonal elements of the R matrix exist in the symmetric S matrix, the details can be found in Ref. [122]. Eventually, the entrance and exit channel can be factorized – only the decay is relevant but not the population mechanism. Under the assumption that the entrance channel has no structure effect in the decay, the width and shift are dominated by the decay channel, and the Breit-Wigner line shape reads as Eq. 4.41.

4.5.2 Single-Particle Width

The width which is sensitive to the angular momentum can be calculated for a pure single-particle state. The estimate of the single-particle width Γ_{sp} that cannot be exceeded is derived in Ref. [123],

$$\Gamma_{\mathrm{sp}} = \frac{2\hbar^2}{\mu a^2} \cdot P_l, \tag{4.42}$$

for $l > 0$. In case of $l = 0$ it is $\Gamma_{\mathrm{sp}} = \left(2\hbar^2/(\mu a^2)\right) \rho$. Bohr and Mottelson [53] derive the single-particle limit for scattering of a spinless neutral particle in a spherical square-well potential as

$$\Gamma_{\mathrm{sp}} = \frac{2\hbar^2}{\mu a^2} \frac{2l-1}{2l+1} \cdot P_l, \tag{4.43}$$

where the additional angular-momentum weighting causes a problem. The width becomes $\Gamma_l > \Gamma_k$ for $l > k$ and large ρ, what is not realistic. Another accepted limit, shown to hold by Teichmann and Wigner [124], is

$$\Gamma_{\mathrm{sp}} = \frac{3\hbar^2}{\mu R^2} \cdot P_l, \tag{4.44}$$

with nuclear radius R.

4.5.3 Breit-Wigner Line Shape for Sequential Decay

The R-matrix method is also applicable to a more complex decay situation, where e. g. more than one decay channel is open or resonances are close together in energy or sequential decays occur, see Ref. [121]. The sequential decay, as introduced in Sec. 2.3, is treated as two subsequent one-neutron decays via an intermediate state.

Following the approach of Kryger et al. [125] and Barker [126] based on the R-matrix theory, the total width depends directly on the intermediate resonance structure, what becomes apparent for states of broad width. The second step, the one-neutron decay from the intermediate state with resonance energy E^r_{fn}, is seen as an ordinary Breit-Wigner decay in a subsystem with available energy U ($U \leqslant E$) or fractional energy $\epsilon = U/E$,

$$\rho(U) = c \frac{\Gamma_2(U)}{\left(U - E^r_{fn}\right)^2 + \Gamma_2^2(U)/4}, \tag{4.45}$$

where c is chosen to normalize ρ,

$$\int_0^\infty \rho(U)\,\mathrm{d}U = 1, \tag{4.46}$$

and $\Gamma_2(U)$ is the width of the intermediate state as introduced in Eq. 4.37. The total width is modified by the intermediate resonance. The total system with three-body energy E is described as

$$\Gamma_1(E,U) = 2\gamma_1^2 P_1(E-U)\cdot\rho(U), \tag{4.47}$$

the total width integrates out

$$\Gamma_{\mathrm{tot}}(E) = \int_0^E \Gamma_1(E,U)\,\mathrm{d}U. \tag{4.48}$$

Eventually, the three-body decay Breit-Wigner line shape for sequential decay, that is applied here to a two-neutron decay, is [127]

$$\frac{\mathrm{d}\sigma}{\mathrm{d}E} \sim \frac{\Gamma_{\mathrm{tot}}(E)}{\left(E^r_{fnn}-E\right)^2 + \Gamma^2_{\mathrm{tot}}(E)/4}. \tag{4.49}$$

The shift function is not explicitly considered, the treatment is detailed in Ref. [126].

4.6 Neutron-Correlation Observables

As explained in Sec. 2.3, three- and many-body systems can exhibit special correlations and decay behaviors. Different methods are available to study the three-body kinematics. The analysis in a Jacobi coordinate system is presented and later applied to $^{29}\mathrm{F}^* \rightarrow ^{27}\mathrm{F}+2n$. The systems are best studied in their Center-of-Mass (c. m.) system to eliminate the c. m. motion, an adequate system are Jacobi coordinates.

The idea is to form pairs of two particles, consider their relative vector and the vector of the two-body c. m. to a third particle. For more particles, the c. m. of the new binary system is determined and serves as origin to couple the next particle and so on. In case of a three-body system including two indistinguishable particles, fragment+neutron+neutron, two particular systems can be looked at, the so called Y- and T-system. In the Y system the fragment and a neutron form the incident binary system, in the T system it is the neutron pair. Figure 4.2 shows a geometrical view of the two choices of systems.

In a mathematical way, the transformation into Jacobi coordinates – treated here in momentum space – is performed in the following way [52, 128], using the notation for fragment (f) and neutron (n) and their momenta p_i, as in Fig. 4.2:

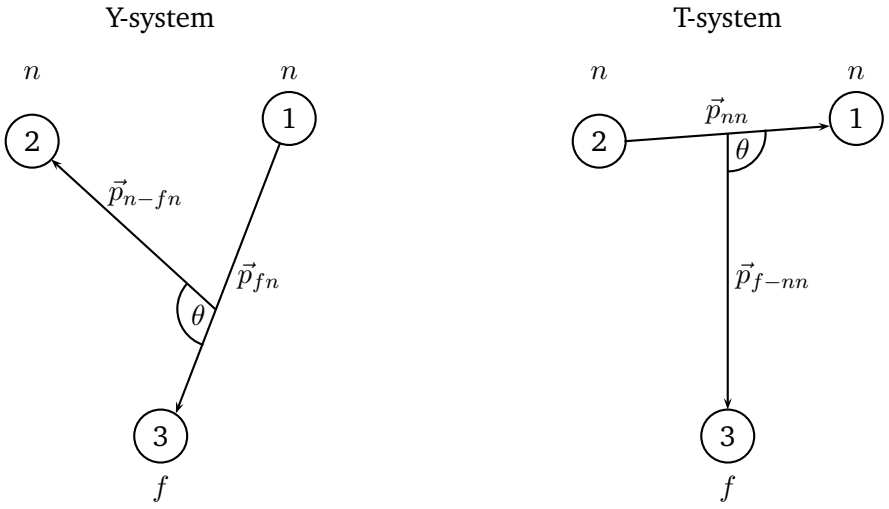

Figure 4.2: The two different systems of Jacobi coordinates for three-body studies in momentum space. The relative-momentum vectors of the binary systems between fragment (f) and neutrons (n) are denoted by $\vec{p}_{ij}$.

Y-system:

$$\begin{aligned} \vec{p}_{fn} &= \mu_{31}\left(\frac{\vec{p}_3}{m_3} - \frac{\vec{p}_1}{m_1}\right), \\ \vec{p}_{n-fn} &= \mu_{2-31}\left(\frac{\vec{p}_2}{m_2} - \frac{\vec{p}_3+\vec{p}_1}{m_3+m_1}\right), \end{aligned} \tag{4.50}$$

with the reduced masses

$$\begin{aligned} \mu_{31} &= \frac{m_3 m_1}{m_3+m_1}, \\ \mu_{2-31} &= \frac{m_2(m_3+m_1)}{m_3+m_2+m_1}. \end{aligned} \tag{4.51}$$

T-system:

$$\begin{aligned} \vec{p}_{nn} &= \mu_{12}\left(\frac{\vec{p}_1}{m_1} - \frac{\vec{p}_2}{m_2}\right), \\ \vec{p}_{f-nn} &= \mu_{3-12}\left(\frac{\vec{p}_3}{m_3} - \frac{\vec{p}_1+\vec{p}_2}{m_1+m_2}\right), \end{aligned} \tag{4.52}$$

with the reduced masses

$$\begin{aligned} \mu_{12} &= \frac{m_1 m_2}{m_1 + m_2}, \\ \mu_{3-12} &= \frac{m_3(m_1 + m_2)}{m_1 + m_2 + m_3}. \end{aligned} \tag{4.53}$$

The relative energy, cf. Sec. 4.4, of the subsystems is in the

Y-system

$$\begin{aligned} E_{fn} &= \frac{p_{fn}^2}{2\mu_{31}}, \\ E_{n-fn} &= \frac{p_{n-fn}^2}{2\mu_{2-31}}, \end{aligned} \tag{4.54}$$

and in the T-system

$$\begin{aligned} E_{nn} &= \frac{p_{nn}^2}{2\mu_{12}}, \\ E_{f-nn} &= \frac{p_{f-nn}^2}{2\mu_{3-12}}, \end{aligned} \tag{4.55}$$

which sum up to the three-body relative energy.

For the study of correlations and decay kinematics, see Sec. 2.3, it is suitable to introduce the relative angle between the momentum vectors θ_{ij}, denoted in Fig. 4.2. The fractional energy,

$$\begin{aligned} \epsilon_{fn} &= \frac{E_{fn}}{E_{fnn}}, \\ \epsilon_{nn} &= \frac{E_{nn}}{E_{fnn}}, \end{aligned} \tag{4.56}$$

is the ratio between the binary and total three-body relative energy E_{fnn}. The choice of $\{\theta_{ij}, \epsilon_{ij}\}$ is made because these variables are based on the Jacobi coordinate system $\{\vec{p}_{ij}, \vec{p}_{k-ij}\}$, which in turn is often used to parametrize hyperspherical harmonics functions as in three-body physics [128]. For a fixed decay energy E_{fnn}, θ_{ij} and ϵ_{ij} are the two degrees-of-freedom that are left in a three-body system where the c. m. motion and Euler rotations are removed [52]. Hyperspherical harmonics are the three-body equivalent to the spherical harmonics functions which are usually used to expand two-body wave functions. In the sequential-decay theory, the fractional energy is de-

scribed as [127]

$$P(\epsilon_{fn}) = C \int_0^\infty \frac{\Gamma_1(E,U)}{(E_1 - E)^2 + \Gamma_{\mathrm{tot}}^2(E)/4}\,\mathrm{d}E, \tag{4.57}$$

with $\epsilon_{fn} = U/E$ and scaling C.

Chapter 5

Experimental Setup

The experiment has been performed at the experimental stage called SAMURAI at the RIBF. This 10-day-long experiment took place at the end of 2015 and was led by Y. Kondo.

The primary goal of this research is the first spectroscopic measurement of the unbound oxygen isotopes ^{27}O and ^{28}O [129]. One driving question is if ^{28}O behaves like a doubly-magic nucleus with a closed *sd*-shell configuration. The results will give insight into the shell-structure, binding mechanisms, and help clarifying the influence of *fp*-shell intruder configurations in the region of the nuclear landscape called the island of inversion.

These very neutron-rich nuclei decay via (multi-) neutron emission. The invariant-mass spectroscopy requires the measurement of the momenta of all the decay products, in particular the reconstruction of the neutron momenta. The latter is in particular challenging because there is no direct detection of neutrons and the interaction probability is low.

The Superconducting Analyzer for MUlti-particles from RAdioIsotope beams (SAMURAI) setup uniquely allows to measure reactions in inverse and complete kinematics, while it combines major improvements in the experimental implementation:

- a high beam intensity,
- an increased luminosity for the secondary reaction,
- an increased neutron-detection efficiency,
- and high resolution detectors,

which allow for the first time the momentum reconstruction of four coincident neutrons.

These aspects as well as the details of the experimental setup are described in the following sections. The chapter starts with the description of the accelerator facility and the secondary-beam production. Following this, the SAMURAI setup is detailed with all its main detector components.

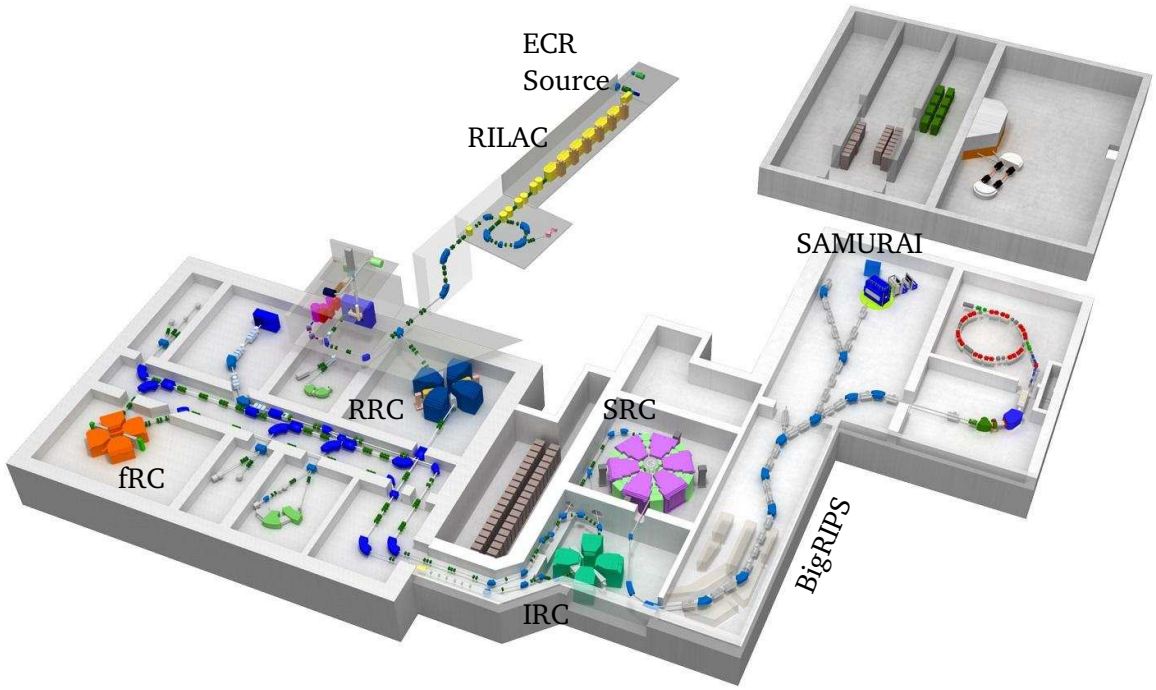

Figure 5.1: Schematic view of the RIKEN Nishina Center. The different accelerators are labeled as well as other experimental stages. The ions are produced in the ECR source and are accelerated in the RILAC and a chain of segmented ring cyclotrons. Figure adapted from Ref. [132].

5.1 Accelerator Facility

The experiment has been carried out at the RIBF of the RIKEN Nishina Center in Tokyo (Japan). The RIBF is the first next-generation radioactive-ion beam facility in the world [130]. The new and world's first Superconducting Ring Cyclotron (SRC) was commissioned in late 2006 and the fragment separator to produce the RI beams in 2007 [131]. This facility opens a new path into unexplored regions of nuclei with large isospin asymmetry using RI beams of a few hundred MeV/nucleon.

5.1.1 Primary-Beam Acceleration

The facility can accelerate stable primary beams from deuterons to ^{238}U up to energies of $345\,\mathrm{MeV/u}$ for heavy ions using the final-stage SRC [133]. The accelerator complex consists of several different accelerators which are used to accelerate the ion of interest and transport the beam to the experimental site. The layout of the RIBF complex is schematically shown in Fig. 5.1. Several ion sources, based on the Electron Cyclotron Resonance (ECR) method, are available to extract the primary ions for acceleration.

After the extraction from the source, the ions are pre-accelerated in a $16\,\mathrm{MV}$ variable-frequency Linear Accelerator (LINAC) called RILAC. A chain of segmented ring cyclotrons for further acceleration is following which serve as injector to the SRC and provide the beam to other experimental stages. The available cyclotrons are

- the RIKEN Ring Cyclotron (RRC),
- the Fixed Frequency Ring Cyclotron (fRC),
- the Intermediate-stage Ring Cyclotron (IRC),
- and the SRC.

A step-by-step acceleration in several cyclotrons allows to reach highest kinetic energies and to adapt to the increasing magnetic rigidity of the beam particles. A key property is the so-called *K*-value or bending limit that is defined as follows

$$\frac{E_{\mathrm{kin}}}{A} = \frac{e^2\,(B\rho)^2}{(\gamma+1)m_u} \cdot \left(\frac{Z}{A}\right)^2 = K \cdot \left(\frac{Z}{A}\right)^2, \tag{5.1}$$

with the kinetic energy E_{kin}, the mass number A, the nuclear charge Z, and the magnetic rigidity $B\rho$ of the beam particles.

According to the requirements of the experiment, such as beam species, energy, and final experimental stage, the particles are accelerated in three different modes. In the following, the acceleration of a ^{48}Ca beam is described as it was applied in the experiment here. Further information and details can be found in Refs. [130] and [131] and the references therein.

5.1.2 ^{48}Ca Beam Acceleration

A stable ^{48}Ca primary beam was used to produce the neutron-rich, short-lived nuclei in BigRIPS.

First, $^{48}\mathrm{Ca}^{16+}$ ions are extracted from the $18\,\mathrm{GHz}$ ECR source and are pre-accelerated in the RIKEN LINAC (RILAC) running at a frequency of $36.5\,\mathrm{MHz}$, cf. Fig. 5.1. This beam, which has an energy of $2.675\,\mathrm{MeV/u}$ after the first stage, passes a first charge stripper and is further accelerated in the RRC [134].

The RRC is a $K540$-MeV ring cyclotron with four separated-sector magnets and two Radio Frequency (RF) resonators. Following a second charge stripper to produce fully-stripped ions and to moderately increase the magnetic rigidity, the acceleration continues in the IRC. The fRC ($K570$-MeV) is by-passed. It is only included for maximum acceleration of ions with larger magnetic rigidity like ^{238}U which can be produced at $345\,\mathrm{MeV/u}$ and highest intensity of $40\,$pnA. Here, the RRC serves as injector for the IRC.

The IRC also consists of four room-temperature sector magnets. Its K-value is $980\,\mathrm{MeV}$, the maximum magnetic field in one sector is $1.9\,\mathrm{T}$ and the maximum extraction energy $127\,\mathrm{MeV/u}$. The final acceleration is performed in the SRC.

The SRC is the first superconducting ring cyclotron of its kind in the world [135]. It provides an immense bending power with a K-value of $2500\,\mathrm{MeV}$. It is built out of six separated-sector magnets, their maximum field is $3.8\,\mathrm{T}$, and four RF cavities.

Finally, the $^{48}Ca^{20+}$ beam is almost-continuously extracted with an energy of $345\,\mathrm{MeV/u}$ at a cyclotron frequency of $36.5\,\mathrm{MHz}$. This acceleration scheme is the so-called variable-energy acceleration mode. The transmission accounts for more than $80\,\%$. In this experiment the intensity did reach maximum values of approximately $600\,$pnA, which recently could be increased up to $730\,$pnA.

5.2 Secondary-Beam Production

These high-intensity primary beams make it possible to produce "exotic" nuclei far from β stability. At the RIBF, the in-flight separation technique is applied to produce a high-energy secondary RI beam. The pioneering work applying this technique has been done at the Lawrence Berkeley National Laboratory (USA) in the 1980's [17].

Other facilities like the ISOLDE at CERN apply a technique called ISOL, see Sec. 4.1. There exist a few facilities presently in the world that provide beams from projectile fragmentation [14], namely

- RIPS and BigRIPS at RIKEN (Japan),
- the Fragment Separator (FRS) at GSI and the future Superconducting Fragment Separator (Super-FRS) at the Facility for Antiproton and Ion Research (FAIR) (Germany),
- the A1900 fragment separator at NSCL and the future Facility for Rare Isotope Beams (FRIB) (USA),

but others are being built.

BigRIPS is designed to produce, transport, and identify not only radioactive-isotope beams from projectile-fragmentation reactions but also medium- and heavy-mass nuclei from in-flight fission reactions. The latter requires in particular large-acceptance ion optics due to the reaction-process and to transmit most-neutron rich nuclei with reasonable statistics. The discovery of more than 120 new nuclei at BigRIPS, mainly neutron-rich isotopes from projectile-fragmentation reactions, has been reported in the last five years [136].

5.2.1 BigRIPS Setup

BigRIPS is a two-stage in-flight separator combining the production stage and a large-acceptance separator with a second separator stage to identify the ions event-wise [137]. The schematic layout of BigRIPS is shown in Fig. 5.2. The ion-optics of the separator is built out of a series of

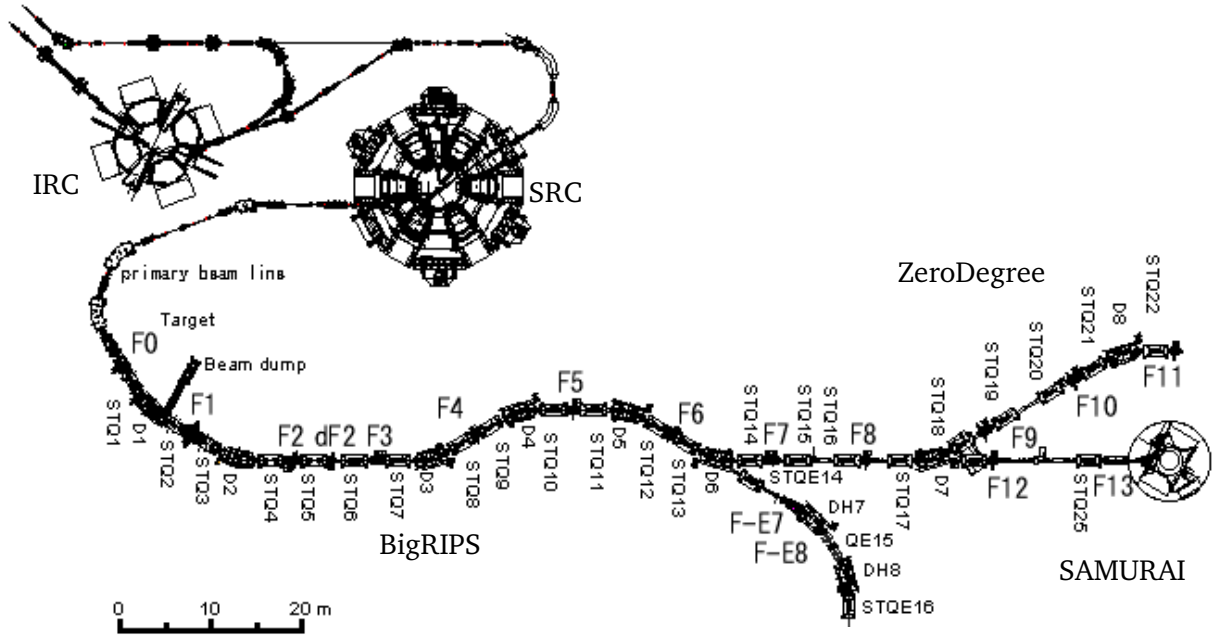

Figure 5.2: Schematic layout of BigRIPS and its beam lines. Focal planes are labeled as F#, dipole magnets as D# and quadrupole-triplet magnets as STQ#. Figure taken from Ref. [139].

dipole magnets (labeled as D#), superconducting quadrupole-triplet magnets (labeled as STQ#), degraders, slits, and in-beam detectors as described in detail in an article by Kubo et al. [138]. Mid-focal planes are labeled as F#.

The first stage is considered from the production target (F0) to the focus F2 with a degrader placed at F1. In between, four of the superconducting quadrupole triplets and two normal-conducting dipole magnets are equipped. The dipole magnets have a bending angle of 30° and a mean bending radius of $6\,\mathrm{m}$.

The selected RI beam is transported through the two quadrupole magnets STQ5 and STQ6 to the second stage, a four bend achromatic spectrometer with its four dipole magnets D3–D6, from F3 to F7. Inserting a second degrader at F5 extends the separation stage. The beam is transported through four more quadrupole triplets to the SAMURAI setup, also called F13. Before, the beam can be deflected to enter the third part of BigRIPS, the analyzing spectrometer ZeroDegree.

The design of the magnets allow a transportation with $\pm 3\,\%$ momentum acceptance and an angular acceptance of $\pm 40\,\mathrm{mrad}$ horizontally and $\pm 50\,\mathrm{mrad}$ vertically. The accepted magnetic rigidity is with $9\,\mathrm{T\,m}$ even larger than that of the SRC accounting for the study of nuclei with large isospin asymmetry. The total length accounts for $78\,\mathrm{m}$ from F0 to F7 and another $39.5\,\mathrm{m}$ from F7 to the entrance of the SAMURAI area. [138]

5.2.2 In-flight Separation

One magneto-optical setting of BigRIPS was optimized to transport ^{29}F with highest intensity. However, the purity is reduced by nuclei of similar magnetic rigidity that are mixed in like ^{30}Ne and ^{31}Ne.

The particular setting of BigRIPS for the production runs of ^{29}F is listed in Table C.1 in App. C.1. The high-energy and intense ^{48}Ca beam from the SRC bombards the thick ^{9}Be production target at the entrance of BigRIPS. In fragmentation reactions lots of different nuclei are produced with masses smaller than the beam ones, including very rare isotopes but with small cross section. Due to the reaction mechanism, the reaction products have a rather broad momentum and angular distribution, cf. Sec. 4.1.

Exploiting the advantage of the high beam energy and the large-acceptance devices, most of the phase space is collected in forward direction. The short-lived ions, such as ^{29}F, ^{30}Ne, and ^{31}Ne with half lives of $T_{1/2} = 2.67\,\mathrm{ms}, 7.39\,\mathrm{ms}$, and $3.40\,\mathrm{ms}$ [140], respectively, reach the final focal plane.

Dipole magnets separate the ions according to their magnetic rigidity. This is a general feature of a dipole magnet that selects according to the momentum. In a magnetic field $\vec{B}$, the Lorentz force acts orthogonally to the direction of the velocity $\vec{v}$ of a charged particle with mass m and charge Q and bends it onto a curved orbit with radius ρ. In the relativistic case this reads as

$$\frac{p}{Q} = \frac{\beta\gamma mc}{Q} = B\rho, \tag{5.2}$$

with momentum $p = \beta\gamma mc$. In case of fully stripped ions, $Q = Z \cdot e$, and similar velocities of projectile and fragment, this becomes basically a separation according to the mass-over-charge ratio

$$B\rho \propto \frac{A}{Z}\beta\gamma. \tag{5.3}$$

Thus, a substantial amount of reaction products having a different magnetic rigidity than the nuclei of interest is dumped into a beam dump. The rest is focused by the quadrupole magnets onto an aperture, still on the dispersive focus F1, to apply a selection on p/Q.

Also at F1, a simple but important device is used, namely a wedge-shaped achromatic degrader. This material is sensitive to the energy loss, thus to charge and velocity – a momentum achromat. Together with the second dipole magnet, the separation is sensitive to $A^{2\gamma-1}/Z^{2\gamma-2}$ (γ is a material constant of the degrader), other than the first dipole with $\sim A/Z$ sensitivity. At the achromatic focus F2 another slit is adjusted to select the isotope cocktail further in the first $B\rho - \Delta E - B\rho$ selection. Further details and the formal derivation needed for the isotope separation can be found in the fundamental works by Dufour et al. [141] and Schmidt et al. [142].

For further purification purposes of the isotope cocktail another aluminum degrader is inserted at the focus F5. In a similar way as described above, after having passed the four-bend achromatic

section, the final shaping is done with an aperture at the achromatic focus F7. There, the ^{29}F ions have a nominal magnetic rigidity of $B\rho_0 = 7.6172\,\mathrm{T\,m}$.

After the separation in the second $B\rho - \Delta E - B\rho$ section (F4 to F6), the second stage from F5 to F13 is in particular used for the ion identification, see Sec. 7.1. Finally, the ions of interest reach the experimental area SAMURAI, which is described in the next section.

5.2.3 Parallel-Plate Avalanche Counter

Two different kind of detectors are installed in BigRIPS to identify the beam particles, namely plastic-scintillator detectors and Parallel Plate Avalanche Counter (PPAC)s. The PPACs are position-sensitive detectors that are used in BigRIPS for the determination of the particle's magnetic rigidity [143].

The maximum available detector size at BigRIPS is $240\,\mathrm{mm}(X) \times 150\,\mathrm{mm}(Y)$. An anode foil separates vertically and horizontally aligned cathode-electrode wires. A few hundreds of volts per millimeter are applied between anode and cathode. The pitch between the wires is $2.55\,\mathrm{mm}$ and the gap between the electrodes is $4.3\,\mathrm{mm}$. Isobutene is used as counter gas with good quenching properties. The wires are read out in the so called delay-line method, where the multi-strip cathode measures the induced charge distribution at each wire. The detector can stand rates up to MHz. [143]

When a heavy ion passes the detector volume, a fast signal is produced by the immediate Townsend-avalanche ionization. The charge signal of the electrons is collected at the electrodes. Eventually, the position of the incident ion is obtained from the time difference between the signals at both ends of the delay-line.

At BigRIPS double PPACs are used. That is simply a combination of two PPACs with x- and y-layer each and thus increasing the detection efficiency. The position resolution is approximately $0.41\,\mathrm{mm}$ (Root Mean Square (RMS)) for particles with $Z = 12$ [143]. Finally, trajectories of the ions can be measured and their magnetic rigidities be determined, cf. Sec. 7.1.

5.3 SAMURAI Setup

The SAMURAI setup, see Fig. 5.3, is a versatile experimental stage for experiments with RI beams in inverse kinematics [26, 144]. This large-acceptance multi-particle spectrometer is designed to perform the invariant-mass spectroscopy. It measures the reactions in complete kinematics. The different detectors are used to determine the momenta of the incoming RI beam as well as the momenta of the heavy reaction products and light particles such as neutrons and protons coincidentally. The heart of the setup is the superconducting dipole magnet also called SAMURAI with a bending power of $7.1\,\mathrm{T\,m}$.

As described above, the RIBF provides very exotic nuclei at around $250\,\mathrm{MeV/u}$ ($\beta = 0.615$) that can be studied at SAMURAI. Main physics goals are nuclear structure studies and the study

of nuclear systems beyond the drip lines, as recently performed [26, 145]:

- shell-structure study of bound and unbound nuclei by nucleon-knockout reactions, e. g. quasi-free $(p, 2p)$ scattering on ^{29}F or ^{A}Ne
- spectroscopy of nuclear systems beyond the neutron drip line and study of neutron correlations, e. g. tetraneutron ^{4}n system
- structure study of neutron-rich light nuclei by heavy-ion induced electromagnetic break-up reactions, e. g. ^{31}Ne(Pb,X)
- study of collective excitations of heavy-mass nuclei, e. g. the low-lying dipole response of neutron-rich Ca isotopes
- study of the nuclear Equation of State (EoS), e. g. heavy-ion collisions in the Sπrit Time-Projection Chamber (TPC)
- study of proton- and neutron-rich nuclei for nuclear astrophysics

This is a selection of the broad physics program that is performed at SAMURAI. The experiments that were using the New Large-Area Neutron Detector (NeuLAND) at SAMURAI are summarized in Ref. [28]. The benefit using the R^{3}B neutron detector NeuLAND at SAMURAI is the increased detection efficiency but also its time resolution. A clear detection of four coincident neutrons becomes possible for the first time due to the combination of NeuLAND and the NEutron Detection System for Breakup of Unstable Nuclei with Large Acceptance (NEBULA).

The rigidity resolution of the spectrometer can reach $1/1500$ [26], a similar resolution will be achieved with the Reactions with Relativistic Radioactive Beams (R^{3}B) setup at FAIR but for particles of much higher rigidities [27]. The invariant-mass resolution is about $30\,\mathrm{keV}$ (σ) at only $100\,\mathrm{keV}$ above the one-neutron decay threshold, whereas R^{3}B is designed to reach even $15\,\mathrm{keV}$ with NeuLAND [146]. In the following, these aspects and the details of the detectors that are used in the experiment are described in detail. Run statistics, detector-cabling configurations, and further experiment-relevant information can be found in Ref. [147].

5.3.1 SAMURAI Dipole Magnet

The SAMURAI superconducting magnet [26] is a classical H-type dipole magnet with two superconducting circular coils. The coil has a diameter of $2\,\mathrm{m}$ and provides a maximum magnetic field of $3.1\,\mathrm{T}$ and a field integral of $7.1\,\mathrm{T\,m}$, respectively. The enclosing iron yoke supports a homogeneous magnetic field, besides field clamps are used to minimize the fringe fields in the region of other close-by detectors.

The feature of the magnet is its large gap, see Fig. 5.4. It covers an acceptance of $\pm 10^\circ$ and $\pm 5^\circ$ ($= 80\,\mathrm{cm}$) in horizontal and vertical direction, respectively, for fast neutrons that are being

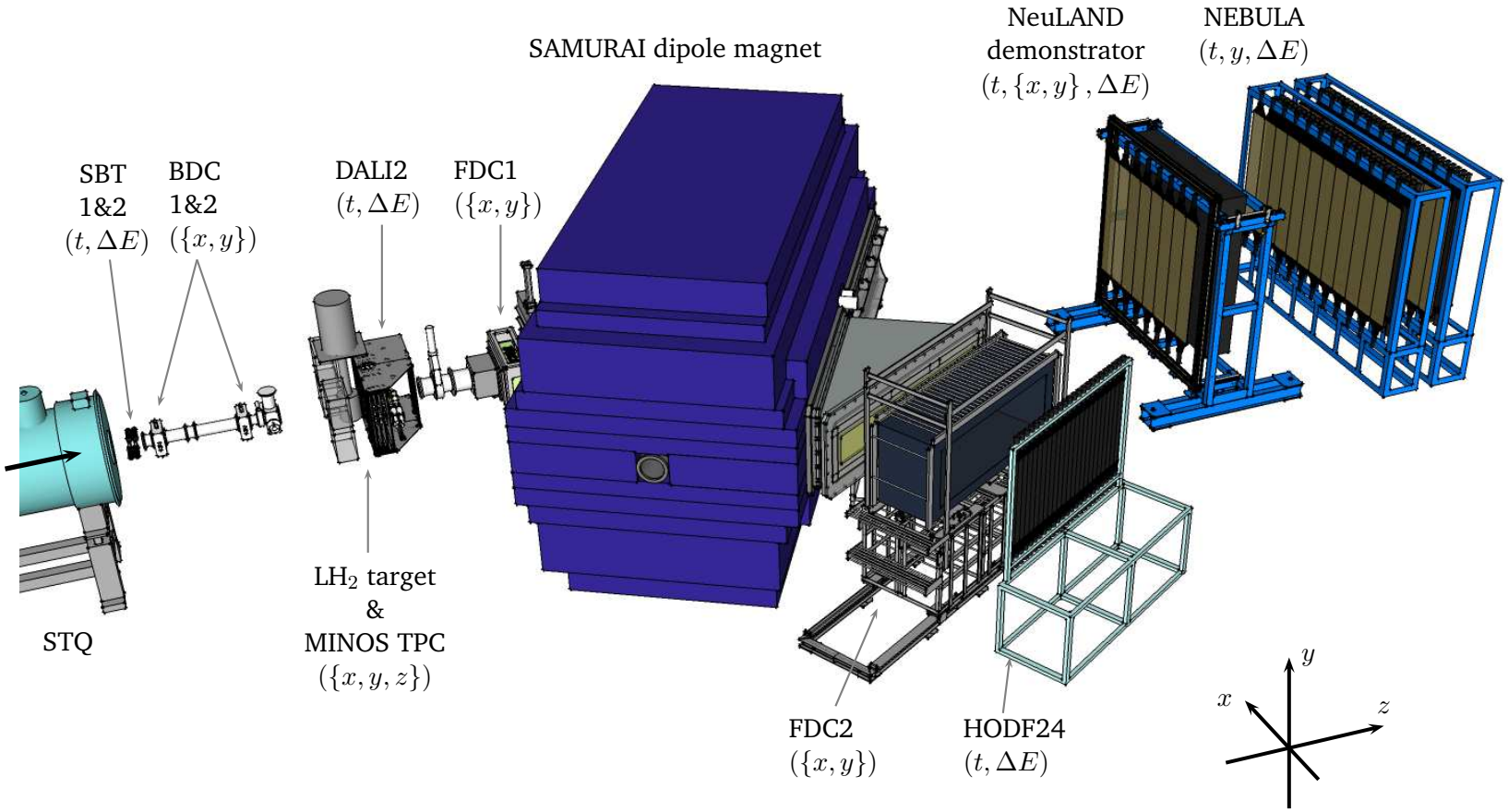

Figure 5.3: Drawing of the SAMURAI setup with name labels on the different detectors, in brackets the measured quantities. The beam is coming from the left and going in $+z$ direction as indicated.

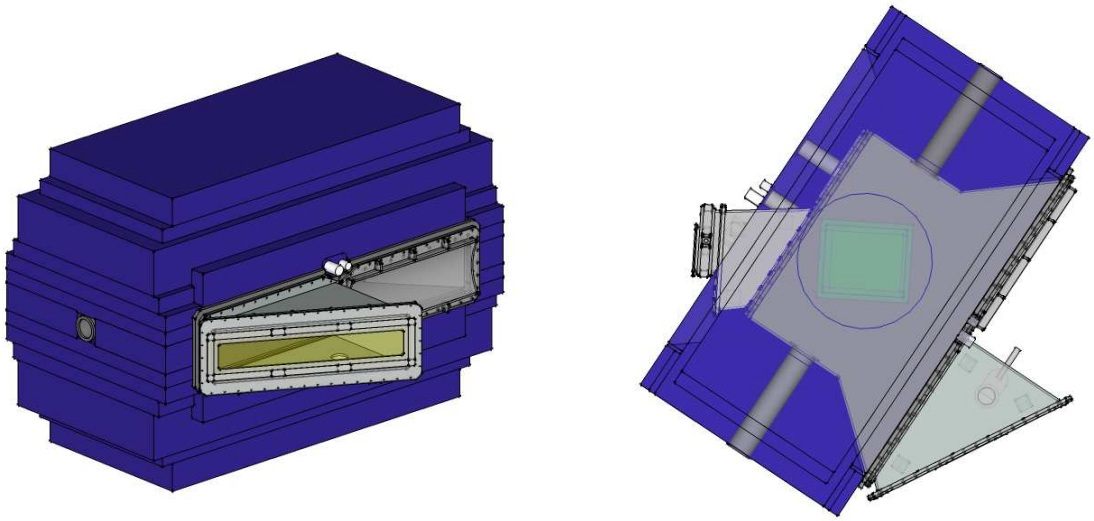

(a) (b)

Figure 5.4: Drawing of the SAMURAI superconducting dipole magnet, (a) in 3D and (b) as top view, showing the vacuum chamber and the triangle exit flange for fragments and the neutron exit window.

detected in NeuLAND and NEBULA at zero degree angle. The charged fragments are deflected in the field according to their magnetic rigidity and are detected in the charged-particle detectors behind. The vacuum chamber is extended by a triangle flange that is covered by a large-size Kevlar-made vacuum window.

The whole yoke is mounted on a rotatable platform to perform experiments with coincident proton measurements or a TPC inside the gap. In the experiment here, the magnet was rotated by 30° for a maximum neutron acceptance and it was operated at $2.9\,\mathrm{T}$. Further details, especially about the behavior of the magnetic field distribution can be found in Refs. [26] and [144].

5.3.2 Detectors

In the following, the detector set to measure charged particles and neutrons is described, addressing the different working principles, to measure basic quantities such as energy loss, time and position, cf. Fig. 5.3.

SBT

At the entrance of the experimental setup in the beam, two $0.5\,\mathrm{mm}$ thin plastic-scintillator detectors (SBT Start Timer (SBT) 1 and 2) are mounted one after the other in vacuum. The material is of quadratic shape $120\,\mathrm{mm} \times 120\,\mathrm{mm}$. Each detector is read out at the left and right edge by one Photo Multiplier Tube (PMT) which is coupled by a light guide to the scintillator sheet, see

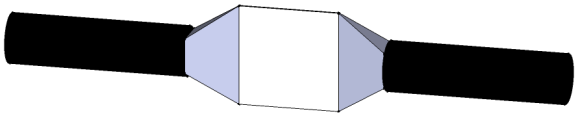

Figure 5.5: Drawing of the in-beam plastic-scintillator detector SBT.

Fig. 5.5. SBT1 and 2 are spaced by $70\,\mathrm{mm}$. The detectors measure the time and energy-loss signal and serve as redundant measurement of ToF, nuclear charge, and provide the beam-trigger signal.

This organic-scintillator detector is made of BC408 plastic material. This kind of detector is widely used in particle physics [148, 149]. When a charged particle passes, the molecules are excited and release their energy as optical photons. The emitted light is converted into electrons at the coupled photo-cathode. The coupled PMT amplifies the charge signal which is measured in a Charge-to-Digital Converter (QDC), and the discriminated signal is recorded with a Time-to-Digital Converter (TDC).

The material itself produces a fast scintillation signal with a rise time $\lesssim 1\,\mathrm{ns}$ and has a high-rate capability. Together with the high light-yield, a picosecond timing resolution can be achieved. At BigRIPS, plastic-scintillator detectors are also used as in-beam detectors, basically to measure the ToF between different focal planes. Their thickness is $3\,\mathrm{mm}$.

Multi-Wire Drift Chambers

In order to measure positions and obtain the trajectories of the incoming and reacted heavy particles, Multi Wire Drift Chamber (MWDC)s in different configurations are equipped, cf. Fig. 5.6. Basically, MWDCs are gaseous detectors consisting of many anode (and potential wires) and cathode layers between which an electrical field is applied [148, 150].

When a particle is passing the gas, electron-ion pairs are created by ionization according to the mean energy-loss. On average, one ion is produced per $30\,\mathrm{eV}$ energy loss, the rate is reduced by e. g. recombination processes. In the vicinity of the electrical field electrons and ions are accelerated towards anode and cathode, respectively. A directed motion with a drift velocity is forced, it is much higher for the electrons compared to the heavier ions and compared to the diffusion process. Eventually, an avalanche of charge carriers is created by multiple ionizations.

The spatial information is obtained by measuring the drift time of the electrons between a reference signal and the wire in common-stop mode. The drift chambers are read out with amplifier-shaper-discriminator boards and multi-hit TDCs [26]. Primarily, this gives the transverse drift length from the point of creation to the wire. Using this information, a track through the detector can be reconstructed.

In order to improve the electrical-field uniformity, the anode wires are surrounded by potential wires. Particular drift cells are formed in case of the FDC2. Combining many cells and layers with

wires orientated in different directions, it becomes possible to reconstruct tracks of the incident particle in three dimensions.

The choice of the gas mixture is a compromise to obtain a good spatial resolution and high-rate capability by requiring a low working voltage, high gain, and good proportionality. The gas is He & CH_4.

The technical details of the different drift chambers used at SAMURAI are described below and are summarized in Ref. [26].

Beam Drift Chamber (BDC) BDC1&2 are placed in front of the target and are $1\,\mathrm{m}$ apart from each other and can accept rates up to $2\,\mathrm{MHz}$ as has been proven [145]. From each BDC the x and y position of the incoming particles is determined, thus allowing to calculate the position and angular distribution of the beam on the target. The active area is $80\,\mathrm{mm} \times 80\,\mathrm{mm}$, where the wires are oriented separately in x and y direction in four layers each. The determined angle from a single drift chamber is not used because the angular resolution is not sufficient, these detectors have a small thickness of $60\,\mathrm{mm}$. The working voltage in the experiment was $625\,\mathrm{V}$. The inclusive detection and reconstruction efficiency accounts for almost $100\,\%$.

Forward Drift Chamber (FDC)1 The FDC1 is located in the beam behind the target but before the particles enter the SAMURAI magnet. This detector is essential to measure the scattering angle of the heavy reaction fragments. It is a Walenta-type drift chamber like the BDCs with similar efficiency. The applied voltage was $725\,\mathrm{V}$. It is larger than the BDCs. The size mirrors the maximum acceptance for neutrons. However, the effective area is limited to a circular area with diameter of $31.5\,\mathrm{cm}$. The wires are oriented in y direction and $+/-30^\circ$ (u/v direction) relative to it. This allows a track reconstruction in three dimensions, giving position and angular information.

FDC2 The FDC2 is by far the largest drift chamber among them, see Fig. 5.6, and thus requiring a different construction. The active volume is $230\,\mathrm{cm} \times 60\,\mathrm{cm} \times 84\,\mathrm{cm}$. The cell structure is hexagonal with 1568 readout channels and in total 4788 field wires to keep the uniformity of the electrical field. The working voltage was $2450\,\mathrm{V}$. This drift chamber is placed at the fragment arm behind the SAMURAI dipole and covers almost the acceptance of the magnet's exit window. It is used to determine the track of the particle behind the dipole magnet, and thus helps with the identification of the reaction products.

MINOS Target and TPC

Quasi-free scattering reactions have recently been studied at the R^3B/LAND setup at GSI with approx. $1\,\mathrm{g/cm^2}$ polyethylene targets [112, 152]. A pure Liquid Hydrogen Target (LH_2 target) is installed here.

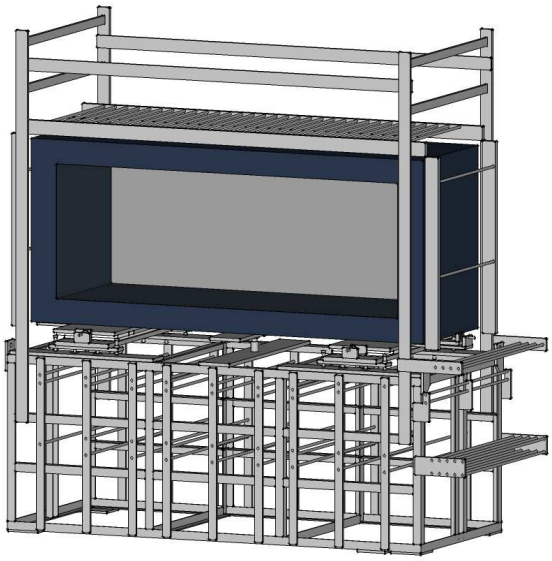

Figure 5.6: Drawing of FDC2 in its frame.

The MagIc Numbers Off Stability (MINOS) device combines a thick LH_2 target with a surrounding TPC to restore the vertex resolution for (p, pN) reactions by tracking the charged nucleons, cf. Fig. 5.7. It has been developed by Obertelli et al. [153] and was taken into operation at the RIBF in 2013. Primarily, it is designed to be combined with DALI2, a γ-ray detector array for in-beam γ-spectroscopy experiments of rare isotopes at BigRIPS.

The in-beam γ-spectroscopy is performed in a different dedicated program called Shell Evolution And Search for Two-plus energies in neutron-rich nuclei At the RIBF (SEASTAR) [154]. The SEASTAR program pursues the study of shell-structure evolution along isotopic and isotonic chains by measuring the most neutron-rich candidates and to identify (sub)shell closures. First shell-structure information can be obtained from the energy of the first excited 2^+ state. Key nuclei to be studied are e. g. ^{62}Ti, ^{78}Ni [155], ^{110}Zr [156], and nuclei around [154].

In the experiment analyzed here, MINOS is operated for the first time at SAMURAI. The LH_2 target serves as secondary target and is surrounded by the TPC and DALI2 such that also the γ-spectroscopy of (prompt) bound-state decays is performed coincidentally. The use of MINOS comprises important features for the invariant-mass spectroscopy:

- LH_2 target as direct probe for nucleon-knockout reactions
- thick ($15\,\mathrm{cm}$) target to increase luminosity
- TPC to track the reaction vertex with good position resolution ($\sigma_z \approx 3.5\,\mathrm{mm}$)

The latter also improves the invariant-mass resolution. Energy-loss, position, and ToF can be accounted for when the reaction position is precisely known in the target. Often, solid targets like

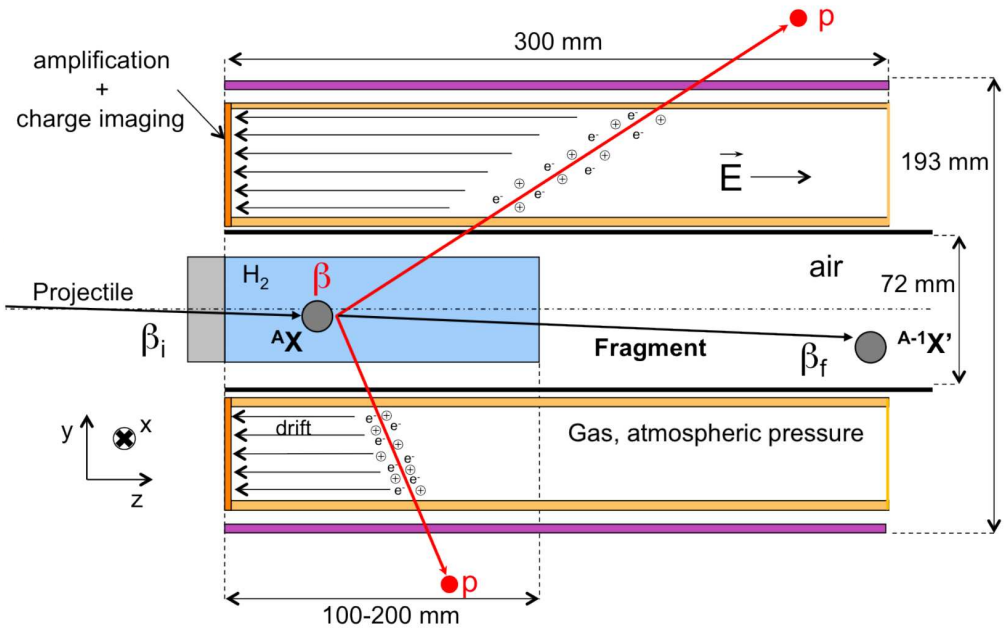

Figure 5.7: Scheme of the MINOS operation. Figure taken from Ref. [151].

CH_2 are used to induce nucleon-knockout reactions in QFS conditions, where the contribution from reactions on carbon needs to be subtracted. Assuming the same cross section for a proton knockout on both targets and including the vertex-reconstruction efficiency ($80\,\%$) and beam loss due to secondary reactions ($20\,\%$) for the LH_2 target, the CH_2 target ($0.94\,\mathrm{g/cm^3}$) would need to have the following length:

$$\begin{aligned} \frac{P^{\mathrm{LH2}}}{P^{\mathrm{CH2}}} &= \frac{\rho^{\mathrm{LH2}}}{M^{\mathrm{LH2}}} \frac{M^{\mathrm{CH2}}}{\rho^{\mathrm{CH2}}} \epsilon \cdot \frac{d^{\mathrm{LH2}}}{d^{\mathrm{CH2}}} = 1 \\ \Rightarrow d^{\mathrm{CH2}} &= \frac{0.0753\,\mathrm{g/cm^3}}{2\,\mathrm{g/mol}} \frac{14\,\mathrm{g/mol}}{0.94\,\mathrm{g/cm^3}} \frac{2}{3 \cdot 0.8 \cdot 0.8} \cdot 15\,\mathrm{cm} = 8.8\,\mathrm{cm}. \end{aligned} \tag{5.4}$$

In this estimation, the CH_2 is approx. half as long as the LH_2 target target to reach the same luminosity. Ultimately, this would result in a position resolution with the solid target that is eight times worse (without vertex reconstruction) compared to the LH_2 target with $\sigma_z \approx 3.5\,\mathrm{mm}$. The technical details of MINOS are described in the following [151, 153].

LH_2 target The used cylindrical target cell, cf. Fig. 5.7, has a length of $150\,\mathrm{mm}$ and is fabricated from Mylar. The entrance window has a diameter of $38\,\mathrm{mm}$ and is $110\,\mu\mathrm{m}$ thick. The cell widens towards the end, the exit window has a diameter of $52\,\mathrm{mm}$ and a thickness of $150\,\mu\mathrm{m}$. The window is slightly spherically deformed and the effective target-cell length becomes $151(1)\,\mathrm{mm}$.

The hydrogen is operated at $15\,\mathrm{K}$ and at a pressure of $143\,\mathrm{mbar}$ what corresponds to a density in the liquid phase of $0.0752\,\mathrm{g/cm^3}$. In the reactions considered here, the energy loss of the heavy

fragment is as much as $\sim 30\,\mathrm{MeV/u}$ and the angular straggling is $\sim 1.4\,\mathrm{mrad}$ (σ) in the LH_2 target.

TPC The TPC that surrounds the target, see Fig. 5.7, is designed to measure the tracks in three dimensions of the proton from the target and the charged nucleon from the projectile like in $(p, pN)^*$ or even $(p, 3p)$ nucleon-knockout reactions. The TPC barrel is $300\,\mathrm{mm}$ long, has an inner radius of $40\,\mathrm{mm}$ and an outer radius of $95\,\mathrm{mm}$. Due to this configuration, the acceptance and detection efficiency is reduced for events with small momentum transfer where the beam proton is not detected in the TPC and the target proton is actually stopped in the target.

As the drift chambers, described in Sec. 5.3.2, the TPC is a gaseous detector where a charged particle that passes the volume ionizes the gas along its track and the electrons drift in the presence of an electrical field to a sensitive readout layer. This basic working principle is shown in Fig. 5.7. The electrons are detected with a Micromegas pad-plane detector in the xy-plane [153] that has in total 3604 anode-pads of constant size $2\,\mathrm{mm} \times 2\,\mathrm{mm}$. They are arranged in rings.

The Micromegas is a thin micromesh that separates the field cage volume in a big volume for ionization and drift and a thin region of $128\,\mu\mathrm{m}$ just before the pads. In this region, a very high electrical field of maximum $70\,\mathrm{kV/cm}$ is applied that causes a high amplification and avalanche.

The detected signals are spatially resolved by the pads. In the TPC, the x and y coordinates from the proton tracks are obtained from the coordinates of the pads in the Micromegas plane. Instead, the z position is determined from the drift time of the electrons, the tracking details are described in Sec. 6.5. The longer the drift time is, the closer to the end of the TPC the electron was produced. The readout electronics records the full trace of the signals with a sampling rate of $50\,\mathrm{MHz}$ and the shaping time is $333\,\mathrm{ns}$. The Data Acquisition (DAQ) can record events with a rate up to a few kHz. These information are summarized in App. C.2.1.

The TPC gas is a mixture of $82\,\%$ argon, $15\,\%$ CF_4, and $3\,\%$ isobutane. The drift velocity is very sensitive to oxygen and water impurities in the gas as evidently shown in Sec. 6.5.

DALI2 Gamma-ray Detector

MINOS is designed to fit into the γ-ray detector array DALI2 for in-beam γ-spectroscopy experiments of very rare isotopes at the RIBF. DALI2, see Fig. 5.8, is a detector with high efficiency and good angular resolution [157].

The de-exciting fragment is moving at $\sim 60\,\%$ speed of light which means that the center-of-mass E_{cm} energy of the transition γ-ray is Doppler shifted as

$$E_{\mathrm{cm}} = \gamma\,(1 - \beta \cos\theta_{\mathrm{lab}}) \cdot E_{\mathrm{lab}}, \tag{5.5}$$

with the energy measured in the laboratory frame E_{lab}, its angular direction θ_{lab} in the lab. frame, and the velocity βc of the de-exciting nucleus and the corresponding Lorentz factor γ. So, the

*the neutron is not measured directly

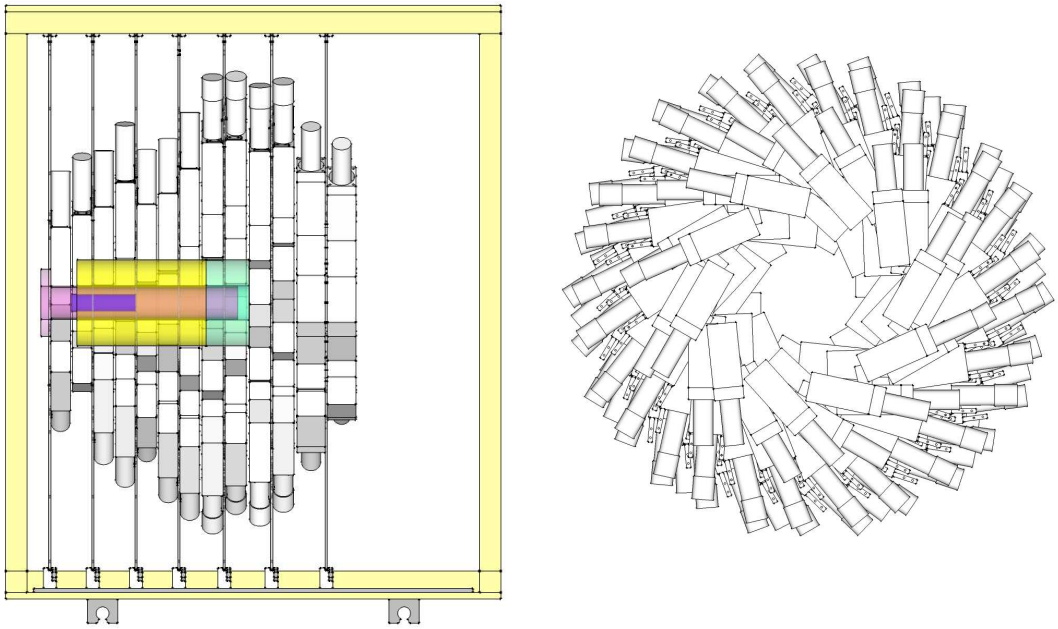

(a) (b)

Figure 5.8: Drawing of the DALI2 γ-ray array, (a) side view with the target cell and TPC around, the beam is coming from the left. (b) Front view.

energy resolution $\Delta E_{\text{cm}}/E_{\text{cm}}$ depends on

1. the angular resolution $\Delta\theta_{\text{lab}}$,
2. the velocity uncertainty of the fast-moving nucleus at the point of emission $\Delta\beta$,
3. and the intrinsic energy resolution ΔE_{lab}.

In a formula this reads

$$\begin{aligned}\left(\frac{\Delta E_{\text{cm}}}{E_{\text{cm}}}\right)^2 = &\left(\frac{\beta \sin\theta_{\text{lab}}}{1-\beta\cos\theta_{\text{lab}}}\right)^2 \cdot (\Delta\theta_{\text{lab}})^2 + \\ &+ \left(\frac{\beta\gamma^2(\beta-\cos\theta_{\text{lab}})}{1-\beta\cos\theta_{\text{lab}}}\right)^2 \cdot \left(\frac{\Delta\beta}{\beta}\right)^2 + \\ &+ \left(\frac{\Delta E_{\text{lab}}}{E_{\text{lab}}}\right)^2 .\end{aligned} \tag{5.6}$$

The detector array is designed to compromise these aspects by

1. granularity of maximum 186 single detectors where the angular resolution is basically determined by the crystal size, on average $\Delta\theta_{\text{lab}} = 7^\circ$ (FWHM),
2. use of MINOS to determine the de-excitation point which is the same as the reaction point for knockout reactions and zero lifetime, $\Delta\beta/\beta \approx 0.15\,\%$ (for tracking with MINOS),

3. use of thallium-doped sodium iodide (NaI(Tl)) inorganic-scintillator detectors with $\Delta E_{\text{lab}}/E_{\text{lab}} \approx 9\,\%$ (FWHM) at $1\,\text{MeV}$, and good detection efficiency (total $\approx 15\,\%$ at $1\,\text{MeV}$ for 120 crystals).

In the experiment discussed here, 140 single detectors are used that has been mounted in 13 layers, which are separated by aluminum plates of $5\,\text{mm}$ as shown in Fig. 5.8a. The detectors have a brick-like shape and build a barrel-like structure around the target.

Important is the coverage around the target in forward direction due to the Lorentz boost. At that position the detectors with best intrinsic resolution are mounted. In particular, three different detector types are used with slightly different size, manufactured by Scionix company with $40\,\text{mm} \times 80\,\text{mm} \times 160\,\text{mm}$, and by Saint-Gobain with $45\,\text{mm} \times 80\,\text{mm} \times 160\,\text{mm}$ and $61\,\text{mm} \times 61\,\text{mm} \times 122\,\text{mm}$. The single detectors have a thin aluminum housing and are coupled to a PMT (shielded by Mu-metal).

The γ-rays interact with the electrons in the material by the photoelectric effect, the Compton effect, or pair creation – the light yield is about 1 photon produced by $100\,\text{eV}$ deposited energy.

The signal from the PMT is fed through a shaping amplifier with two different time constants ($3\,\mu\text{s}$ and $100\,\text{ns}$). The split signal is analyzed in an Analog-to-Digital Converter (ADC) to obtain the energy information and in a TDC, after having passed a Constant-Fraction Discriminator (CFD), to determine the hit time although the time resolution is not of foremost importance. The array is internally triggered by an OR trigger from the CFD signals and externally in an AND logic together with the beam trigger or others. The readout is synchronized with MINOS.

Hodoscope for Fragment-24 (HODF24)

The HODF24 [26], see Fig. 5.9, is placed at the end of the fragment arm behind the FDC2. The detector is segmented and built out of 24 vertically aligned plastic-scintillator paddles, wrapped in light-tight foil. The detection principle is introduced in Sec. 5.3.2. Each paddle is $120\,\text{cm}$ long, $10\,\text{cm}$ wide, and has a thickness of $1\,\text{cm}$ in beam direction. This makes a total width of $240\,\text{cm}$ to cover the FDC2. The scintillation light is read out by one PMT on each end of a paddle. The PMTs are coupled by light guides to the effective area. HODF24 is used to determine the nuclear charge of the heavy fragments from their energy loss in the material and it creates the stop signal to determine the particle's ToF through the setup.

Neutron Time-of-Flight Spectrometers

The main advantage of the SAMURAI setup for this particular experiment is the coincident measurement of fast neutrons. The neutron measurement requires special techniques because the particle is neutral. A detection is only possible by detecting secondary particles.

Two large-area neutron ToF-detectors, called NeuLAND demonstrator (Fig. 5.10) and NEBULA (Fig. 5.11), are placed at zero degrees with a maximum distance of $15\,\text{m}$ to the target.

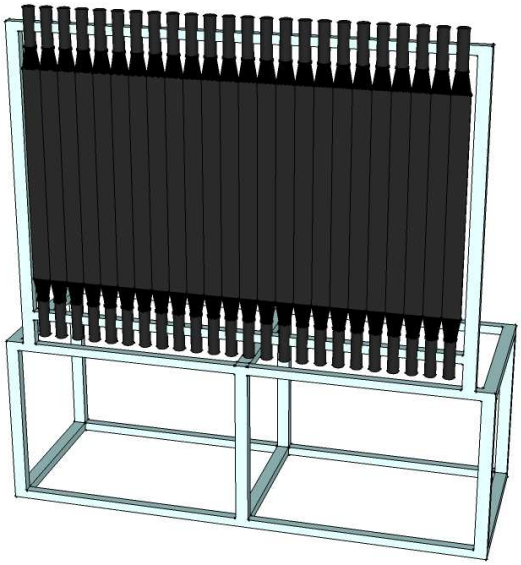

Figure 5.9: Drawing of HODF24.

Both are fully-active detectors which are built completely out of plastic-scintillator paddles. Since the neutron is an electrical neutral particle, it interacts via elastic and inelastic scattering with the carbon and proton of the detector material or in nuclear reactions with the carbon. The secondary particles such as recoil protons or γ-rays then interact, as described already, with the scintillator material. This response is measured and by using dedicated algorithms, the initial neutron interaction and eventually the neutron momentum is reconstructed . Thus, the detectors need a high detection efficiency, especially to detect up to four coincident neutrons, and a good position and ToF resolution.

The NeuLAND demonstrator is only a part of the full NeuLAND. NeuLAND is originally designed and built for the R^3B experiment at GSI and the future FAIR. However, when there was a shutdown planned at GSI, the first part of NeuLAND that had been built by 2014 was sent to Japan and was integrated into the SAMURAI setup. The existing NEBULA would not have been sufficient in terms of tracking efficiency to perform the spectroscopy of ^{28}O with a reasonable amount of beam time. The total efficiency for the reconstruction of four neutrons is $0.3\,\%$ [158]. Adding NeuLAND also improves the invariant-mass resolution. The “NeuLAND demonstrator” is often abbreviated in this thesis as “NeuLAND”, but the demonstrator is meant with its reduced number of scintillator paddles.

As stated above, both detectors are based on the same working principle. Plastic-scintillator paddles are arranged as big volume to allow particle tracking. The detectors are equipped with veto detectors in-front that are $1\,\mathrm{cm}$ thin plastic-scintillator paddles with a length of $190\,\mathrm{cm}$ and width of $32\,\mathrm{cm}$. The secondary particles lose energy in the material and thus create scintillation

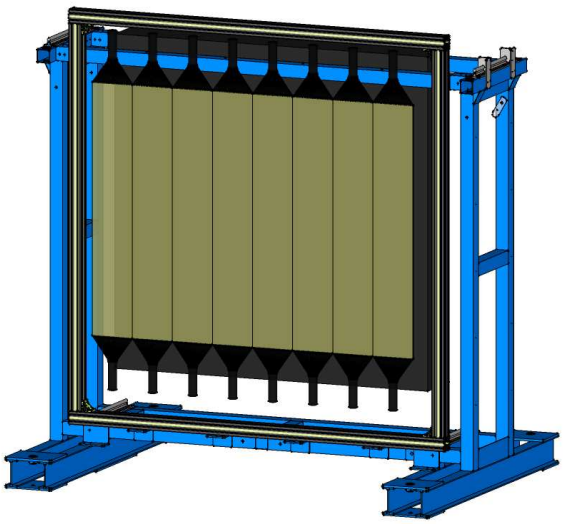

Figure 5.10: Drawing of the NeuLAND demonstrator with veto detector in front.

photons which travel through the material and are collected at the PMTs. In detail, the response of such organic scintillator-materials is not linear to the ionization density [149]. The effective light yield is described by Birks' law. These effects as well as the attenuation and PMT saturation need to be considered in the analysis of the data.

The position information x of the signal can be obtained from the time difference of both PMT measurements t_1 and t_2 of one paddle of length L as derived in the following,

$$\begin{aligned} t_1 &= \frac{L-x}{2v} + t_0, \\ t_2 &= \frac{L+x}{2v} + t_0, \end{aligned} \tag{5.7}$$

$$\Delta t = t_2 - t_1 = \frac{x}{v}, \tag{5.8}$$

$$x = v \cdot \Delta t, \tag{5.9}$$

with the effective speed-of-light v of the scintillation photons and a general time offset t_0. It is worth mentioning that also the energy signal can be used to calculate the hit position. The next paragraphs discuss particular differences between both detectors.

NeuLAND demonstrator The NeuLAND demonstrator, see Fig. 5.10, is built out of 400 scintillator paddles (BC408 equivalent) with a cross section of $5\,\mathrm{cm} \times 5\,\mathrm{cm}$ and length of $250\,\mathrm{cm}$ each [146]. 50 paddles are arranged horizontally, in the same frame the next layer has 50 vertically aligned paddles, what together is called a double plane. Four double planes are packed together at SAMURAI creating a $40\,\mathrm{cm}$ thick detector volume of high granularity with 800 readout

channels. One paddle is read out at the two ends by a PMT, the supply high-voltage is typically in a range of $1000\,\mathrm{V} - 1100\,\mathrm{V}$.

The PMTs are read out with the so called TacQuila electronics, a GSI development [159]. The boards combine a QDC and TDC and for communication a multiplexer unit coupled to a front-end board. The cards, each providing sixteen channels, are connected with each other. The signals are processed in a chain but the trigger or pulser signals are distributed in a tree-like scheme [160].

The time measurement is performed relative to the so called channel 17 that serves as a reference on each board, whereas the 17th intrinsic channel is aligned to the trigger. The time difference between channel 17 and a signal channel is counted in cycles c_{cl} of a reference clock with a frequency of $f_{cl} = 40\,\mathrm{MHz}$. The time measurement of an incoming signal within one clock cycle is the so called `tac` value, measured relative to the trailing edge. The time of one channel t_i is calculated in the following way:

$$t_i = t(\mathrm{tac}_i) - t(\mathrm{tac}_{17}) + \frac{c_{\mathrm{cl}}}{f_{\mathrm{cl}}}. \tag{5.10}$$

In the end, channel 17 is measured relative to the trigger in the same way. The master-start signal is additionally measured in one channel of NeuLAND to correct for time jitter intrinsically. The electronics and DAQ system of NeuLAND are described in great detail in the thesis of C. Caesar [161].

The time resolution of the detector is ideally $\sim 150\,\mathrm{ps}$ [146]. Thus, the position resolution is in all directions $\sigma \approx 1.5\,\mathrm{cm}$.

In addition to the detector volume itself, NeuLAND is equipped with a veto detector in front, see Fig. 5.10. That are eight slats of $1\,\mathrm{cm}$ thickness and $190\,\mathrm{cm}$ length of plastic scintillator material. It is used to veto signals caused by charged background particles. The same veto detector and its readout are used for NEBULA.

NEBULA NEBULA is a less granular neutron detector compared to NeuLAND. It consists of only vertical paddles (BC408 material) which have a size of $12\,\mathrm{cm} \times 12\,\mathrm{cm} \times 180\,\mathrm{cm}$ [26]. 120 paddles are arranged in four layers of 30 paddles each, the horizontal extent is $360\,\mathrm{cm}$. This covers an angular acceptance of $\pm 130\,\mathrm{mrad}$ vertically and $\pm 65\,\mathrm{mrad}$ horizontally in this experiment (considering only the detector size). The four layers are divided into two walls with a distance of $85\,\mathrm{cm}$, see Fig. 5.11. Together with NeuLAND this makes three walls which can be used for a particular neutron crosstalk-rejection analysis, see Sec. 7.6. Each wall is equipped with the same veto detector as it is used for NeuLAND but in total 24 slats are used to cover the full detector. Each scintillator paddle is read out at both ends. The position in x direction can only be obtained from the paddle position but this is sufficient in terms of angular resolution since the detector is placed that far from the target. The signals from the PMTs (same for veto) are processed in a conventional way by using ADCs, leading-edge discriminators, and TDCs.

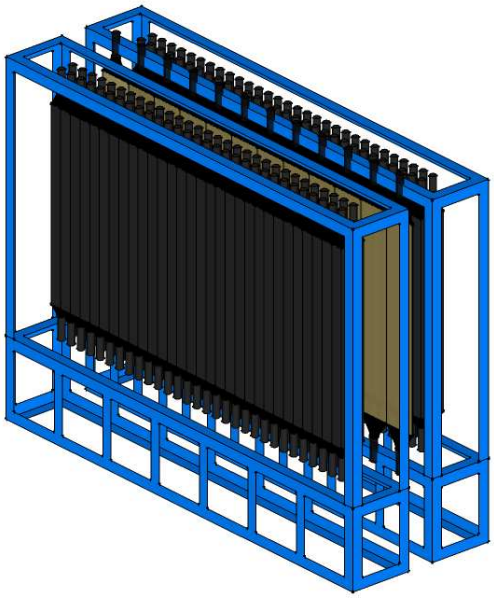

Figure 5.11: Drawing of the NEBULA walls (the veto detector is not shown for the first wall).

5.3.3 Photogrammetry

The absolute positions of the detectors in the experimental hall are obtained by a photogrammetric measurement. The whole experimental setup is analyzed from photographs with a commercial software called V-STARS [162]. The geodetic system allows to determine precisely the space coordinates of each detector frame. The point of reference is here the center of the SAMURAI magnet.

The measurement, that has been carried out before and after the experiment, was analyzed by T. Ozaki [163]. The floor plan with the detector positions can be found in App. C.2.3. The RMS of the standard deviation of all measured points is for the x coordinate $120\,\mu\mathrm{m}$, $92\,\mu\mathrm{m}$ for y, and $104\,\mu\mathrm{m}$ for z [163].

The photogrammetry measurement is applied to the housing of the detectors so that the active area has to be deduced from additional information like technical drawings. The position information is important for the tracking of the particles through the setup. The final position calibration is performed using experimental data, for example extrapolated positions from different detectors have to match each other at a common focus as outlined in Sec. 7.3.

5.3.4 Data Acquisition

The DAQ system at the RIBF provides a hierarchical event building structure and a parallel readout of several sub-systems [164]. As described in this section, there are several detector systems used at SAMURAI. Their data readout is handled by their own DAQ sub-systems that are waiting for a

Table 5.1: Experiment triggers.

Trigger input	Condition
0	Beam
1	Beam $\times$ NEBULA ($\times$ HODF24)
2	Beam $\times$ NeuLAND ($\times$ HODF24)
3	Beam $\times$ DALI2
4	Beam $\times$ NEBULA (γ)[†]
5	Beam $\times$ NeuLAND (γ)
7	Miscellaneous (during calibration only)

common master trigger. The sub-systems at SAMURAI are the beam-line scintillation detectors, BDCs, FDC1, FDC2 (separated into two readouts), HODF24, NEBULA, NeuLAND, DALI2, and BigRIPS. DALI2 and MINOS are handled separately.

The detectors are directly read out by e. g. TDC, ADC, or other modules. Following, these data are buffered by a Front End Computer (FEC), that works also as control unit of the DAQ sub-system. The data blocks are processed in the slave event-builder. The event builders, as the name implies, construct the event-data structure with proper event number and other relevant overhead.

The raw-data format is called "`ridf`", the software package is called "`babirl`". The single slave event-builders "`babild`" are controlled by one master event-builder which manifests in the hierarchical event-building structure. The comprised data blocks are sent to the global storage system and the online analysis-server "`babian`" which allows to check the data from stream already during the experiment. [165]

All readouts rely on the same master trigger and a common dead-time handling. The data are collected event-wise. The DAQ readout rate is limited by the dead time of the sub systems, which is here dominated by the BDC readout with $250\,\mu$s. NeuLAND has a deadtime of $90\,\mu$s.

When a certain detector generates a signal, it can create a trigger signal. The available triggers in the experiment are listed in Table 5.1, these are logical combinations of single triggers. Single triggers are the logical signals originating from the coincidences in the different detectors. The single trigger "Beam" stands for a coincidence in the SBT. In case of NEBULA, at least two PMTs have to be fired to make a coincident trigger signal. In case of NeuLAND it was four. In the production runs of the ^{29}F setting, the reaction trigger was set to the non-downscaled Beam trigger and no other condition was requested additionally. Due to the low intensity of the secondary beam ($\sim 400\,\mathrm{pps}$) every event that has triggered the SBTs was written to tape with regard to the dead time of $\sim 10\,\%$.

The main DAQ in the master branch collects the information from the sub-systems and operates which data are recorded. In order to handle the dead-time locking and to ensure that

[†] trigger on particular fast and low energy signal, used in calibration runs

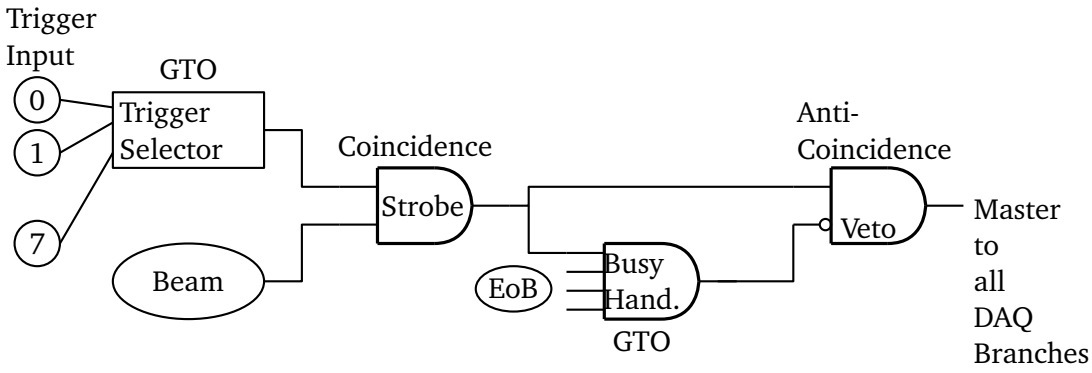

Figure 5.12: Scheme for creation of the master trigger.

no following event is recorded as long as the previous event has not been processed, two Field-Programmable Gate Array (FPGA)-based logic modules are used, namely the Logic Unit for Programmable Operation (LUPO) and the Generic Trigger Operator (GTO) [166]. Every detector provides an end-of-busy signal when its own data processing is finished. The signal is handled by the LUPO modules. The signal to take data is instead the accepted trigger which releases the signal to read and build an event from the data (and generate accordingly gate signals). The (accepted) main trigger is produced from the GTO module.

One GTO is in particular working as trigger selector and the second one as busy handler. The trigger working scheme is depicted in Fig. 5.12. The seven trigger signals listed in Table 5.1 are the input to the first GTO, the selector GTO. It multiplexes (and scales down) the inputs and checks if the reaction-trigger condition is matched. From there, the selected trigger makes again a coincidence with the beam trigger to the so called strobe signal such that the beam signal determines the timing. The other GTO has the end-of-busy (EoB) signals as input and as such can veto the strobe signal. If the strobe survives the veto the common master trigger is sent out to all DAQ branches and data are recorded again.

DALI2 and MINOS run their own DAQ systems so that it can be run in standalone mode also, but are connected via the common dead time handling. NeuLAND can also run in standalone mode using the Multi Branch System (MBS) DAQ from GSI. The cabling documentation can be accessed online, Ref. [147].

Chapter 6

Data Calibration

This chapter describes in detail the calibration steps and algorithms to obtain calibration parameters for the different detectors. The aim is to convert raw data to physical values and in the end to quantities as e. g. particle momenta, what is described in the analysis Ch. 7. In the previous Ch. 5, the detectors and their readout were described. The commonly used modules as TDC and ADC measure the time and charge, respectively, in units of channels – the so called raw data. The purpose of the calibration is to convert these values into physical values as times given in nanoseconds (ns), positions in millimeter (mm) and energies in megaelectron volt (MeV). Furthermore, the consistency of quantities from different measurements is checked and partly already analyzed in this chapter.

6.1 Analysis Framework

The whole analysis is performed in the programming languages `C/C++` using the object-oriented frameworks `ROOT` [167] and `ANAROOT` [165]. `ANAROOT` is the toolkit developed at RIBF that is based on `ROOT` and tailored for the analysis of the RIBF experiments. Within this framework, libraries to decode, reconstruct, and analyze the data exist but others are added. The `TClonesArray` class provides the underlying data structure.

As mentioned in Sec. 5.3.4, the raw data are listed in `ridf` files as hexadecimal values. In the first step, these data blocks are decoded from the written event into measured integer values for each detector readout and channel – the raw data in units of channels. The next step is the analysis to determine calibration parameters for the different detectors and to apply them, which is described in the following sections.

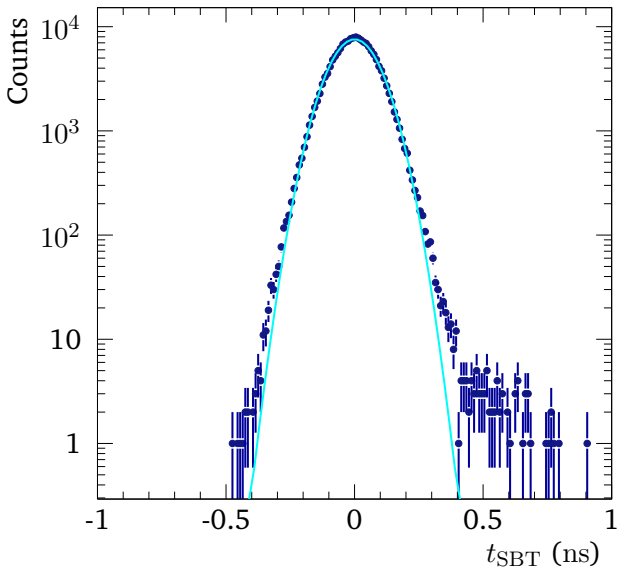

Figure 6.1: Start time measured with the two SBT in-beam plastic-scintillator detectors (blue dots), fitted with a Gaussian function (cyan line).

6.2 In-Beam Plastic-Scintillator Detectors

The in-beam plastic-scintillation detectors are used to measure time and energy-loss from which ToF, nuclear charge Z, and in case of the detector at the BigRIPS focal plane F5 also the x position is deduced. Five in-beam plastic-scintillation detectors with two channels each are used. That are namely the detectors at F3, F5, F7, and the two start counters at SAMURAI (SBT1 and 2).

6.2.1 Time Calibration

The time signal is measured with a TDC relative to the strobe signal. In a first step, the calibration from TDC channels to time in nanoseconds t_{TDC} is done. Therefore, dedicated calibration data are taken where a time calibrator sends a sharp pulse to the TDC channels of plastic-scintillator detectors precisely every $10\,\mathrm{ns}$.

Knowing the frequency of the signals, the calibration relation between time in channels $\mathrm{ch}_{\mathrm{TDC}}$ and in nanoseconds is a simple linear function. The slope parameter α of the linear function is the conversion factor,

$$t_{\mathrm{TDC}} = \alpha \cdot \mathrm{ch}_{\mathrm{TDC}}. \tag{6.1}$$

The start time t_{SBT}, see Fig. 6.1, is defined as mean of the time measurements of the two SBT counters,

$$t_{\mathrm{SBT}} = \frac{1}{4}\left(t_{\mathrm{SBT1,0}} + t_{\mathrm{SBT1,1}} + t_{\mathrm{SBT2,0}} + t_{\mathrm{SBT2,1}}\right). \tag{6.2}$$

The time resolution of a SBT is deduced from the time difference between the two SBT measurements, $\sigma(t) = \sigma(t_{\mathrm{SBT2}} - t_{\mathrm{SBT1}})/2$, where the time walk is corrected for and it is assumed that all the PMTs show the same time resolution. The SBT detectors reach a time resolution of $\sigma(t) = 40\,\mathrm{ps}$.

6.2.2 Energy-Loss Calibration

The Bethe-Bloch formula describes the energy loss $\mathrm{d}E/\mathrm{d}x$ of a particle with charge Z passing matter along a path. Although the plastic-scintillation detectors have a poor energy resolution, the beam is a mix of light ions where the energy-loss difference between different Z is large, as the energy loss ΔE scales with Z^2 and $1/\beta^2$. Thus, the calibration step from the charge measured with a QDC to energy loss in MeV and the attenuation correction are skipped. A direct calibration from the raw signal ΔQ to Z is done,

$$Z \propto \Delta Q = \sqrt{Q_0 \cdot Q_1},$$

with the signals Q_0 and Q_1, that are attenuated after traveling to the PMT, measured at PMT0&1 of the detector. The velocity dependence of Z is approximated in a linear relation as function of the ToF between the foci.

The pedestal values are subtracted beforehand. Intrinsically, the QDC measures always a small charge although no input signal is applied. A capacitor-integrated current is measured as offset when a gate is applied. The value of the pedestal is obtained from the same calibration data as for the time calibration where only a gate signal is sent to the QDCs.

6.2.3 Position Measurement

As shown in Eq. 5.9, the time difference between the two PMTs of a scintillator detector allows to deduce the x position of the hit. The x-position information at the dispersive focus F5 is later used to calculate the beam magnetic-rigidity.

The plastic-scintillation detector is calibrated on absolute scale using the PPAC, that is mounted infront. The PPAC is once operated together, while only used for calibration.

The relation between the position measured by the PPAC x_{PPAC} and the time difference of the plastic-scintillator detector Δt_{01} is shown in Fig. 6.2. The second PPAC at F5 has an experimentally determined efficiency of $83\,\%$. The other PPAC at F5 is not working properly, it shows a small efficiency, and is thus not used. The relation $x_{\mathrm{Sci}} = f(\Delta t_{01})$ is modeled with a polynomial function of 9th order. The result of the calibration is shown in Fig. 6.3, where the difference between the PPAC position and the position calculated from the time difference is shown as function of the measured PPAC x-position. The width of the y-projection is $\sigma = 3.4\,\mathrm{mm}$.

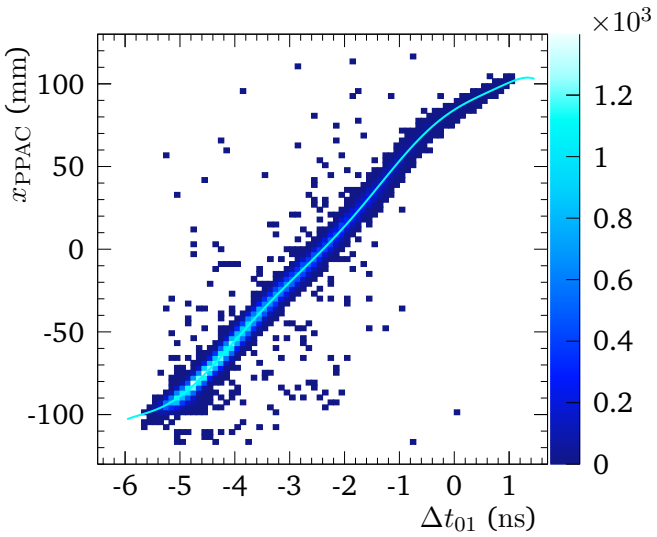

Figure 6.2: Relation between x-position measured with the PPAC at F5 and the time difference of the plastic-scintillator detector Δt_{01}. This relation is fit with a 9th order polynomial and used to calibrate the position of the scintillation detector.

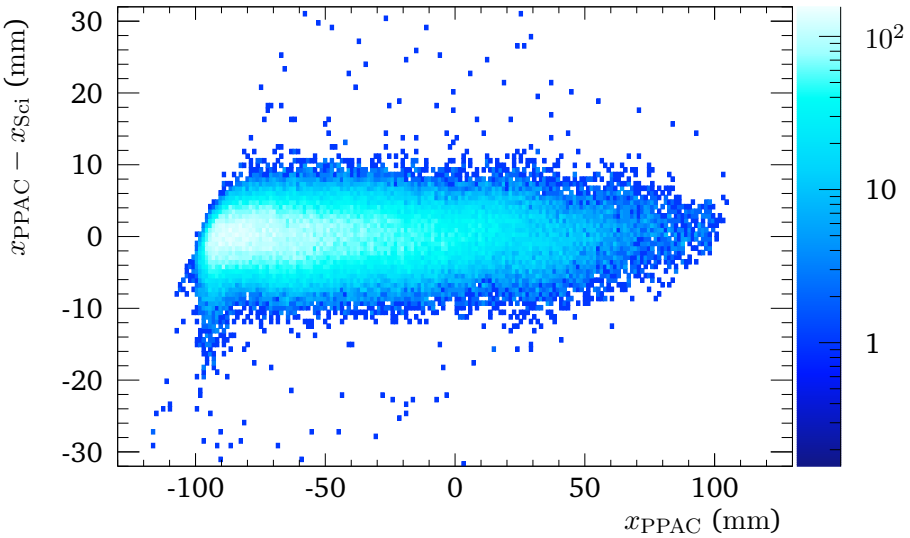

Figure 6.3: Result of the position calibration of the plastic-scintillator detector at F5 using the PPAC. The position difference between measured and calibrated position $x_{\mathrm{PPAC}} - x_{\mathrm{Sci}}$ is shown vs. the measured position.

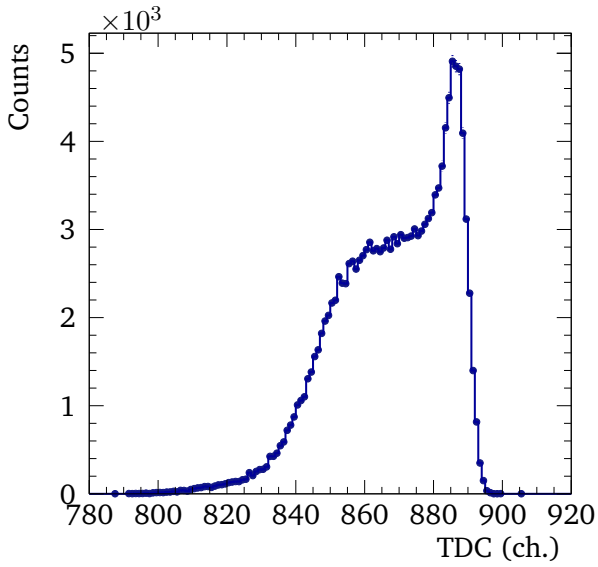

Figure 6.4: Raw TDC spectrum of BDC1 for incoming charge $Z = 10$ and one layer.

6.3 Multi-Wire Drift Chambers

The working principle of a multi-wire drift chamber is described in Sec. 5.3.2. First, the drift time is converted into a drift length. Second, the track of the heavy particle is reconstructed from the single interactions in each layer.

The maximum drift length between anode and potential wire is known: $2.5\,\mathrm{mm}$, $5.0\,\mathrm{mm}$, or $10.0\,\mathrm{mm}$ for BDC, FDC1, and FDC2, respectively. This drift length corresponds to the maximum drift time t_d measured. For each drift chamber, layer, and nuclear charge of interest a characteristic drift-time spectrum exist. An example for BDC1 and $Z = 10$ is shown in Fig. 6.4. This spectrum does not correspond to a linear relation between drift time and drift length. Due to field ambiguities and insensitivity directly at the wires it is not of box shape.

The basic assumption for the calibration is that the N beam particles illuminate the cell of size x uniformly,

$$\frac{\mathrm{d}N}{\mathrm{d}x} = \text{const.}, \tag{6.3}$$

which is well fulfilled regarding the beam profile and detector construction. Hence, the position relative to the wire is obtained by integration,

$$x(t_d) = C \int_{t_0}^{t_1} \frac{\mathrm{d}N}{\mathrm{d}t}\,\mathrm{d}t, \tag{6.4}$$

with the constant C. The integration boundaries $[t_0, t_1]$ are chosen to correspond maximal to the difference between anode and potential signal, e. g. the difference between TDC channel ~ 800

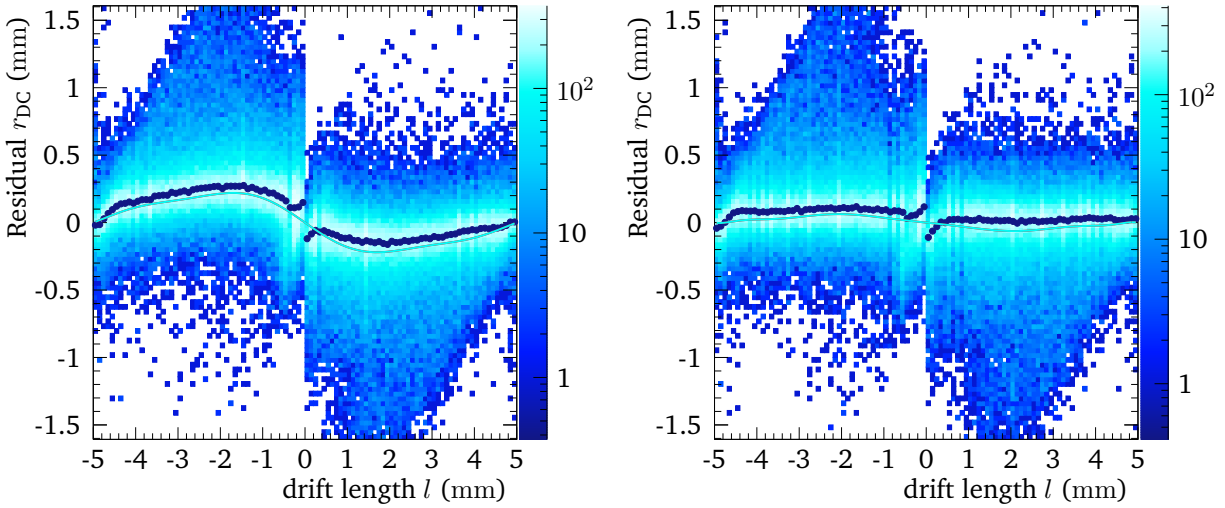

Figure 6.5: FDC1 drift-length correction for one layer. (a) Correlation between drift length l and residual r_{DC} before the correction. The residual is the difference between measured drift length and drift length deduced from the track. The mean values of each drift length (blue dots) are fit with a correction function of 8th order (cyan line). (b) Correlation after three correction steps. The width of the residual is remarkably reduced.

and ~ 900 in Fig. 6.4 corresponds to a drift length of $2.5\,\mathrm{mm}$. This spectrum is used to determine the drift-time t_d to drift length $l = x(t_d)$ relation in a step-wise integration, varying t between t_0 and t_1. This provides the input for the reconstruction of the particle's track. The drift velocity is not explicitly determined.

From the single interactions $\{u, v\}$ from each layer k the best linear fit is determined. The single interactions are the wire positions plus drift length. Applying the tracking algorithm [165], which is not described any further here, the position of the passing heavy ion $\{x, y, z\}$ is determined relative to the center of the detector. The positions along the track are

$$x_k^{\mathrm{track}} = (\alpha z_k + x_0) \cdot \cos(\theta_k) + (\beta z_k + y_0) \cdot \sin(\theta_k)\,, \tag{6.5}$$

with the wire angle $\cos(\theta_k)$ and the parameters α and β (cf. Eq. D.9).

The quality of the tracking result is monitored by the residual value r_{DC} that is defined as the difference between measured input drift-length and the drift length as it corresponds to the reconstructed track. The latter is the orthogonal distance from the reconstructed track to the wire. The residual versus the measured drift length shows a dependence that is corrected for on the input stage, see Fig. 6.5a. This dependence is modeled with a polynomial of 8th order $f(l)$ where the center at zero and the maximum drift length l_m are fixed as zero of the function,

$$f(l) = l \cdot (l - l_m) \cdot (l + l_m) \cdot (a + bl^2 + cl^4 + dl^6 + el^8). \tag{6.6}$$

Table 6.1: Performance of the multi-wire drift chambers (MWDC) evaluated for $Z = 10$ and $E_{\mathrm{kin}} \approx 258\,\mathrm{MeV/u}$, and $Z = 9$ and $E_{\mathrm{kin}} \approx 220\,\mathrm{MeV/u}$ for the BDCs and FDCs, respectively. In case of the BDCs, the efficiency is evaluated relative to the SBT start counter. For the FDCs it is obtained relative to the HODF24. The position resolution is calculated according to App. D.1

MWDC	Total Residual (μm) (before corr.)		Resolution (μm) (σ)	Efficiency ϵ (%)
BDC1	111	121	155	93
BDC2	117	127	161	91
FDC1	181	276	206	92
FDC2	207	388	240	86

An iterative two- or three-step correction is often applied, depending on the quality of the correction. The result is shown in Fig. 6.5b. The total residuals for all layers together and the different drift chambers are summarized in Table 6.1 before and after the correction. In addition, the position resolution is evaluated. The method is described in App. D.1. The average values for all layers for the position resolution are also given in Table 6.1.

6.3.1 BDC

The position of the beam particles determined in the beam drift chambers BDC1&2 is used to extrapolate the position and angle of the incoming beam onto the target. The calibration is performed for incoming $Z = 10$ particles. The target spot and the angular distribution are shown in Fig. 6.6. It is calculated for the x (and y) direction as

$$\alpha_x = \arctan\left(\frac{x_{\mathrm{BDC2}} - x_{\mathrm{BDC1}}}{d_{\mathrm{BDC2-BDC1}}}\right), \tag{6.7}$$

$$x = \tan(\alpha_x) \cdot d_{\mathrm{BDC2-Tgt}} + x_{\mathrm{BDC2}}, \tag{6.8}$$

$d_{\mathrm{BDC2-BDC1}}$ is the z-distance between the BDCs and $d_{\mathrm{BDC2-Tgt}}$ is the distance between BDC2 and the target-cell entrance. The size of the target entrance-window is indicated with a solid line in Fig. 6.6a. The quadrupole-triplet magnet at the entrance of the SAMURAI area was steered to focus the beam onto the target.

The efficiency ϵ_{BDC} including detection and tracking efficiency is determined relative to the combined measurement with both SBTs. The tracks are selected according to a good χ^2 in the reconstruction to compromise high efficiency and good resolution. The efficiency values for the two BDCs are only slightly different with $\epsilon_{\mathrm{BDC1}} = 93\,\%$ and $\epsilon_{\mathrm{BDC2}} = 91\,\%$ for BDC1 and BDC2, respectively.

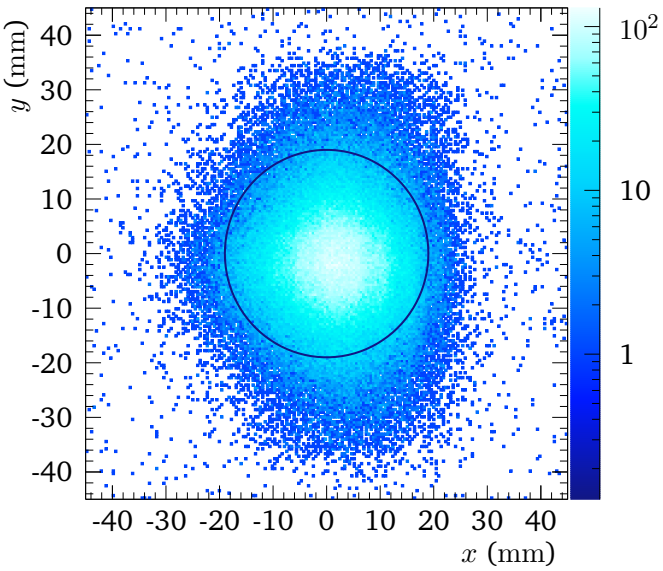

(a)

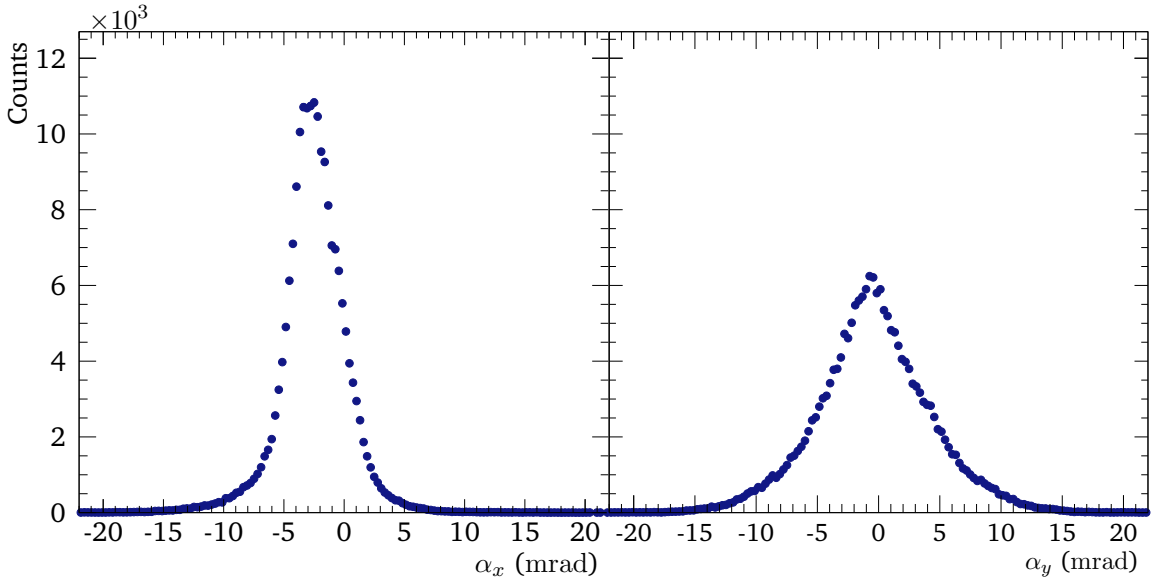

(b)

Figure 6.6: Position distribution of the incoming beam on the target, extrapolated from BDC positions. (a) x-y-position distribution on the target entrance window, the circle indicates the target-cell cross section. (b) Angular distribution of the incoming beam in x and y direction.

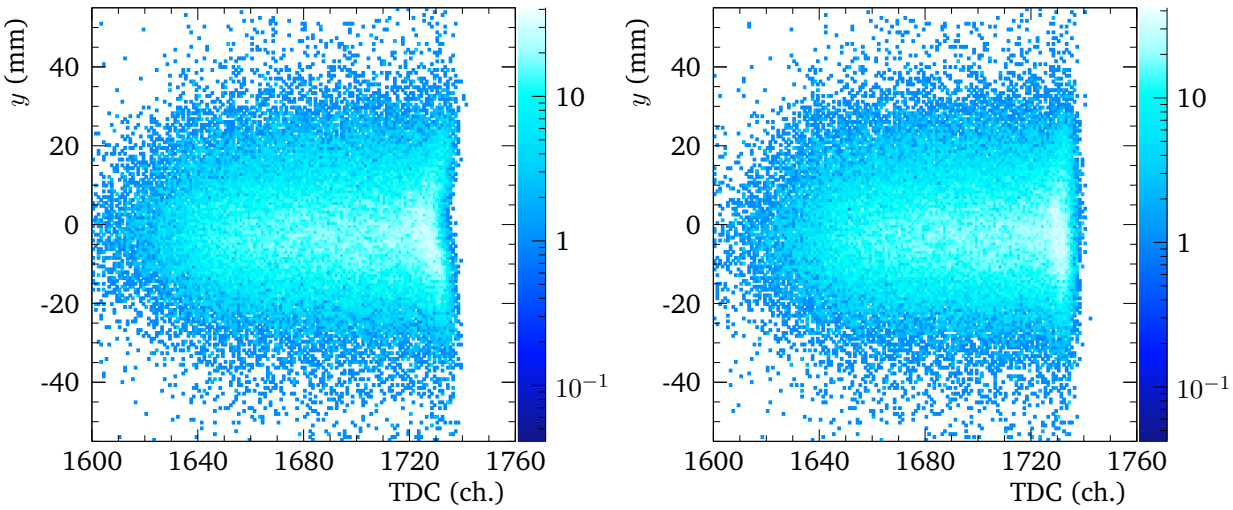

Figure 6.7: FDC1 time-over-threshold correction shown for the tracked y-position depending on the TDC time for one wire in x direction. (a) Correlation before the correction, a dip is seen for large TDC times and center positions. (b) Correlation after the correction.

6.3.2 Forward Drift Chambers

The same procedure as for the BDCs is applied to the forward drift chambers FDC1 & FDC2. Due to the different cell size and structure also the drift-time spectra look different. The drift length correction is applied in the same way but for $Z = 9$ ions, for the reaction products of interest.

It is found that the reconstructed position depends on the drift time of an orthogonal (or crossed u, v) wire as shown in Fig. 6.7a. Shown is the dependence of the reconstructed y-position on the TDC time of a wire in x direction. The reason for the dependence is the signal height, i. e. the Time-over-Threshold (ToT) of the measured signal, which manifests in a kink at small positions. The ToT dependence is corrected with a linear function on raw-level data before any other calibration,

$$t'_{\mathrm{TDC}} = (-0.11 \cdot \mathrm{ToT} + 27.5) + t_{\mathrm{TDC}}. \tag{6.9}$$

The same correction function is applied globally for all wires, the resulting distribution after the correction is shown in Fig. 6.7b. This behavior emerges also for the BDCs but not for the FDC2. In case of the BDCs it is not corrected since the effect is negligible on the resulting position distributions.

The performance of the MWDCs is summarized in Table 6.1 including their position resolution and efficiency. The efficiency is evaluated relative to the HODF24 that is placed behind the magnet and thus accounts for acceptance losses compared to the SBTs. The χ^2 cut reduces the efficiency most.

6.4 Hodoscope for Fragments-24

The hodoscope for fragment-24 (HODF24) is used for identification of the nuclear charge Z, and therefore the reaction channel, and for the ToF measurement of the heavy fragments. In conjunction with the magnetic rigidity, see also Sec. 7.2 for calculation, the mass-over-charge ratio A/Z is obtained.

6.4.1 Charge *Z* Calibration

A direct calibration from the measured charge with the QDC to Z is performed. The energy-loss signal is measured at both ends of each paddle and is converted to $Z = f(\sqrt{Q_0 \cdot Q_1})$, where Q_0 and Q_1 are the pedestal-subtracted charges.

A so-called sweep run is the starting point, where the magnetic field is tuned to move the beam over the complete x acceptance of the HODF24. Since the gain is different for every paddle and channel, the energy loss is aligned according to the x position first.

Furthermore, the y-position dependence for each paddle is corrected, whereas the x-position dependence within one paddle is omitted. In the final step, experimental data showing reaction products from $Z = 10$ to $Z = 6$ are exploited to map the measured charge to Z for each paddle separately. The raw spectra are fitted with a sum of multiple Gaussian functions. The charge Z is obtained from a linear function

$$Z = a \cdot \sqrt{Q_0 \cdot Q_1} + b, \tag{6.10}$$

with the parameters a and b. The velocity dependence of the energy loss, especially in case of the thick LH_2 target, is approximated by a quadratic function of the ToF and corrected with the offset $\Delta Z = Z_{\text{fix}} - g(\text{ToF})$.

The charge resolution after this calibration procedure amounts to $\sigma(Z)/Z = 1.4\,\%$. This is obviously sufficient to separate the charge of interest from $Z = 10$ and 9.

6.4.2 Time-of-Flight Calibration

In order to deduce the A/Z ratio or to determine the momentum of the charged reaction fragment, a ToF measurement is needed.

The ToF is measured between SBT and HODF24, $t_{\text{ToF}} = t_{\text{HODF}} - t_{\text{SBT}}$. The HODF24 time is calculated as the mean

$$t_{\text{HODF}} = \frac{1}{2}(t_0 + t_1), \tag{6.11}$$

with the times t_0 and t_1 measured at the two PMTs of a paddle. The t_{ToF} is corrected for the time-walk effect by looking in particular to events with multiplicity 2 in the HODF24. The dependence

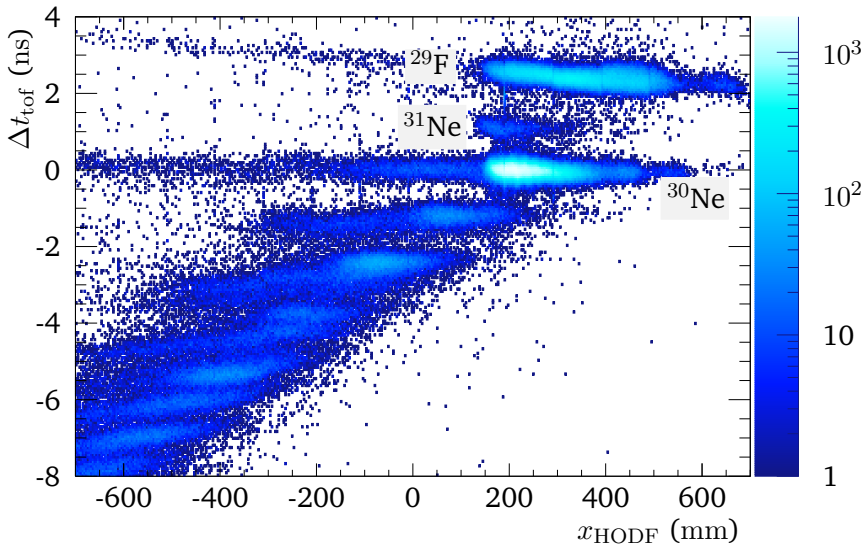

Figure 6.8: Time synchronization for HODF24 where all paddles are aligned in ToF. The ToF difference between measurement and simulation, $\Delta t_{\mathrm{tof}} = t_{\mathrm{exp}} - t_{\mathrm{sim}}$, versus the HODF24 x-position is shown after synchronization. The loci, which correspond to increasing A/Z, are continuous in x. They are labeled for unreacted beam.

of the time measurement on the height of the charge signal for a fixed charge threshold is called walk effect.

The paddles need to be synchronized in time. Therefore, the sweep run can be used again but the final alignment is optimized using the experimental runs. This final alignment is done after the time calibration from channel to ns has been performed for every TDC channel, as described in Sec. 6.2.1.

When a particle hits in a very narrow x region between two paddles, the ToF is the same for all the particles in this region within the time resolution. This overlap region is selected by looking to events in the HODF24 with multiplicity 2. These are events where one particle passes two neighboring paddles but not in their full depth, corresponding to the paddle spacing in the x-position distribution which is $500\,\mu\mathrm{m}$ (σ). The x position is extrapolated from the FDC2.

With the assumption just explained, the single paddles are aligned in time to each other, one by one. The result is shown in Fig. 6.8 for experimental data. The ToF difference between measurement and simulation, $\Delta t_{\mathrm{tof}} = t_{\mathrm{exp}} - t_{\mathrm{sim}}$ is plotted against the HODF24 x-position. The simulated ToF is calculated for unreacted ^{30}Ne only, the simulation is described in detail in Sec. 7.4. This corresponds to the locus for the unreacted beam at $\Delta t_{\mathrm{tof}} = 0$ which looks flat. The other separated distributions in this plot correspond to different A/Z and are also continuous and synchronized over the different paddles (each is of $100\,\mathrm{mm}$ width).

Finally, the ^{30}Ne distribution is adjusted to $\Delta t = 0$. The final adjustment is performed by checking the momentum matching, cf Sec.7.3. The ToF resolution is obtained from an empty-target run to be $107\,\mathrm{ps}$ (σ), or $\sigma(t_{\mathrm{tof}})/t_{\mathrm{tof}} = 0.21\,\%$.

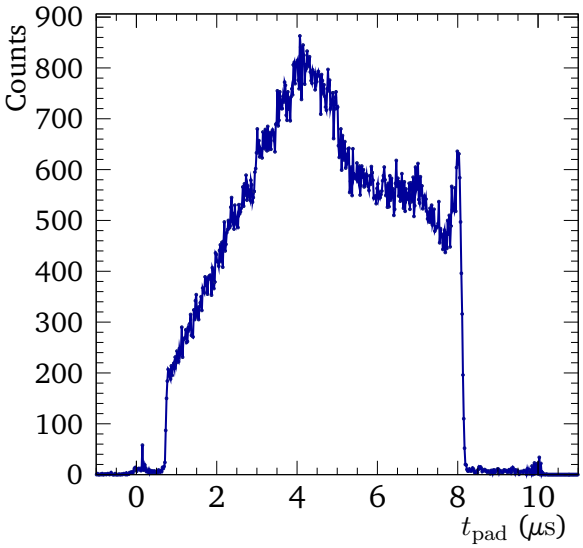

Figure 6.9: Typical t_{pad} spectrum from MINOS TPC. The width ($\sim 1\,\mu$s to $8\,\mu$s) corresponds to the TPC length.

6.5 MINOS

The MINOS TPC is used to track protons from the quasi-free scattering reactions. The x and y position are obtained from the absolute positions of the pads as described in Sec. 5.3.2. The z position is obtained from the time-resolved drift of the electrons. The calibration needed for the particle tracking and the tracking itself is described in the following.

6.5.1 Drift Time

The readout samples the signal trace for each pad. From the trace the arrival time relative to the trigger time, the t_{pad}, is determined which is the start of the leading edge of the signal. The signal shape as a function of drift time t is described by the following function, cf. Ref. [153],

$$f(t) \propto q_{\mathrm{pad}} \cdot \exp\left(-3\frac{t-t_{\mathrm{pad}}}{\tau}\right) \sin\left(\frac{t-t_{\mathrm{pad}}}{\tau}\right) \left(\frac{t-t_{\mathrm{pad}}}{\tau}\right)^3 + q_b, \tag{6.12}$$

with the shaping time τ and q_{pad} defined as the maximum signal height. A typical t_{pad} spectrum is shown in Fig. 6.9. With t_{pad} and the drift velocity the initial z-position of the created electron-ion pair is calculated.

However, fitting each signal and determining t_{pad} is computationally costly and time consuming. The leading edge of the signal, which is of importance to extract t_{pad}, is generically described by a Gaussian shape. The characteristic standard deviation σ is simply obtained from the FWHM,

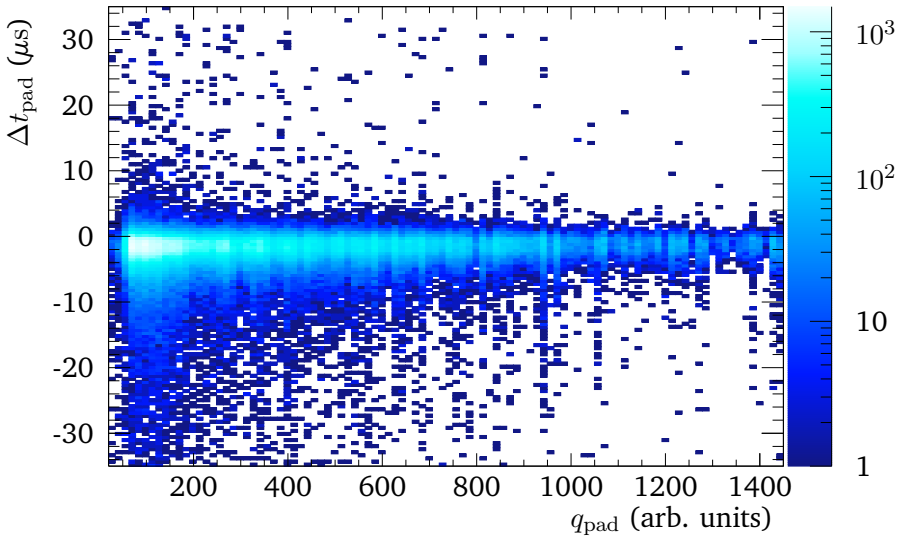

Figure 6.10: Difference between the t_{pad} that is determined with the full fit using Eq. 6.12 and t_{pad} from the phenomenological approach (Eq. 6.13) versus the maximum charge q_{pad} is shown. The difference is well aligned close to zero, thus the heuristic approach is used in the analysis.

$\mathrm{FWHM} = 2\sqrt{2\ln 2}\cdot\sigma$. Instead, t_{pad} is then defined as difference from the maximum,

$$t_{\mathrm{pad}} = t(q_{\mathrm{pad}}) - 2.5\,\sigma. \tag{6.13}$$

The validity and quality of this approach is examined in Fig. 6.10. The difference between the t_{pad} value that is determined with the full fit using Eq. 6.12 and the t_{pad} obtained with the phenomenological approach versus the maximum charge q_{pad} is shown. The distribution is flat and centers around $-1.5\,\mu\mathrm{s}$ with a systematic offset, the width accounts for $1.25\,\mu\mathrm{s}$. Instead of using the "full" approach, this convincing result allows to use the "simple" approach to determine t_{pad} throughout the analysis.

6.5.2 Drift Velocity

Looking to the t_{pad} spectrum, its range corresponds to the length of the TPC, $l_{\mathrm{TPC}} = 300\,\mathrm{mm}$. Thus, the drift velocity v_{drift} is calculated by

$$v_{\mathrm{drift}} = \frac{l_{\mathrm{TPC}}}{\left(t_{\mathrm{pad}}^{\mathrm{max}} - t_{\mathrm{pad}}^{\mathrm{min}}\right)\cdot 20\,\mathrm{ns}}, \tag{6.14}$$

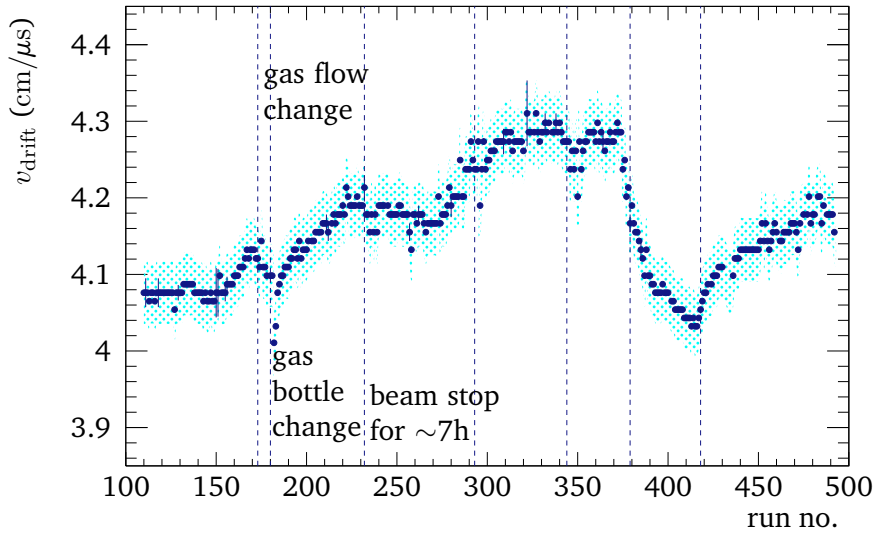

Figure 6.11: Behavior of the drift velocity v_{drift} in the MINOS TPC as function of time (run number). Gas-flow changes are indicated by dashed lines (if not stated differently). The error bars are statistical uncertainties originating from the fit, the cyan-colored band depicts the estimated systematic uncertainties of $1\,\%$.

with $t_{\mathrm{pad}}^{\mathrm{max}}$ and $t_{\mathrm{pad}}^{\mathrm{min}}$ being the maximum and minimum t_{pad} in channels, respectively, cf. Fig. 6.9. While $t_{\mathrm{pad}}^{\mathrm{min}}$ is the hardware-wise fixed offset, $t_{\mathrm{pad}}^{\mathrm{max}}$ is determined by a fit of a Fermi function,

$$f(t_{\mathrm{pad}}) = \frac{A}{\exp\left[(t_{\mathrm{pad}} - t_{\mathrm{pad}}^{\mathrm{max}})/a\right] + 1} + B, \tag{6.15}$$

to the trailing edge of the spectrum. A is the amplitude, B the baseline, and a describes the diffuseness. Using v_{drift} the z position of the hits in the x-y-plane along the track is calculated,

$$z = v_{\mathrm{drift}} \cdot t_{\mathrm{pad}}. \tag{6.16}$$

The behavior of v_{drift} over the time of the experiment is shown in Fig. 6.11. Variations of more than $5\,\%$ are measured. The changes can mainly be addressed to increasing impurities in the drift gas e. g. by water diffusion. A regulation of the gas flow helps to stabilize the drift velocity. The drift velocity v_{drift} is determined for each experimental run separately.

6.5.3 Track Finding

Knowing the coordinates from each interaction in the TPC, the tracks can be reconstructed. Here, the procedure proposed by C. Santamaria [151] is followed. The procedure is superficially described as:

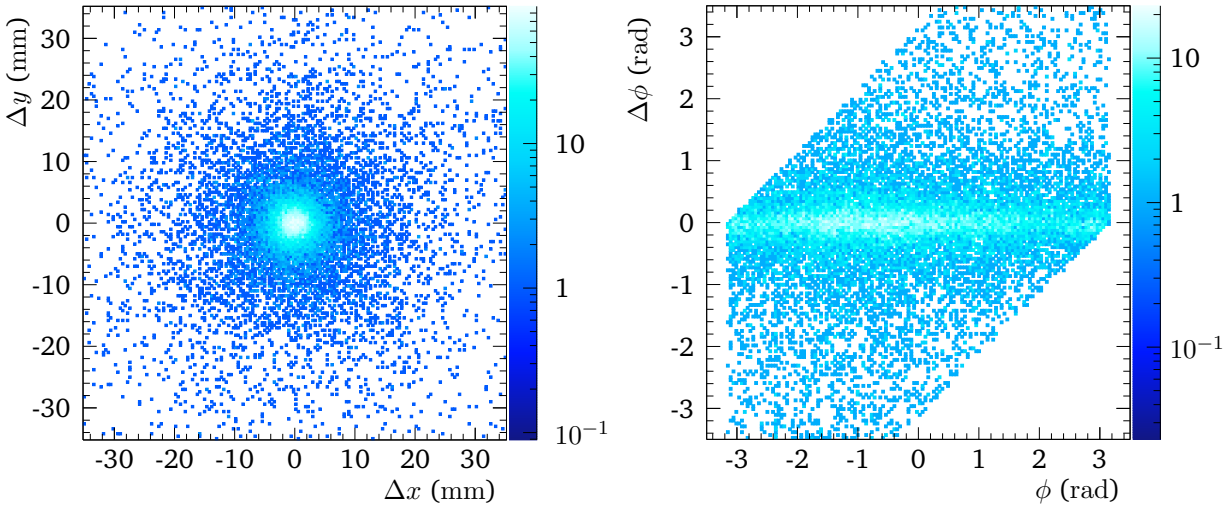

(a) (b)

Figure 6.12: MINOS track calibration. (a) Difference between the vertex position (x, y) obtained with BDCs and MINOS, $\Delta x(y) = x(y)^{\mathrm{BDC}}_{\mathrm{vtx}} - x(y)^{\mathrm{MINOS}}_{\mathrm{vtx}}$. (b) Difference in azimuthal angle ϕ as function of ϕ obtained with BDC information.

1. Apply 2D Hough transform* performed on the (x, y) pads to obtain 2D tracks.
2. Determine the z position from $q(t)$ signal and t_{pad}.
3. Apply 3D Hough transform to filter noise tracks caused by e. g. δ electrons; for (p,2p) reactions there should be max. two tracks.
4. Fit tracks in 3D, obtaining linear parametrizations.
5. Calculate the vertex point (x, y, z) from a minimum-distance approach for two tracks.

The absolute vertex position in (x, y) is calibrated using the BDC information extrapolated onto the target. The position and the azimuthal angle ϕ are adjusted after comparison with the BDC information. The result is shown in Fig. 6.12, the widths (σ) of the position differences are $\Delta x = 2.5\,\mathrm{mm}$ and $\Delta y = 2.4\,\mathrm{mm}$, in angle it is $\Delta\phi = 0.25\,\mathrm{rad}$ without particular conditions on the track quality.

In case only one track has been reconstructed, e. g. due to inefficiency or in a (p, pn) reaction, the incoming-beam information is used to determine the vertex. The target vertex is calculated from the minimum-distance approach between the beam track, that is determined by the BDCs, and the single track in the TPC.

The efficiency for at least one track being reconstructed amounts to $79.8(23)\,\%$ as extracted from experimental data. In case no track is reconstructed, the center of the target is considered to be the z position of the vertex, and together with the extrapolated BDC position the reaction point

*Technique to identify shapes in an object space.

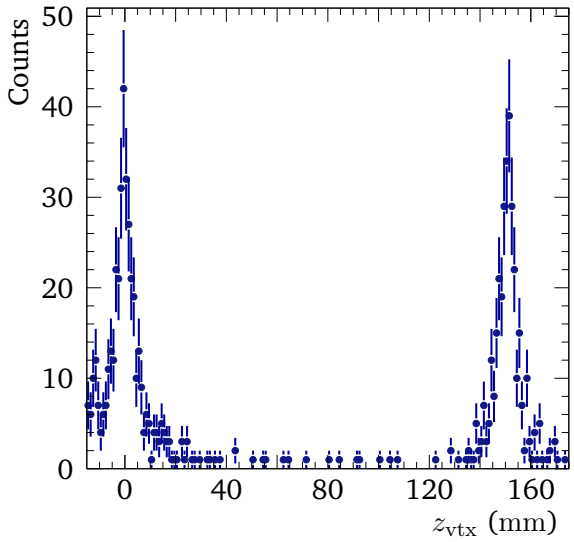

Figure 6.13: Vertex position in z direction obtained with MINOS in an empty-target run. Scattering happens in the thin entrance and exit windows. The peak width corresponds to the z-position resolution of $8.2\,\mathrm{mm}$ (FWHM). The distance is the calibrated target-cell length of $151\,\mathrm{mm}$.

is set. For low-momentum transfer scattering, the beam proton moves more or less unperturbed into beam direction and is not in the acceptance of the TPC and the second proton is also not tracked because it is of low energy and is stopped in the target.

The actual position resolution in z direction is determined from empty-target data when the target cell was not filled with LH_2. Reactions happen at the thin entrance and exit Mylar-windows of the target cell. After having selected two proton tracks with their minimum distance smaller than $10\,\mathrm{mm}$, the z position is shown in Fig. 6.13. Clearly, two peaks are seen which stem from the mentioned reactions with the target-cell material. Their distance of $l = 151\,\mathrm{mm}$ corresponds to the target-cell length and incidentally confirms a good calibration of v_{drift}.

The width of each peak gives the z-position resolution which is $8.2\,\mathrm{mm}$ (FWHM). In terms of ToF resolution this gives an uncertainty of only $15\,\mathrm{ps}$, considering the minor difference in energy-loss in LH_2 on this small distance. The energy-loss straggling (approx. $150\,\mathrm{keV/u}$) would contribute the same order of magnitude.

In total, the beam experiences a significant energy loss of $\sim 12\,\%$ of its kinetic energy while passing the LH_2 target as well as an angular straggling of $1.4\,\mathrm{mrad}$ in the target material. Together with the straggling in material in the beam line, this is larger than the resolution of the MWDCs.

6.6 DALI2

DALI2 is the NaI detector to measure γ-rays around the target. In the deployed configuration it consists of 140 single detector crystals which are readout separately as described in Sec. 5.3.2. Both, energy and time are calibrated as explained in the following.

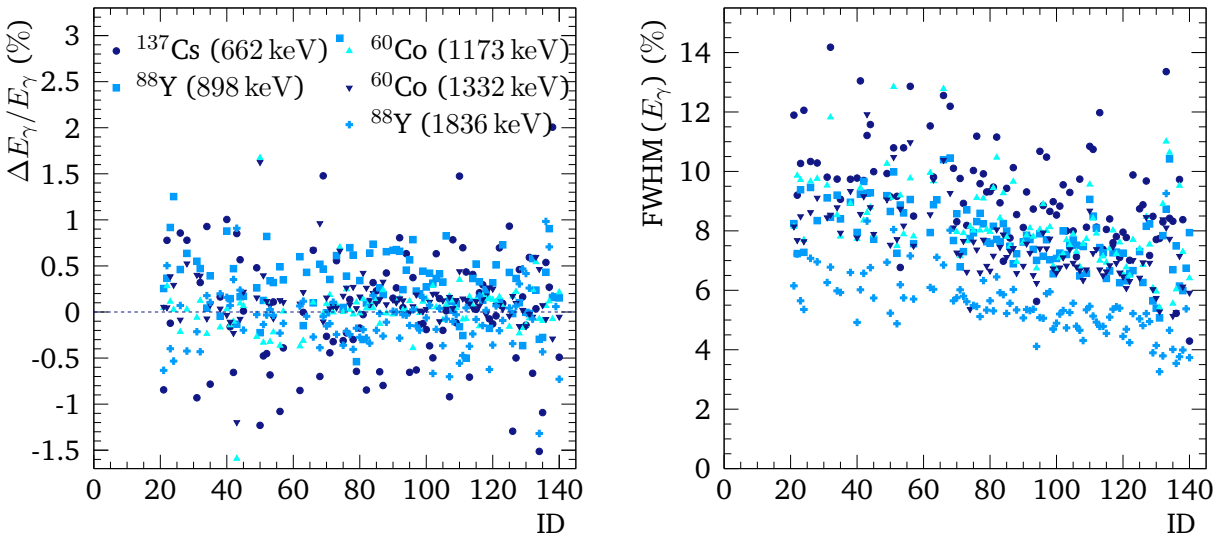

(a) (b)

Figure 6.14: DALI2 result of the energy calibration with different γ-ray sources shown for each detector crystal separately. Bad crystals are already excluded (particularly ID$<$20). (a) Relative energy difference between source energy and calibrated experimental energy. (b) Energy resolution of the full-energy peak.

6.6.1 Energy Calibration

Three different stationary γ-calibration sources are used to calibrate the single detectors. The three sources, namely ^{137}Cs, ^{60}Co, and ^{88}Y, provide five different γ-ray energies between $661\,\mathrm{keV}$ and $1836\,\mathrm{keV}$. Further details about the sources can be found in App. D.2.

Each raw-data γ-spectrum is fit simultaneously with one (or two) Gaussian function(s) and an exponential function, which describes the background, to determine the mean value of the γ-peaks. The maximum five data points from the three sources are fit with a linear function where the slope depicts the calibration parameter for channels ch to keV and the offset fixes the absolute energy,

$$E_\gamma = a \cdot E_\mathrm{ch} + b. \tag{6.17}$$

The result for all crystals after having applied the calibration is shown in Fig. 6.14a as relative difference between the source energy and the deduced energy after calibration. The distribution is centered around zero and has a width (σ) of $0.3\,\%$. Several crystals are rejected due to either bad resolution or efficiency. The latter is critical for crystals with number 1 to 20. The source had been shadowed by the MINOS TPC such that not sufficient calibration data are acquired for these crystals which means they cannot be used for the further analysis. A common energy cut on $200\,\mathrm{keV}$ laboratory energy is applied later.

The other excluded crystals were either not working properly or their energy resolution is sig-

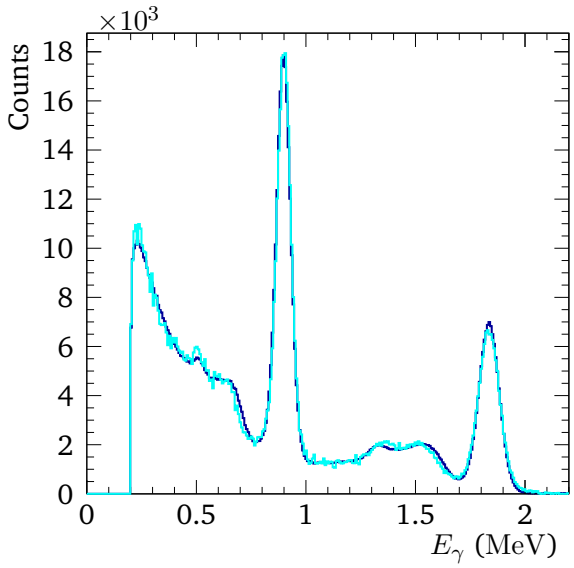

Figure 6.15: Comparison between ^{88}Y γ-source measurement (cyan) and simulation (blue) with DALI2. The integrals are normalized to each other.

nificantly worse compared to the other detectors. Crystals that are excluded from the analysis are listed in App. D.2. The energy resolution for each crystal and source energy is shown in Fig. 6.14b in percent (FWHM). Those crystals with best resolution are installed in forward direction. The resolution of each detector is described by

$$\sigma(E_\gamma) = r \cdot \sqrt{E_\gamma}, \tag{6.18}$$

with parameter r.

6.6.2 Efficiency Determination

The efficiency of the array is obtained by normalizing the integral of the full-energy peak to the number of emitted γ-rays. The integral of the full-energy peak is, again, determined by fitting a Gaussian function plus an exponential function to the spectrum. The background coming from natural sources or activation processes that take place during experimental runs is subtracted beforehand. Therefore, a measurement with γ-ray source is performed and normalized to the measurement time.

The number of emitted γ rays is calculated from the source activity A as listed in Table D.2. Considering the measurement time t, the downscale factor DS, and the lifetime LT of the DAQ, the efficiency ϵ_γ per transition energy is calculated as ratio of detected and emitted γ-rays,

$$\epsilon_\gamma = \frac{N(\gamma_{\text{det}})}{N(\gamma_{\text{source}})}, \tag{6.19}$$

Table 6.2: Efficiency of the DALI2 detector array evaluated with γ-ray sources and compared to simulation results.

Source	γ energy (keV)	ϵ_γ (%)	
		experiment	simulation
^{137}Cs	661.657	17.5	19.9
^{60}Co	1173.228	13.8	15.7
	1332.501	12.0	12.8
^{88}Y	898.042	13.7	15.8
	1836.063	8.5	9.9

with

$$N(\gamma_{\text{source}}) = \frac{A \cdot t}{\text{DS} \cdot \text{LT}}. \tag{6.20}$$

The results are listed in Table 6.2.

More importantly, these results are compared to simulation data. A comparison between experimental and simulated energy spectrum for ^{88}Y is shown in Fig. 6.15. The level schemes for the decay radiation as input to the simulation are taken from the National Nuclear Data Center (NNDC) [140], the energy resolution is incorporated according to Eq. 6.18. The normalized spectra agree well, the efficiencies are listed in Table 6.2. The efficiency values obtained with the simulation are systematically larger by about $1.7\,\%$. One reason for this can be the source position that is not known precisely enough.

6.6.3 Time Calibration

The time resolution of that detector type is not good enough to e. g. discriminate signals from γ-rays from proton or neutron signals. However, the time information can be used to discriminate decay γ-rays from uncorrelated background.

It is sufficient to synchronize the time signals for all the single detectors. This has been done after the conversion of the TDC signal to nanoseconds. The single time spectra follow a Landau distribution, cf. Ref. [151].

6.7 Neutron Detectors

Both, NeuLAND and NEBULA are large-size granular plastic-scintillator detectors read out with PMTs whereas NeuLAND is equipped with TacQuila Electronics (TacQuila) electronics and NEBULA with conventional ADCs and TDCs. The calibration steps are similar though, including the time and position calibration as well as the synchronization of all detector segments.

6.7.1 NeuLAND Demonstrator

The basic calibration parameters were determined in multiple steps by I. Gasparic [168]. The procedure is described in the following.

Time and Position Calibration

The time calibration starts with the conversion from the time measurement in channels to ns using pulser data. Based on the TacQuila electronics, the time measurement of one interval covers a range of $25\,\mathrm{ns}$ with a time resolution of the electronics of $10\,\mathrm{ps}$ where either a simple linear relation can be applied between channels and ns or, as done here, a look-up table is created that accounts for nonlinearities.

In the time calibration three parameters are determined `TDiff`, `TSync`, and `TWalk`. The calibrated PMT times are

$$\begin{aligned} t_0 &= tt_0 - \frac{1}{2}\mathtt{TDiff} - \mathtt{TSync} + \mathtt{TWalk}_0, \\ t_1 &= tt_1 + \frac{1}{2}\mathtt{TDiff} - \mathtt{TSync} + \mathtt{TWalk}_1, \end{aligned} \tag{6.21}$$

$$x_i = v_{\mathrm{scint}} \cdot (t_1 - t_0)\,, \tag{6.22}$$

with the measured ones tt_i.

First, the time-walk correction is applied. It is determined by the electronics and is phenomenologically modeled as

$$\mathtt{TWalk}_i = \alpha \cdot ee_i^{\beta} - \alpha \cdot 400^{\beta}, \tag{6.23}$$

where $\alpha = 1500$ and $\beta = 0.000\,75$, and ee_i is the energy at one PMT.

The time-difference calibration is performed to synchronize the time measurement between the two PMTs, t_0 and t_1, of one scintillator bar by using cosmic data. The result is shown in Fig. 6.16a [168]. The obtained calibration parameter is called `TDiff`. The time difference $t_{\mathrm{diff}} = t_1 - t_0 = 0$ needs to be calibrated since the hit coordinate along a bar is deduced from the time-difference measurement, cf. Eq. 5.7. The remaining two coordinates are fixed by the bar position. The time difference $t_{\mathrm{diff}} = 0$ corresponds to the bar-center position and the maximum difference corresponds to the length of the bar. Complete tracks through the detector from cosmic particles are used to linearly relate the expected hit position x_c of one bar and its time difference. The slope of $x_c = (t_2 - t_1) \cdot v_{\mathrm{scint}}$ gives the effective speed of light in the material v_{scint}.

The next step is to synchronize different bars and planes with respect to each other. This is obtained by determining the synchronization parameter `TSync` from the tracks of cosmic muons. Starting with the synchronization within one plane, time differences between the time of a hit in any bar T_i and the time of a hit in a reference bar T_r are considered where $T = \frac{1}{2}(t_1 + t_0)$. The time

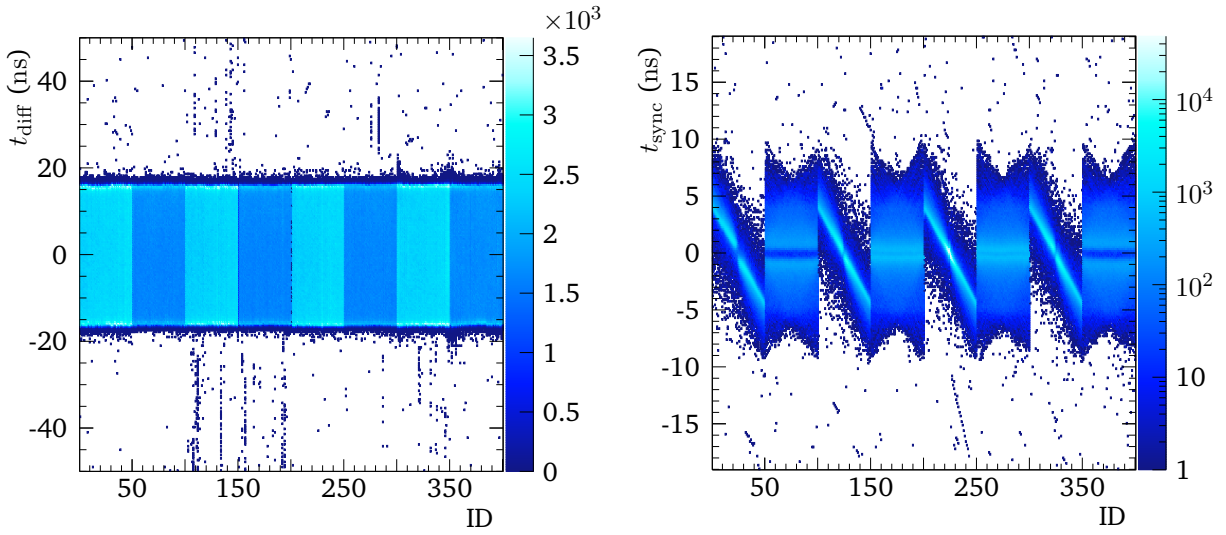

(a) (b)

Figure 6.16: Calibrated time spectra for NeuLAND with cosmic data [168]. (a) Time difference between the two PMTs of one bar shown for all bars IDs, aligned around zero. (b) Calibrated time difference of a hit in a bar and a hit in the bar 225 vs. bar number. A typical correlation pattern between different horizontal and vertical bars to a horizontal bar in the middle of the detector is apparent.

difference must equal the expected ToF of the particle between those two hits, $T_i - T_r - l/c = 0$ with the flight path l. In a multi-step process the times of the reference bars are aligned, separately for horizontal and vertical bars first, and finally the time of the horizontal and vertical center bars are aligned to each other such that the whole detector is synchronized in time and aligned in position. The result is shown in Fig. 6.16b [168].

The obtained time calibration is fine-tuned with experimental data where γ-rays from a reaction at the target are used to verify the ToF calibration. This approach is limited by statistics because only few γ-rays are produced on the LH_2 target. However, it is absolutely necessary to use the experimental data in addition because misalignment is seen when applying the calibration parameters from cosmic data to experimental data. And the validity of the calibration needs to be monitored over the course of the experiment. The disadvantage of this approach is a decreasing total ToF resolution when bars cannot be properly aligned due to low statistics. The ToF resolution from this approach is deduced from the width of the prompt γ-ray peak. The projection for NeuLAND and NEBULA together is shown in Fig. 6.17. The width amounts to $\sigma = 259(4)$ ps (the resolution of the start counter is removed). It is worse than the resolution of the individual bars and is mainly addressed to difficulties when aligning the bars to an absolute ToF and small light yield. Eventually, individual runs are corrected, as discussed in Sec. 6.9.3.

The final calibration for the relative-energy determination is done with experimental data. The difference in the momentum components between fragment and neutron for every layer must

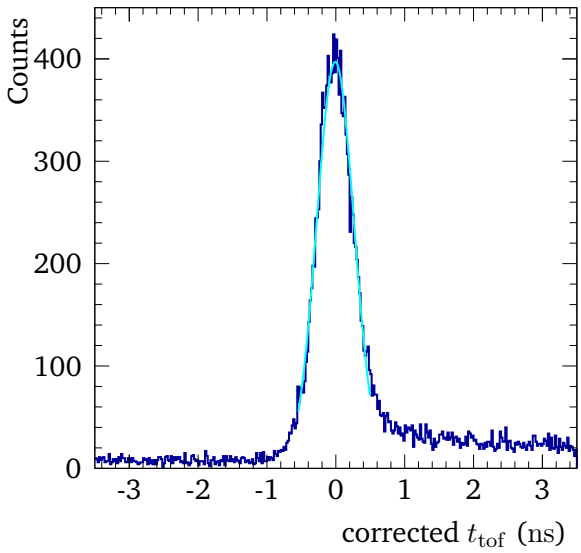

Figure 6.17: NeuLAND and NEBULA ToF resolution. Prompt γ-ray peak projected for all bars together from experimental data with LH2 target (blue) and fit with a Gaussian function (cyan). The width of the peak is $\sigma = 259(4)\,\mathrm{ps}$.

peak at zero. Differences are treated as ToF offsets for the time alignment of the neutron detectors. In addition, the velocity difference must be independent of the reaction-vertex position. Before, the position alignment between layers is tested with secondary-proton scattering. Also there it is true that the x, y-position difference between neighboring layers must be zero.

One way to evaluate the ToF resolution of individual bars is to analyze the width of the γ-ray peak in each bar from experimental data, where the ToF is corrected for the length of the flight path and an energy-loss cut of $6\,\mathrm{MeV}$ is applied. The mean value for all bars is $\langle\sigma_{\mathrm{tof}}\rangle = 182(32)\,\mathrm{ps}$. An analysis with high-energy γ-rays produced in a thick aluminum target results in a slightly better resolution of $149(17)\,\mathrm{ps}$ [169]. However, the uncertainty of the interaction point needs to be subtracted,

$$\Delta t_{\mathrm{tof}} = \frac{\Delta x}{c}\frac{1}{\sqrt{12}} = \frac{5\,\mathrm{cm}}{30\,\mathrm{cm/ns}}\frac{1}{\sqrt{12}} = 48\,\mathrm{ps}, \tag{6.24}$$

$$\langle\sigma_{\mathrm{tof}}\rangle = 176(32)\,\mathrm{ps}. \tag{6.25}$$

The factor $1/\sqrt{12}$ accounts for the standard deviation of a uniform distribution, like the lateral size of one bar. The value of $\langle\sigma_{\mathrm{tof}}\rangle = 180\,\mathrm{ps}$ ($\times\sqrt{2}$ per PMT) is later used in the simulation assuming that the same time resolution holds for massive particles. The ambiguities are then treated as systematic uncertainties.

The time resolution of single bars can be determined in a different way. Proton-scattering events that are the first interaction of a neutron in the detector between two bars are used. Here,

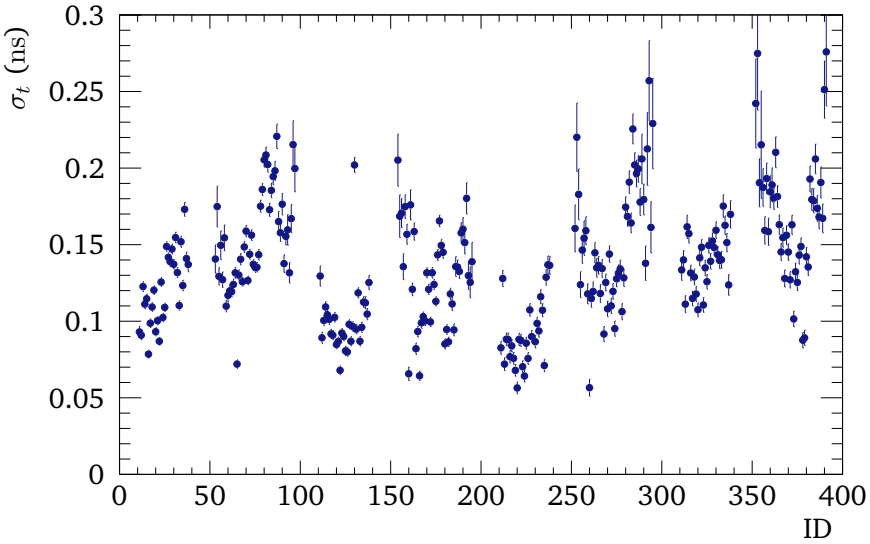

Figure 6.18: NeuLAND time resolution (σ) determined from secondary-proton scattering for individual bars (with sufficient statistics).

pairs among three bars σ_i ($i = \{1, 2, 3\}$) are taken to remove the resolution of the reference bar,

$$\begin{aligned} \sigma_{\mathrm{I}}^2 &= \sigma_1^2 + \sigma_2^2, \\ \sigma_{\mathrm{II}}^2 &= \sigma_1^2 + \sigma_3^2, \\ \sigma_{\mathrm{III}}^2 &= \sigma_2^2 + \sigma_3^2, \end{aligned} \tag{6.26}$$

where

$$\sigma_i = \sigma\left(\frac{1}{2}\left[t_{0,i} + t_{1,i}\right]\right), \tag{6.27}$$

this gives e. g.

$$\sigma_2^2 = \frac{1}{2}\left(\sigma_{\mathrm{I}}^2 - \sigma_{\mathrm{II}}^2 + \sigma_{\mathrm{III}}^2\right). \tag{6.28}$$

The results for the time resolution from this method are presented in Fig. 6.18 for center bars where sufficient statistics is available. It shows that bars with relatively poor resolution are installed in the planes in the back. In general, the obtained resolution values meet the design values for NeuLAND of $150\,\mathrm{ps}$ [146]. Very small resolution values might arise from systematic influence of the reference bar.

Energy Calibration

For the energy calibration, first pedestal values are obtained with pulser data and subtracted.

The energy-difference calibration is very similar to the time-difference calibration but calculat-

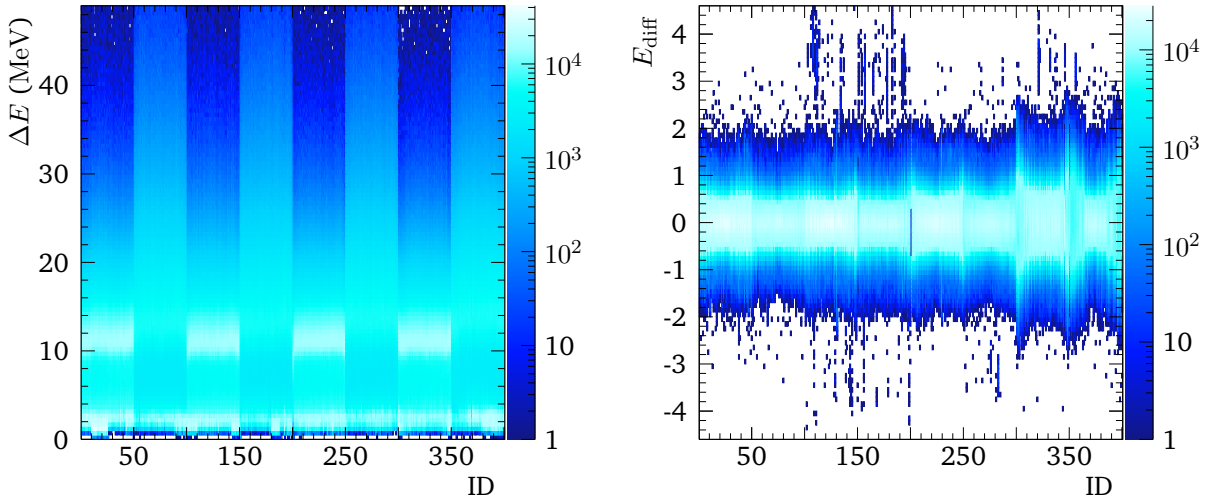

(a) (b)

Figure 6.19: Calibrated energy spectra for NeuLAND with cosmic data [168]. (a) Energy loss $\Delta E = \sqrt{e_0 e_1}$. (b) Energy-difference calibration for each bar $E_{\text{diff}} = \log(e_1/e_0)$.

ing $\log(e_1/e_0)$ which is essentially proportional to a position measurement. The calibrated energy is given for the two PMTs as

$$\begin{aligned} e_0 &= ee_0 \cdot \texttt{EDiff} \cdot \texttt{ESync}, \\ e_1 &= ee_1 / \texttt{EDiff} \cdot \texttt{ESync}, \end{aligned} \tag{6.29}$$

with the energy measurements $ee0$ and $ee1$ at each end of a single bar. The result after calibration is shown in Fig. 6.19b [168]. `EDiff` is the energy-difference calibration parameter, and `ESync` the one for the synchronization. Besides, the attenuation coefficient can be calculated.

The synchronization of the energy-loss measurement for the bars to each other is done using the mean energy-loss of cosmic particles in scintillator material. Minimum-ionizing particles leave approx. $2\,\text{MeV}\,\text{cm}^2/\text{g}$, thus $11\,\text{MeV}$ in a $5\,\text{cm}$ thick bar. The calibration parameter is `ESync`, the result is shown in Fig. 6.19a [168].

6.7.2 NEBULA

In order to calibrate NEBULA, the same description as for NeuLAND formulated in Eqs. 6.21 and 6.29 is applied.

The general time calibration from channels to ns is again performed as for any conventional TDC measurement described in Sec. 6.2.1. Time difference and speed of light in the material are also determined for the maximum time difference that needs to match the bar size. The time synchronization is basically done by using γ-rays from a dedicated experimental run with a ^{20}F beam onto a thick aluminum target to produce high-energy γ-rays, the calibration is adjusted

afterwards with experimental data as described for NeuLAND.

The correction for time walk is obtained using cosmic tracks. The time difference between one PMT time $t_{0,i}$ and another one of another bar $t_{0,j}$, corrected for the path length, is evaluated as function of the energy loss. The functional behavior to describe the dependence is

$$t_{0,i} - t_{0,j} = \frac{a}{\sqrt{e_{0,i}}} + b, \tag{6.30}$$

with parameters a and b. Since the reference time $t_{0,j}$ is also affected by walk, very strict conditions are put to its energy-loss to eliminate this effect in the calibration.

Finally, experimental data can be applied to check the overall synchronization between the detectors NeuLAND and NEBULA in time and position. The absolute ToF between target and neutron detector, necessary for a precise momentum analysis, is calibrated analyzing particles that are traveling with the speed of light, see Fig. 6.17. The ToF resolution determined from the γ-ray peak as done for NeuLAND, cf. Eqs. 6.24 and 6.25, is $\langle\sigma_{\mathrm{tof}}\rangle = 171(63)\,\mathrm{ps}$ with $\Delta t_{\mathrm{tof}} = 115\,\mathrm{ps}$. The uncertainty is again large because of ambiguities in using the LH_2 target.

Besides the use of cosmic data, a source measurement with ^{241}AmBe was performed to calibrate the energy loss. The mean energy loss of cosmics is $30\,\mathrm{MeV}$ and that of the high-energy γ-ray from the source is $4.2\,\mathrm{MeV}$ as evaluated in Ref. [170].

6.8 Beam-Line Energy-Loss

Three detectors are used in the analysis to determine the ToF of the charged particles, the in-beam plastic-scintillator detector equipped at F7, the combined SBTs, and the HODF24. However, this measurement is only an average value, as the ions are slowed down step by step in each material in the beam-line.

In order to e. g. obtain the projectile energy at the reaction vertex or the energy of the fragment, it is important to take the energy loss into account. This allows to characterize the reaction, determine the momenta, and to apply the proper Doppler correction in the γ-ray analysis. Furthermore, the ToF from SBT to the reaction vertex is needed to define the start time of the fragment from the vertex.

The energy loss ΔE of a heavy particle passing matter is described by the Bethe-Bloch formula. A more elaborated theory has been developed by Lindhard and Sørensen [171] which calculates the electronic stopping power for any ion at relativistic energy. Together with further corrections, detailed in Ref. [172], the energy loss is calculated in the ATIMA code [172].

Here, the energy-loss determination is based on the relation between stopping power $\mathrm{d}E/\mathrm{d}x$

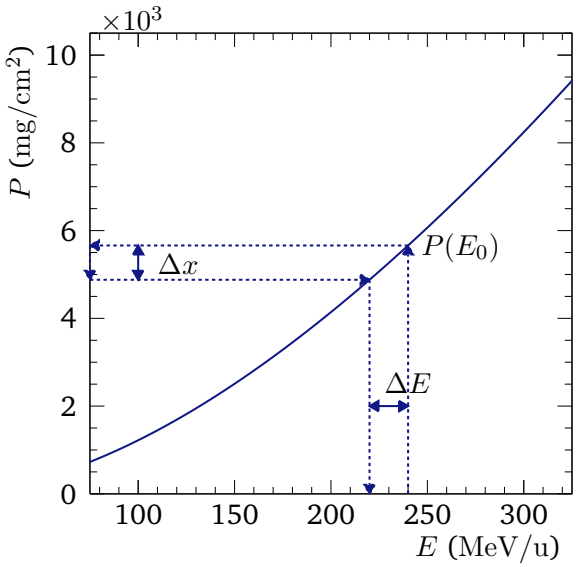

Figure 6.20: Method to determine the energy loss ΔE from an energy-range curve in one exemplary material. Starting with initial energy E_0 and range $P(E_0)$, the passed material thickness Δx is subtracted, and the energy is re-evaluated.

and mean range P,

$$\begin{aligned}\Delta x &= \int_{E_0-\Delta E}^{E_0} \left(\frac{\mathrm{d}E}{\mathrm{d}x}\right)^{-1} \mathrm{d}E \\ &= P\left(E_0\right) - P\left(E_0 - \Delta E\right).\end{aligned} \tag{6.31}$$

Consider a heavy ion with initial kinetic energy E_0 and range $P(E_0)$. When it enters the material, it is continuously slowed down. Leaving the material after length Δx, it lost the energy ΔE and its maximum range is reduced. Thus, the energy loss is determined by evaluating the relation between range and energy at $P(E_0)$ and $P(E_0 - \Delta E)$.

The relation between P and energy E is specifically determined with `JavaATIMA` for a large range of energies and all the different materials used. The curve is the interpolation between the calculated points at different energies. The energy-loss ΔE is obtained by evaluating the created graph at the initial energy, and the range associated with the passed material thickness is subtracted from the obtained initial range, cf. Fig. 6.20. The graph is re-evaluated at the reduced range to obtain the outgoing energy. The workflow follows $E_0 \rightarrow P(E_0) \rightarrow P(E_0) - \Delta x \rightarrow E(P - \Delta x)$. Finally, a relation between initial energy and energy after having passed a series of materials, e. g. from SBT to the target, is used to evaluate the energy-loss for each isotope and event separately. At the same time, the ToF is calculated considering the reduced kinetic energy after having passed each material. This is repeated for the other flight paths from target to the magnet. The energy-loss in the LH_2 target is treated separately according to the reaction vertex position and the nuclear charge before and after the reaction.

The material budget is listed in Table C.3 in the appendix. The validation of this approach and the matching of energies is discussed in Sec. 7.3.

6.9 Time-dependent Calibration

The experiment was running for 10 days in total, seven days were dedicated to the ^{29}F beam setting. The stability of the detector response and calibration parameters is investigated in the following for all detectors, their energy and time signals. PMT gains change and other signals drift due to the load on the detectors or other influences. The MWDCs and DALI2 are not affected but the electronics of the plastic-scintillator detectors (except NEBULA) are. In these cases, drifts are corrected run-wise such that the resolution is maintained over the whole experiment.

6.9.1 In-Beam Plastic-Scintillator Detectors

The plastic-scintillator detectors at the entrance of the SAMURAI area determine the beam trigger and thus the start signal for the time measurement. A drift of the time signal would drastically effect the ToF determination.

A rather strong change of max. $150\,\mathrm{ps}$ is observed for the SBT time signal $t_{\mathrm{start}} (= t_{\mathrm{SBT}})$. The signal is shown as function of run number in Fig. 6.21 for the ^{29}F beam setting. The reason for this behavior is not obvious. The changes do not coincide with changes in the gain of the energy signal. In order to correct this behavior, the start time t_{start} is corrected with a run-wise offset t_{corr},

$$t'_{\mathrm{start}} = t_{\mathrm{start}} + t_{\mathrm{corr}}. \tag{6.32}$$

The start time after correction is shown in Fig. 6.21b. The width (σ) of t_{start} reduces by $12\,\mathrm{ps}$. Drifts of the time signals are also seen for the other in-beam plastic-scintillator detectors in BigRIPS that are used to perform ToF measurements. This behavior is corrected for in a similar way.

The energy-loss signals do not drift that strongly. Nevertheless, the run dependence is corrected. The average energy-loss signals of the two SBTs, $Q_{\mathrm{SBT1,2}}$, are considered separately. The change in gain is corrected as

$$Q'_{\mathrm{SBT,i}} = Q_{\mathrm{SBT},i} / Q_{\mathrm{corr},i}. \tag{6.33}$$

6.9.2 HODF24

In case of the HODF24, drifts in time and charge are observed which are even different for the different paddles. The same approaches as described above in Sec. 6.9.1 are applied for correction. For the paddles on the high-rigidity site, namely 1 to 6, no correction is applied because not

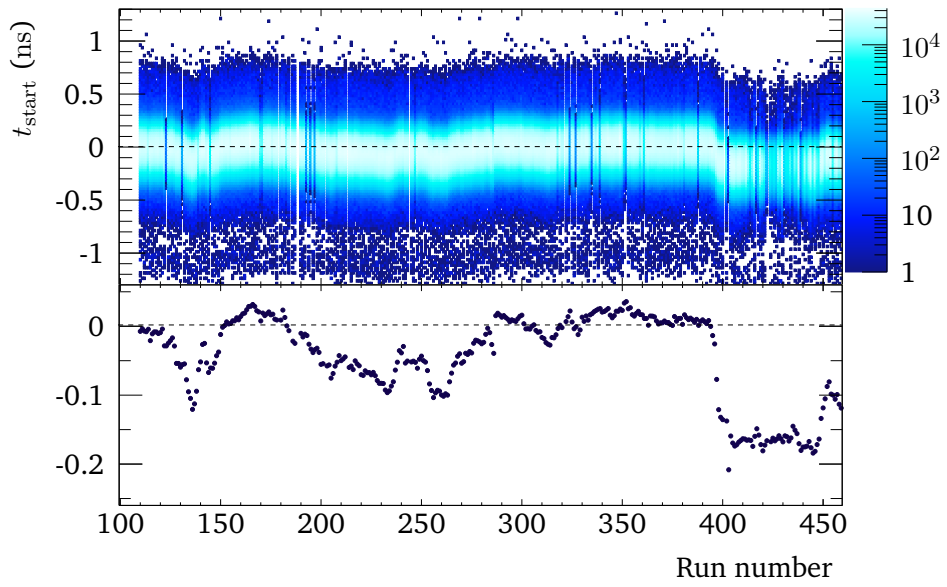

(a)

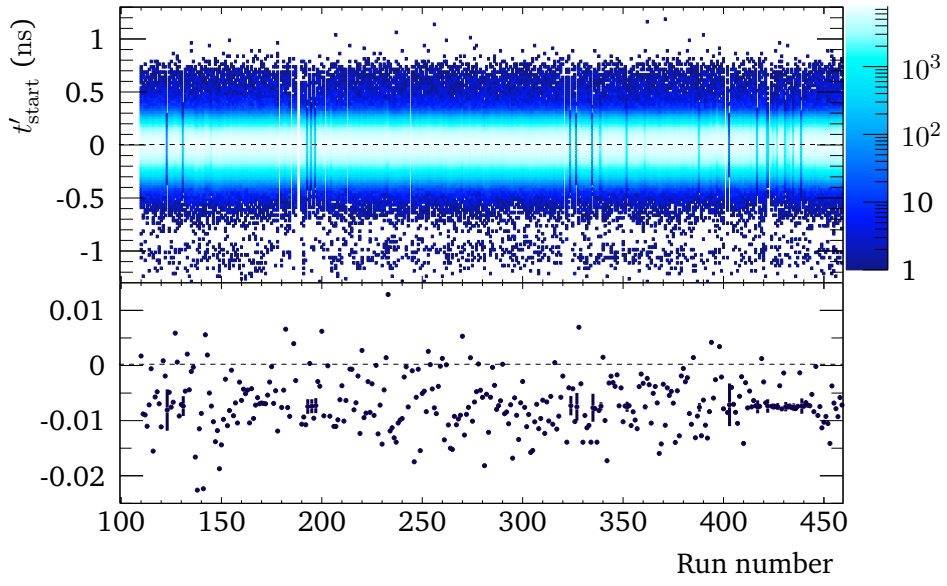

(b)

Figure 6.21: Example of the run dependence for the time measurement t_{start}. (a) Time before the run-wise correction. The lower pad shows the fluctuation of the mean value. (b) Time after the correction, the mean value scatters within the resolution (lower pad).

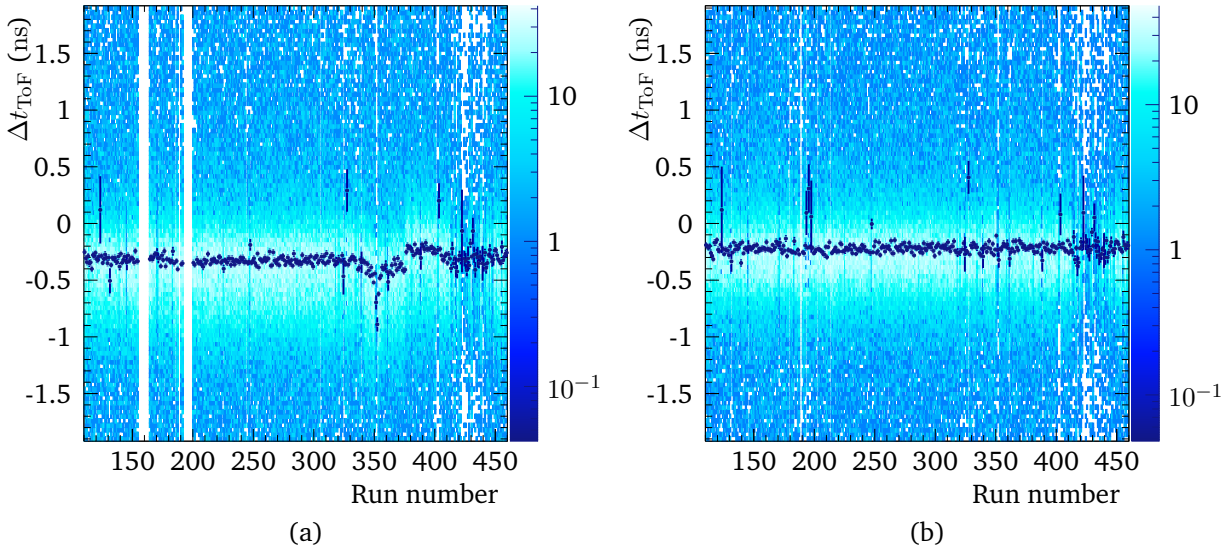

Figure 6.22: Run-dependent correction for NeuLAND, exemplarily shown for the ToF measurement for one bar relative to the ToF in the following plane. (a) Before the correction, jumps are seen around the run numbers 350 and 380. (b) After the correction.

enough statistics is acquired. This is not critical since no reaction channel of interest is measured with these paddles.

6.9.3 Neutron Detectors

For NEBULA no drifts are seen that need to be corrected. In case of NeuLAND it is different, indeed gradual changes or even jumps are seen for some channels in the time and energy measurement that are addressed to threshold drifts in the TacQuila electronics. This threshold drift of one channel affects its energy measurement, the time measurement, and thus the position measurement. The signature of a shift is shown in Fig. 6.22a for one bar and needs to be investigated for each of the 800 channels and approx. 350 runs separately. The ToF difference is plotted between the bar of interest and one bar of the following plane. The difference in ToF should be constant as function of run number/time of the experiment, but it is not. At around run 350 a shift begins and at around run 380 a jump is seen. Another indication can be the position measurement that can be reduced to a time-difference, or the energy measurement. In addition, it needs to be identified which PMT causes the problem. Eventually, run-correction parameters are determined. The data after correction are shown in Fig. 6.22b, the distribution is flat.

Chapter 7

Data Analysis

After having calibrated the detectors, the data are combined to extract physics results. In this chapter, the reaction channel is selected by identifying the incoming and outgoing particles and their momenta are determined. In addition, the γ-ray spectra are obtained and the neutron tracking is performed.

7.1 Incoming-Beam Identification

As described in Sec. 5.2, the RI beam is produced and separated in BigRIPS. The event-wise identification of the beam particles takes place in the second stage of BigRIPS using the in-beam plastic scintillator detectors at the foci F5, F7, and F13. The particles are identified in the so-called $B\rho - \mathrm{ToF} - \Delta E$ method.

Equation 5.3 shows the relation between A/Z and $B\rho$ and the velocity β of the particles. Thus, to obtain the mass A, the velocity and Z need to be determined. The magnetic rigidity is measured at the dispersive focus F5.

The nominal magnetic rigidity $B\rho_0$ for the reference trajectory is known by the setting of the magnet. The deviation from this, determined with the position measurement x_{F5} at F5, determines the relative magnetic rigidity. A first-order ion-optical approach leads to the simplified magnetic rigidity

$$B\rho = B\rho_0 \cdot \left(1 + \frac{x_{\mathrm{F5}}}{(x|\delta)}\right), \tag{7.1}$$

with the dispersion matrix element $(x|\delta)$. The first-order approach is sufficient due to good resolution for these light ions. In the analysis, $(x|\delta)$ is adjusted to a value of $29\,\mathrm{mm}/\%$ which eventually reduces the A/Z dependence on the kinetic energy. The magnetic-rigidity spectrum as measured at F5 is shown in Fig. 7.1a.

To determine the velocity βc, t_{ToF} and flightpath S need to be known. The measurements

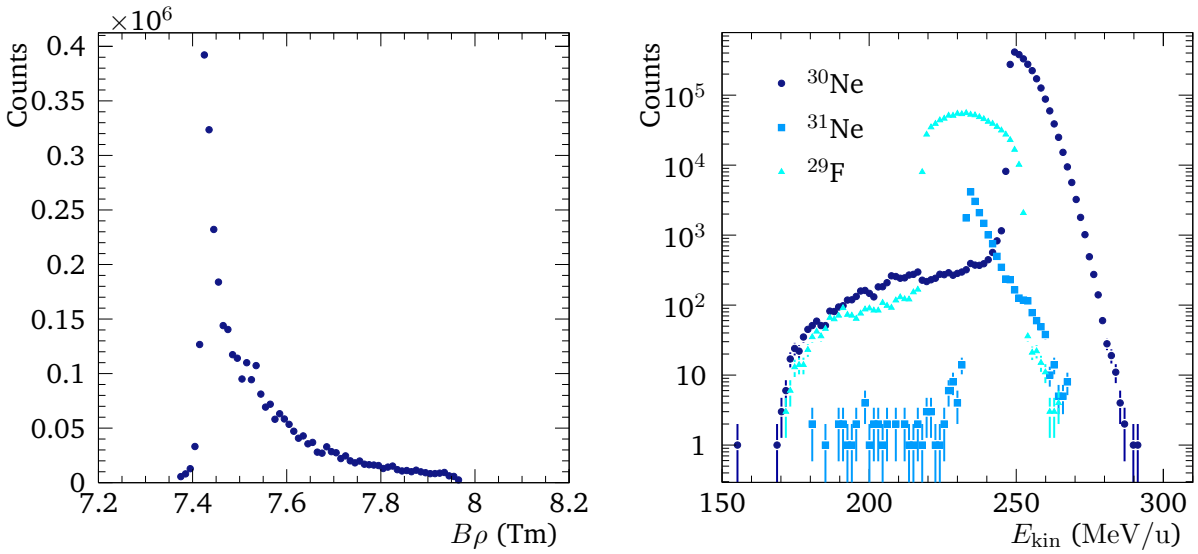

(a) (b)

Figure 7.1: Incoming beam properties. (a) Magnetic rigidity $B\rho$ of the ^{29}F beam setting measured at BigRIPS focus F5. (b) Incoming kinetic-energy E_{kin} determined at the entrance-window of the target cell, the beam-line energy-loss is considered.

between F5 and F7 for identification, and between F7 and F13 for the determination of the kinetic energy are considered. The following approach describes how both, ToF and S, can be calibrated on absolute scale at the same time. Starting from

$$\beta = \frac{S}{t_{\mathrm{ToF}} \cdot c}, \tag{7.2}$$

where the t_{ToF} needs to be the time-of-flight that is adjusted with a correct offset t_{off} compared to the pure time-of-flight Δt that is just the difference between e. g. the time measurement at F7 and F13. The offset originates from e. g. the different cable lengths for the readout. This is an effect of the experimental apparatus and is fixed for the duration of the experiment. Equation 7.2 can be rewritten as

$$\begin{aligned} \beta &= \frac{S}{(\Delta t - t_{\mathrm{off}}) \cdot c} \\ \Rightarrow \beta \cdot \Delta t &= \frac{S}{c} + \beta \cdot t_{\mathrm{off}}. \end{aligned} \tag{7.3}$$

This is a linear function where the intercept with the y axis defines the flightpath S and the slope defines the absolute time offset t_{off}.

The different BigRIPS settings allow to extract $\beta_{\mathrm{set}} \cdot \Delta t$ for several different known velocities β_{set}. Since there were no runs with primary beam in BigRIPS available, $\beta_{\mathrm{set}} \cdot \Delta t$ is determined for secondary beams with a well-defined beam energy, i. e. with a narrow setting of the slit at

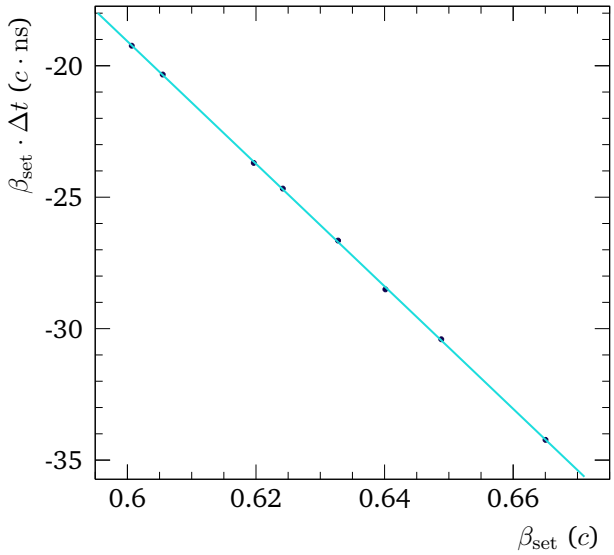

Figure 7.2: Determination of ToF and flight length offset for BigRIPS measurement. Shown is a linear fit (cyan line) to experimental data points to calibrate the measurement between F7 and F13 in BigRIPS. For well-defined beam velocities, $\beta_{\mathrm{set}} \cdot \Delta t$ is determined, the intercept with the y axis relates to the flightpath S and the slope gives the time offset t_{off}.

F1, traveling at the central trajectory. In these cases, the beam-energy is known from the dipole-magnet settings in BigRIPS.

For the measurement between F7 and F13, the data points and the linear fit are shown in Fig. 7.2. The resulting offset is $t_{\mathrm{off}} = 233.00\,\mathrm{ns}$ ($t_{\mathrm{off}} = 41.90\,\mathrm{ns}$ for F5 to F7) and the deduced flightpath is $S_{713} = 36\,193\,\mathrm{mm}$ ($S_{57} = 23\,088\,\mathrm{mm}$). The advantage of this method is that it delivers both, time offset and flight path, using experimental data.

Having determined the magnetic rigidity $B\rho$ and the kinetic energy of the particles in BigRIPS, cf. Fig. 7.1, the A/Z can be calculated to identify the particles,

$$\frac{A}{Z} = C \cdot \frac{B\rho}{\beta\gamma}, \tag{7.4}$$

with the constant $C = 3.107\,13/(\mathrm{T\,m})$. Together with the nuclear charge Z that is determined at F13 as described in Sec. 6.2.2, the incoming-beam particles are unambiguously identified as shown in Fig. 7.3.

In order to clean up the incoming-beam identification, the multiplicity on the start detector is restricted to one and the time profile of the beam is limited to the main sequence. Also, the charge measurement is restricted by gating on the correlation between the measurement at F7 and F13.

The intensity of the different isotopes and the fraction in the beam are listed in Table 7.1. The experimental values are compared to a simulation with the `LISE++` software [173]. There, BigRIPS is implemented as set up during the experiment and the `EPAX2.15` parametrization is used for calculating the cross section in fragmentation processes. Furthermore, an average intensity of

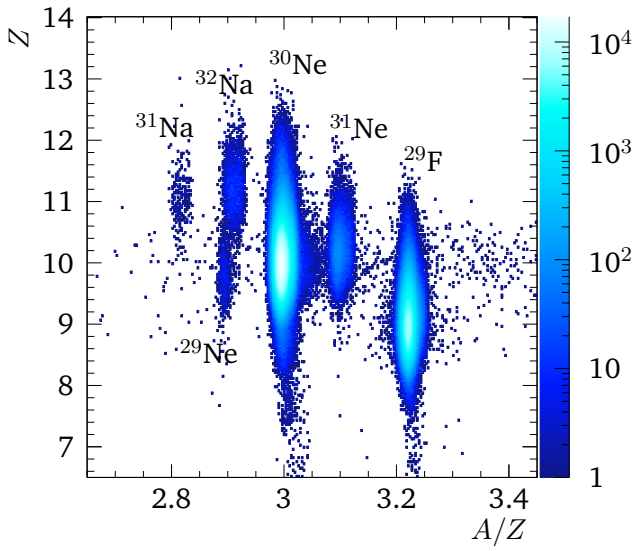

Figure 7.3: Incoming-particle identification of the ^{29}F beam setting. The isotope admixtures are labeled.

Table 7.1: Isotopes in the secondary beam of the BigRIPS setting which is optimized for ^{29}F. Given are the intensities, corrected for DAQ lifetime, and the admixture ratio. The results are compared to a simulation with LISE++.

Isotope	Intensity (cps)		Fraction (%)
	sim.	exp.	exp.
^{29}F	120.40	94.80	26.57
^{31}Ne	36.40	1.71	0.48
^{30}Ne	298.40	259.83	72.84
^{29}Ne	0.01	0.08	0.02
^{32}Na	0.03	0.28	0.08
^{31}Na	0	0.03	0.01

$500\,e\,\mathrm{nA}$ is used for the primary-beam intensity. The magnetic field settings differ by less than $0.5\,\%$ compared to the experiment to obtain the optimum transmission in the simulation. The simulation reproduces the experimental isotope fractions reasonably well. As expected, no charge states are seen, since it is not very likely for such light beams.

7.2 Reaction-Channel Identification

The SAMURAI setup allows to unambiguously identify the reaction channel of interest – the projectile, the heavy fragment, and scattered nucleons are identified. The previous sections described how the incoming beam and the nucleons from the quasi-free scattering are identified. In the following, the identification of the heavy reaction product using the SAMURAI spectrometer is

described. The reactions of interest are:

- ^{29}F$(p,pn)^{27}$F$+n$
- ^{30}Ne$(p,2p)^{27}$F$+2n$
- ^{31}Ne$(p,2p)^{29}$F$+n$

The SAMURAI spectrometer deflects the charged particles, which move with nearly beam velocity, according to their momentum-over-charge ratio p/Q,

$$B\rho = \frac{p}{Q} = \frac{\beta\gamma m}{Q}. \tag{7.5}$$

By determining the nuclear charge and in addition the velocity, the momentum and mass can be identified when the magnetic rigidity $B\rho$ is known.

First, the measurement of the fragment's magnetic rigidity is described. The trajectory of the particle through the magnetic field of SAMURAI is governed by the momentum and charge, as mentioned, and by the position and angle under which the particle enters the field. Incoming position and angle are determined with FDC1, the deviation from a reference trajectory is measured with FDC2.

In order to determine $B\rho$, there exist different standard methods, for instance one based on the matrix optics or a dedicated particle tracking using the Runge-Kutta method. Here, the way of finding a parametrization which relates $B\rho$ and the trajectories is followed as it became a standard method in high-energy physics but is now applied to a large-acceptance spectrometer. A function $B\rho = f(X)$ is determined that uses a n-tuple X of measured observables and results in a new observable, namely the magnetic rigidity at the center of the SAMURAI magnet.

This function is determined from simulation data, where all $B\rho$ and X are known from the outset. The n-tuple of observables $X = \{x_1, y_1, \alpha_{x_1}, \alpha_{y_1}, x_2, \alpha_{x_2}\}$ comprises

- x_1 and y_1 position measured with FDC1,
- angle in x and y direction, α_{x_1} and α_{y_1}, measured with FDC1,
- x_2 position and angle α_{x_2} measured with FDC2,

which uniquely relates the trajectory and the magnetic rigidity. The full phase space that is covered by the spectrometer is used as input to the simulation. In detail, ^{27}F particles ($A/Z = 3$) with the following properties are simulated starting at the target position:

- $5.0\,\mathrm{T\,m} < B\rho < 8.5\,\mathrm{T\,m}$
- $|x_{\mathrm{target}}| < 40\,\mathrm{mm}$ and $|y_{\mathrm{target}}| < 40\,\mathrm{mm}$
- $|\alpha_{\mathrm{x,target}}| < 50\,\mathrm{mrad}$ and $|\alpha_{\mathrm{y,target}}| < 50\,\mathrm{mrad}$.

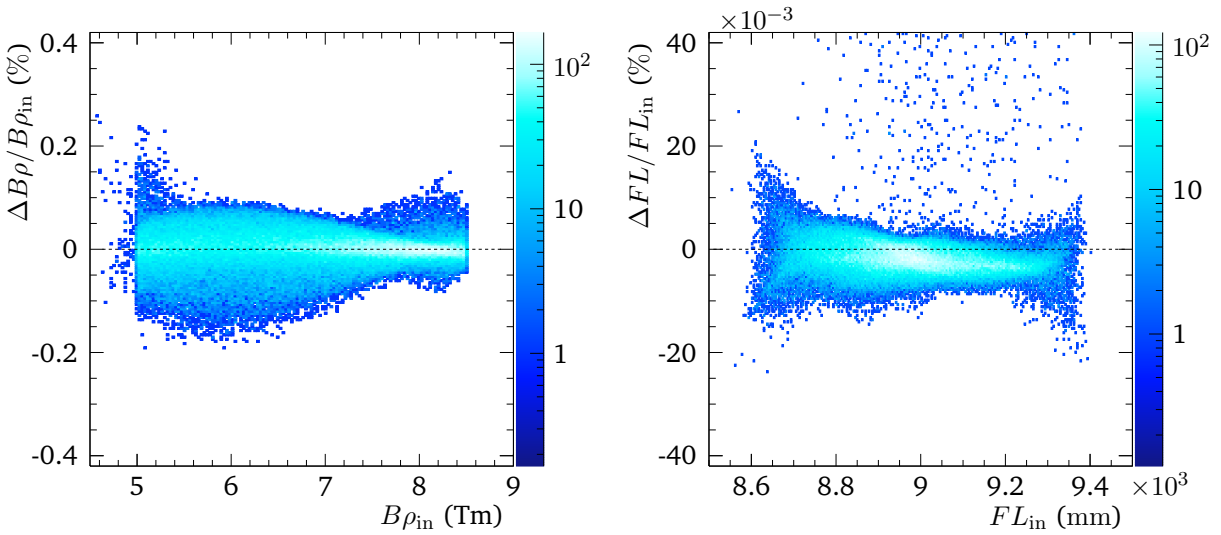

Figure 7.4: Result of the multi-dimensional fit approach for particle tracking. The obtained fit function is applied to the simulation-input data, $f(X_{\mathrm{in}})$. (a) Magnetic rigidity, $\Delta B\rho = B\rho_{\mathrm{in}} - B\rho(X_{\mathrm{in}})$. (b) Flight length, $\Delta FL = FL_{\mathrm{in}} - FL(X_{\mathrm{in}})$.

For each of these particles the position and angle at FDC1 and at FDC2 are extracted knowing their $B\rho$. A multi-dimensional fit [167] is performed on the training sample to derive the relation

$$B\rho = f(X) = \sum_{n=1}^{N} c_n F_n(X), \tag{7.6}$$

with

$$F_n(X) = \prod_{m=1}^{6} M_{n,m}(x_m), \tag{7.7}$$

where $M_{n,m}$ are chosen to be monomials for the six input variables. The fit routine determines the number of terms N, the coefficients c_n, and the functions $M_{n,m}$ in a least-squares approach.

The obtained function is evaluated with the same simulation-data set that has been used to create the function itself to evaluate the quality of $f(X)$. The result is shown in Fig. 7.4. The maximum deviation for $B\rho$ is $0.1\,\%$, which is in the order of the design value of the spectrometer $\Delta B\rho/B\rho = \Delta p/p = 0.14\,\%$ [26]. This procedure is repeated using the same training sample X to determine a function for the trajectory length, $FL = g(X)$. Together with the measured ToF and the velocity, the A/Z of the heavy reaction products is calculated eventually. The absolute ToF offset is determined from matching the energies at the reaction vertex as described in Sec. 7.3. Combining the A/Z and charge measurement, as described in Sec. 6.4.1, the reaction products can be identified as shown in Fig. 7.5. Many reaction channels can be identified due to the large

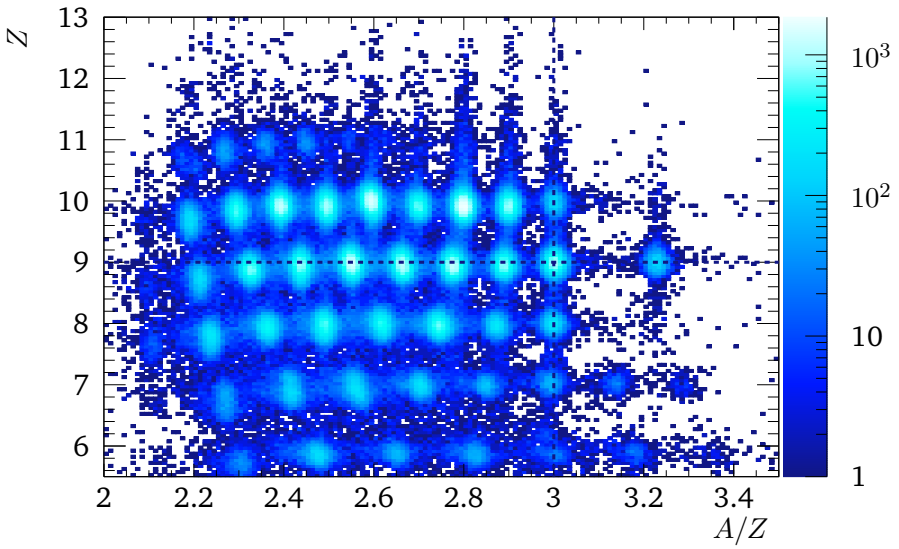

Figure 7.5: Outgoing-particle identification of the ^{29}F beam setting after reactions on the LH_2 target, with the condition of at least one track in MINOS. $A/Z = 3$ and $Z = 9$ are indicated by the dashed vertical and horizontal line, respectively.

acceptance of the setup. The Z number shows a slight A/Z dependence originating from the x-position dependence of the Z measurement.

In order to identify a QFS reaction and to e. g. exclude excitation reactions into the continuum, information from MINOS is used in addition. In a $(p, 2p)$ reaction two protons need to be identified in the MINOS TPC where the kinematic conditions as explained in Sec. 4.2 should be recognized. These include an opening angle between the two protons of approx. $80°$ and a coplanar scattering where the azimuthal angle is $180°$. Figures 7.6 & 7.7 show the polar angles $\theta_{1,2}$ of the two protons measured relative to the beam axis and the azimuthal angles $\phi_{1,2}$ in the x-y plane for the ^{30}Ne$(p, 2p)^{29}$F reaction – a clear QFS characteristic. As expected, the polar angles show a strong correlation, where the opening angle peaks at $77.4°$, cf. Fig. 7.7a. The opening angle θ_{pp} is calculated as

$$\cos(\theta_{pp}) = \sin(\theta_1)\sin(\theta_2)\cos(\phi_2 - \phi_1) + \cos(\theta_1)\cos(\theta_2). \tag{7.8}$$

A value of less than $80°$ is expected for nuclei with a proton-separation energy larger $20\,\mathrm{MeV}$ as calculated in Ref. [113]. The azimuthal scattering clearly shows coplanar kinematics where the relative angle $\Delta\phi$ peaks at $180°$, cf. Fig. 7.7b, $\Delta\phi = \phi_2 - \phi_1$ ($\Delta\phi = 360° - \Delta\phi$ for $\Delta\phi > 180°$). The use of MINOS and the TPC allows for the selection of QFS reactions by their kinematics signature. However, the energy of the emerging protons is not measured and thus the missing-mass analysis of the reaction product is not possible.

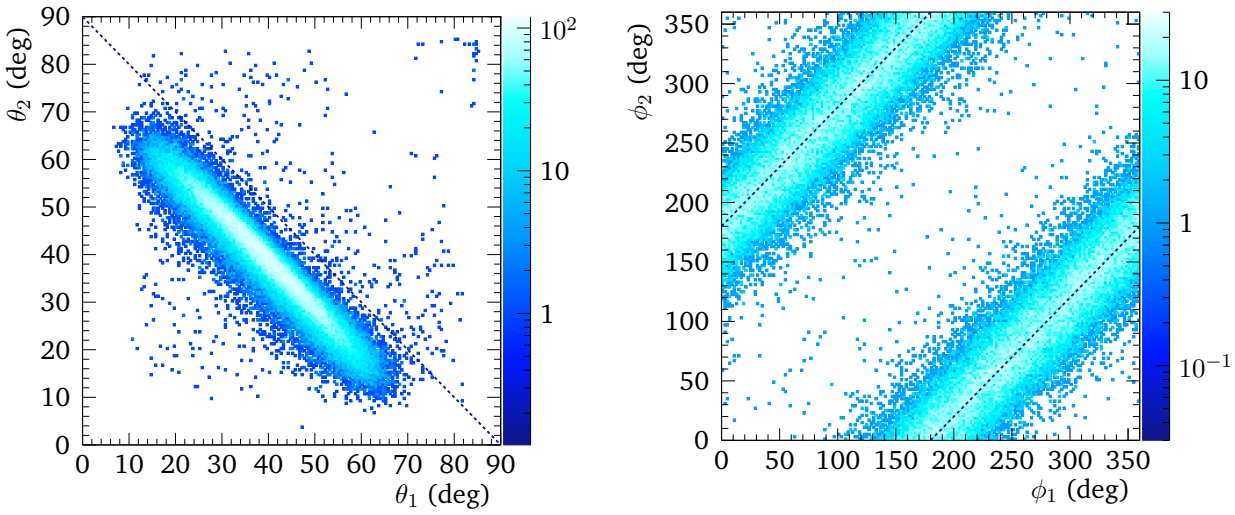

(a) (b)

Figure 7.6: Experimental proton correlations in the QFS reaction ^{30}Ne$(p, 2p)$. (a) Correlation of the polar angles $\theta_{1,2}$ of the two scattered protons. The dashed line represents a $90°$ opening angle. (b) Correlation of the azimuthal angles $\phi_{1,2}$. The dashed lines show the x-y-coplanar relative angle of $180°$.

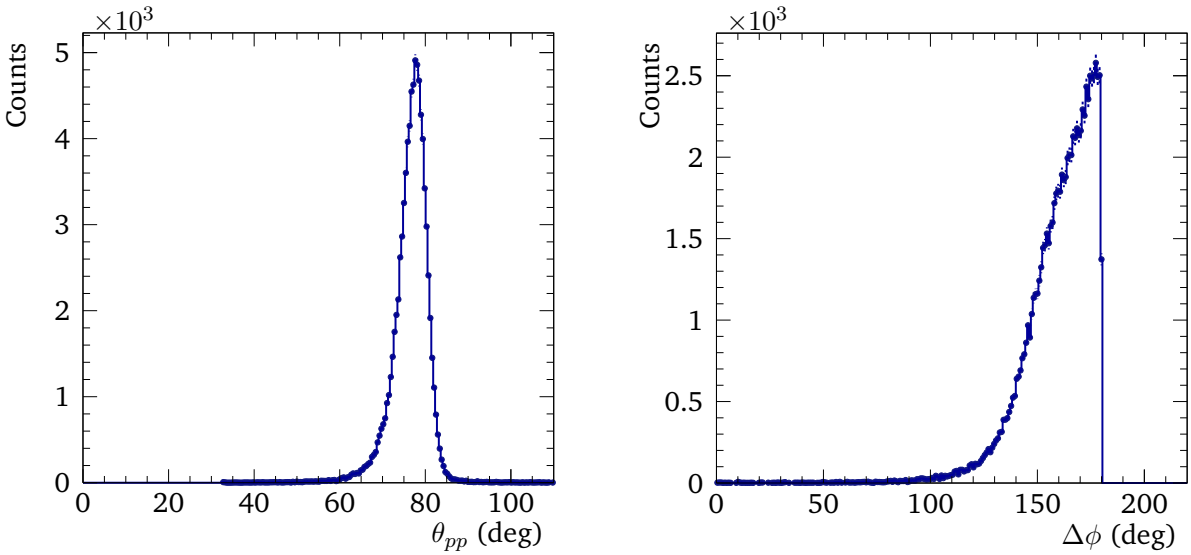

(a) (b)

Figure 7.7: Experimental signature of the QFS reaction ^{30}Ne$(p, 2p)$. (a) Opening angle between the two scattered protons, the mean value is at $77°$. (b) Coplanar angle between the two protons $\Delta\phi = \phi_2 - \phi_1$, peaking at $180°$.

7.3 Momentum Distributions

7.3.1 Energy matching

There are two independent measurements of the beam energy available – for the incoming and the outgoing beam. For consistency, the kinetic energy from these measurements has to match e. g. at the center of the LH_2 target for unreacted beam.

The way the energy loss is calculated for the upstream part is described in Sec. 6.8. For the determination of the downstream energy, two different methods are available, namely using the measured ToF or the magnetic rigidity. In the latter case, the obtained magnetic rigidity is the value at the center of the SAMURAI dipole magnet. This means the energy loss before needs to be considered.

This is done in the same way as described in Sec. 6.8 for the in-beam materials. The absolute ToF is fine-tuned in comparison to simulation to match the incoming energy after evaluating the energy loss. Momentum and energy are eventually determined from the magnetic-rigidity calculation since it shows a better resolution than using the ToF measurement as described in the next section.

7.3.2 Momentum Resolution

A sensitive way to prove the consistency of the particle tracking is the analysis of the momentum distribution. The total momentum is calculated from the magnetic rigidity

$$p = B\rho \cdot Q, \tag{7.9}$$

where the particle identification has been performed as described in Sec. 7.2. Thus, the momentum resolution is governed by the magnetic-rigidity resolution $\Delta B\rho$,

$$\frac{\Delta p}{p} = \frac{\Delta B\rho}{B\rho}. \tag{7.10}$$

First, the resolution is determined by investigating the momentum distributions of unreacted beam particles. The momentum of ^{29}F measured with the fragment arm is examined in the projectile rest-frame. The momentum is transformed into the center-of-mass system of the incoming ^{29}F beam as derived in Eq. 4.16 with direction of the incoming beam. So, the width of the longitudinal momentum in the projectile frame is only sensitive to the resolution of the apparatus, the tracking procedure, and the Coulomb-multiple scattering. The scattering angle of the outgoing particles is obtained from the FDC1 measurement and the incoming angle from the BDCs. The longitudinal, transverse, and single-component momentum distributions are shown in Fig. 7.8 & Fig. 7.9. The experimental resolution values determined from unreacted beam are summarized in Table 7.2. The width of the longitudinal momentum accounts for $31.2\,\mathrm{MeV}/c$ or $0.16\,\%$ relative to

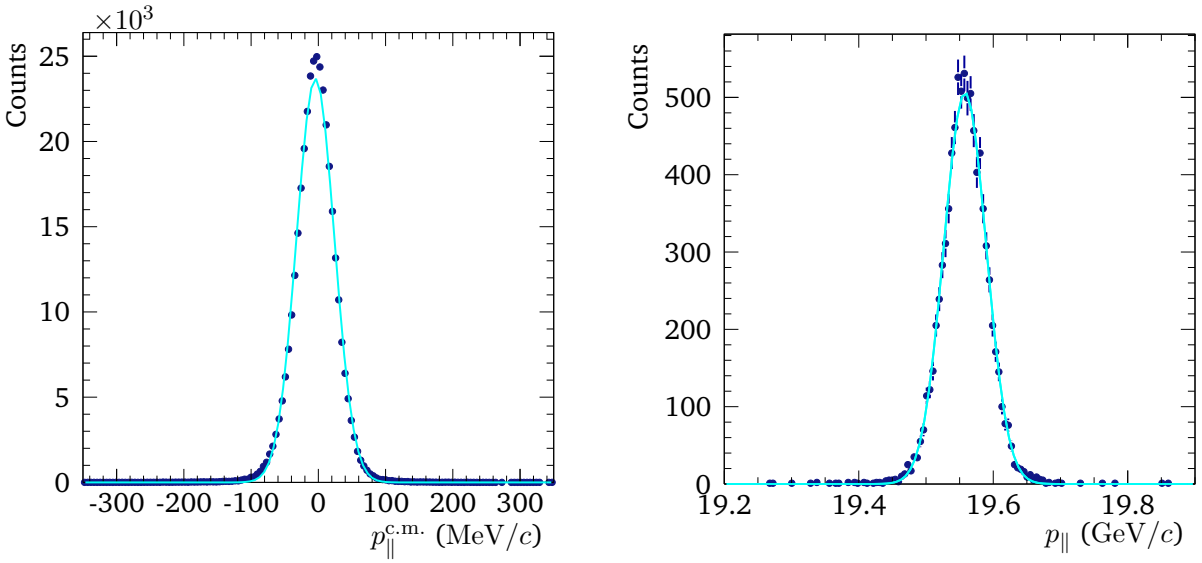

(a) (b)

Figure 7.8: Longitudinal-momentum distribution of the unreacted ^{29}F beam. (a) Longitudinal component in projectile rest frame and (b) longitudinal component in lab. system with $0.5\,\mathrm{MeV}$ gate in incoming energy, fit with a Gaussian function (cyan line).

Table 7.2: Momentum resolution (σ) determined from a Gaussian fit (range $\pm 80\,\mathrm{MeV}/c$) to the distributions for unreacted ^{29}F beam.

Momentum	σ (MeV/c)
p_x	39.6
p_y	37.9
$p_\parallel$	31.2
$p_\parallel$(c.m.)	27.2

the total momentum. After the calibration, it also proves the alignment of detectors and matching of kinetic-energy calculations. The transverse components are a bit wider than the longitudinal part. Those are mainly affected by the position resolution.

Eventually, a possible remaining reaction-vertex dependence of the momentum is corrected. The velocity difference between fragment and neutron that is crucial for the relative-energy reconstruction is corrected for the vertex z-position, the result is shown in Fig. 7.10.

As stated before, the momentum can be calculated from the ToF measurement, $p = \beta\gamma mc$. The resolution becomes

$$\frac{\Delta p}{p} = \gamma^2 \frac{\Delta\beta}{\beta} \approx \gamma^2 \frac{\Delta\mathrm{ToF}}{\mathrm{ToF}}. \tag{7.11}$$

The ToF resolution is also determined from unreacted beam particles that are measured between SBT and HODF24. The resolution is $\Delta\mathrm{ToF}/\mathrm{ToF} = 2.03 \times 10^{-3}$ which is enhanced by $\gamma^2 = 1.524$

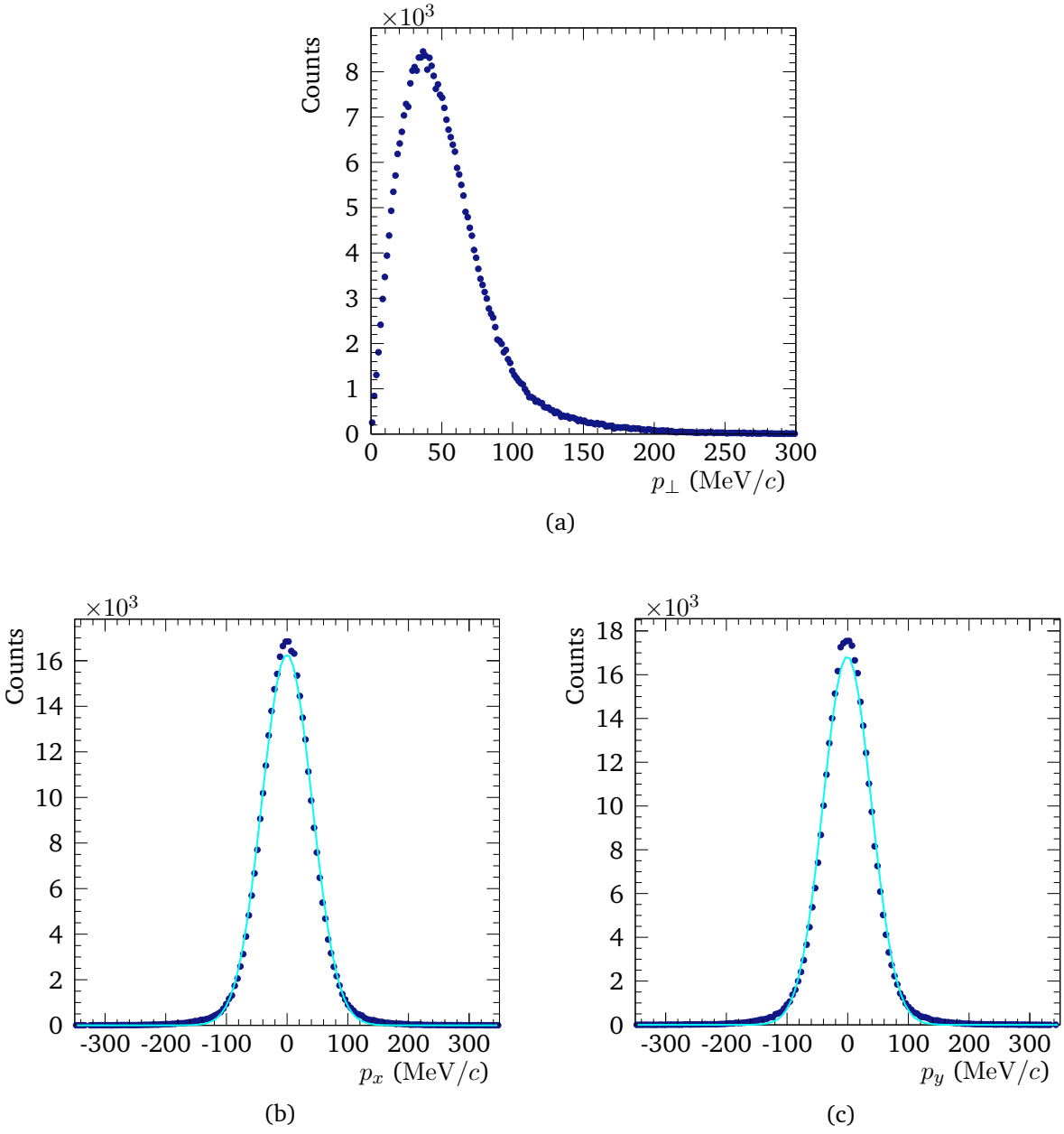

Figure 7.9: Transverse-momentum distribution of the unreacted ^{29}F beam (in projectile frame). (a) Total transverse momentum. (b) X-component (in projectile frame) and (c) y-component fit with a Gaussian function (cyan line).

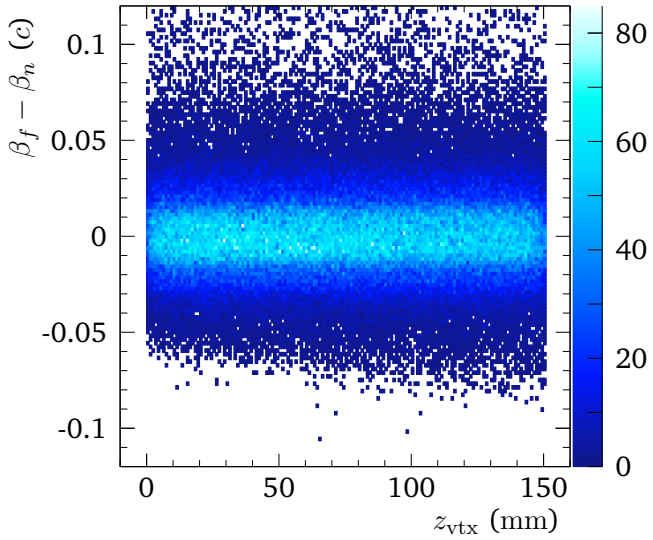

Figure 7.10: Corrected remaining velocity dependence of the MINOS vertex z-position. Shown is the velocity difference between fragment and neutron for the reaction ^{30}Ne$\rightarrow^{27}$F$+1n$.

(for $\beta = 0.586$). Thus, the momentum resolution based on the ToF measurement is worse, it is decreased by the boost γ^2 although the ToF resolution itself is comparable to the $B\rho$ resolution.

To complement the picture, the mass resolution depends on both, $\Delta B\rho$ and $\Delta\beta$, it is

$$\frac{\Delta A}{A} = \sqrt{\left(\frac{\Delta B\rho}{B\rho}\right)^2 + \left(\gamma^2\frac{\Delta\beta}{\beta}\right)^2 + \left(\frac{\Delta Z}{Z}\right)^2}. \tag{7.12}$$

The calculated resolution of $0.35\,\%$ agrees well with the experimentally deduced one ($\Delta Z = 0$). Light ions are well separated with this resolution as shown before, but for experiments with heavier systems this becomes critical.

7.4 Simulation Framework

Simulation studies are an integral part of the analysis. It is exploited to determine particle trajectories in the presence of the SAMURAI magnetic field as described in Sec. 7.2, or to determine the response of the γ-ray and neutron detectors. The detector details are discussed separately in Sec. 7.5 and 7.6.

The simulations are performed in the `SAMURAISimulator` framework [174] which is based on the `GEANT4` simulation toolkit [175, 176] and models the downstream part of the setup including DALI2, the FDC tracking detectors, and the HODF24, as well as the neutron detectors NeuLAND and NEBULA and the SAMURAI magnet. Importantly, the data format of simulation and experimental analysis is the same on the level of calibrated data such that the same analysis software is used and it is ensured the data are treated in the same way.

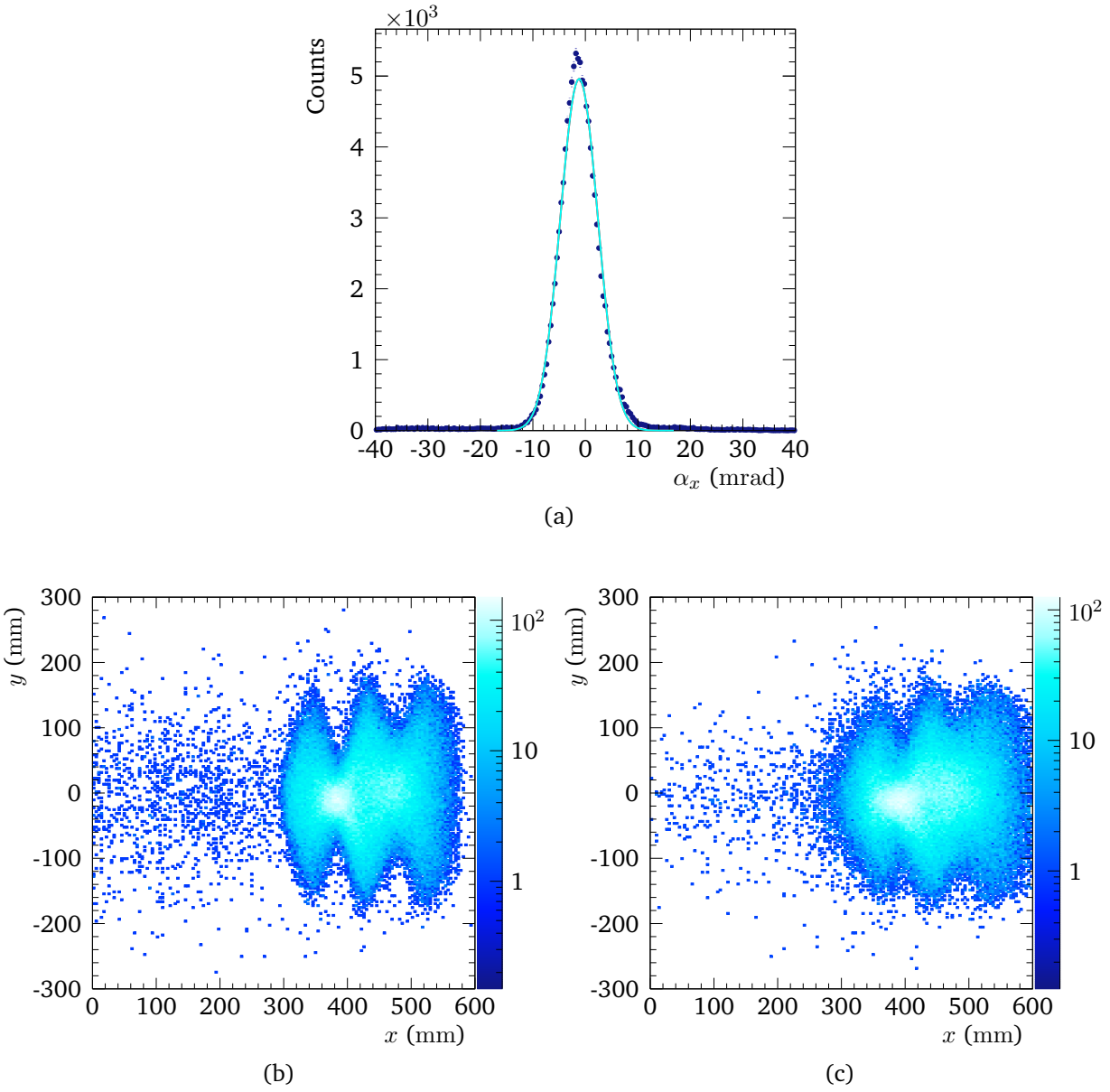

Figure 7.11: Comparison of fragment tracking between experiment and simulation for unreacted ^{29}F beam on FDC2, fit with a Gaussian function. (a) Difference of x angle measured with FDC2. (b) Experimental position distribution. (c) Position distribution from simulation.

The simulation starts from the reaction products that are tracked through the setup. The initial four-momenta P of the particles are determined for instance in ordinary c. m. phase-space decays. However, the knockout reaction on the LH_2 target is not explicitly treated since the recoil momentum is small compared to the total momentum. The incoming energy distribution as well as experimental position and angular distributions of the beam spot are used to sample starting conditions for the simulation. In case of the thick LH_2 target for a $(p,2p)$ reaction, a possible vertex position is randomized according to the experimental conditions and the energy loss is calculated

for the initial nucleus before a decay happens. The simulation then treats only the decay products.

The particle transport is modeled using the `QGSP_INCLXX_XS` physics list [174, 175]. This includes for intermediate-energy scattering of protons and neutrons with nuclei the `INCL++` model [177], covering approx. $20\,\mathrm{MeV/u}$ to $15\,\mathrm{GeV/u}$. Low-energy interactions are modeled using adapted `NeutronHP` evaluated-data libraries that are especially suited for low-energy neutron elastic and inelastic scattering, high-energy reactions would be covered in the Quark-Gluon-String (`QGS`) model.

One check for the goodness of the simulation is the analysis of the tracking of the heavy fragment. Figure 7.11 shows the comparison between experimental and simulation data. That is unreacted ^{29}F beam, which is tracked through the setup. The energy and target-position information are used as input to the simulation to check the position distribution of the downstream fragment detectors. The simulation data agree well with the experiment, e. g. the difference in the x angle between experimental and simulation for FDC2 peaks at $-1.2\,\mathrm{mrad}$ as shown in Fig. 7.11a. The positions of the tracking detectors are aligned to each other similarly as shown in Sec. 6.5.3.

The quality of the simulation is further discussed in detail in the detector sections below. It is worth noting how the detector resolutions are included. The resolution for the fragment detectors is inclusively incorporated in the data-analysis step by smearing the momenta with a Gaussian distribution based on the experimental resolution as extracted in Sec. 7.3.2. The total fragment-neutron resolution $P(f+n)$ is dominated by the fragment's resolution, whereas the invariant-mass resolution is critically affected by the neutron-momentum resolution, in particular the ToF resolution that dominates the longitudinal-momentum resolution.

In case of the neutron detectors, the time resolution at each PMT is $\Delta t = \sqrt{2} \cdot \Delta t_{\mathrm{tof}}$, where Δt_{tof} is the ToF resolution as determined in Sec. 6.7.1 under the well-fulfilled assumption that the resolution is very similar for γ-rays and heavy particles. For the DALI2 detectors the resolution is also taken as experimentally obtained, see Sec. 6.6.1. Individually for every single detector crystal, the resolution is taken as of Gaussian form with the width from the naive parametrization $\sigma(E_\gamma) = A \cdot \sqrt{E_\gamma}$. This approach reproduces the source measurement well.

7.5 Gamma Spectroscopy

The DALI2 detector is installed for the prompt γ-ray detection around the target. It covers a large solid angle with high segmentation using 140 NaI detectors. The kinematic conditions in the experiment require a Doppler correction of the detected γ-ray energy according to Eq. 5.5. The velocity at the reaction vertex βc is derived from the MINOS information and the energy loss in the LH_2 target. The scattering angle corresponds to the position relative to the center of the detector segment in which the γ-ray is detected.

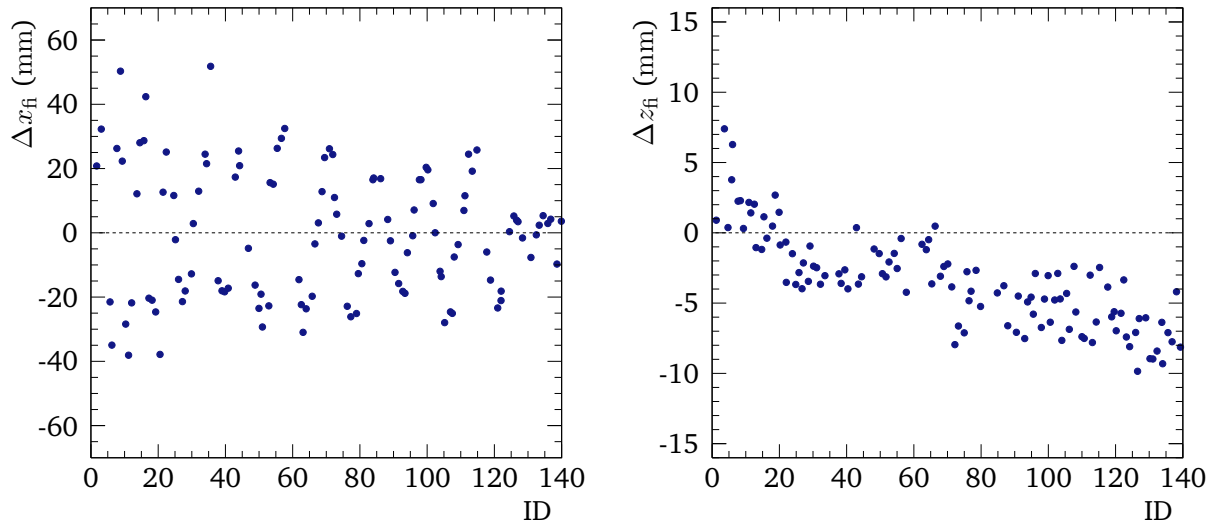

Figure 7.12: DALI2 first interaction points for improvement of the Doppler correction. Shown is the difference between the first interaction in a crystal $\vec{x}_{\mathrm{fi}}$ from simulation and its actual geometrical position $\vec{x}$, $\Delta\vec{x}_{\mathrm{fi}} = \vec{x}_{\mathrm{fi}} - \vec{x}$, for each crystal. (a) x-position, (b) z-position.

Since the whole detector is built in a nested structure, cf. Fig. 5.8, the center of a single detector is not necessarily the most probable point of the first interaction for a γ-ray. But knowing this point can improve the resolution because the point of interaction is statistically known more precisely in this case. In order to determine those points, simulations are performed for the given geometry and experiment conditions that result in a heat map showing the most probable first interaction in each detector segment. The difference between the geometrical center of the detector and the deduced point of first interaction is shown in Fig. 7.12, the difference can be as large as $\sim 20\,\mathrm{mm}$. Thus, the point of first interaction is used to determine the scattering angle θ_{lab} for the Doppler correction. The improvement on the resolution is $3\,\%$ (or $15\,\mathrm{keV}$) at $E_\gamma = 1\,\mathrm{MeV}$.

Besides the first interaction, a γ-ray can interact several times in a crystal and does not necessarily deposit all its energy in a single crystal. Instead, scattering into neighboring ones happen and energy is deposit there. To reduce misidentifications, an algorithm is developed to find the interactions that belong to one initial γ-ray. This so-called addback algorithm starts from an energy-sorted list of hits and builds clusters. A hit is considered to be part of one cluster if the detector is less than $20\,\mathrm{cm}$ apart from the initial hit in the cluster. When all hits are iterated, the laboratory energies in each cluster are summed up and the Doppler correction is applied to the cluster taking the position of the first detector in the cluster as interaction point. The effect on the background reduction is shown in Fig. 7.13, in a comparison between γ energies with and without addback for simulation data of a $950\,\mathrm{keV}$ state. The addback algorithm finds proper clusters, thus reduces the background region and increases the intensity of the full-energy peak. However, the resolution does not improve significantly.

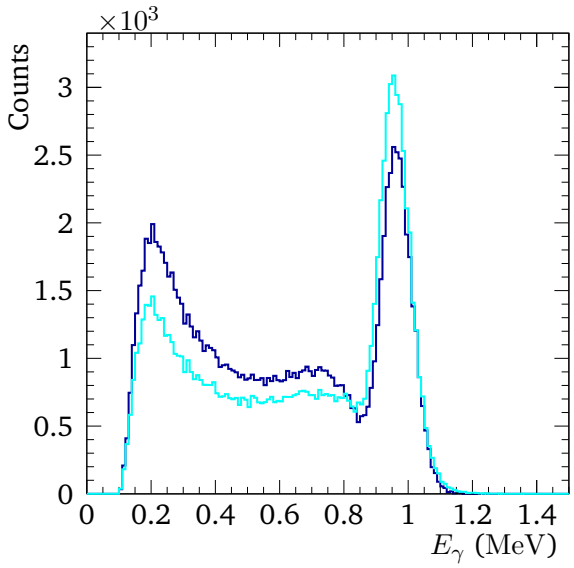

Figure 7.13: Addback algorithm for DALI2. Comparison between γ-ray energy spectrum with (cyan line) and without (blue) addback and using the most probable first-interaction point, applied to simulation data for a $950\,\mathrm{keV}$ decay. The addback improves the photo-peak efficiency.

Later, full simulations for γ-ray decays are performed to compare to the experimental spectra and determine the decay energies. The simulations include the DALI2 geometry as well as the materials that surround the target like the MINOS TPC. The experimental beam distribution in position, energy, and reaction channel are used as input to the simulation where a γ-ray is emitted isotropically in the c. m. frame. If not specified differently, the decay is modeled as a prompt and direct decay without branching. The simulated data are analyzed in the same way as the experimental data. This includes that the energy threshold in the laboratory frame is commonly set to $200\,\mathrm{keV}$ which corresponds to the maximum hardware threshold among all crystals.

Other background reactions are not included in the simulation. A reaction channel where no γ-ray decay is expected is well suited to describe the experimental background contribution. The proton knockout reaction on ^{29}F$(p, 2p)$ populates ^{28}O that decays directly into ^{24}O and four neutrons. As ^{24}O has no bound excited state, the DALI2 response to a $(p, 2p)$ reaction without γ-rays can be studied. The two protons in this QFS reaction are of high energy and also interact with the DALI2 crystals. They are charged and the energy loss is usually so large that the signals cause an overflow in the ADC. However, the protons may also scatter and leave less energy in the detectors. The background stemming from this as well as γ-rays are measured in coincidence with the ^{24}O reaction. The obtained spectrum is later used as background description in the fit of the experimental γ-ray spectra.

7.6 Neutron Tracking

A major task is to identify initial neutron hits from multiple secondary interactions. In the kind of experiment performed here, where the reaction channel is unambiguously identified and the incoming beam and the heavy reaction fragment are measured as well as target-like particles, the number of expected neutrons that decay in-flight is known. In the reaction $^{30}\mathrm{Ne}(p,2p)^{27}\mathrm{F}$ two neutrons need to be identified. Considering the geometrical acceptance of the detector and setup, as well as the interaction probability, only a fraction of the decay neutrons is detected.

Often, plastic-scintillator detectors are used to detect fast neutrons, as in this experiment, where kinetic energies between $\sim 100\,\mathrm{MeV/u}$ and $300\,\mathrm{MeV/u}$ are covered. The neutron can interact via elastic and inelastic scattering with the protons and carbon nuclei in the material. Charged secondary particles cause good signals in the detectors. In Ref. [178], the reactions are investigated in detail from simulation and the reaction products are grouped by impact studying NeuLAND as example. Neutrons are the most common reaction products, followed by protons, α-particles, heavier fragments, deuterons, and uncharged particles like γ-rays [178].

These particles are likely to interact in various secondary reactions and deposit energy in the detector that eventually leave many signals in a segmented detector such as NeuLAND. That means, one initial neutron causes several signals in the detector – called crosstalk – and in the analysis steps the first interaction of this neutron needs to be identified to eventually determine its momentum. This becomes more challenging the more initial neutrons are expected from the reaction channel. The algorithm to perform the neutron reconstruction and find the crosstalk hits, where neutron misidentification needs to be kept small, is presented in this section, based on the method presented in Ref. [179].

7.6.1 Neutron Identification

In case of a one-neutron event, the crosstalk causes a hit multiplicity larger than one but it is assumed that the first interaction, in a list of hits sorted according to their ToF, is the initial-neutron interaction. In addition, a certain energy-loss threshold, usually set to a few MeV to mainly discriminate low-energy γ-rays decaying from $^{12}\mathrm{C}^{*}$, is applied. Using the ToF and the position of this hit, the neutron momentum is calculated.

In case of multiple incident neutrons, the first two detected hits in a fully active detector often do not correspond to the initial interactions of two different neutrons. It is the designated task of a crosstalk algorithm to identify the actual initial two neutron hits. There are several approaches established like cluster-building methods, or techniques that focus only on a class of particles like scattered protons that leave clearly recognizable tracks to backtrace the initial neutron-scatter point.

This work makes use of a cluster approach and the geometry of the neutron-detector walls based on the method described in Ref. [179]. Two different classes of events are discussed, the so

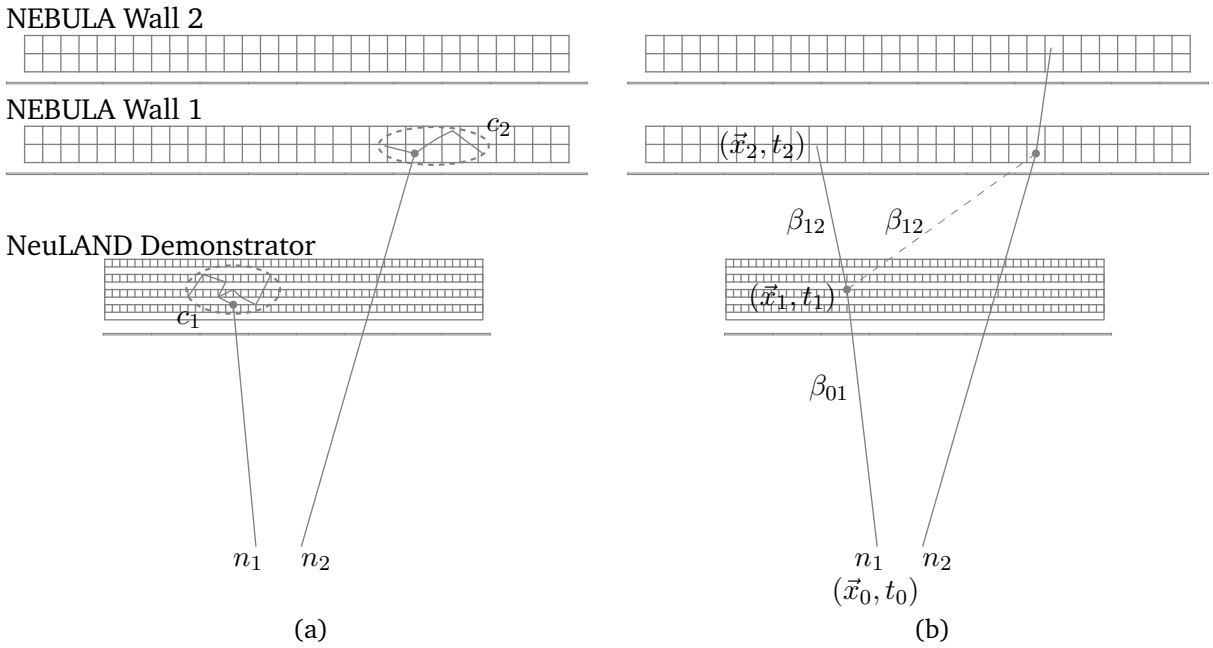

Figure 7.14: Schematic representation of the neutron crosstalk analysis, scenario for two initial neutrons n_1 and n_2. (a) Same-wall events are depicted, two clusters are formed, c_1 and c_2, where different-wall events are not explicitly shown here. (b) Different-wall events are shown, the relative velocity β_{12} is a criterion to cluster the hits 1 and 2.

called

- same-wall events and
- different-wall events.

The neutron-detection system, shown in Fig. 5.3, is physically divided into three detection modules, namely the NeuLAND demonstrator labeled as "wall1" and the two parts of NEBULA ("wall2" & "wall3"). Hits that are within one wall are called same-wall events and hits involving two walls are called different-wall events, cf. Fig. 7.14.

The neutron-identification algorithm starts from a list including all hits that are sorted according to their ToF in ascending order. Each hit ($\texttt{hit}_i$) is compared to all other hits and assigned to common clusters based on certain conditions that are discussed in the following.

Same-Wall Events

Practically, `hit2` is compared to `hit1`. If both hits originate from neutron interactions within the same detector wall, their distance in space and time looks like in Fig. 7.15, exemplarily shown for NeuLAND and the one-neutron decay from ^{29}F$(p,pn)^{28}$F$\rightarrow^{27}$F$+n$. All the hits shown in this plot are actually crosstalk hits because one-neutron events are studied. One can identify the most

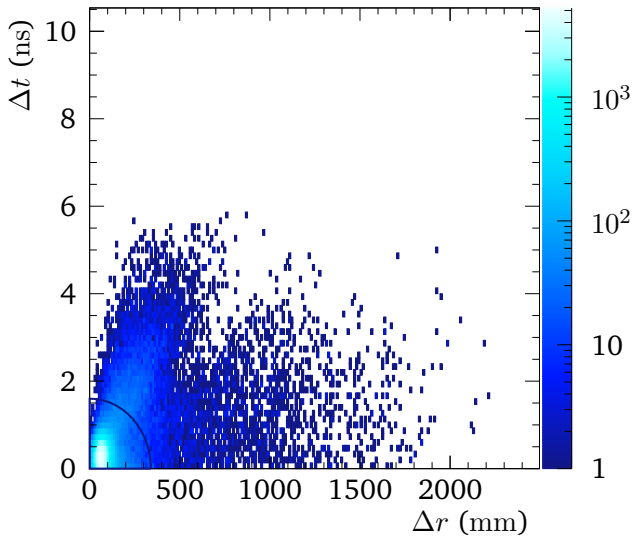

Figure 7.15: NeuLAND same-wall crosstalk for an experimental one-neutron channel. The distance in space Δr and time Δt between all hits is shown. Events within the blue ellipse are associated with proton crosstalk, the rest originates mainly from scattered neutrons and γ-rays.

important secondary particles in this plot, namely scattered protons which have a short mean free path compared to slow neutrons that are also visible. Gamma-rays travel farthest in the shortest amount of time.

The first condition to decide whether these two hits stem from the same neutron and get assigned to the same cluster is determined from this correlation plot. Those hits caused by scattered protons in a region indicated in Fig. 7.15 are clustered as same-wall events. An elliptic causality condition is applied according to the interdistance in space $\Delta r = |\vec{r}_2 - \vec{r}_1|$ and time $\Delta t = |t_2 - t_1|$,

$$\sqrt{\left(\frac{\Delta r - \Delta r_0}{R}\right)^2 + \left(\frac{\Delta t - \Delta t_0}{T}\right)^2} < 1, \tag{7.13}$$

with the offsets Δr_0 and Δt_0, and the size of the gate R and T, that are different for NeuLAND and NEBULA.

Secondly, γ-rays and slow neutrons are assigned to a cluster according to the relative velocity between hits, $\beta_{12}c = |\vec{x}_2 - \vec{x}_1|/(t_2 - t_1)$. Figure 7.16 shows the inverse of the relative velocity for remaining events after proton-crosstalk rejection. Negative velocities mean that the second hit has a smaller z position than the first hit, $z_2 < z_1$. The energy-loss ΔE_2 is that of the second hit. One can identify γ-rays with $|1/\beta_{12}| \sim 1$ and a moderate energy-loss. Those events are assigned to a cluster if they are within the blue-colored box as depicted in Fig. 7.16. In addition, a cut around $|1/\beta_{12}| \sim 1$ is set where events with smaller velocity are considered crosstalk. However, this cut needs to be optimized for the particular multi-neutron channel, but Ref. [158] shows that crosstalk events peak at $|1/\beta_{12}| > 1$ in the two-neutron case.

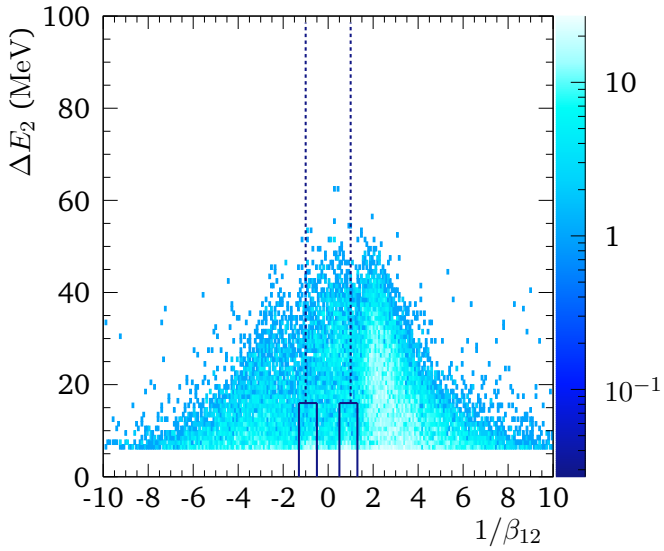

Figure 7.16: NeuLAND same-wall crosstalk for experimental one-neutron channel where the proton crosstalk is removed. Shown is the inverse of the relative velocity $1/\beta_{12}$ between pairs of all hits with the energy loss of the second hit ΔE_2. Events marked in the blue box come from γ-rays with $|1/\beta_{12}| \sim 1$ and events beyond the dashed line $|1/\beta_{12}| > 1$ are also considered as main crosstalk sources in a multi-neutron scenario.

If `hit2` does not belong to any of the mentioned gates, it becomes the first hit of a new cluster. All the other hits are then compared to the previously assigned clusters and the hits therein in the same way as long as it is assigned to any cluster.

Different-Wall Events

The secondary particles are not necessarily stopped within one wall in a few interactions but can scatter from one wall into another one. The conditions how such different-wall hits are identified as crosstalk are discussed in the following. Assume a situation as in Fig. 7.14b, where two hits $(\vec{x}_i, t_i)$ are measured in two different walls. Either these are two initial hits from two different neutrons, or scattered events from the same initial neutron, or scattered events from two different neutrons. In order to relate the hits, the velocity between the target point and the first hit β_{01},

$$\beta_{01} c = |\vec{x}_1 - \vec{x}_0|/t_1, \tag{7.14}$$

and the relative velocity β_{12} between the two detected hits, defined as

$$\beta_{12} c = |\vec{x}_2 - \vec{x}_1|/(t_2 - t_1), \tag{7.15}$$

is used, where the velocity is defined negative if $z_2 < z_1$, i. e. the particle is back scattering.

Particles share energy in a scattering process, thus the velocity ratio becomes $|\beta_{01}/\beta_{12}| > 1$ and

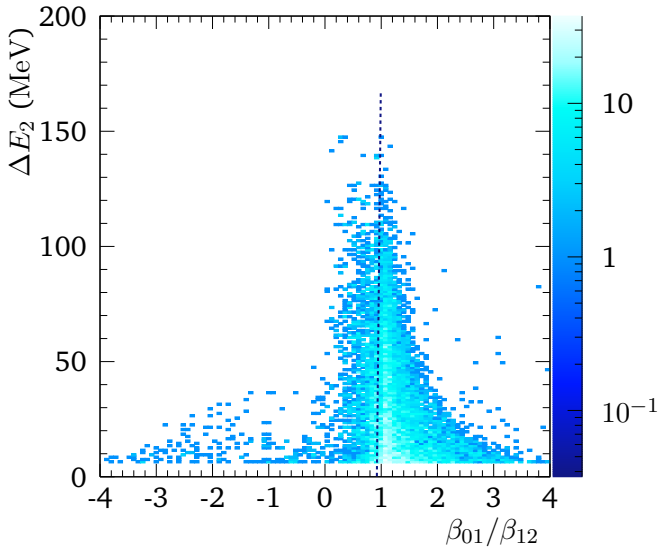

Figure 7.17: Different-wall crosstalk between NeuLAND and NEBULA for the experimental one-neutron channel where the proton scattering from the veto detector is removed. Shown is the velocity ratio between the initial hit β_{01} and the relative velocity β_{12} between pairs of all hits and with the energy loss of the second hit ΔE_2. Events beyond the dashed line $|\beta_{01}/\beta_{12}| \gtrsim 1$ are considered as main crosstalk source in a multi-neutron scenario.

it is concluded that the two hits are crosstalk and related in one cluster. Those events are mainly caused by slow neutrons. The condition is tuned according to the distribution shown in Fig. 7.17 for the same one-neutron channel as discussed before, where proton scattering is removed already with the intermediate veto walls. All events to the right of the blue dashed line are considered as crosstalk as well as the back-scattered events between ($|\beta_{01}/\beta_{12}| \gtrsim 1$).

In addition, γ-ray events can be identified. In order to discriminate those, the inverse of the relative velocity $1/\beta_{12}$ is considered. Again, secondary γ-rays have $\beta = 1$ but do not deposit high energies in the detectors. Neutron-cluster multiplicities larger one are almost completely eliminated under those conditions, having a remaining contribution of only $1\,\%$ in the studied one-neutron channel.

The applied crosstalk conditions are different for NeuLAND and NEBULA and are optimized with the aim to reduce misidentification by employing simulations and experimental one-neutron data, as discussed above and described in the following Sec. 7.7.

The advantage of separating the detector into separate walls is a gain of efficiency for multiple-neutron events with a small relative energy. Those neutrons come close in space under the given experimental conditions. In the c. m. of the decaying system the neutron and fragment momenta balance each other but due to the much larger mass of the fragment, the opening angle is dominated by the neutron angle. The relative energy can be seen geometrically as

$$E_{\mathrm{rel}} \approx \frac{E_{\mathrm{kin}}}{A}\theta_n^2, \tag{7.16}$$

with incident-beam energy per nucleon E_{kin}/A and the dominating neutron angle θ_n. This means, the angular acceptance of the setup and the detector size limit the maximum measurable relative energy with highest efficiency, in this case $E_{\mathrm{rel}} \approx 1.7\,\mathrm{MeV}$, in accordance with the full acceptance of NeuLAND. A larger beam energy would increase that value due to a larger Lorentz boost. Instead, multiple neutrons with very small relative energies have a small cone and impinge closer on the detector. In same-wall events it is more difficult to differentiate those events from crosstalk and the efficiency decreases strongly to zero for small relative energies. In the extreme case of different-wall events at the same x-y-position they can be differentiated in the different walls, considering the ToF resolution.

7.6.2 Neutron Simulation

In the simulation the neutron detectors are built from plastic-scintillator bars that are arranged as in the experiment together with the other fragment detectors and the magnet.

Basic quantities such as the simulated energy-loss behavior, ToF, and multiplicity distributions need to agree with experimental data to reliably describe the detector response. The experimental one-neutron decay channel $^{29}\mathrm{F}(p,pn)^{27}\mathrm{F}{+}n$ is used as reference channel to study the neutron-detector response. The input to the simulation are events that decay into a neutron and $^{27}\mathrm{F}$ with a relative energy that is similar to the experimental relative-energy spectrum. The ToF and multiplicity spectra after the above discussed crosstalk rejection are compared for NeuLAND in Fig. 7.18, the spectra are normalized to each other to be more independent of the absolute efficiency. The distributions agree well.

The light transport for NeuLAND is modeled as described in the following. The simulation models the path of particles in steps through the materials, the energy deposit is obtained from the energy loss along the path. The transformation from energy loss $Q_{0,i}$ to scintillation light Q_i is modeled according to an empirical relation found in Ref. [180]. The produced light propagates in the next step to the end of the bar while undergoing attenuation processes,

$$Q_i' = Q_i \cdot \exp(-l/\lambda), \tag{7.17}$$

with the attenuation length λ and l as the path length between hit and end of the bar. The light is collected from all interactions in a bar at the PMTs. Depending on the way the experimental data are calibrated, the saturation effect of the PMTs needs to be included. It is described by

$$Q'' = \frac{Q'}{1 + \kappa Q'}, \tag{7.18}$$

with a saturation coefficient $\kappa = 0.018$ for NeuLAND. At the same time the energy resolution is incorporated with $5\,\%$. The total energy loss is the energy at the position in the bar that is assigned to the first interaction point.

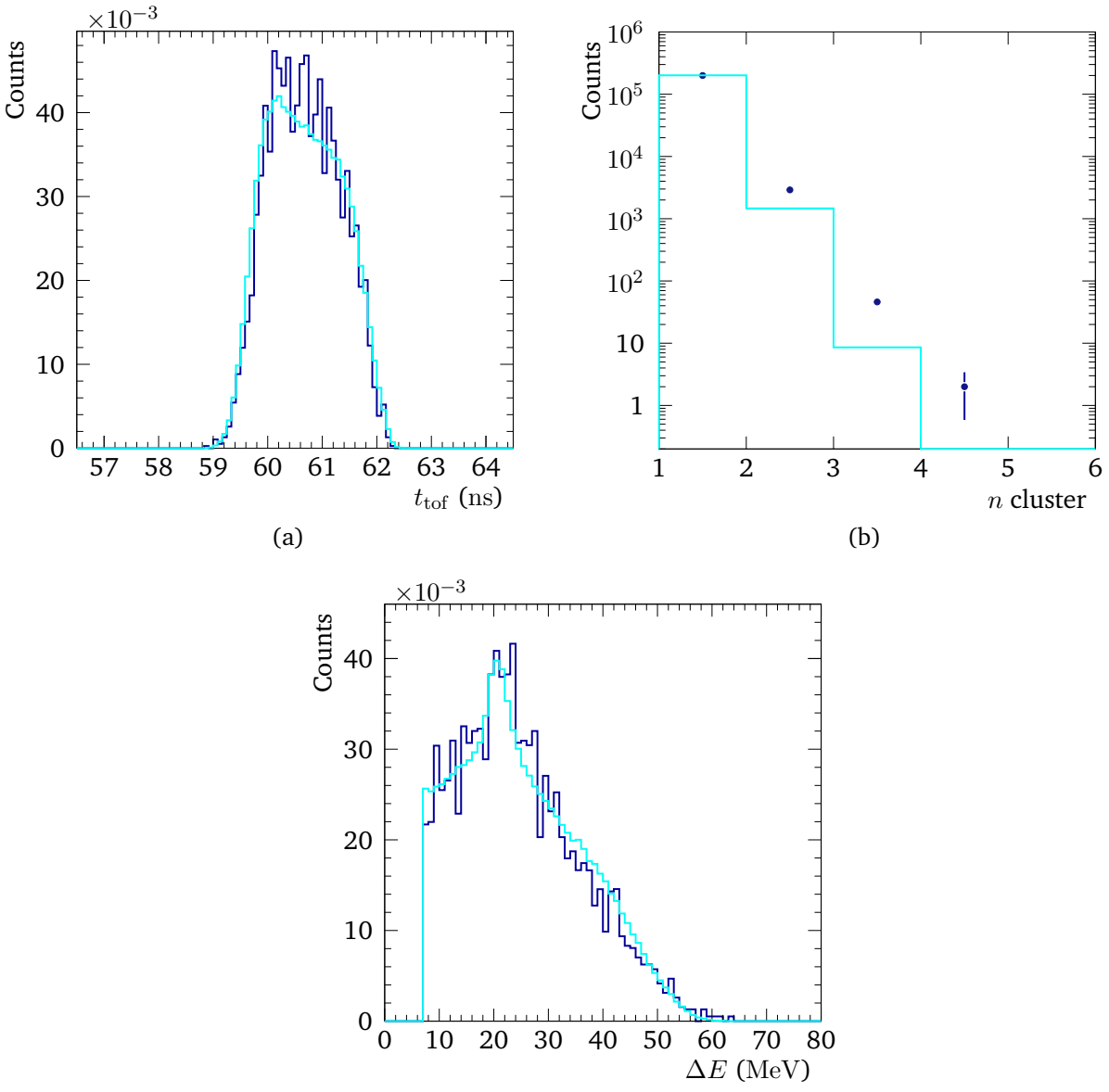

Figure 7.18: Basic neutron quantities measured with NeuLAND compared between experiment (blue) and simulation (cyan line) in a one-neutron channel after crosstalk rejection. (a) Time-of-flight. (b) Reconstructed neutron multiplicity. (c) Energy loss.

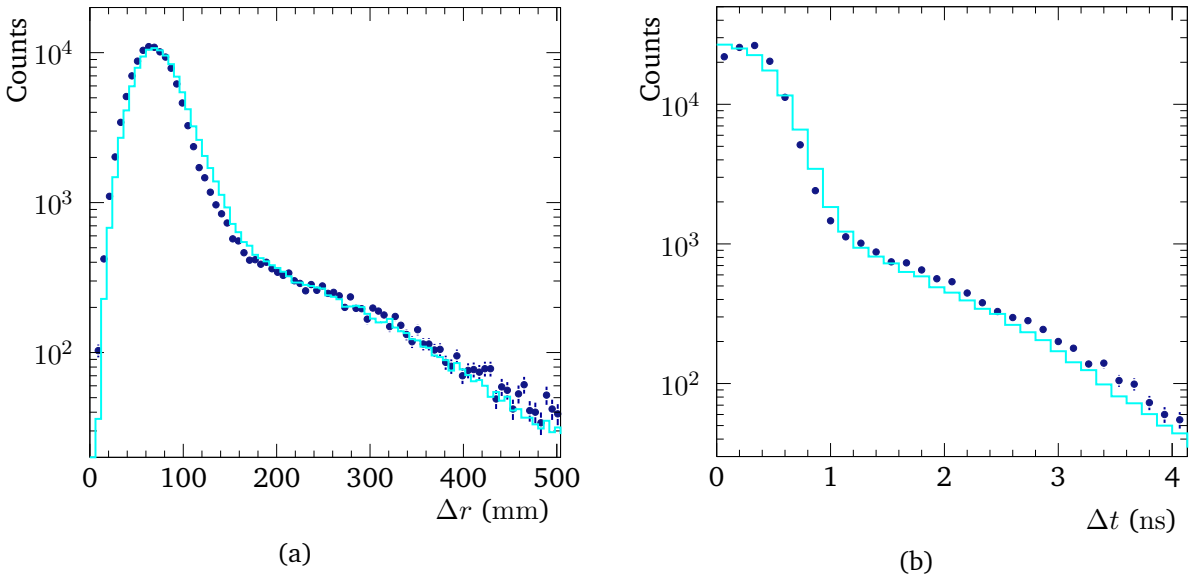

Figure 7.19: Comparison between experiment (blue dots) and simulation (cyan) for proton-crosstalk rejection in NeuLAND same-wall events for one-neutron channel, projections of Fig. 7.15. (a) Spatial distance between pairs of all same-wall hits. (b) Time difference.

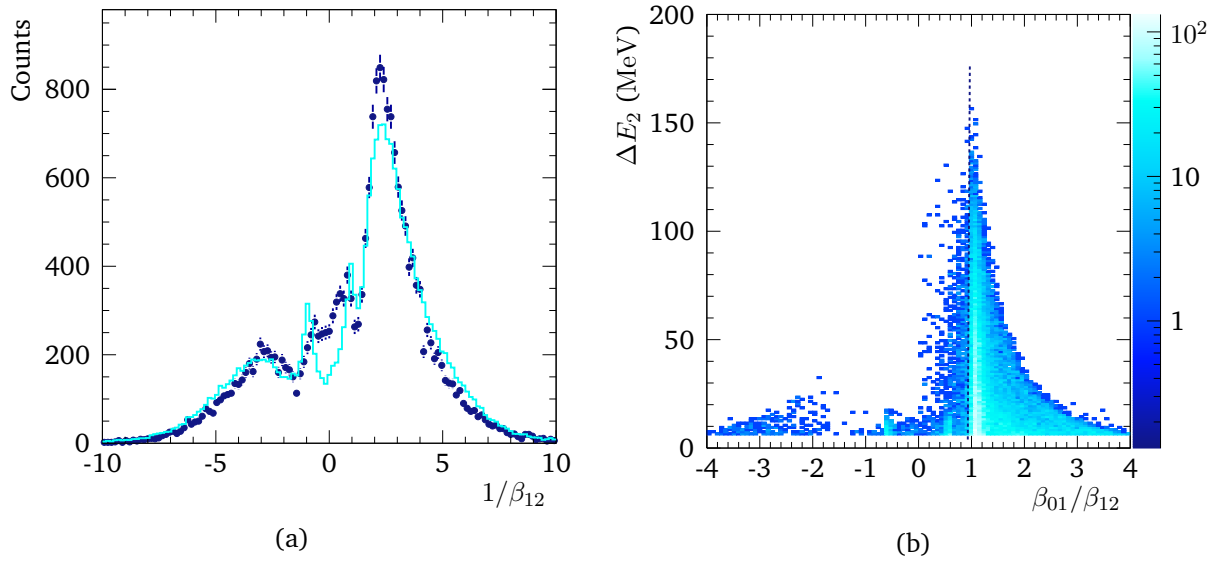

Figure 7.20: Comparison of one-neutron simulation and experiment for same- and different-wall events. (a) Inverse velocity ratio for same-wall events in NeuLAND after proton-crosstalk rejection, cf. Fig. 7.16, for experiment (blue dots) and simulation (cyan). (b) Velocity ratio for different-wall events to reject crosstalk in simulation. Hits with $|\beta_{01}/\beta_{12}| \gtrsim 1$ are considered as crosstalk in the multi-neutron analysis.

The collected light is then reversely attenuated, the energy deposit is

$$Q_0 = Q'' \cdot \exp(L/2 \cdot \lambda^{-1}), \tag{7.19}$$

with paddle length L. The comparison between experimental and simulated data is shown in Fig. 7.18c. The peak arising from proton scattering is well reproduced as well as the shape for high energy losses. Eventually, the simulation is used to describe the detector response and to study the multi-neutron tracking.

The Figs. 7.19 and 7.20 show the comparison between simulation and experiment for the neutron crosstalk analysis as discussed in the above Sec. 7.6.1. The same-wall crosstalk analysis for NeuLAND dedicated for secondary-proton rejection, Fig. 7.19, agrees well (cf. Fig. 7.15). The inverse relative velocity $1/\beta_{12}$ after proton-crosstalk rejection agrees similarly well, Fig. 7.20a, although the used physics list in the simulation seems to overproduce γ-rays. The different-wall events for NeuLAND and NEBULA are shown in Fig. 7.20b, and the experimental data in Fig. 7.17.

Response Matrix

In order to extract observables like cross sections or resonance parameters the detector response as resolution, geometrical acceptance and efficiency needs to be considered. For the analysis of the relative-energy spectra, the model, namely the Breit-Wigner line shape, is folded with the experimental response and fit to the experimental spectrum such that resolution and acceptance effects are included as coming from the experimental data. A response matrix is simulated that relates the input relative-energy to the reconstructed relative energy with resolution, acceptance, and efficiency, as well as neutron-reconstruction effects. Simulation and experimental data are analyzed in the same way.

For the one-neutron decay channel, a decay into fragment and neutron for a given relative energy is calculated and used as input for the simulation together with input from experimental data like beam-spot and energy distributions, cf. Sec. 7.4. The reconstructed relative-energy spectrum for the decay of a sharp peak at $0.1\,\mathrm{MeV}$, $1.0\,\mathrm{MeV}$, and $2.0\,\mathrm{MeV}$ for $^{28}\mathrm{F}{\rightarrow}^{27}\mathrm{F}{+}n$ is presented in Fig. 7.21 where the neutron is only detected with NeuLAND. In the same figure, the response for the two-neutron decay of $^{29}\mathrm{F}^{*} \rightarrow^{27}\mathrm{F}{+}n{+}n$ is shown where the neutrons are detected together with NeuLAND and NEBULA. The resonances are well reproduced what shows that the neutron simulation, tracking, and identification work well. The simulations are repeated for an input energy-range up to $10\,\mathrm{MeV}$. The behavior of the relative-energy resolution could fairly be described for the $2n$ case by $\sigma(E_{fnn}) = a \cdot (E_{fnn}/\mathrm{keV})^{b}$ (with $a = 2.35\,\mathrm{keV}$ and $b = 0.56$), but here the complete response matrix is used instead.

The response matrix that relates the original relative energy $E_{\mathrm{rel}}^{\mathrm{in}}$ with the reconstructed one $E_{\mathrm{rel}}^{\mathrm{rec}}$ over the range of $10\,\mathrm{MeV}$ is shown in Fig. 7.22, where one and two neutrons decay and exactly one and two neutrons are reconstructed, respectively. Figure 7.23 shows the combined

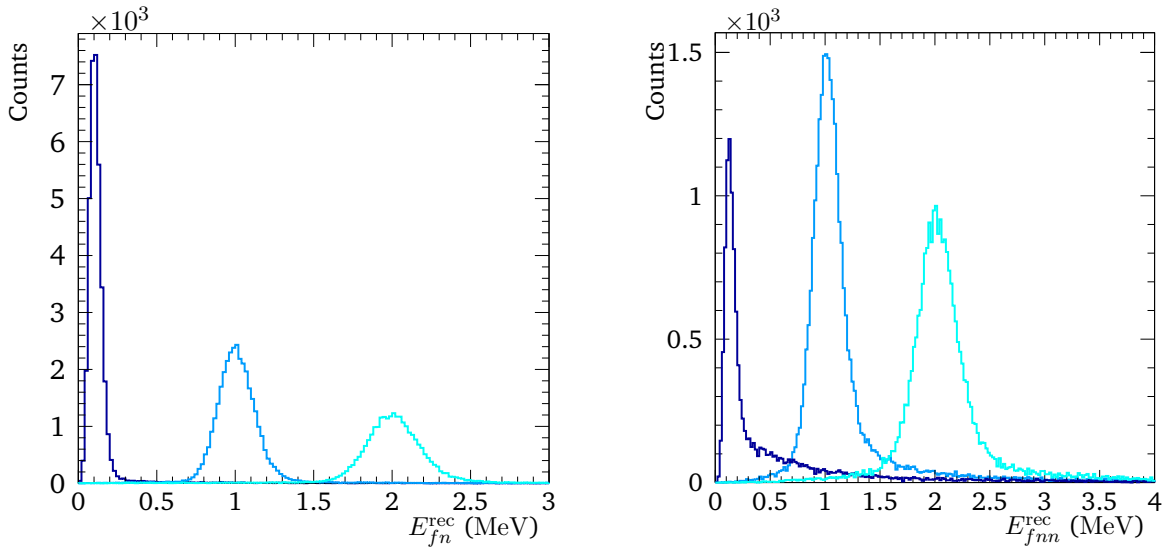

(a) (b)

Figure 7.21: Neutron-detector response function determined from simulation with input resonance energies at $0.1\,\mathrm{MeV}$, $1.0\,\mathrm{MeV}$, $2.0\,\mathrm{MeV}$ (blue, light blue, cyan). (a) One-neutron decay channel of ^{28}F reconstructed with NeuLAND. (b) Two-neutron decay channel of ^{29}F reconstructed with NeuLAND and NEBULA.

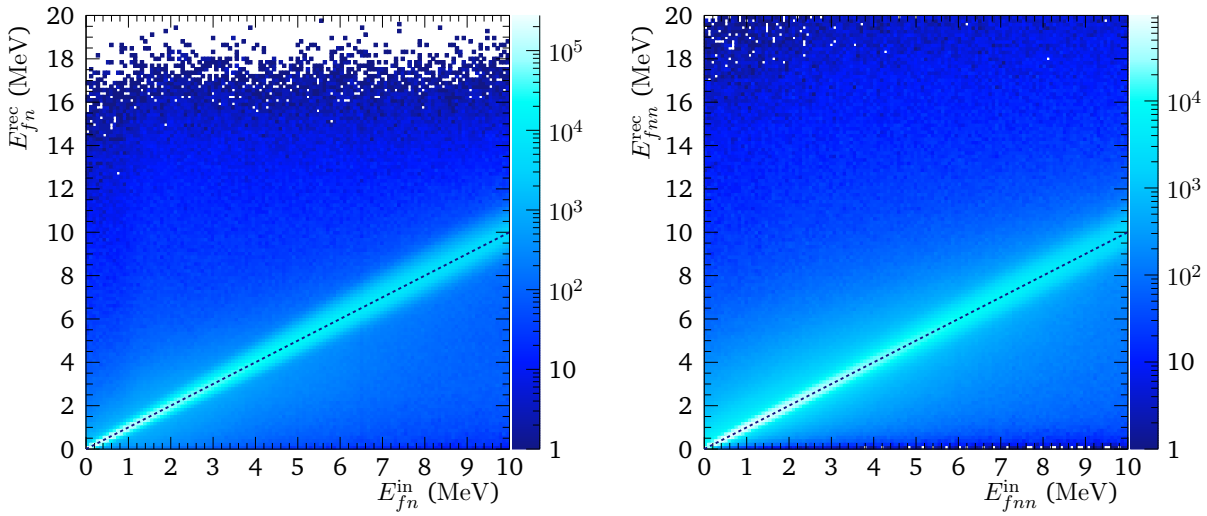

(a) (b)

Figure 7.22: Neutron-detector response matrix determined from simulation relating the initial relative energy $E_{\mathrm{rel}}^{\mathrm{in}}$, in a range up to $10.0\,\mathrm{MeV}$, with the reconstructed relative-energy $E_{\mathrm{rel}}^{\mathrm{rec}}$ response. The dashed line represents the identity between initial and reconstructed energy. (a) One-neutron decay channel of ^{28}F reconstructed with NeuLAND. (b) Two-neutron decay channel of ^{29}F reconstructed with NeuLAND and NEBULA.

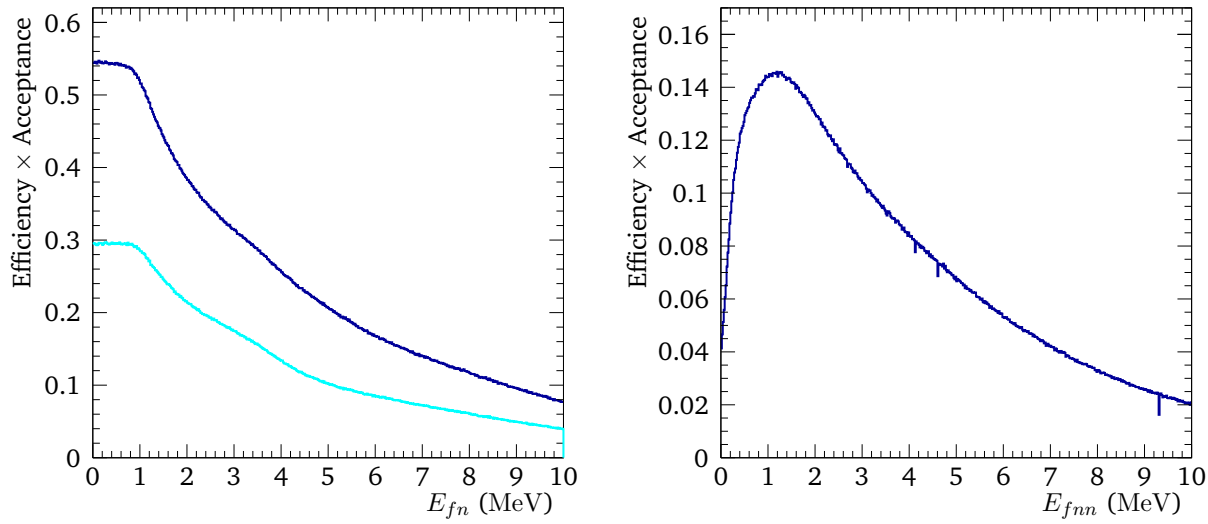

(a) (b)

Figure 7.23: Neutron-detector efficiency and acceptance curve determined from simulation up to $10.0\,\mathrm{MeV}$ relative energy. (a) One-neutron decay channel of ^{28}F reconstructed with NeuLAND and NEBULA in blue, and only NeuLAND in cyan. (b) Two-neutron decay channel of ^{29}F reconstructed with NeuLAND and NEBULA.

efficiency and acceptance curve as function of the relative energy for NeuLAND only and combined with NEBULA. The number of reconstructed neutron events is normalized to the total number of simulated events. At around $1.5\,\mathrm{MeV}$ the $1n$-curve drops, which is related to the horizontal acceptance of the neutron exit window of the SAMURAI magnet.

In case of a two-neutron decay the response is similar to the one-neutron channel, cf. Fig. 7.21, but the multi-neutron identification is critical here. The stronger tails in the response arise from misidentification, which is already optimized and reduced by the neutron tracking. However, the efficiency is very different between the one- and two-neutron channels including not only the detection but also the neutron-reconstruction efficiency. For relative energies below $1\,\mathrm{MeV}$ the efficiency decreases strongly as the two neutrons are spatially close (see discussion above, Eq. 7.16). The accuracy of the simulation to result in the correct absolute efficiency is discussed in the following section, Sec. 7.7, where a dedicated experiment was performed to investigate this point.

7.7 One-Neutron Detection Efficiency of the NeuLAND Demonstrator

7.7.1 Motivation

In this particular experiment, the NeuLAND demonstrator is used at SAMURAI for the first time to study physics questions. In general, it is essential to know the interaction, detection, or tracking efficiency of the detector to determine absolute cross sections. For the investigated neutron-reaction channels, the neutron-detection efficiency is of particular interest.

In order to evaluate the one-neutron detection efficiency and to characterize the detector, a distinct experiment using a neutron beam at two energies, $110\,\mathrm{MeV}$ and $250\,\mathrm{MeV}$, was carried out. The results provide an explicit data point for the one-neutron detection efficiency at a defined energy for the NeuLAND demonstrator that is also used as benchmark value to validate the simulations in several aspects. Detector calibrations and resolutions are also tested on the basis of this commissioning experiment.

There exist different established techniques to determine the efficiency, for example by measuring the efficiency relative to a characterized detector of known efficiency or calculating the detection efficiency where the beam flux is known. Here, the latter is the method of choice. In the same way, NEBULA has been studied before at $200\,\mathrm{MeV}$, when the SAMURAI setup was commissioned [158]. In the charge-exchange reaction $p\left(^7\mathrm{Li}, ^7\mathrm{Be}\right)$ an almost monoenergetic neutron field of known flux is produced.

7.7.2 Method and Reaction Cross Sections

In order to determine the one-neutron detection efficiency ϵ_{1n} the following experiment is carried out. The probe, a neutron beam of well-defined energy and known intensity n_{in}, needs to be produced and the number of interacted and detected neutrons n_{det} needs to be determined. The ratio $\epsilon_{1n} = n_{\mathrm{det}}/n_{\mathrm{in}}$ is the basic definition of the efficiency.

The charge-exchange reaction $p\left(^7\mathrm{Li}, ^7\mathrm{Be}(\mathrm{g.s.} + 430\,\mathrm{keV})\right) n$ of a proton beam on lithium is a standard method to produce a quasi-monoenergetic neutron beam. It is often applied in high-energy neutron research [181]. Such studies address basic radiation-physics questions as the study of the neutron-energy spectra at different incident energies and under different scattering angles. Furthermore, there are experiments to explicitly deduce the reaction cross section for $p\left(^7\mathrm{Li}, ^7\mathrm{Be}\right)$, which is the necessary input for the calibration experiment here to determine n_{in}.

Neutron ToF facilities like at TRIUMF (Canada), iThemba Laboratory for Accelerator-Based Sciences (iThemba LABS) (South Africa) or in Japan (Rikagaku Kenkyūjyo, Designated National Research and Development Institute (RIKEN), Takasaki Ion Accelerators for Advanced Radiation Application (TIARA), or Research Center for Nuclear Physics (RCNP)), or the Los Alamos Meson Physics Facility (LAMPF) (USA), and others provide high-intense proton beams up to a few hundred MeV and a neutron-energy resolution of $2\,\mathrm{MeV}$ and better [181]. At the RCNP, experiments

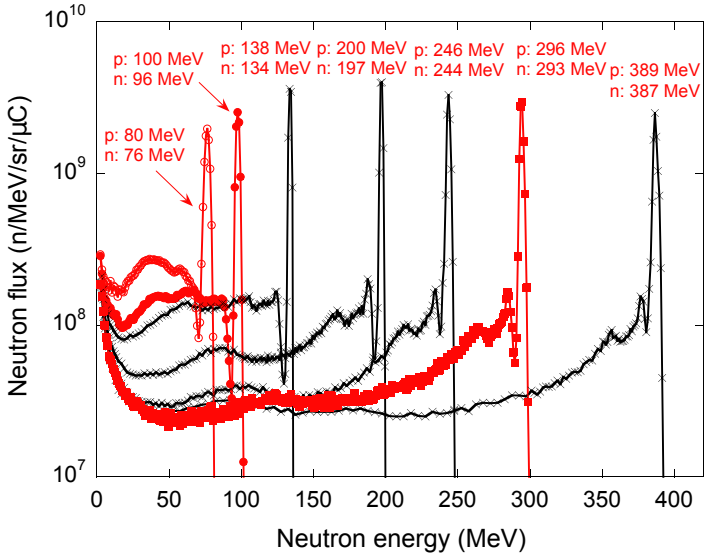

Figure 7.24: Neutron energy spectra for Li(p, xn) reactions at zero degrees, measured at RCNP for different proton energies. Reprinted figure with permission from Ref. [181], copyright 2019 by Elsevier.

with proton beams between $80\,\mathrm{MeV}$ and $400\,\mathrm{MeV}$ [181] are performed, Taddeucci et al. [182] report experiments using $800\,\mathrm{MeV}$.

At the RCNP, the proton beam impinges onto the Li target producing the neutrons that are detected in a liquid-scintillation detector. In a tunnel with a flightpath of up to $100\,\mathrm{m}$ the ToF is measured precisely for different scattering angles for that the kinetic-energy spectrum is deduced. In Fig. 7.24 characteristic neutron spectra taken at RCNP [181] for zero-degree scattering are shown.

All the spectra commonly show a strong peak close to the incident proton energy and a tail region below. The peak intensity makes roughly $50\,\%$ of the total spectrum, these quasi-monoenergetic neutrons originate mainly from the $p\,(^7\mathrm{Li}, ^7\mathrm{Be})$ reaction populating the ground and the excited state at $430\,\mathrm{keV}$ in ^{7}Be, where the excited state decays via γ-ray emission. The smaller peaks at $\sim$10 MeV and $30\,\mathrm{MeV}$ below the main peak are associated with the population of highly excited states in ^{7}Be, where broader contributions from the quasi-free scattering on a neutron and collective excitations play a role [183]. At even lower energies, less than $\sim 100\,\mathrm{MeV}$ below the main peak, the main contribution comes from the three-body break-up $p\,(^7\mathrm{Li}, \alpha)\,^3\mathrm{He} + n$. Evaporation processes produce the lowest-energy neutrons.

For the studies here, the peak neutrons with a sharp energy are of foremost interest to characterize the detector. The (p, n) charge-exchange reaction on ^{7}Li populates the ground state in ^{7}Be as well as its low-lying excited state at $430\,\mathrm{keV}$ and thus produces almost monoenergetic neutrons. The Q-value of this reaction is $-1.644\,\mathrm{MeV}$. The cross section is largest at 0° forward scattering because the reaction proceeds primarily through an angular-momentum transfer of $l = 0$ [182].

As mentioned before, one basic quantity needed in the analysis is the cross section for the charge-exchange reaction. This has been measured at different n-ToF facilities [181, 182, 184] and differential cross-section distributions are extracted from integrating the peak intensity for different laboratory scattering angles (but often the error estimates are unclear). Here, the zero-momentum transfer center-of-mass cross section determined by Taddeucci et al. [182] is used. The cross sections are $\sigma_0^{\mathrm{c.m.}} = 26.1(9)\,\mathrm{mb/sr}$ and $\sigma_0^{\mathrm{c.m.}} = 25.6(7)\,\mathrm{mb/sr}$ at $E_p = 120\,\mathrm{MeV}$ and $200\,\mathrm{MeV}$, respectively. There, the total laboratory cross section for normalization of the angular differential cross section is taken from a parametrization based on the momentum-transfer integral* and the activation-method total cross section. It is assumed that the c. m. cross section is constant as function of the proton energy, which is well satisfied above $100\,\mathrm{MeV}$ as the authors show [182].

Taddeucci et al. [182] found a parametrization for the low-momentum transfer $q^{\mathrm{c.m.}}$ region of the differential cross section $\sigma^{\mathrm{c.m.}}$ in the c. m.

$$\sigma^{\mathrm{c.m.}}(q^{\mathrm{c.m.}}) = \sigma_0^{\mathrm{c.m.}} \exp\left[-(q^{\mathrm{c.m.}})^2 \frac{\langle r^2 \rangle}{3}\right], \tag{7.20}$$

with the zero-momentum transfer c. m. cross section $\sigma_0^{\mathrm{c.m.}}$ in $\mathrm{mb/sr}$ and the mean-square radius $\langle r^2 \rangle$ which is associated with an effective interaction, and charge and magnetization density [182].

For the experimental analysis, this distribution is transformed into laboratory coordinates and integrated over the covered scattering range. First, the differential cross section in the laboratory frame as function of the scattering angle $\sigma(\theta)$ is calculated from $\sigma^{\mathrm{c.m.}}(q^{\mathrm{c.m.}})$ applying the transformation derived in Ref. [185],

$$\left(\frac{\mathrm{d}\sigma}{\mathrm{d}\Omega}\right)_{\mathrm{lab}} = \left(\frac{\mathrm{d}\sigma}{\mathrm{d}\Omega}\right)_{\mathrm{c.m.}} \frac{\mathrm{d}\cos(\theta^{\mathrm{c.m.}})}{\mathrm{d}\cos(\theta^{\mathrm{lab}})}. \tag{7.21}$$

The transformation factor becomes

$$\left(\frac{\mathrm{d}\sigma}{\mathrm{d}\Omega}\right)_{\mathrm{lab}} = \sigma^{\mathrm{c.m.}}(q^{\mathrm{c.m.}}) \cdot \frac{\left[\gamma^2 \left(\alpha + \cos^2\left(\theta^{\mathrm{c.m.}}\right)\right)^2 + \sin^2\left(\theta^{\mathrm{c.m.}}\right)\right]^{3/2}}{\gamma\left(1 + \alpha \cdot \cos\left(\theta^{\mathrm{c.m.}}\right)\right)} \tag{7.22}$$

with

$$\alpha = \beta \frac{E_n^{\mathrm{c.m.}}}{p_n^{\mathrm{c.m.}}}, \tag{7.23}$$

β and γ are the kinematic factors of the incident proton and the c. m. quantities describe the following scattering process. The reaction can be treated kinematically as two-body scattering using Lorentz transformations to connect the center-of-mass and laboratory systems. Here, the

*referred to as method (b). Method (a) uses a more simple parametrization with a slightly worse χ^2.

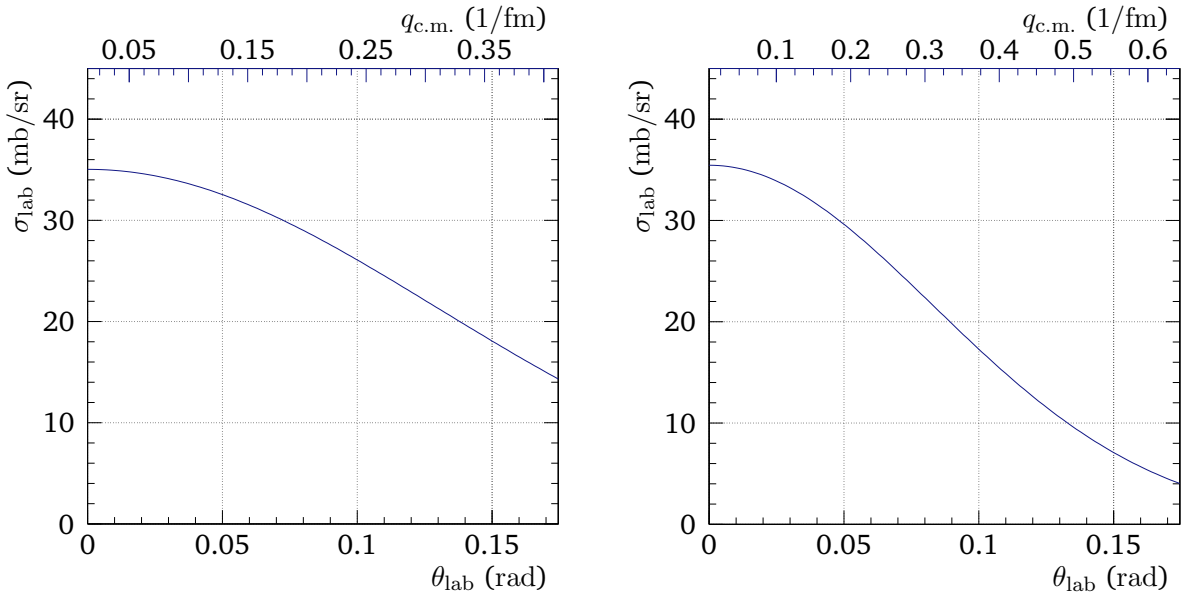

Figure 7.25: Differential cross section for $p(^7\mathrm{Li},^7\mathrm{Be})n$ according to Eq. 7.22 for (a) $110\,\mathrm{MeV}$ and (b) $250\,\mathrm{MeV}$ proton energy.

two-body relativistic kinematics code `RELKIN` [186] is used to determine the energies and c. m. scattering angles of neutron and ^{7}Be as function of the scattering angle and the reaction energy. The momentum transfer $q^{\mathrm{c.m.}}$ is

$$q^{\mathrm{c.m.}} = \sqrt{\left(p_p^{\mathrm{c.m.}}\right)^2 + \left(p_n^{\mathrm{c.m.}}\right)^2 - p_p^{\mathrm{c.m.}} p_n^{\mathrm{c.m.}} \cdot \cos\left(\theta^{\mathrm{c.m.}}\right)}. \tag{7.24}$$

The differential cross section in the laboratory system for the $p\left(^7\mathrm{Li}, ^7\mathrm{Be}(\mathrm{g.s.} + 430\,\mathrm{keV})\right) n$ scattering at $110\,\mathrm{MeV}$ and $250\,\mathrm{MeV}$ incident proton energy is shown in Fig. 7.25. The mean-square radius $\langle r^2 \rangle$ is estimated from Ref. [182] to be $\langle r^2 \rangle = 15.75\,\mathrm{fm}^2$.

Finally, the distribution is integrated in spherical coordinates in the low-momentum region up to the angle $\theta_{\mathrm{lab}} = 40\,\mathrm{mrad}$. The total cross section is $\sigma_n = 0.1659(58)\,\mathrm{mb}$ and $0.1625(45)\,\mathrm{mb}$ for $110\,\mathrm{MeV}$ and $250\,\mathrm{MeV}$, respectively.

7.7.3 Experimental Details

The experiment was performed in the same campaign as the ^{28}O experiment at SAMURAI. The secondary proton beam with an intensity of about $1\,\mathrm{MHz}$ is produced from a ^{48}Ca primary beam in BigRIPS and transported to the SAMURAI setup. The last defining dipole magnet in the two BigRIPS settings has a magnetic rigidity set-value of $B\rho_{D7} = 1.5913\,\mathrm{T\,m}$ and $2.4628\,\mathrm{T\,m}$ for the "$110\,\mathrm{MeV}$" and "$250\,\mathrm{MeV}$" runs, respectively. The resulting proton kinetic energy at the center of the target is $109.1\,\mathrm{MeV}$ and $252.7\,\mathrm{MeV}$.

Although the energy-loss in the beamline is included in the energy value, it cannot be evaluated event-wise. The reason is that the BigRIPS in-beam detectors were not active during the production runs because of the high beam intensity which exceeded $1\,\mathrm{MHz}$ in BigRIPS at early foci. However, the spread of the beam-momentum, evaluated with `LISE++` [173], is as small as $7\,\mathrm{MeV}/c$ (FWHM) so that this information is not of importance and in the end only the separate neutron ToF measurement is needed.

Due to the high beam intensity, the gaseous drift chambers were also not powered up. The used in-beam and high-intensity stable detectors at SAMURAI are the SBTs, which deliver the reference start time, and two veto detectors in-front of the target. The veto detectors are $1\,\mathrm{cm}$ thick plastic-scintillation detectors with a hole diameter of $3\,\mathrm{cm}$ and as such replace the beam tracking. The detectors are readout on the left and right end by a PMT. The holes of the detector are constructed to limit the spatial distribution of the beam on the target. When the veto detector creates a signal, the event is rejected because the proton does not match the acceptance. The position of the veto detectors and of the solid target are labeled in Fig. C.1, the target-NeuLAND distance is $10\,935\,\mathrm{mm}$.

The target is made out of four sheets of natural lithium that are packed in an aluminized plastic bag in argon atmosphere to prevent them from oxidization. The natural lithium has an admixture of $7.6\,\%$ of ^{6}Li besides ^{7}Li. The area density is determined from mass and size measurement to $1.046(14)\,\mathrm{g/cm^2}$.

The unreacted protons are strongly bent in the SAMURAI dipole magnet under a magnetic field of $B = 1.75\,\mathrm{T}$ and $2.9\,\mathrm{T}$ that correspond to typical experimental conditions. This means on the other hand, the protons do not leave the exit window of SAMURAI but are dumped in the yoke and partly hit the NINJA detector that is mounted in the vacuum chamber of the magnet and was commissioned in this experiment.

The neutrons are detected in NeuLAND and NEBULA where the reaction trigger to read out the data combines: `Beam & BxNeuLAND & BxNEBULA`. In order to increase the lifetime of the DAQ the single beam trigger is downscaled by a factor of 2000. Only every 2000th event, counting independently of deadtime locking, that produces a beam-trigger signal releases a downscaled-beam trigger signal that as a result can trigger the event readout.

7.7.4 Analysis

The analysis method of extracting the number of detected neutrons is discussed in the following.

First, the beam conditions are evaluated where only events are considered that do not cause pile-up in the SBTs and do not trigger the beam-veto detector. The pile-up events are caused by the high beam intensity but are rejected by checking the time and energy-loss signal in the SBTs. The SBTs are readout with a multi-hit capable TDC so that only events with a single recorded time signal are considered. In addition, the energy-loss signal is used to discriminate pile-up events when two or more protons arrive in the same beam bunch that cause a signal twice as large. In the

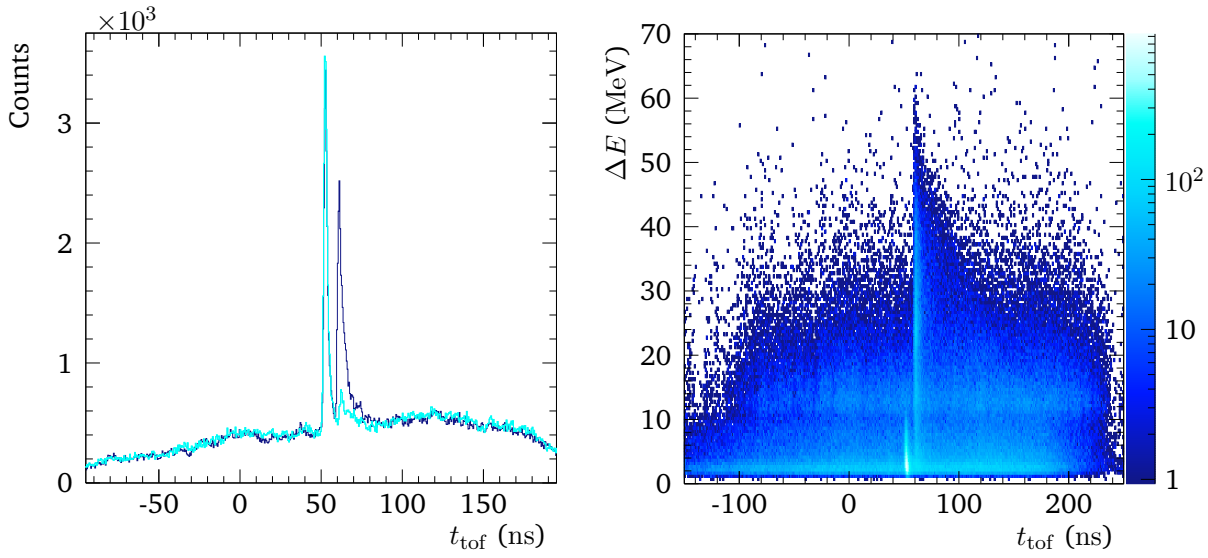

Figure 7.26: NeuLAND raw data from efficiency measurement in $250\,\mathrm{MeV}$ case. (a) Time-of-flight spectrum without any condition. The data with target in blue and without target in cyan, normalized to the incoming proton number. The peak at around $65\,\mathrm{ns}$ corresponds to the response of quasi-monoenergetic neutrons, the rest is background. The strong peak at around $55\,\mathrm{ns}$ is background and arises from dumped protons. (b) The time-of-flight spectrum vs. energy loss for the measurement with target. The background peak causes only a small energy loss.

same way, beam impurities with higher nuclear charge would be eliminated although the beam was expected to be pure.

The neutron response is detected in NeuLAND and NEBULA where a single neutron usually causes multiple hits – called crosstalk. For each hit the ToF and energy-loss is measured and analyzed. A raw experimental spectrum is shown in Fig. 7.26. A strong contribution from background events is recognized due to the high-beam intensity and the long readout-time window of $1\,\mu\mathrm{s}$ for NeuLAND but also due to the dumped unreacted protons. The latter causes also a particular γ-peak in the ToF spectrum that appears a few nanoseconds earlier.

It is assumed that the first hit in terms of ToF that in addition crosses a certain energy-loss threshold determines the neutron properties. Events with an interaction in the NeuLAND veto are rejected from the beginning. The so called “first hit” is the interaction with the shortest ToF in a list of all hits. When a hit happens first in NEBULA it is not counted. The ToF is determined from the target to the measured interaction point in the detector. Knowing the position and the ToF, the kinetic energy of the neutron is determined where neutrons are rejected whose scattering angle is larger than $40\,\mathrm{mrad}$.

The background contributions are determined in a separate measurement, which is performed and analyzed under the same conditions, but without a lithium target. At the target position only the plastic bag, in which the target was placed before, is inserted for the measurement. The

spectra without ^{nat}Li target, cf. Fig. 7.26a, need to be normalized and subtracted from the one with target inserted. The different trigger patterns are counted for the normalization purpose. The following single triggers are of relevance in the analysis

- Beam DS (Trig 0),
- Beam$\times$NeuLAND (Trig 4),
- and the coincidence: Beam(DS) & Beam$\times$NeuLAND.

Those events including the Beam DS trigger are counted multiple according to the downscaling factor.

The following paragraph describes the difficulties that are encountered during the analysis concerning the DAQ and the downscaling. The downscaling is applied in the trigger-selector GTO. Independently of the lifetime, the beam trigger that is the coincidence from the SBT signals is incremented and when a multiple of the downscaling factor is reached, the Beam DS trigger is sent out.

The applied downscale factor is checked from recorded scaler data. The ratio of the raw beam triggers to the downscaled-beam triggers must equal the downscaling factor but deviations of up to $3\,\%$ from the set value are found. It was ensured that the scaler itself worked properly. Eventually, an effective downscaling factor $\mathrm{DS}_{\mathrm{eff}}$ is introduced for the normalization. The effective downscale factor is determined for each run separately from the scaler values.

It is worth noting that the lifetime of the DAQ does not need to be considered no matter downscaling is applied or not. For the normalization, the number of protons that hit the target within the active lifetime gate of the DAQ is the number of interest. The downscaled beam trigger is produced independently of the deadtime locking but this trigger needs to lie within the active gate to trigger the data readout. This means, every single beam-trigger has the same probability as the downscaled beam-trigger to be recorded as the incoming proton (given that the lifetime does not change). In other words, for all the different triggers that cause the same lifetime, all the protons have the same probability to produce a neutron and thus just the recorded events must be counted and in case be multiplied with the downscale factor.

However, it is found that depending on which trigger causes the readout, the lifetime is slightly different. For events with Beam$\times$NeuLAND the deadtime is larger, possibly because the data size transmitted might become larger. The lifetime of the single triggers is calculated from the particular triggers that are produced in the GTO relative to those triggers counted in the recorded experimental data where, of course, no conditions are applied. The lifetime difference between Beam(DS) and Beam$\times$NeuLAND is in the order of $7\,\%$. This effect is corrected for with the factor $\mathrm{LT}_{\mathrm{corr}}$, otherwise a bias for events without a signal in NeuLAND would be introduced in the

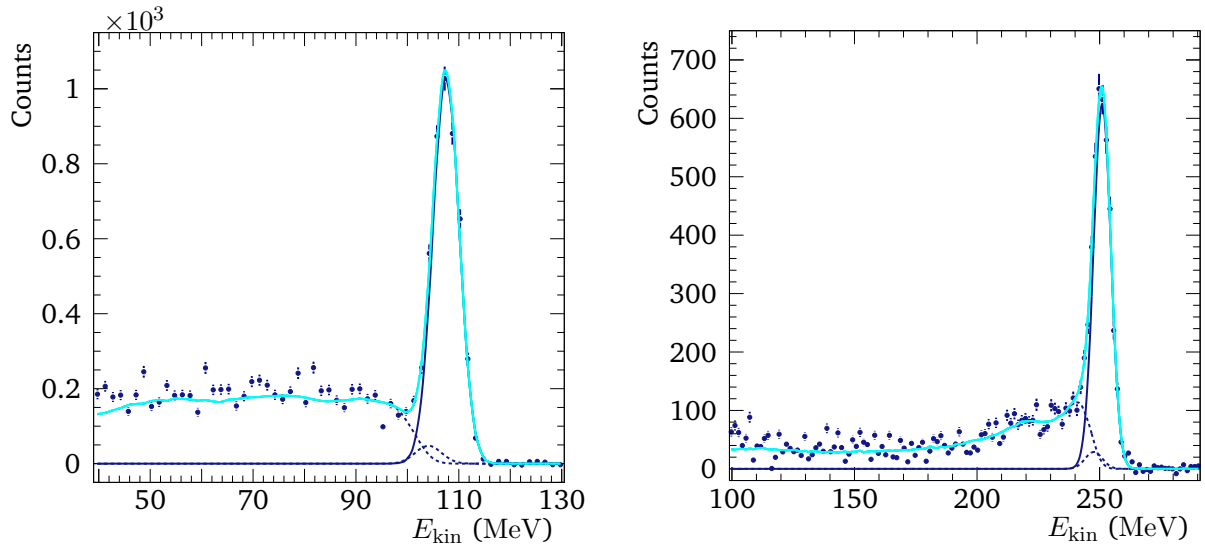

Figure 7.27: NeuLAND neutron kinetic-energy spectrum in the efficiency measurement after background subtraction and acceptance cut. The spectrum is fit with a Gaussian function for the quasi-monoenergetic neutron peak (blue line), with the data from Y. Iwamoto [181] for the tail region, and with the contribution for target impurities (dashed lines). (a) Quasi-monoenergetic neutrons at $107.5\,\mathrm{MeV}$, and (b) $251.0\,\mathrm{MeV}$.

normalization. Finally, the number of protons is calculated based on the number of triggers as

$$\begin{aligned} n_{\mathrm{in}} = n(\mathrm{Trig0}) \cdot \frac{\mathrm{DS}_{\mathrm{eff}}}{\mathrm{LT}_{\mathrm{corr}}} \\ + n(\mathrm{Trig0}\,\&\,\mathrm{Trig4}) \cdot \mathrm{DS}_{\mathrm{eff}} \\ + n(\mathrm{Trig4}). \end{aligned} \tag{7.25}$$

This is done for the target and empty-target runs where the spectrum for the empty-target run is scaled with $n_{\mathrm{in}}^{\mathrm{tgt}}/n_{\mathrm{in}}^{\mathrm{notgt}}$ and subtracted from the spectrum taken with target.

The resulting kinetic-energy spectra of one-neutron events are shown in Fig. 7.27. The same characteristics as in the spectra measured at RCNP, cf. Fig. 7.24, but with worse resolution are seen – a strong peak representing the quasi-monoenergetic neutrons and a tail region. In addition, the γ-ray spectrum in coincidence with the monoenergetic neutrons is measured, see Fig. 7.28, confirming the population of the excited state in ^{7}Be with experimentally $E_\gamma = 424(7)\,\mathrm{keV}$. Next, the number of the quasi-monoenergetic neutrons n_{det} is determined from the peak-events.

These peak neutrons overlap with the neutron-background region. In order to disentangle both contributions, the RCNP data at zero-degree scattering for $100\,\mathrm{MeV}$ and $246\,\mathrm{MeV}$, which are provided by Y. Iwamoto [187], are adduced, but below $40\,\mathrm{MeV}$ and $100\,\mathrm{MeV}$, respectively, the agreement is poor. These high-statistic data with better resolution are taken for excitation energies larger than $3.5\,\mathrm{MeV}$ (0° scattering in c. m.), smeared out with the experimental resolution

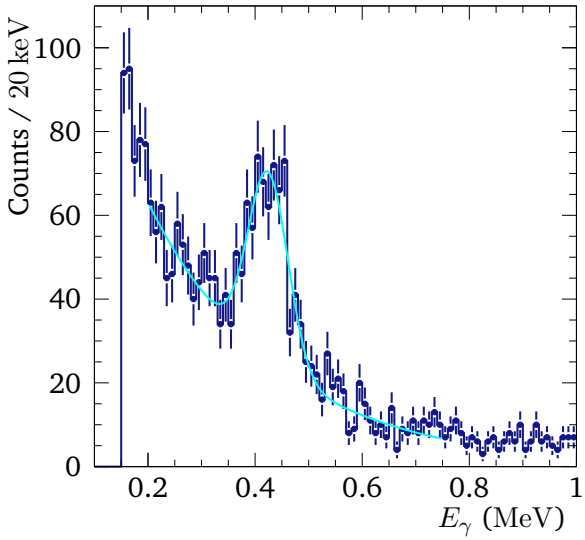

Figure 7.28: Coincident γ-ray spectrum of ^{7}Be with the quasi-monoenegetic neutrons showing the population of the excited state at $E_\gamma = 424(7)\,\mathrm{keV}$.

at SAMURAI and used in a fit to the data. The energy resolution is simply determined from the standard deviation of the monoenergetic neutron peak, $2.5\,\mathrm{MeV}$ and $3.5\,\mathrm{MeV}$ respectively, but considering the incoming-beam momentum width.

Another contribution to the spectrum is the charge-exchange reaction on ^{6}Be which is an admixture in the $^{\mathrm{nat}}$Li target. The reaction Q value of $p\left(^{6}\mathrm{Li}, ^{6}\mathrm{Be}\right) n$ is $-5.071\,\mathrm{MeV}$. Knowing the Q value and the relative contribution of ^{6}Li in the target, while assuming the same reaction cross section as for ^{7}Li, all parameters to determine the neutron peak from ^{6}Li are fixed relative to ^{7}Li.

Three contributions are fit simultaneously to the experimental spectrum, see Fig. 7.27: two Gaussian functions for the monoenergetic neutron peak mainly from the $p + ^{7}\mathrm{Li}$ reaction, and relative to this from $p + ^{6}$Li, while the tail region is described by the RCNP data. In addition, the fit region is limited to not less than $30\,\mathrm{MeV}$ from the neutron-peak energy to cope with different energy-loss thresholds. The integral of the Gaussian function determines n_{det}.

7.7.5 Results

With the results from the previous section the one-neutron detection efficiency $\epsilon_{1n} = n_{\mathrm{det}}/n_{\mathrm{in}}$ is calculated for the NeuLAND demonstrator from the zero-degree scattering $p\left(^{7}\mathrm{Li}, ^{7}\mathrm{Be}\right) n$ at $107.5\,\mathrm{MeV}$ and $251.0\,\mathrm{MeV}$ neutron kinetic energy. The resulting efficiency is $\epsilon_{1n} = 29.8(12)\,\%$ ($107\,\mathrm{MeV}$) and $26.9(9)\,\%$ ($251\,\mathrm{MeV}$) for an energy-loss threshold of $7\,\mathrm{MeV}$. It is noted that the largest contribution to the uncertainty originates from the systematic uncertainty of the zero-degree cross section.

Next, ϵ_{1n} is studied as function of the energy-loss threshold ΔE, the behavior is shown in Fig. 7.29. It is noted that the experimental data are not corrected for PMT saturation but the sim-

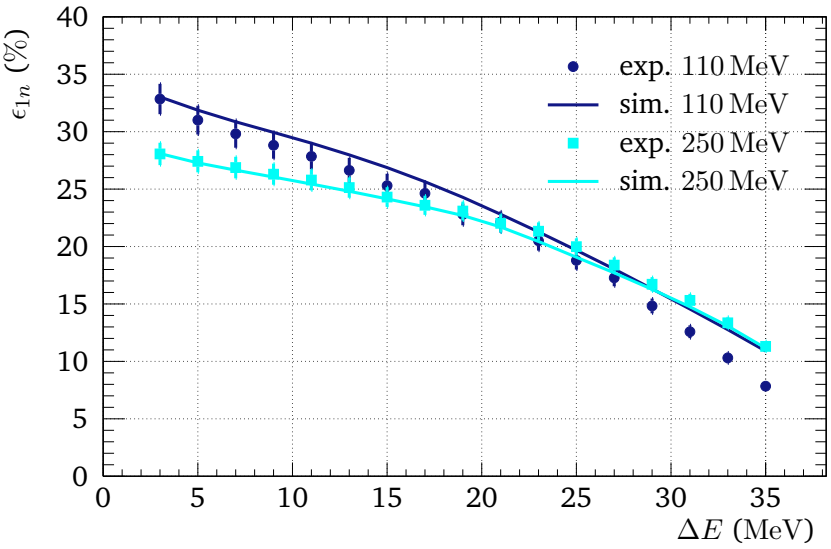

Figure 7.29: One-neutron detection efficiency ϵ_{1n} of the NeuLAND demonstrator at $110\,\mathrm{MeV}$ and $250\,\mathrm{MeV}$ comparing experiment and simulation as function of the energy-loss threshold ΔE.

ulation includes this effect. The interaction probability per centimeter is 9.9×10^{-3} and 8.2×10^{-3} for $110\,\mathrm{MeV}$ and $250\,\mathrm{MeV}$, respectively, at $\Delta E > 3\,\mathrm{MeV}$ according to

$$\epsilon = 1 - (1 - p)^n. \tag{7.26}$$

Scaling ϵ_{1n} of the NeuLAND demonstrator to the thickness of NEBULA ($48\,\mathrm{cm}$ thick plastic scintillator) with the interaction probability results in $\epsilon_{1n} = 31.8(11)\,\%$ for $250\,\mathrm{MeV}$ (and $\Delta E \geq 6\,\mathrm{MeV}$). This value is within the uncertainty comparable to the result of $\epsilon_{1n} = 32.5(9)\,\%$ obtained for NEBULA at $200\,\mathrm{MeV}$ [158]. For increasing ΔE, the efficiency ϵ_{1n} decreases as expected, especially for a threshold value close to the "proton peak" the efficiency decreases even stronger. The "proton peak" refers to the energy-loss of protons from neutron-proton (forward) elastic scattering in the neutron detector with large momentum transfer.

The absolute values and the behavior along ΔE are compared to simulations for both settings. In the simulation, only a monoenergetic neutron beam is produced at the target position with an angular parametrization as in Eq. 7.22. The hits detected in NeuLAND and NEBULA are analyzed in the same way as the experimental data. The results for $110\,\mathrm{MeV}$ and $250\,\mathrm{MeV}$ are shown together with the experimental values in Fig. 7.29.

In both cases, the behavior of ϵ_{1n} depending on ΔE is reproduced by the simulation, except for a large energy loss compared to the neutron energy of $110\,\mathrm{MeV}$. The absolute values agree within the uncertainty for the $250\,\mathrm{MeV}$ setting but in case of $110\,\mathrm{MeV}$ the results from the simulation lie consistently above the experimental data. This result supports the quality of the simulation[†], as applied and discussed for a physics case in Sec. 7.6.2. The results are summarized in Table 7.3.

[†]Ref. [178] compares different physics lists, but to preliminary exp. data

Table 7.3: Results from the one-neutron detection-efficiency experiment for the NeuLAND demonstrator at two different energies.

		Setting	
		110 MeV	250 MeV
$B\rho_{D7}$	(Tm)	1.5913	2.4628
p kin. energy	(MeV)	109.1	252.7
σ_0^{lab}	(mb/sr)	35.04(123)	35.45(97)
ϵ_{1n} ($\Delta E > 5\,\mathrm{MeV}$)	(%)	31.0(13)	27.4(10)
ϵ_{1n} (sim.)	(%)	31.9	27.3

In addition, this experiment can be used to investigate and determine conditions for the neutron clustering and crosstalk analysis because it provides true one-neutron events. However, due to strong background, another experimental one-neutron channel is presented above in Sec. 7.6. The $p\left(^7\mathrm{Li}, ^7\mathrm{Be}\right)$ measurement shows similar results, see also Refs. [158, 179].

In summary, the one-neutron detection efficiency has been determined experimentally for the NeuLAND demonstrator at two particular energies. Eventually, absolute cross sections can be obtained for other experiments that have been performed at SAMURAI using the NeuLAND demonstrator . The simulations and used physics list agree with the experimental results in the particular energy regime. This does not mean that it also applies as good at higher energies like $600\,\mathrm{MeV}$ or $1000\,\mathrm{MeV}$ that are available at GSI/FAIR where NeuLAND will be used in the future. It will be necessary to perform a particular calibration experiment at higher energies there. Another suitable reaction is the ^{2}H breakup on a proton target to produce neutrons, where the charged particles are tracked.

Chapter 8

Results and Discussion

This chapter discusses the results of the spectroscopy of ^{30}F & ^{29}F. First, the one-neutron decay channel of ^{30}F is analyzed and discussed in terms of shell structure. The analysis of ^{29}F follows, in particular its two-neutron unbound states and the decay kinematics which is analyzed in Jacobi coordinates. Together with that, ^{28}F is investigated. The resulting decay scheme is compared to theory calculations in the end.

8.1 Spectroscopy of ^{30}F

As described in Sec. 3.4, little is known about ^{30}F. The results presented here provide the first spectroscopic information about ^{30}F. The proton-knockout reaction ^{31}Ne$(p, 2p)$ is used ($S_p \approx 24.22\,\mathrm{MeV}$) to populate ^{30}F that itself is neutron unbound ($S_n < 0$) and decays into ^{29}F$+n$. Those two reaction products are measured together with the knockout protons.

8.1.1 Relative-Energy Analysis

Eventually, the invariant mass, cf. Sec. 4.4, is reconstructed from the measured neutron and fragment momenta, while the relative energy E_{fn} is calculated using the masses from Ref. [23]. The relative-energy spectrum is shown in Fig. 8.1, on the left-hand side NeuLAND and NEBULA data are combined where one neutron is reconstructed, see Sec. 7.6, and no explicit condition on the number of reconstructed tracks in MINOS is applied. The statistics is in general limited because of the low ^{31}Ne incoming-beam intensity. The right-hand side spectrum in Fig. 8.1 includes only NeuLAND data and two reconstructed tracks in MINOS from the $(p, 2p)$ reaction, the track's minimum distance at the vertex is smaller $45\,\mathrm{mm}$. Figure 8.2 shows the same data but with a broader binning.

One resonance structure at $\sim 500\,\mathrm{keV}$ can be identified. It can be described with the following approach. In the naive shell-model picture, the neutron ground-state configuration corresponds

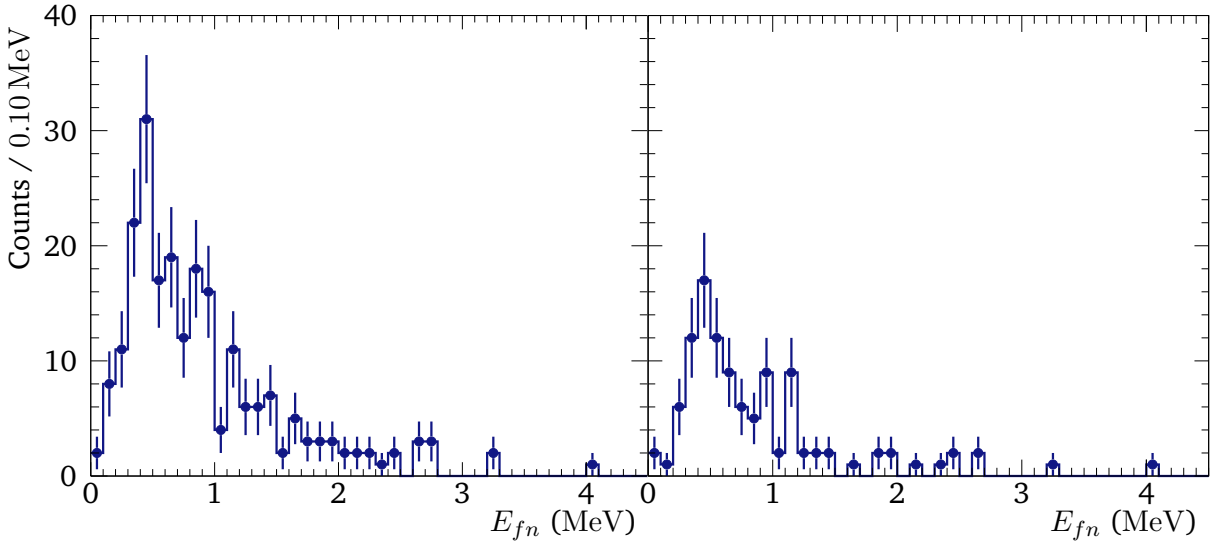

Figure 8.1: Relative-energy spectrum for ^{30}F from ^{31}Ne$(p, 2p)^{29}$F$+n$, obtained with different conditions. Left: NeuLAND and NEBULA data combined and no condition on the track reconstruction in MINOS. Right: Only NeuLAND data and two tracks reconstructed in MINOS for the $(p, 2p)$ reaction.

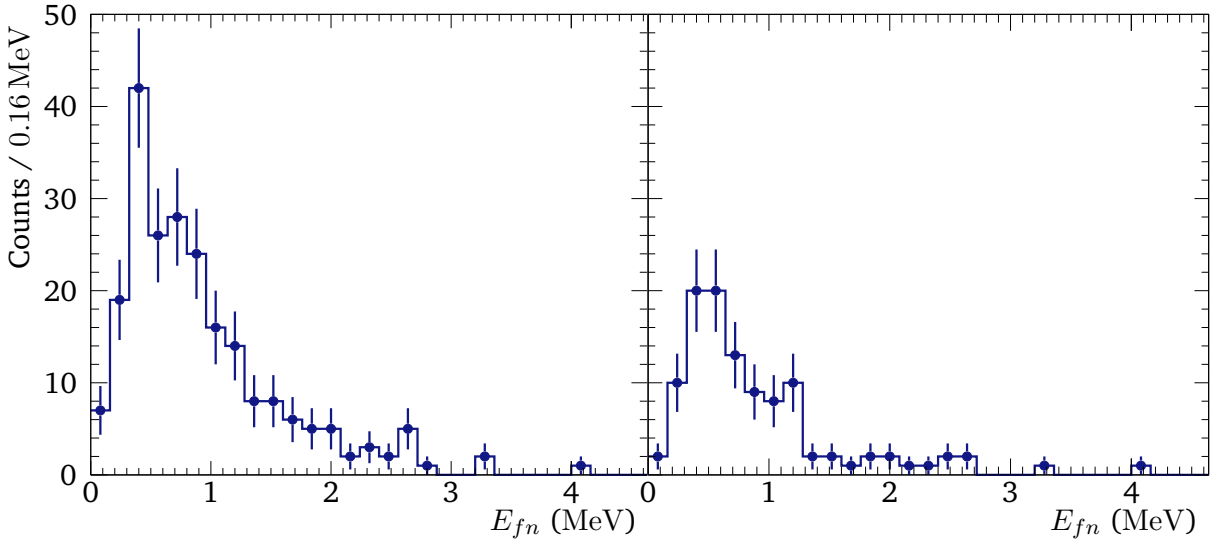

Figure 8.2: Same as Fig. 8.1 but with broader binning of $160\,\mathrm{keV}$.

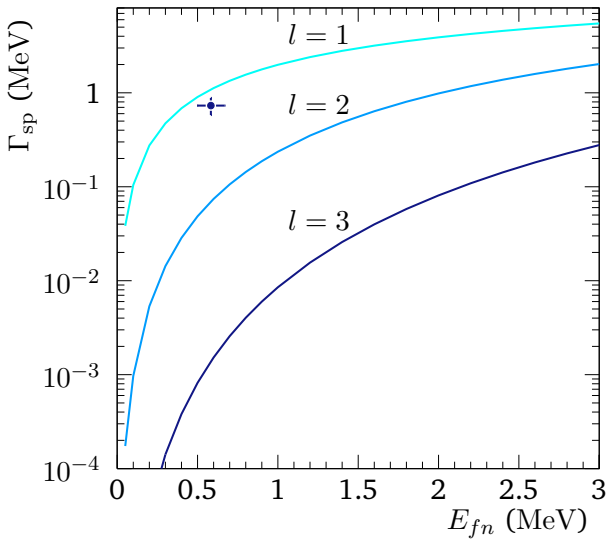

Figure 8.3: Single-particle width Γ_{sp} for ^{30}F and different angular momenta l, calculated with Eq. 4.42. The experimentally obtained resonance position and width is depicted by the blue marker, particularly with $E^r_{fn} = 0.583(85)\,\mathrm{MeV}$ and $\Gamma_r = 0.731(151)\,\mathrm{MeV}$.

to a $1f_{7/2}$ neutron above a closed sd shell. The resonance is described by the single-level energy-dependent Breit-Wigner distribution as discussed in Sec. 4.5. It reads

$$\frac{\mathrm{d}\sigma}{\mathrm{d}E_{fn}} \sim \frac{\Gamma_l\left(E_{fn}\right)}{\left(E^r_{fn} + \Delta_l\left(E_{fn}\right) - E_{fn}\right)^2 + \left(\Gamma_l\left(E_{fn}\right)/2\right)^2}, \tag{8.1}$$

with the partial width

$$\Gamma_l(E_{fn}) = \Gamma_r \cdot \frac{P_l(E_{fn})}{P_l(E^r_{fn})}, \tag{8.2}$$

and the shift

$$\Delta_l\left(E_{fn}\right) = \Gamma_r \cdot \frac{S_l(E^r_{fn}) - S_l(E_{fn})}{2P_l(E^r_{fn})}, \tag{8.3}$$

where variables annotated with r correspond to the value at the resonance position.

Referring to the single-particle picture, see Sec. 4.5, the resonance width Γ_r cannot be larger than the single-particle width Γ_{sp}, which depends on the angular momentum l of the decay neutron. Figure 8.3 shows Γ_{sp} as function of the relative energy E_{fn} for angular momenta $l = 1, 2,$ and 3. The single-particle width is calculated according to Dover et al. [123] using Eq. 4.42. The critical input is the value of the channel radius a. This quantity is extracted from comparison to shell-model calculations. The Γ_{sp} is compared to calculations by Fortune et al. [188, 189]. For their calculated width for ^{15}Be [189], the channel radius must be $a = 3.24\,\mathrm{fm}$ to reach agreement

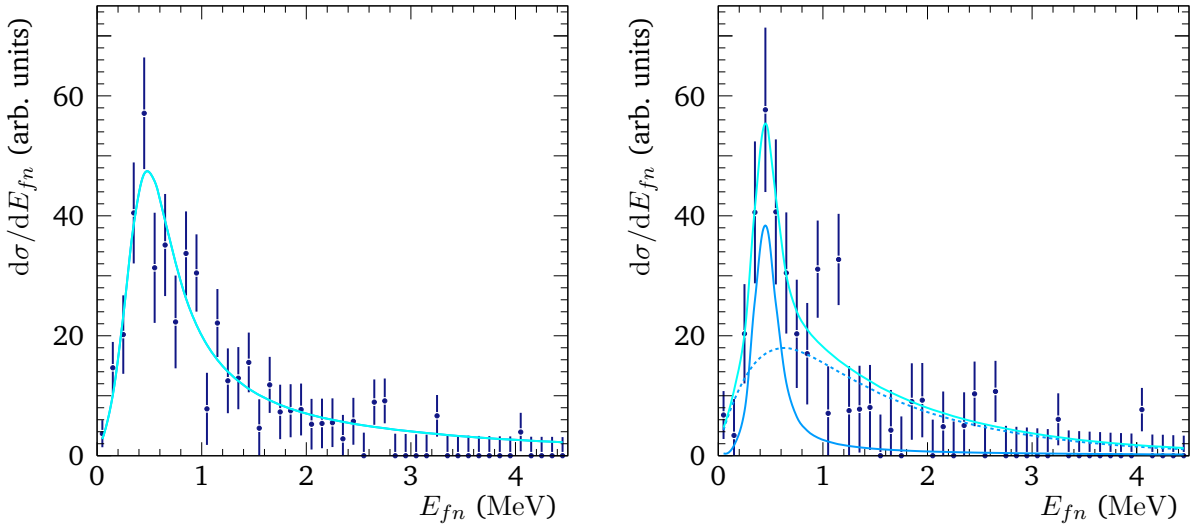

Figure 8.4: Fit result of E_{fn} for ^{30}F. (a) One Breit-Wigner resonance for $l = 1$ ($\Delta_l(E_{fn}) = 0$). The data are corrected for the neutron efficiency and acceptance, energy bins in $0.1\,\mathrm{MeV}$. The data include NeuLAND and NEBULA, the fit result is $E^r_{fn} = 583(37)\,\mathrm{keV}$ and $\Gamma_r = 730(151)\,\mathrm{keV}$. (b) Fit result with one Breit-Wigner resonance (solid blue line) and a non-resonant background (dashed line). The data include only NeuLAND, the fit result is $E^r_{fn} = 461(25)\,\mathrm{keV}$ and $\Gamma_r = 136(56)\,\mathrm{keV}$.

with the Γ_{sp} calculation in Eq. 4.42. It is assumed that it scales according to $a = a_0 A^{1/3}$ where a_0 is extracted from the previous result to be $1.345\,\mathrm{fm}$. Using this value gives agreement with the results for other nuclei in Refs. [188, 189]. Thus, the calculated channel radius for ^{30}F is $a = 4.13\,\mathrm{fm}$. A phenomenological way to estimate the channel radius is to use

$$a = 1.4\,\mathrm{fm} \cdot \left(A^{1/3} + B^{1/3}\right), \tag{8.4}$$

with A and B the mass number of the partners that form the resonance. This results in $a = 5.70\,\mathrm{fm}$. The nuclear radius compared to this is $R \approx 1.2\,\mathrm{fm}(A+B)^{1/3} = 3.73\,\mathrm{fm}$, and it is used with Eq. 4.44.

First, the relative-energy spectrum is fit with a single energy-dependent Breit-Wigner function for $l = 3$ but without shift function, $\Delta_l(E_{fn}) = 0$, and with channel radius $a = 4.13\,\mathrm{fm}$. The resulting width exceeds the expected Γ_{sp} multiple times. This implies, if there is only one resonance, that the f wave is not dominant. Next, a $l = 1$ dependent Breit-Wigner is used. The p wave is the next most likely contribution for an island-of-inversion nucleus. The fit result is shown in Fig. 8.4a.

The fit minimization follows the procedure described in App. B.2, which is especially suited for low-statistics data where the uncertainties are taken from the fitted curve. In a least-squares approach the trial distributions are fit simultaneously to the experimental spectrum until convergence is reached. In each minimization step, position, width, and amplitude of the Breit-Wigner

resonance are varied and convoluted with the experimental response of the detectors using the response matrix from Sec. 7.6.2. After the fit process, the spectrum is corrected for efficiency and acceptance according to the curves as shown in Fig. 7.23a but calculated for the particular experimental and analysis conditions. The integral of the resonances is proportional to the cross section given that the detection efficiency for reacted and unreacted beam is the same.

The fit results are $E_{fn}^{r} = 583(37)\,\mathrm{keV}$ and $\Gamma_r = 730(151)\,\mathrm{keV}$ for NeuLAND and NEBULA data together (Fig. 8.4a). Taking only NeuLAND data into account results in $E_{fn}^{r} = 575(50)\,\mathrm{keV}$ and $\Gamma_r = 768(216)\,\mathrm{keV}$. Both results agree well. The fit region goes from $0.2\,\mathrm{MeV}$ to $4.5\,\mathrm{MeV}$ and the reduced chi-square values are $\chi^2_{\mathrm{red}} = 0.88$ and $\chi^2_{\mathrm{red}} = 0.84$, respectively. The fit is repeated including Δ_l. The resonance energy becomes $E_{fn}^{r} = 540(113)\,\mathrm{keV}$ ($\Gamma_r = 1013(587)\,\mathrm{keV}$) and $E_{fn}^{r} = 527(39)\,\mathrm{keV}$ ($\Gamma_r = 1122(429)\,\mathrm{keV}$) for the two data sets. The results of the two line shapes agree within uncertainty, whereas the first provides smaller uncertainties. Thus, the systematic uncertainty might be quoted as difference in resonance energy to be $48\,\mathrm{keV}$.

It cannot be ruled out that there exist unresolved resonances in the E_{fn} spectrum. In order to capture those contributions, an additional background is fit to the spectrum for test purposes. A shape like $\mathrm{d}\sigma/\mathrm{d}E_{fn} = \mathrm{erf}(a \cdot E_{fn}) \cdot \exp(-b \cdot E_{fn})$ is used to model non-resonant contributions, as applied in Ref. [190]. The choice of the distribution is discussed in more detail in the next section. The fit results for only NeuLAND data is shown in Fig. 8.4b, the values for a $l = 1$ resonance are $E_{fn}^{r} = 461(25)\,\mathrm{keV}$ with $\Gamma_r = 136(56)\,\mathrm{keV}$, whereas it is $E_{fn}^{r} = 457(26)\,\mathrm{keV}$ with $\Gamma_r = 148(255)\,\mathrm{keV}$ for the combined NeuLAND and NEBULA data. The width is larger than the pure detector response. The goodness of the fit is $\chi^2_{\mathrm{red}} = 0.89$ and $\chi^2_{\mathrm{red}} = 0.85$, respectively.

8.1.2 Gamma-ray coincident Decay

In addition, possible coincident γ-ray decays in ^{29}F with the ^{30}F resonance are analyzed to determine the excitation energy, cf. Eq. 4.29. Figure 8.5 shows the coincident γ-energy spectrum, independent of the population mechanism. The background level is shown in the same plot normalized to the number of reactions. It is deduced from an experimental $(p, 2p)$-reaction channel where no coincident γ-ray is expected, namely $^{29}\mathrm{F}(p, 2p)^{24}\mathrm{O}{+}n$. There is no significant peak (larger 3σ) found in the spectrum, in particular not at $E_\gamma \sim 1080\,\mathrm{keV}$ for the known state. There exist also no particular relative-energy value that is statistically favored when investigating gates on different γ-ray energy regions. In summary, there is no significant coincident γ-ray decay branch found and the resonance energy seems to correspond to the ground-state energy of ^{30}F.

8.1.3 Conclusions

Independently of a prediction from theory, the obtained experimental spectrum gives no reason to describe it with more than a single resonance. In this case, ^{30}F is unbound relative to ^{29}F by $583 \pm 37(\mathrm{stat}) \pm 48(\mathrm{sys})\,\mathrm{keV}$. Thus, using the masses from Ref. [23] the nuclear binding energy

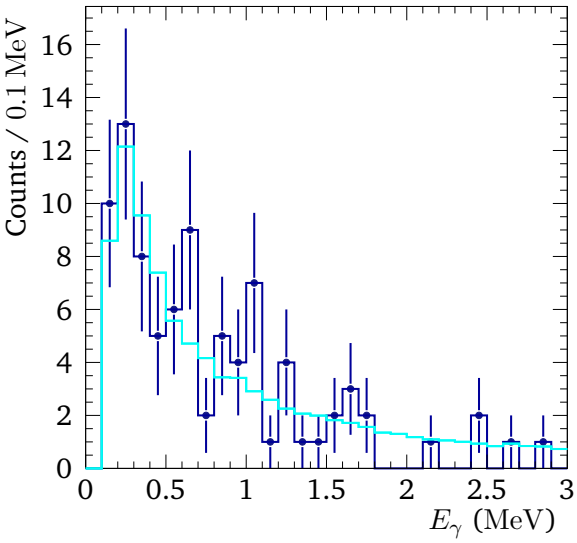

Figure 8.5: Gamma-ray spectrum in coincidence with ^{30}F. The background level is obtained from ^{29}F$(p, 2p)^{24}$O$+n$, depicted in cyan line. No significant peak is found.

of ^{30}F is $BE(9, 21) = -186.294(532)$ MeV.

The behavior of the one-neutron separation energy S_n along the fluorine isotopic chain is shown in Fig. 8.6, where the result obtained for ^{30}F is inserted, the values for ^{27}F and ^{28}F are also determined in this experiment, obtained in Ref. [60]. The results agree within uncertainty with the prediction of the atomic-mass evaluation 2016* [23]. A definite answer on the binding limit of the fluorine isotopes cannot be extracted. Information for ^{31}F is essential to make predictions whether ^{33}F is bound or not, whereas the fact that ^{32}F is unbound is simply derived from the trend and expected neutron-neutron pairing. A comparison to sodium or neon at $N = 24$ is also not possible because experimental data are not available. In the two-neutron separation energy, Fig. 8.6b, a plateau develops around $N = 20$. This differs from the signature of a shell closure, where typically a sharp decrease is seen, and thus hints to the characteristic of an island-of-inversion nucleus. A comparison to theory is needed to discuss the shell-gap energy.

The deduced experimental resonance width $\Gamma_r = 730(151)$ keV is now compared to the single-particle width Γ_{sp} derived using Eq. 4.42 by Dover et al. [123], as shown in Fig. 8.3. The experimental value for the single-resonance case without background contribution, Fig. 8.4a, can be seen as upper limit. The width is only in agreement with $l = 1$. Following an argumentation that can be found e. g. in Ref. [189], the spectroscopic factor S for a particular state of the decay neutron is the ratio between experimental and single-particle width,

$$S = \frac{\Gamma_r}{\Gamma_{\mathrm{sp}}(l = 1)} = \frac{730\,\mathrm{keV}}{1084\,\mathrm{keV}} = 0.67, \tag{8.5}$$

*The evaluation predicts ^{30}F to be bound although it is known that the ground state is unbound.

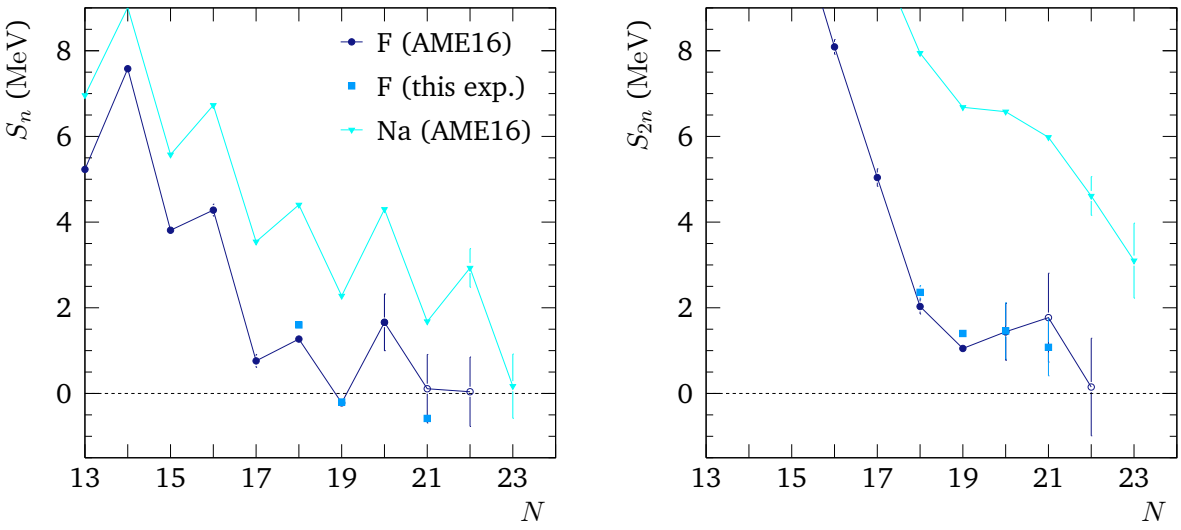

Figure 8.6: Trend of the neutron-separation energies for fluorine ($Z = 9$) and sodium ($Z = 11$) as function of neutron number, including the values obtained in this experiment, compared to the atomic-mass evaluation data (AME16) [23]. (a) One-neutron separation energy S_n, the open symbols correspond to systematic values. (b) Two-neutron separation energy S_{2n}. The values from "this exp." include two AME values for the calculation.

with channel radius $a = 4.13\,\mathrm{fm}$. Using the maximum difference in energy and width, the spectroscopic factor is $S = 0.67^{+0.31}_{-0.14}$ (and $S = 0.93$ for $\Gamma_r = 1013\,\mathrm{keV}$). As the discussion from above shows, Γ_{sp} and thus S depend on the choice of the channel radius and are model dependent quantities. When using the classical approximation for the channel radius from Eq. 8.4, the result is $S = 0.63$. Applying Eq. 4.44 with the nuclear radius gives $S = 0.37$. However, in all the calculations the width for $l = 2$ is not larger $160\,\mathrm{keV}$, Γ_{sp} is even more than two orders of magnitude lower for $l = 3$. For a $l = 3$ resonance, the width would be completely dominated by the experimental response. The results imply that the valence-neutron configuration shows substantial $l = 1$ character. The ground-state could be expanded in a simple way like

$$|^{30}\mathrm{F(g.s.)}\rangle = |^{29}\mathrm{F(g.s.)}\rangle \otimes \left\{\alpha\,|\left(\nu 2p_{3/2}\right)^1\rangle + \beta\,|\left(\nu 1f_{7/2}\right)^1\rangle + \ldots\right\}, \tag{8.6}$$

with $\alpha^2 + \beta^2 \leq 1$. When considering the width of $\Gamma_r = 148\,\mathrm{keV}$ (obtained in a fit with resonance and background) the spectroscopic factor is $S(\nu 2p) = 0.18$ with $\Gamma_{\mathrm{sp}} = 808\,\mathrm{keV}$ at $E_{fn} = 457\,\mathrm{keV}$.

The results show that the neutron p-wave contribution is present. This implies that the $1f_{7/2}$ and $2p_{3/2}$ orbitals are close in energy, as predicted in Fig. 3.2, and the occupancy of the valence neutron in the p orbital must cause a gain in correlation energy. This makes the ground state a negative-parity state $|\pi(1d_{3/2})^1\rangle \otimes |\nu(2p_{3/2})^1\rangle$. Following this argumentation, it also seems that there is a significant overlap between the structure of ^{31}Ne and ^{30}F, while both nuclei have a substantial p-wave contribution. ^{31}Ne is seen as a deformed neutron p-wave halo [191] in the

island of inversion.

Summarizing the analysis of ^{30}F, position and width of the ground-state resonance indicate that the shell structure is different from the simple shell-model picture and p-wave contributions cannot be ignored.

8.2 Spectroscopy of ^{29}F

In this section, the complete spectroscopy of ^{29}F in a proton-knockout reaction on ^{30}Ne is discussed. The SAMURAI setup allows to study bound but also unbound states. The resonances decay via two-neutron emission, $^{29}\text{F}^* \rightarrow ^{27}\text{F}+2n$, because ^{28}F itself is particle unstable in its ground state. The three-body decay is investigated in terms of Jacobi coordinates, and in this context also the spectroscopy of ^{28}F is presented. Eventually, the decay scheme is constructed and compared to theory.

8.2.1 Bound-excited States

In the decay of ^{30}F no significant decay to bound excited states is found as discussed above in Sec. 8.1. However, a previous in-beam γ-ray spectroscopy experiment found a state at $1080(18)\,\text{keV}$ in ^{29}F, cf. Sec. 3.4.

Here, a quasi-free proton-knockout reaction on the LH_2 target is used to populate excited states in ^{29}F, instead of a proton removal on a carbon target as in Ref. [81]. The coincident γ-ray spectrum measured with DALI2 from $^{30}\text{Ne}(p,2p)^{29}\text{F}$ is shown in Fig. 8.7a. It shows the Doppler-corrected γ-ray spectrum where the addback algorithm is applied, cf. Sec. 6.6 & 7.5, and all cluster multiplicities are included. Clearly, a peak is identified at around $1050\,\text{keV}$ but there is also additional strength at approx. $300\,\text{keV}$. This becomes more clear under the condition when additionally only single clusters with a single hit are allowed, only the forward hemisphere of DALI2 is considered, and a time cut is applied to suppress background, as shown in Fig. 8.7b.

In order to obtain the γ-decay energy, the spectra are fit with simulated γ-ray spectra for different energies. The simulation includes the experimental conditions, cf. Sec. 7.4, and is performed for prompt single γ-decays. The background contribution is extracted from experimental data in the same way as the channel of interest but from a reaction where no γ-decay is present, namely $^{29}\text{F}(p,2p)^{24}$O. ^{24}O with $S_n = 4.19\,\text{MeV}$ has no bound excited state. It is of advantage to use the experimental data because the response is the same, in particular residual effects from the nucleons that scatter from the QFS reaction into DALI2 are included which are not covered in the simulation.

The smallest χ^2 value is achieved for the γ-energies $E_\gamma = 1063(7)\,\text{keV}$ and $E_\gamma = 287(4)\,\text{keV}$ where the fit region is limited to $250\,\text{keV} < E_\gamma < 1500\,\text{keV}$, see Fig. 8.8. The strength below $\lesssim 250\,\text{keV}$ is not described by the contributions from the two γ-decays and the background. This could only be described with the onset of an additional background contribution at low energies

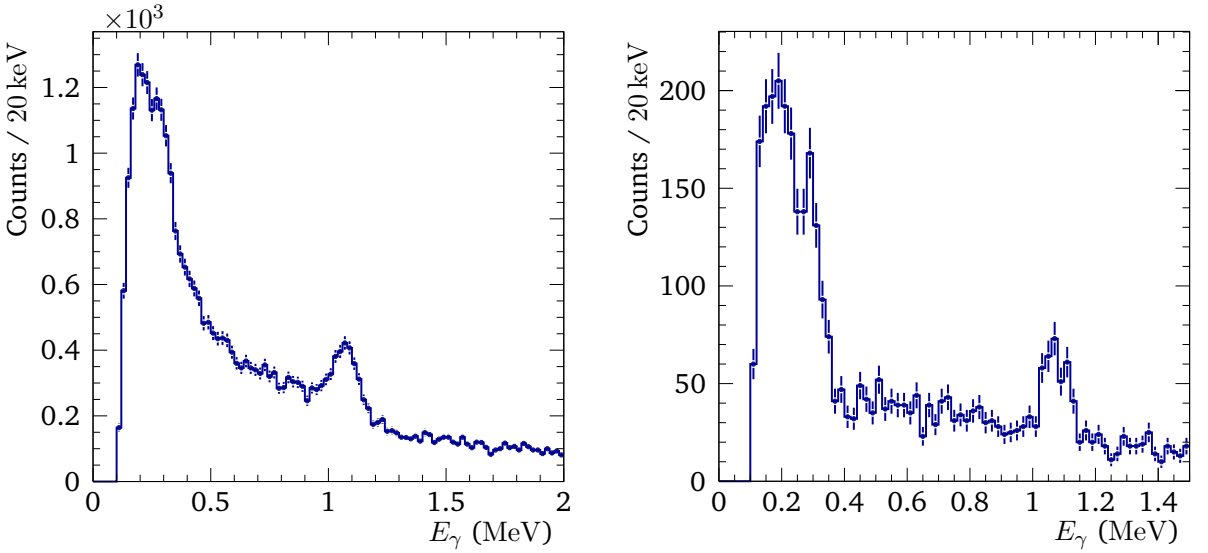

(a) (b)

Figure 8.7: Doppler corrected γ-ray spectrum of ^{29}F from the ^{30}Ne$(p, 2p)$ reaction. Peaks at $\sim 1.1\,\mathrm{MeV}$ and $\sim 0.3\,\mathrm{MeV}$ can be identified. (a) All cluster multiplicities after addback are filled in the spectrum. (b) Spectrum taking only events with multiplicity one, additional time condition, and detectors in forward direction.

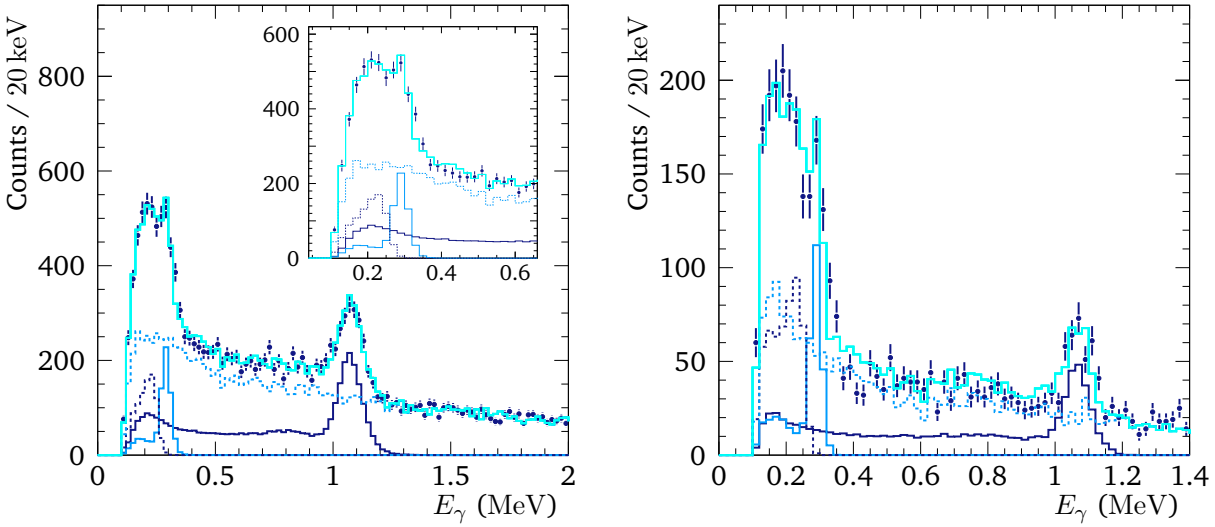

(a) (b)

Figure 8.8: Fit to Doppler-corrected γ-ray spectrum of ^{29}F in the ^{30}Ne$(p, 2p)$ reaction with the following contributions: $E_\gamma = 1063\,\mathrm{keV}$ (dark blue line), $287\,\mathrm{keV}$ (blue line), $250\,\mathrm{keV}$ and $T_{1/2} = 200\,\mathrm{ps}$ (dashed dark-blue line), and experimental background obtained from ^{29}F$(p, 2p)^{24}$O (dashed blue line). The total fit is shown by the cyan line, the blue dots are the experimental data. (a) Taking only the first reconstructed γ-cluster, the inset shows the zoom up to $650\,\mathrm{keV}$, the fit goodness is $\chi^2_{\mathrm{red}} = 1.67$. (b) Plot with the results as obtained on the left, cf. the spectrum in Fig. 8.7b.

or an additional γ-decay. Since the peak looks rather broad, it could only originate from a state with a comparably long lifetime. The resulting fit to the spectrum is shown in Fig. 8.8 with an additional decay energy of $E_\gamma = 250(20)\,\mathrm{keV}$ and a half-life of $T_{1/2} = 200(100)\,\mathrm{ps}$ where the uncertainties are of systematic character and need further studies. On the other hand, it cannot be excluded that the missing strength is only background. A small contribution could come from the charge difference between beam and ^{29}F reference beam resulting in a different bremsstrahlung spectrum [156]. A description with an exponential-background shape results in a similar conclusion where the strength is missing. It is also not a question of the threshold settings for the energy measurement. Those are set to maximum $200\,\mathrm{keV}$ in the laboratory system.

The $\gamma\gamma$-coincidence analysis does not result in a significant branching between the $1063\,\mathrm{keV}$ state via $287\,\mathrm{keV}$, the γ-ray tracking-efficiency is $\sim 16\,\%$ as obtained in the simulation. The sum-energy spectrum also does not show a peak above $1063\,\mathrm{keV}$ which means there is a state lower in energy.

In summary, the γ-spectroscopy of ^{29}F in the reaction ^{30}Ne$(p,2p)^{29}$F confirms the state at $1063(7)\,\mathrm{keV}$ that was previously measured at $1080(18)\,\mathrm{keV}$ by Doornenbal et al. [81], but also finds a new transition with energy $E_\gamma = 287(4)\,\mathrm{keV}$. So far, there is no experimental argument for distinguishing either a state at only $287\,\mathrm{keV}$ after direct population or just observing the decay energy $287\,\mathrm{keV} = 1063\,\mathrm{keV} - 776\,\mathrm{keV}$. In the latter case, the $776\,\mathrm{keV}$ state could be long-lived and it is thus not detected in DALI2. This discussion is continued in Sec. 8.2.7 in comparison to theory. Further analysis is necessary to understand the origin of the missing strength for $E_\gamma \lesssim 250\,\mathrm{keV}$. The inelastic scattering $^{29}\mathrm{F}(p,p')$ reaction can give complementary information.

8.2.2 Resonances in the Continuum

The neutron-decay channel opens at higher excitation energies and the excited states in ^{29}F* decay via two-neutron emission, $^{30}\mathrm{Ne}(p,2p)^{29}\mathrm{F}^* \rightarrow^{27}\mathrm{F}+2n$ ($S_p = 24\,160\,\mathrm{keV}$). The two-neutron separation energy is $S_{2n}(^{29}\mathrm{F}) = 1443(436)\,\mathrm{keV}$ [82].

In order to obtain the excitation energy, the invariant-mass technique, cf. Sec. 4.4, is applied. The reaction channel is unambiguously identified, the incoming beam ^{30}Ne is identified together with the scattered protons in the QFS reaction, as well as the heavy reaction fragment ^{27}F and two neutrons are tracked, cf. Sec. 7.6.

The obtained three-body relative-energy spectrum for $^{27}\mathrm{F}+n+n$ is shown in Fig. 8.9a, where exactly two reconstructed neutrons are requested in NeuLAND and NEBULA as well as two proton tracks in MINOS. Two clear resonance structures can be identified at approx. $300\,\mathrm{keV}$ and $1400\,\mathrm{keV}$. Figure 8.9b shows the separate contributions from same-wall and different-wall neutrons, the different-wall events show indeed a larger efficiency at small relative energies, cf. Eq. 7.16.

First, the possible coincidence with a prompt γ-ray decay of ^{27}F is analyzed. The final nucleus ^{27}F cannot only be populated in its ground state but also in an excited state. There is one bound

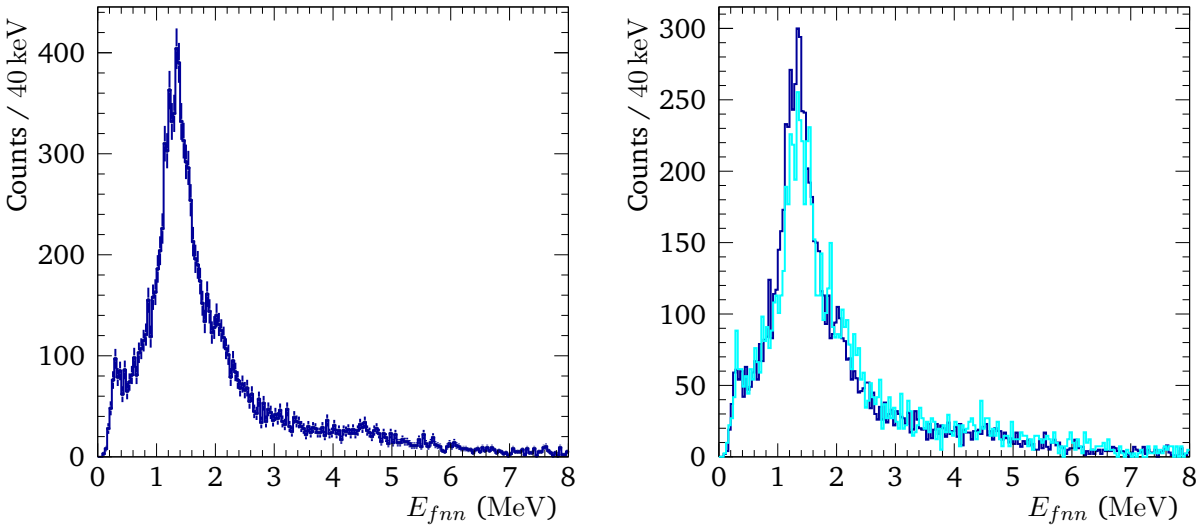

(a) (b)

Figure 8.9: (a) Three-body relative-energy spectrum for ^{29}F* in the ^{30}Ne$(p,2p)^{27}$F$+n+n$ reaction with NeuLAND and NEBULA. (b) Showing the separate contributions from same-wall (blue) and different-wall neutrons (cyan). The spectra are normalized to the blue curve.

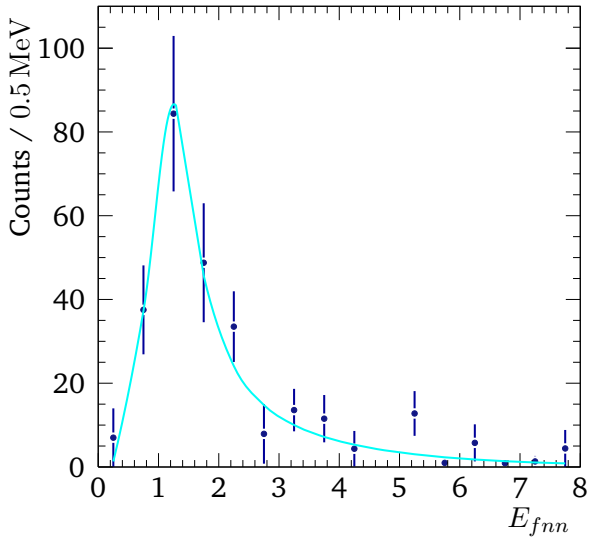

Figure 8.10: Three-body relative-energy spectrum for ^{29}F* in the ^{30}Ne$(p,2p)^{27}$F$^* + n + n$ reaction in coincidence with the γ-ray at $919\,\mathrm{keV}$ in ^{27}F. The spectrum is fit with a Breit-Wigner line shape. The resonance parameters are $E^r_{fnn} = 1253(51)\,\mathrm{keV}$ & $\Gamma^r = 1111(240)\,\mathrm{keV}$.

excited state known in ^{27}F at $E_\gamma = 919(4)\,\mathrm{keV}$ that has been measured before by Doornenbal et al. [81], cf. Sec. 3.4, and is confirmed in the experiment here, further details are given in Sec. 8.2.4. Excitations above the neutron-separation threshold in ^{27}F, i. e. the three-neutron decay channel, are not considered. The ^{29}F relative-energy spectrum that is in coincidence with the γ-ray in ^{27}F is shown in Fig. 8.10.

This E_{fnn} spectrum is obtained by analyzing the γ-spectrum for separate energy regions in the relative-energy spectrum. The relative-energy spectrum is binned in $0.5\,\mathrm{MeV}$ steps and for each segment, the coincident γ-ray spectrum is similarly analyzed as described in Sec. 8.2.1 but for the fit with a $919\,\mathrm{keV}$ state and background. The intensity of the ^{27}F* full-energy peak becomes the bin content in E_{fnn}.

The resulting E_{fnn} resonance is fit with a sequential Breit-Wigner distribution as introduced in Eq. 4.49 where angular momentum $l = 1$ is assumed, without a particular physical meaning at the moment. The obtained resonance position is $E^r_{fnn} = 1253(51)\,\mathrm{keV}$ and the width $\Gamma_r = 1111(240)\,\mathrm{keV}$ with a goodness of $\chi^2_{\mathrm{red}} = 2.10$ of the fit.

In summary, one three-body resonance is extracted in the decay of ^{29}F$^* \rightarrow ^{27}$F$^* + 2n$ that populates ^{27}F* in its bound excited state. Thus, the excitation energy of the found resonance is $E^*_{fnn} = 2172\,\mathrm{keV} = 1253\,\mathrm{keV} + 919\,\mathrm{keV}$. The resonance is later fixed in shape and intensity in the fit of the full E_{fnn} spectrum.

8.2.3 Two-Neutron Correlation

The three-body decay opens more degrees-of-freedom, see Sec. 2.3. The decay-kinematics is investigated in Jacobi coordinates in the Y-system (cf. Sec. 4.6) in terms of the fractional energy of the two-body subsystem between ^{27}F$-n$ with its relative energy E_{fn}. For different energy ranges in the ^{29}F three-body relative-energy spectrum the fractional energy $\epsilon_{fn} = E_{fn}/E_{fnn}$ is calculated, exemplary spectra are shown in Fig. 8.11 for $1.2\,\mathrm{MeV} < E_{fnn} < 1.5\,\mathrm{MeV}$ and $1.5\,\mathrm{MeV} < E_{fnn} < 1.8\,\mathrm{MeV}$, further spectra can be found in App. E.2.

All the spectra show peak structures, what is different from a phase-space or di-neutron decay, cf. Ref. [60]. The peaks are symmetric because ϵ_{fn} is normalized to E_{fnn} and a random neutron out of the two neutrons is picked for the calculation. The peak structure implies that a resonance in the decay subsystem ^{27}F$+n$ is formed. In this sequential-decay scenario, the three-body resonance decays via one-neutron emission to ^{28}F, which subsequently decays again via one-neutron emission into ^{27}F$+n$ as depicted in Fig. 2.3c. The position and width of the peaks in the fractional-energy spectrum correspond also to the resonance properties in the intermediate system. The fits are performed by L. Chulkov using Eq. 4.57 [127, 192]. The extracted resonance parameters are listed in Table 8.1. The goodness of the fits is $\chi^2_{\mathrm{red}} = 1.04$ and 1.23 for the two energy regions ($\langle E_{fnn}\rangle = 1.35\,\mathrm{MeV}$ and $1.65\,\mathrm{MeV}$), respectively.

The resolution that is used to unfold the resonance parameters from the response in the fractional-energy spectrum is obtained from simulations, similarly to Sec. 7.6.2. A sequential

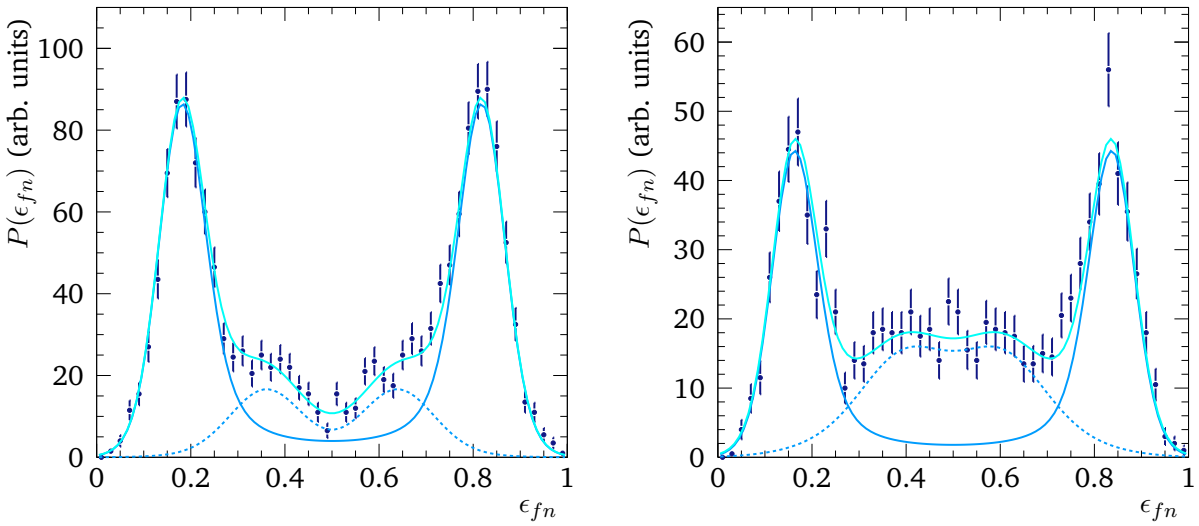

Figure 8.11: Fractional-energy spectra ϵ_{fn} of ^{29}F in Y-system for two different energy regions in E_{fnn}. Peak structures are seen in both spectra that are a signature for sequential decay via the subsystem ^{28}F. The data (blue dots) are fit with a theory for sequential decay, the total fit is depicted as cyan line. (a) Fractional energy for $1.2\,\mathrm{MeV} < E_{fnn} < 1.5\,\mathrm{MeV}$. Two contributions are fit, resulting in two intermediate resonances at $E^r_{fn} = 243(2)\,\mathrm{keV}$ (blue line) and $E^r_{fn} = 477(50)\,\mathrm{keV}$ (dashed blue line). (b) For $1.5\,\mathrm{MeV} < E_{fnn} < 1.8\,\mathrm{MeV}$ with intermediate resonances at $E^r_{fn} = 243(2)\,\mathrm{keV}$ (blue line) and $E^r_{fn} = 1027(41)\,\mathrm{keV}$ (dashed blue line).

Table 8.1: Resonance parameters (position E^r_{fn} and width Γ_r) of the intermediate ^{28}F resonances in a sequential-decay scenario as obtained from the fractional-energy spectrum ϵ_{fn} for different three-body energy regions E_{fnn} in ^{29}F. The uncertainties are statistical only.

E_{fnn} (MeV)	E^r_{fn} (keV)	Γ_r (keV)
$(1.2, 1.5]$	243(2)	59(8)
	477(9)	<50
$(1.5, 1.8]$	243(fix)	59(fix)
	1027(41)	247(161)

decay, modeled as two subsequent one-neutron phase-space decays, is simulated for a fixed three-body energy $E_{fnn} = 1.3\,\mathrm{MeV}$ and several different intermediate-resonance energies, i. e. different ϵ_{fn}. The data are analyzed in the same way as the experimental data. The width of the peaks in the reconstructed fractional energy determines the resolution. The ϵ_{fn} resolution (σ) is described by

$$\sigma(\epsilon_{fn}) = a \cdot (\epsilon_{fn})^b \cdot (1 - \epsilon_{fn})^b, \tag{8.7}$$

with the parameters $a = 0.146$ and $b = 0.612$. Here it is assumed that $\sigma(\epsilon_{fn})$ is independent of E_{fnn}.

In summary, it is found that the ^{29}F three-body decay proceeds dominantly as sequential decay through different intermediate resonances in ^{28}F for $0.9\,\mathrm{MeV} \lesssim E_{fnn} \lesssim 2.5\,\mathrm{MeV}$. For lower relative energies no definite conclusion can be made about the intermediate resonances due to low statistics. However, strong FSI between fragment and neutron are also dominate in the low-energy region. For $E_{fnn} \gtrsim 2.5\,\mathrm{MeV}$, a contribution from phase-space decay needs to be included to describe the ϵ_{fn} spectra, see Fig. E.1 in the appendix.

8.2.4 Spectroscopy of ^{28}F

The analysis in the previous section shows a sequential decay via ^{28}F. Resonances are identified at $\sim 230\,\mathrm{keV}$, $\sim 440\,\mathrm{keV}$, and $\sim 1000\,\mathrm{keV}$.

An independent way to study resonances in ^{28}F, that are may also populated in the three-body decay, is to use a direct reaction. A neutron-knockout reaction on ^{29}F$(p, pn)^{28}$F$\rightarrow^{27}$F$+n$ is used to study ^{28}F in the same experiment. The relative-energy spectrum E_{fn} for the one-neutron decay channel is shown in Fig. 8.14 using only NeuLAND data. Three clear resonances are visible.

Before continuing with the relative-energy analysis, the bound excited states in ^{27}F are studied because the same (p, pn) reaction is suitable to do the γ-ray spectroscopy. The Doppler-corrected γ-ray spectrum, shown in Fig. 8.12, is measured in the ^{29}F$(p, pn)^{27}$F reaction, where one track in MINOS from the scattered proton is requested. The reaction vertex is reconstructed with the track information and the incoming-beam tracking. The spectrum shows events with cluster multiplicity of one after addback. Additional peaks besides the prominent one at $919\,\mathrm{keV}$ are neither found in the spectrum including all multiplicities nor in the sum-energy spectrum or single-hit spectrum.

The γ-ray energy is determined in a χ^2-minimization approach. The experimental spectrum is fit simultaneously with a prompt-decay spectrum obtained in the simulation and a background contribution that is determined from experimental data in the reaction ^{29}F$(p, 2p)^{24}$O, as described in Sec. 8.2.1. The fit is repeated for several different γ-ray energies, thus the decay energy is obtained from the minimum of the χ^2 curve as well as the uncertainty (σ) that is inferred at $\chi^2 \pm 1$. The result is shown in Fig. 8.12, the bound excited state in ^{27}F has an energy of $E_\gamma = 919(4)\,\mathrm{keV}$. This measurement confirms the result by Doornenbal et al. [81] of $E_\gamma = 915(12)\,\mathrm{keV}$.

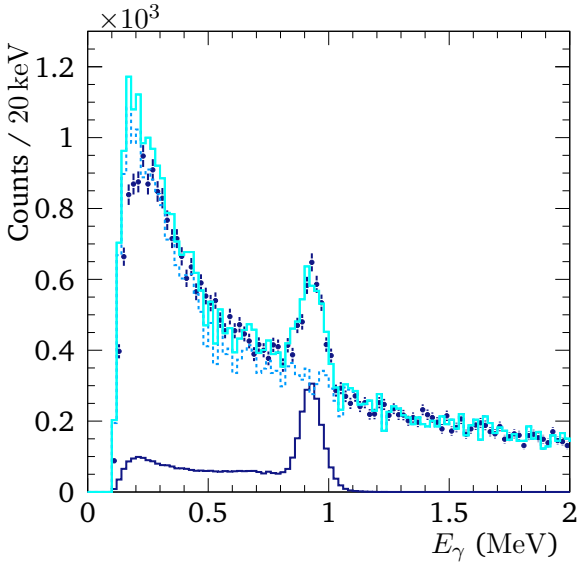

Figure 8.12: Doppler-corrected γ-ray spectrum of ^{27}F in the ^{29}F$(p,pn)^{27}$F reaction, taking only cluster multiplicity of one. The decay energy is determined to be $919(4)\,\mathrm{keV}$ (blue line), and fit together with experimental background (dashed blue line) to the experimental data (blue points), the total fit is shown as cyan line.

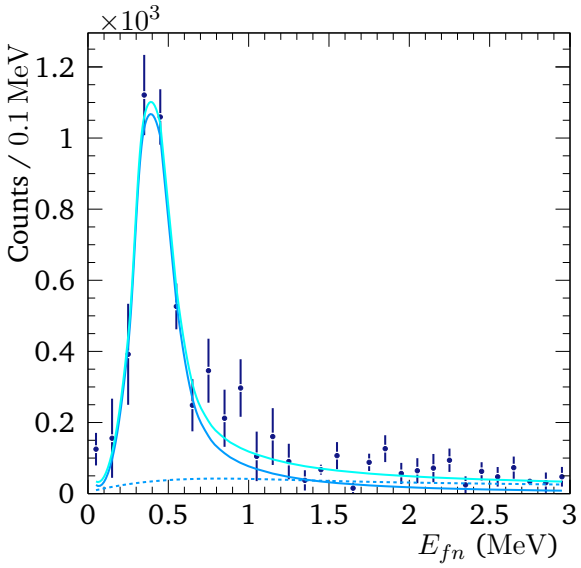

Figure 8.13: Relative-energy spectrum for ^{28}F in the ^{29}F$(p,pn)^{27}$F$+n$ reaction in coincidence with the γ-ray at $919\,\mathrm{keV}$ in ^{27}F. The spectrum is corrected for the γ-ray detection efficiency of $15.1\,\%$ and fit with a Breit-Wigner line shape (blue line) and a background contribution (dashed blue line). The resonance parameters are $E^r_{fn} = 433(3)\,\mathrm{keV}$ and $\Gamma_r = 139(12)\,\mathrm{keV}$.

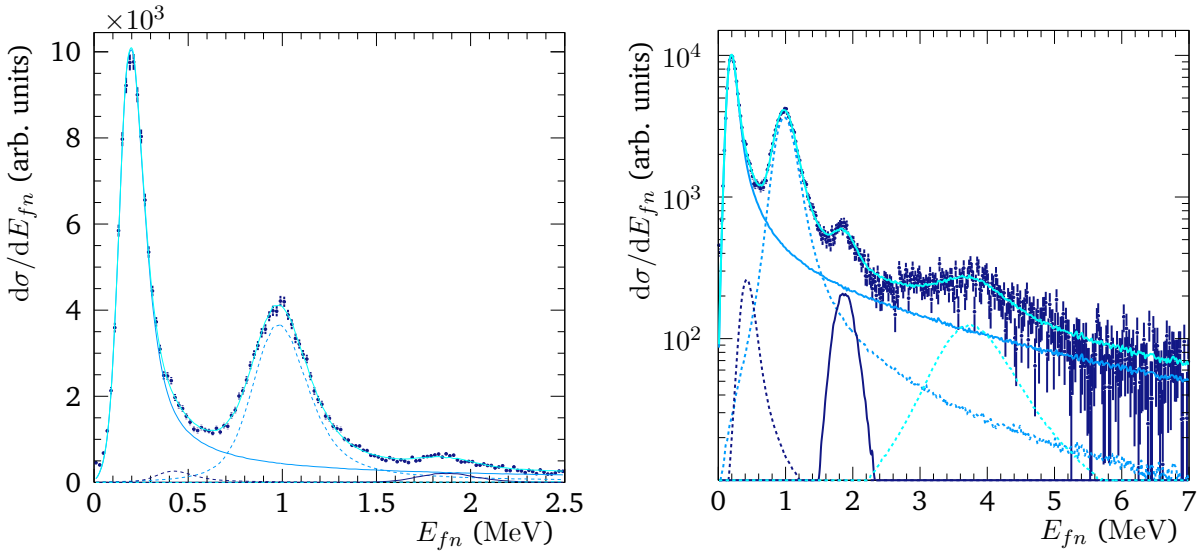

Figure 8.14: Relative-energy spectrum of ^{28}F in the ^{29}F$(p,pn)^{27}$F$+n$ reaction. The experimental data (blue points) are binned in steps of $20\,\mathrm{keV}$. The spectrum, considering only NeuLAND data, is fit with five Breit-Wigner resonances, the total fit is shown by the cyan line with $\chi^2_{\mathrm{red}} = 1.18$. The spectrum is corrected for efficiency and acceptance of the neutron detection. The resonance parameters are listed in Table 8.2. (a) Zoom up to $E_{fn} = 2.5\,\mathrm{MeV}$. (b) Logarithmic representation.

This analysis supports also the conclusions that are made for the study of the excited states in ^{29}F, see. Sec. 8.2.1 – the background describes the experimental spectrum sufficiently well. There is no significant strength missing in the energy region below $\sim 300\,\mathrm{keV}$ as discussed for ^{29}F*. The differences at low energies can be attributed to the scattered neutron that also interacts in DALI2 but shows a different response than a proton from ^{30}Ne$(p,2p)$.

Now, the γ-coincident decay in the fragment ^{27}F with a resonance in ^{28}F (^{27}F$+n$) is investigated, as done in Sec. 8.2.2. One resonance up to $3\,\mathrm{MeV}$ is identified in Fig. 8.13, it is fit with a Breit-Wigner distribution as given in Eq. 8.1. The parameters are $E^r_{fn} = 433(3)\,\mathrm{keV}$ and $\Gamma^r = 139(12)\,\mathrm{keV}$, angular momentum $l = 1$ is assumed. Thus, the excitation energy of the resonance in ^{28}F is $1352\,\mathrm{keV}$.

Finally, the one-neutron relative-energy spectrum of ^{27}F$+n$ is fit with the energy-dependent Breit-Wigner line shapes as given in Eq. 8.1 (channel radius $a = 4\,\mathrm{fm}$). Five resonances are fit simultaneously to the spectrum in a least squares approach as described in App. B.2. The integral, resonance position, and width are free parameters – except for the resonance at $433\,\mathrm{keV}$ that is coincident with the γ-ray which is fixed. For now, all resonances are assumed to have an angular momentum of $l = 1$. The resulting fit to the spectrum using only NeuLAND data is shown in Fig. 8.14, the goodness of the fit is $\chi^2_{\mathrm{red}} = 1.18$. The statistics is high and NeuLAND shows a better relative-energy resolution than NEBULA. The presented spectrum is corrected for the efficiency

Table 8.2: Resonance parameters (position E^r_{fn} and width Γ_r) of ^{28}F resonances in the ^{29}F$(p,pn)^{27}$F$+n$ reaction, cf. Fig. 8.14. The second part of the table lists the results that are found in Ref. [60] from the ^{29}Ne$(p,2p)^{27}$F$+n$ reaction in the same experiment. Those resonances that are labeled with a "$*$#" are considered to be the same in ^{28}F according to the resonance energy.

Resonance	E^r_{fn} (keV)	± (stat)	± (syst)	Γ^r (keV)	± (stat)	± (syst)
1	205	± 1	± 11	151	± 4	± 22
2	433†	± 3	± 33	139	± 12	± 4
3	990	± 2	± 10	159	± 5	± 14
4	1875	± 3	± 30	< 1	± -	± -
5	3756	± 38	± 4	822	± 124	± 204
$*1$	204	± 16		180	± 140	
$(*2)$	363†	± 17		110	± 70	
	940	± 20		150	± 50	
	1280	± 30		170	± 90	
$*4$	1840	± 30		170	± 90	
$*5$	2810†	± 360		470	± 610	
$*5$	3660	± 100		660	± 260	

and acceptance of the neutron detection using the curve determined in Sec. 7.6.2. The combined data and analysis can be found in Ref. [60]. The obtained resonance parameters are given in Table 8.2, see also the level scheme Fig. 8.20. The systematic uncertainties are evaluated by using a response matrix that is calculated using a better neutron-ToF resolution of $150\,\mathrm{ps}$ in the simulation. The contribution in the spectrum from nuclear excitation into the continuum, a (p,p') reaction, is negligible. In both cases, the scattered proton and one neutron in forward direction would be measured but the momentum transfer in the inelastic scattering is so small that it will rarely leave the target and is tagged.

The state in ^{28}F that is associated with the coincident γ-ray decay could also decay directly ($E_{fn} = 1352\,\mathrm{keV} = 433\,\mathrm{keV} + 919\,\mathrm{keV}$) but is not explicitly included in the shown spectrum because it gets suppressed strongly in the fit and eventually does not improve the goodness of the fit. Since this is the only way the branching of a $1352\,\mathrm{keV}$ state can be determined, the conclusion is that this state decays dominantly via the bound excited state in ^{27}F. This decay path accounts for $> 92\,\%$. Coincident γ-decays are also seen at higher relative energies but are not connected to a particular resonance. The two states claimed at $3180(260)\,\mathrm{keV}$ and $3980(260)\,\mathrm{keV}$ in Ref. [60] are treated here as a single resonance, resulting in $3756(38)\,\mathrm{keV}$. Compared to Table 8.1, the resonance at $243\,\mathrm{keV}$ could be different than that at $205\,\mathrm{keV}$ – this discussion is continued in Sec. 8.2.7.

† in coincidence with γ-ray decay in ^{27}F at $919\,\mathrm{keV}$

The fit of the relative-energy spectrum shows small sensitivity to different angular momenta for the Breit-Wigner line shape. However, the best fit result with smallest $\chi^2_{\rm red}$ is achieved with $l = 1$. The neutron-knockout reaction is a selective tool to study the ground-state mixing of ^{29}F. Particular single-particle levels are probed in the QFS reaction, resulting in different states in ^{28}F. The result shows already that the ^{29}F ground state is strongly mixed.

The work by A. Revel [60] find additional resonances in ^{28}F from the same experiment but in a different beam setting and reaction channel, namely the proton-knockout reaction ^{29}Ne$(p, 2p)^{28}$F$\rightarrow^{27}$F$+n$ that is sensitive to different configurations. The results are listed together in Table 8.2. The resonances at $363\,\mathrm{keV}$, which can be assumed to be the same as $433\,\mathrm{keV}$, and $2810\,\mathrm{keV}$ are found to decay in coincidence with the γ-ray in ^{27}F, the assigned excitation energies are $1280\,\mathrm{keV}$ and $3740\,\mathrm{keV}$, respectively. In the work here, the low-energy γ-ray coincident resonance is placed at $433(33)\,\mathrm{keV}$ that is determined in a different approach, namely explicitly by studying the γ-ray coincident relative-energy spectrum E_{fn} as described above. Assuming that the $1280(30)\,\mathrm{keV}$ state is the same as the $433(33)\,\mathrm{keV} + 919(4)\,\mathrm{keV} = 1352\,\mathrm{keV}$ state, the found branching ratio to the ground state in ^{27}F of $41\,\%$ [60] would be much larger than that in the ^{29}F(p, pn) reaction what might indicate that the states are actually different.

In summary, the ground-state energy of ^{28}F is obtained to be $205(11)\,\mathrm{keV}$, it is the first precise measurement of the neutron-separation energy of ^{28}F. In addition, many different excited states are found as depicted in Fig. 8.20.

8.2.5 Momentum Distributions of ^{28}F in QFS Theory

As described in Sec. 4.2, the neutron-knockout reaction is a tool to obtain spectroscopic information about the neutron configuration. The shape of the momentum distribution of the heavy fragment is sensitive to the angular momentum of the knocked-out neutron in the sudden approximation. The momentum profile is shown in Fig. 8.15 for ^{28}F from ^{29}F(p, pn). It is the momentum width as function of the relative energy E_{fn}, the technique is described in Ref. [96]. The total momentum is reconstructed from the decay, $\vec{p}(^{28}\mathrm{F}) = \vec{p}(^{27}\mathrm{F}) + \vec{p}(n)$. Figure 8.15a shows the x-component where the width is the standard deviation (σ) from a Gaussian fit to the distribution between $\pm 175\,\mathrm{MeV}/c$. The profile for the longitudinal-momentum distribution is shown in Fig. 8.15b. The fit region is limited between -150 and $100\,\mathrm{MeV}/c$ because the distribution is asymmetric.

Apart from the general dependence of the width to increasing relative energy, strong differences in the width indicate that different angular momenta are involved. Narrow distributions are expected for s wave, while the width increases for p and d wave. The resonance region at $E_{fn} \sim 200\,\mathrm{keV}$, $990\,\mathrm{keV}$, $1800\,\mathrm{keV}$, and $3100\,\mathrm{keV}$ show such a difference. That are in particular those resonances that have been identified in the relative-energy spectrum of ^{28}F, see Fig. 8.14. The profile indicates that there might be indeed an additional resonance at $\sim 3100\,\mathrm{keV}$ that was not in particular considered in the analysis above. In order to learn about the angular momentum

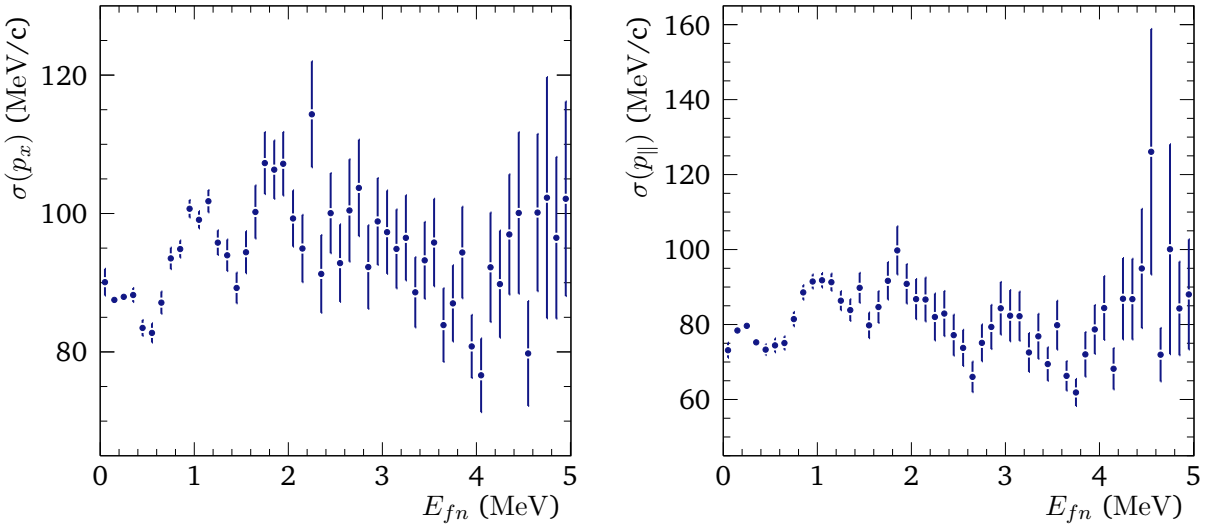

Figure 8.15: Momentum profile of ^{28}F from ^{29}F$(p,pn)^{27}$F$+n$, using the standard deviation σ of the momentum component for different relative energies E_{fn}. (a) x-component of the transverse momentum. (b) Longitudinal momentum.

the momentum width needs to be compared to theory.

The calculation of the momentum distribution in QFS theory is provided by C. Bertulani [193], based on the formalism in Ref. [115] (see also Sec. 4.3). The eikonal distorted waves are calculated for states at $E_{fn} = 215\,\mathrm{keV}$ and $999\,\mathrm{keV}$ ($S_n = 1440\,\mathrm{keV}$) for both $l = 1$ ($\nu p_{3/2}$) and $l = 2$ ($\nu d_{3/2}$). The theoretical distributions are convoluted with the experimental resolution, namely the distributions in Figs. 7.8 and 7.9, and are compared to the experimental data. Both, the $l = 1$ and $l = 2$ spectra are fit simultaneously to the p_y and $p_\parallel$ distribution where the ratio between $l = 1$ and 2 is kept the same for both distributions. The fit regions are $\pm 250\,\mathrm{MeV}/c$ and -200 to $100\,\mathrm{MeV}/c$, respectively. The results are shown in Fig. 8.16 for the associated ground state at $205\,\mathrm{keV}$ ($100\,\mathrm{keV} < E_{fn} < 300\,\mathrm{keV}$) and the excited state at $990\,\mathrm{keV}$ ($900\,\mathrm{keV} < E_{fn} < 1100\,\mathrm{keV}$).

For both E_{fn} regions, the $l = 1$ is dominant with $86\,\%$ and $66\,\%$ with statistical uncertainty of $\pm 1\,\%$, respectively. When there are different angular momenta involved, this means that different decay branches are involved. In the region of the ground state there might be another resonance close in energy which is not resolved in the E_{fn} spectrum. The resonance at $\sim 990\,\mathrm{keV}$ also does not seem to be a single one. Except for the $l = 1$ contribution coming from the ground-state resonance tail, there are other angular momenta involved (other than $l = 1, 2$ are not tested so far).

In the naive shell model, the ^{29}F ground-state has a valence-neutron pair in the $1d_{3/2}$ ($l = 2$) orbital but the momentum and relative-energy analysis shows that different angular momenta contribute and the ground state is mixed as the reaction leads to different final states. Resonances at larger relative energies might be produced in a knockout from stronger bound neutron shells.

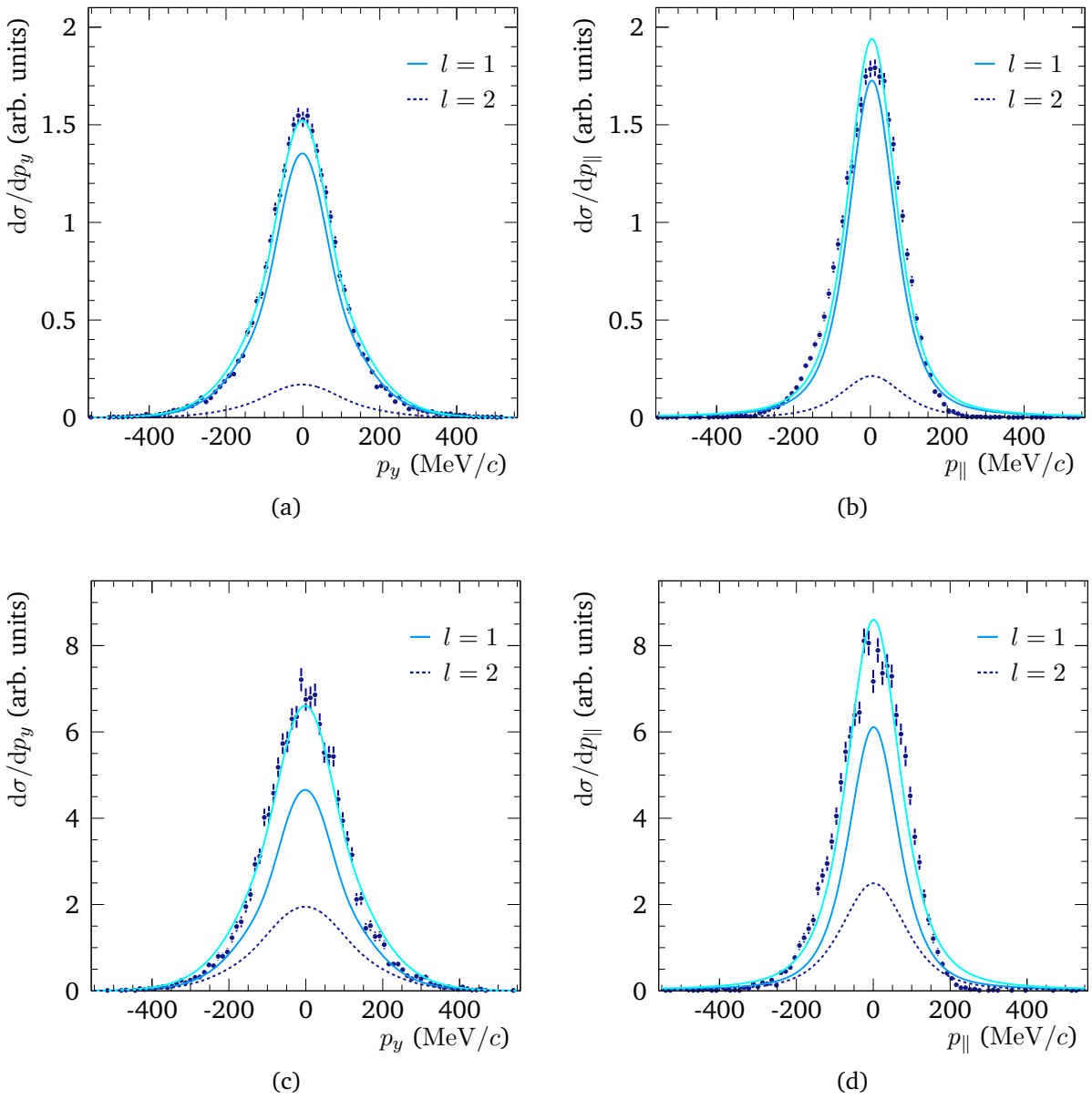

Figure 8.16: Momentum distributions of ^{28}F from the ^{29}F$(p, pn)^{27}$F$+n$ reaction, fit with theoretical predictions in QFS theory involving $l = 1$ and $l = 2$ angular momenta [193]. Transverse momentum y component (a) and longitudinal momentum distribution (b) for $100\,\mathrm{keV} < E_{fn} < 300\,\mathrm{keV}$, with $86(1)\,\%$ for $l = 1$. (c) y component and (d) longitudinal momentum distribution for $900\,\mathrm{keV} < E_{fn} < 1100\,\mathrm{keV}$, $66(1)\,\%$ for $l = 1$.

The ^{29}F valence neutrons are expected to be paired (even number of neutrons), thus the ^{28}F valence neutron would also reside partially in the $2p_{3/2}$ orbital instead of $1d_{3/2}$. Other contributions like an excited ^{27}F core are also possible. In both cases, ^{29}F and ^{28}F, a significant contribution from $2p$-orbital neutrons is found contrary to the naive shell model but confirming a signature of the island of inversion.

8.2.6 Decay Scheme of ^{29}F

In the previous sections it was found that the three-body decay of ^{29}F proceeds dominantly as sequential decay via intermediate resonances in ^{28}F. Those resonances are identified in the fractional-energy spectra of the two-neutron decay and in the relative-energy spectrum of ^{28}F, where the latter allows a more precise analysis due to higher statistics and better resolution.

The intermediate resonances found at $\sim 230\,\mathrm{keV}$, $\sim 440\,\mathrm{keV}$, and $\sim 1000\,\mathrm{keV}$ are mapped to the resonances at $205\,\mathrm{keV}$, $433\,\mathrm{keV}$, and $990\,\mathrm{keV}$ in ^{28}F. The ground-state resonance at $205(11)\,\mathrm{keV}$ is $38\,\mathrm{keV}$ smaller than the intermediate resonance found in the region $E_{fnn} \sim 1.5\,\mathrm{MeV}$ what may hint to two different states close in energy at $\sim 230\,\mathrm{keV}$. Maybe not the ^{28}F ground state is populated in the sequential decay but a slightly higher state. This possibility is further discussed in Sec. 8.2.7, a clear distinction from the fractional-energy analysis only is not possible.

The resonance at $433\,\mathrm{keV}$ in ^{28}F is associated with the coincident γ-ray decay in ^{27}F, a similar resonance is found in the fractional energy. The question is, if this resonance is also associated with the excited state in ^{27}F and thus is the three-body resonance with γ-coincidence as found in Sec. 8.2.2. Therefore, the E_{fnn} region between $0.8\,\mathrm{MeV}$ and $1.6\,\mathrm{MeV}$ is studied for two different regions of the intermediate resonances E_{fn1} as depicted in Fig. 8.17a. E_{fn1} is the relative energy that is associated with the fragment and the neutron that has particularly lower energy than the second neutron in the decay. The condition in box 1 selects the E_{fn} region around $450\,\mathrm{keV}$ in ^{28}F, where gate 2 is sensitive to $E_{fn} \sim 250\,\mathrm{keV}$. In Fig. 8.17b the coincident γ-ray spectrum is shown for the previously mentioned relative-energy regions. It is found that the coincident $919\,\mathrm{keV}$-decay is only observed for $E_{fn1} \sim 450\,\mathrm{keV}$ at $E_{fnn} \sim 1200\,\mathrm{keV}$ but not for $E_{fn1} \sim 250\,\mathrm{keV}$. The intensity of the γ-peak in Fig. 8.17b agrees reasonably with the total intensity of the $E_{fn1} \sim 440\,\mathrm{keV}$ resonance in the fractional-energy spectrum. The conclusion is that the only three-body resonance at $E_{fnn} = 1253(51)\,\mathrm{keV}$ that populates the bound-excited state at $919\,\mathrm{keV}$ in ^{27}F decays via the $E_{fn} = 1352\,\mathrm{keV}$ state in ^{28}F, that was found before to dominantly decay via ^{27}F*. The three-body excitation energy associated with this decay is $E^{*}_{fnn} = 2172\,\mathrm{keV} = 1253\,\mathrm{keV} + 919\,\mathrm{keV} = 433\,\mathrm{keV} + 872\,\mathrm{keV} + 919\,\mathrm{keV} = 1352\,\mathrm{keV} + 872\,\mathrm{keV}$, cf. Fig. 8.20.

Given the results from the γ-ray analysis and the three-body analysis for the fractional energy, including resonance positions, widths and branching ratios, the E_{fnn} spectrum is eventually fit with line shapes from Breit-Wigner theory for the sequential decay as introduced in Sec. 4.5 (with $\Delta_l = 0$ for simplification, $a = 4\,\mathrm{fm}$). The intermediate resonances are taken as given in

[‡] for γ-ray coincident resonance at $1253\,\mathrm{keV}$ only, fixed

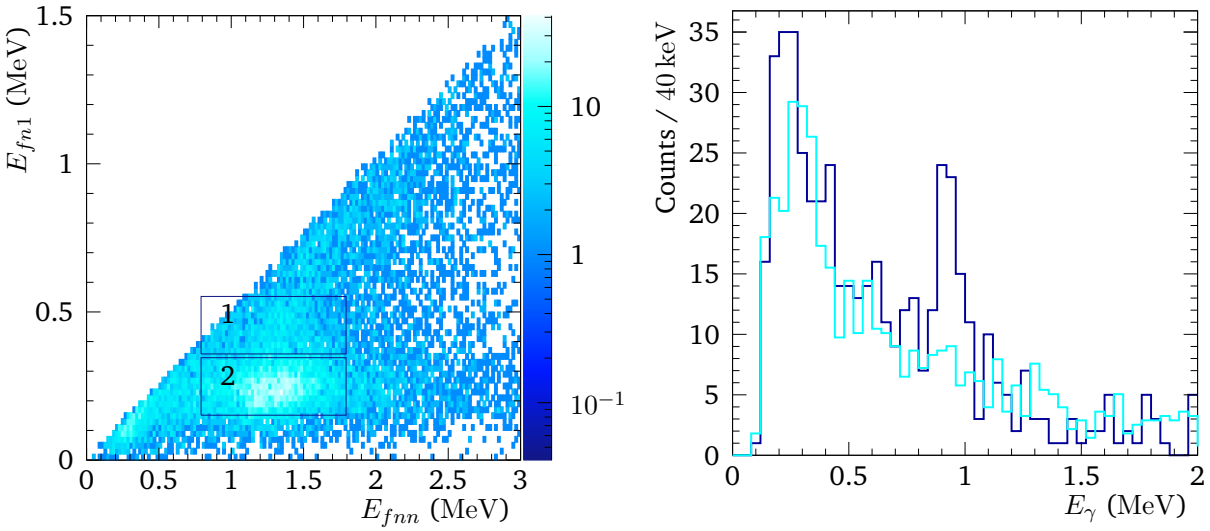

(a) (b)

Figure 8.17: Correlation between E_{fnn} and E_{fn1} for ^{29}F, where E_{fn1} is the relative energy between ^{27}F and the neutron with explicitly smaller energy than the second neutron. (a) For the different E_{fnn}, the intermediate resonances become visible as E_{fn1}. The indicated boxes 1 and 2 correspond to gates for the same E_{fnn} but E_{fn}(^{28}F) at $\sim 250\,\mathrm{keV}$ and $\sim 450\,\mathrm{keV}$. The coincident γ-ray spectrum is shown in Fig. (b) for region 1 (blue) and region 2 (cyan). Region 2 is normalized to 1 (stat. uncertainties are not indicated). Only region 1 shows the γ-ray coincidence with ^{27}F at $919\,\mathrm{keV}$. The E_{fnn} resonance at $1253\,\mathrm{keV}$ decays with $E_{fn} = 433\,\mathrm{keV}$ and thus through the $1352\,\mathrm{keV}$ state in ^{28}F. The excitation energy is $E^*_{fnn} = 2172\,\mathrm{keV}$.

Table 8.3: Decay branches of ^{29}F for different E_{fnn} regions with the ^{28}F intermediate resonances for sequential decay. The width for E_{fn} can be found in Table 8.2.

E_{fnn} (keV)	E_{fn} (keV)	Branching (%)
0−500	phase space	-
500−900	205	-
900−1200	205	88
	433‡	
1200−1500	205	79
	433	
1500−1800	205	63
	990	37
1800−2300	205	49
	990	51
2300−3000	205	33
	990	25
	phase space	42
3000−4000	205	19
	990	6
	phase space	75

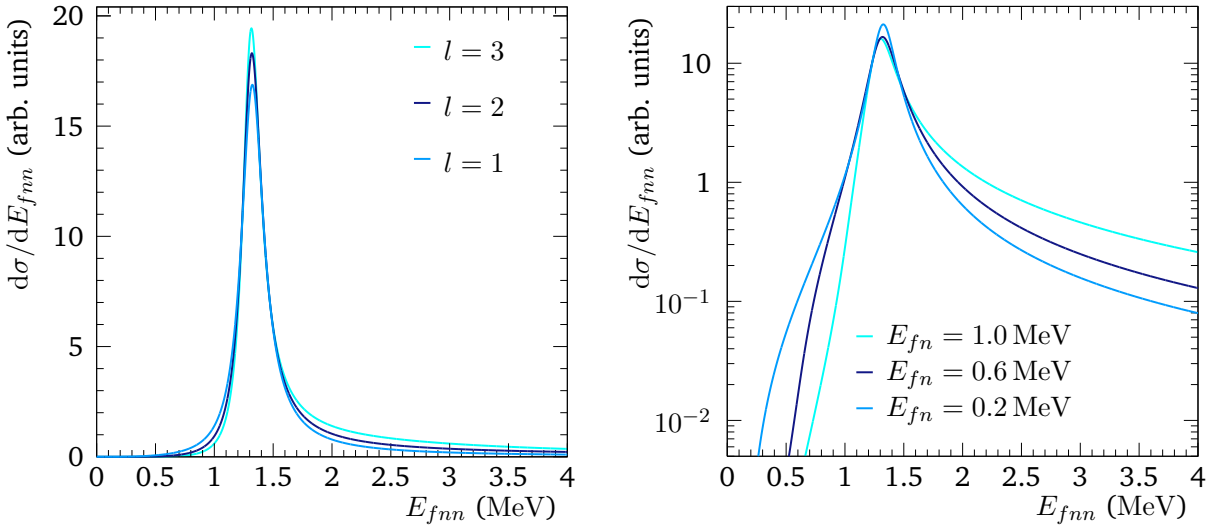

Figure 8.18: Sequential Breit-Wigner line shape for $E_{fnn} = 1330\,\mathrm{keV}$, (a) and $\Gamma = 375\,\mathrm{keV}$, and $E_{fn} = 205\,\mathrm{keV}$ with $\Gamma = 151\,\mathrm{keV}$ for different angular momenta l of the three-body resonance. (b) The $l = 1$ resonance ($\Gamma = 300\,\mathrm{keV}$) for three different intermediate-resonance energies. The larger E_{fn} is, the more the three-body resonance gets confined.

Table 8.3 for the different E_{fnn} regions. It looks like that the sequential-decay mode opens from $E_{fnn} \gtrsim 2E_{fn}$ comparing to the conditions given in Eqs. 2.30-2.32. For the fit, it is assumed that the sequential decay proceeds only through known resonances in ^{28}F that are determined in the neutron- or proton-knockout reaction on ^{29}F or ^{29}Ne, respectively. The effect on the Breit-Wigner line shape is negligible if those resonances are slightly different to those in the fractional-energy analysis – the energy is still well separated from the three-body resonance energy. The fit procedure works as described before (App. B.2) but using the $2n$ response matrix for the convolution. Neutron misidentification, like only one neutron has hit the detector and two are reconstructed, is small but is included.

Figure 8.18 shows the behavior of the Breit-Wigner line shape for sequential decay for different angular momenta of the three-body resonance and it shows the impact of different intermediate resonances. The different angular momenta have only a small impact (as well as the channel radius). For intermediate resonances that are closer to the three-body resonance, the leading edge falls stronger because the intermediate resonance suppresses this edge.

The final fit result is shown in Fig. 8.19, the obtained three-body resonance energies and the partial widths are given in Table 8.4, see also Fig. 8.20. The resonance width cannot be extracted in most of the cases because it is dominated by the experimental resolution. Five resonances are included, the goodness of the fit is $\chi^2_{\mathrm{red}} = 1.23$.

The residual between fit and experimental data shows a slight excess between $E_{fnn} \sim 2.6\,\mathrm{MeV}$

[§] for γ-ray coincident resonance with decay energies $433\,\mathrm{keV} + 820\,\mathrm{keV} + 919\,\mathrm{keV}(\gamma)$

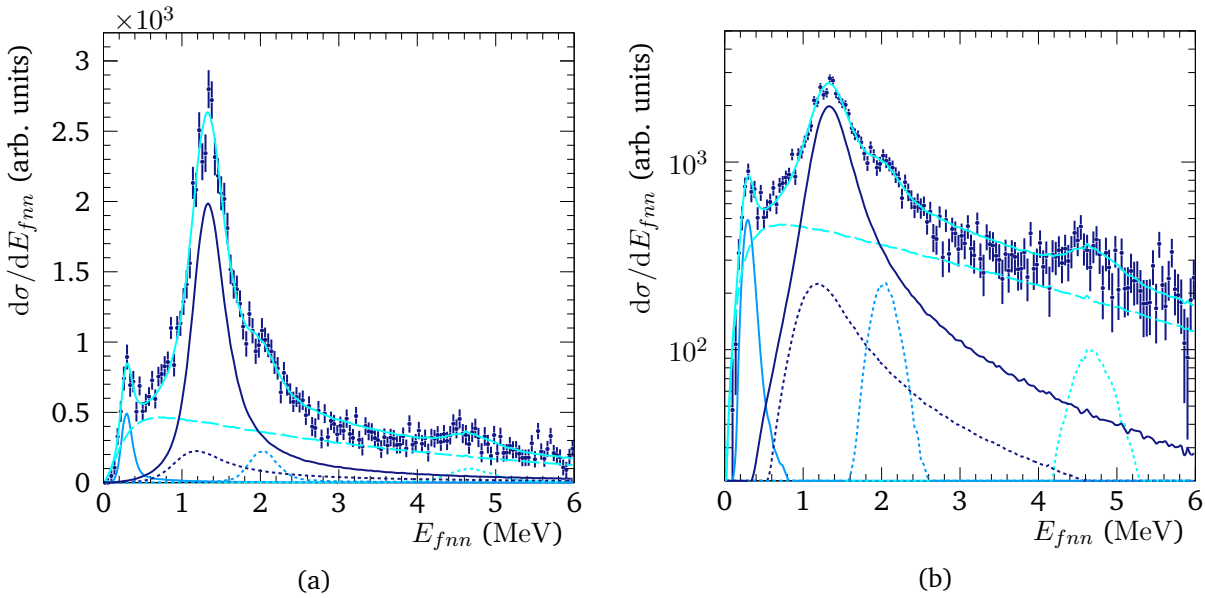

Figure 8.19: Relative-energy spectrum of ^{29}F* (blue dots, 40 keV bins) fit with five sequential Breit-Wigner line shapes, based on Table 8.3. (a) The total fit is shown as cyan line, the background as dashed line. (b) In logarithmic scale.

Table 8.4: Three-body resonance parameters (position E^r_{fnn} and width Γ_r) of ^{29}F* resonances in the ^{30}Ne$(p,2p)^{27}$F$+2n$ reaction, cf. Fig. 8.19, for the sequential decay. The dominant decay branch that is considered is also given.

Resonance	E^r_{fnn} (keV)	± (stat.)	± (syst.)	Γ_r (keV)	± (stat.)	± (syst.)	Decay E_{fn} (keV)
1	300	± 4	± 33	<1	± -	± -	phase space
5	1253[§]	± 51	± -	1111	± 240	± -	1352
3	1337	± 6	± 21	360	± 16	± 33	205
4	2030	± 9	± 20	<1	± -	± -	205, 990
5	4670	± 19	± 140	<1	± -	± -	phase space

and $\sim 3.6\,\mathrm{MeV}$. Several different distribution to describe the background have been studied. Experimental background is absolutely suppressed by the exclusive selection criteria of the reaction mechanism. It is emphasized that the "non-resonant" background is dominated by FSI between ^{27}F and neutron, as it becomes obvious in the fractional-energy spectra where phase-space contributions become significant only for $E_{fnn} \gtrsim 2\,\mathrm{MeV}$. The best fit result is obtained with the background description in the shape of

$$\frac{\mathrm{d}\sigma}{\mathrm{d}E_{fnn}} \sim \mathrm{erf}(a \cdot E_{fnn}) \cdot \exp\{-b \cdot E_{fnn}\}\,, \tag{8.8}$$

with the error function $\mathrm{erf}()$, and fit parameters a and b, as it is proposed in Ref. [190]. Another distribution that was tested is of Maxwellian shape for beam-like neutrons with a temperature parameter a, applied for instance in Refs. [87, 194],

$$\frac{\mathrm{d}\sigma}{\mathrm{d}E_{fnn}} \sim \sqrt{E_{fnn}/a^3} \cdot \exp\{-E_{fnn}/a\}\,. \tag{8.9}$$

The event-mixing technique was also investigated but it always leaves spurious signatures of the three-body correlations and is thus not used. Ambiguity is left by the shape of the "non-resonant" background description, and thus not more than the five resonances are considered. In App. E.3 a fit to the spectrum with an additional resonance at $E_{fnn} \sim 800\,\mathrm{keV}$ can be found to account for strength that appears, however, not to be significant.

8.2.7 The ^{29}F Level Scheme and Discussion

In the previous sections, a complementary analysis of the neutron-rich fluorine isotopes has been performed to determine the level and decay schemes. The proposed scheme is shown in Fig. 8.20.

For the first time, excited states above the neutron-separation threshold are studied for ^{29}F. Those decay dominantly by sequential decay through resonances in ^{28}F, which have been studied with unprecedented precision in this experiment at SAMURAI too.

Before comparing the results to theory, an open aspect is discussed. The correlations in the Jacobi systems are sensitive to the involved angular momenta. An analysis in hyperspherical harmonics shows that the hypermomentum K depends on the angular momentum of the decay neutrons $K \propto l_1 + l_2$, for details see Ref. [52]. The analysis of the fractional-energy spectra shows a significant decay via a state at $E_{fn} \sim 230\,\mathrm{keV}$. So far, it was assumed that it corresponds to the ^{28}F ground state at $205\,\mathrm{keV}$. From the fractional-energy analysis itself it cannot be concluded whether there exist an additional resonance slightly above $205\,\mathrm{keV}$ (cf. beginning of Sec. 8.2.6). Figure 8.21 shows the angular correlation in the Y-system for $1.2\,\mathrm{MeV} < E_{fnn} < 1.5\,\mathrm{MeV}$ with the additional conditions $0.1 < \epsilon_{fn} < 0.2$ or $0.2 < \epsilon_{fn} < 0.3$ for the fractional energy in the Y-system. One distribution is increasing towards $\cos(\theta_{n-fn}) = \pm 1$ and the other one is decreasing. The left figure can be described with odd angular momentum $l = 1$ for both neutrons but the right one

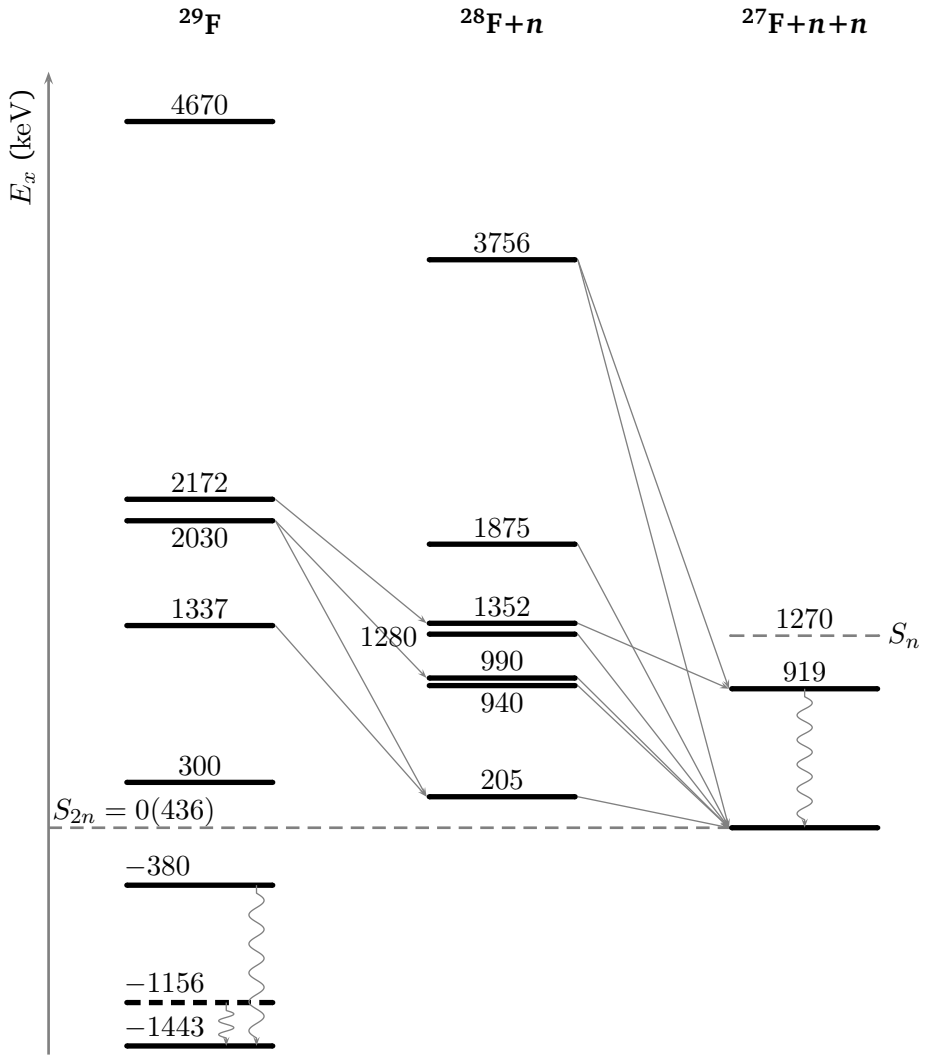

Figure 8.20: Proposed decay scheme of ^{29}F. The level energies of the intermediate and final nuclei, ^{28}F and ^{27}F, are also given in keV. Decay paths are depicted as gray line. The second γ-decay in ^{29}F is tentatively placed at $E_\gamma = 287\,\mathrm{keV}$.

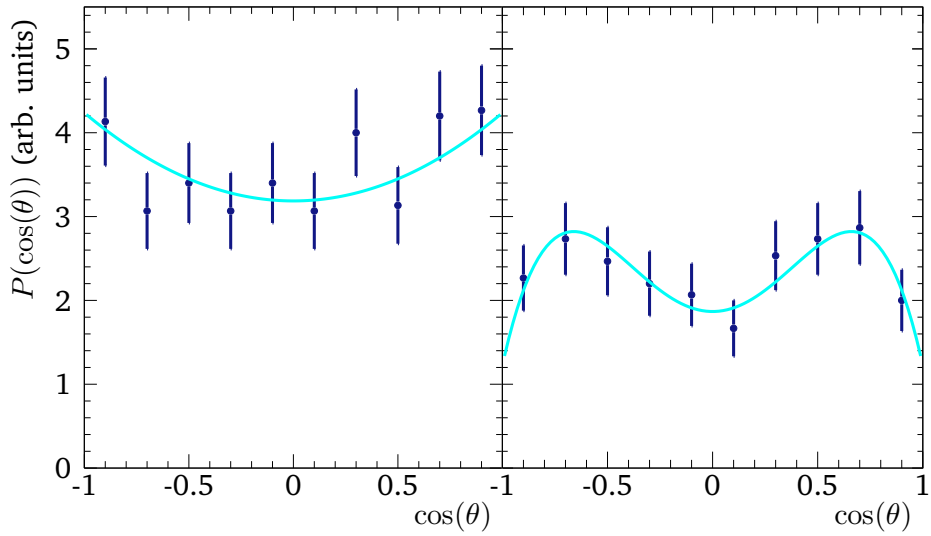

Figure 8.21: Angular correlation of ^{29}F in Y-system between fragment and neutrons, θ_{n-fn}, for $1.2\,\mathrm{MeV} < E_{fnn} < 1.5\,\mathrm{MeV}$. Left: With additional condition on the fractional energy in Y-system, $0.1 < \epsilon_{fn} < 0.2$, fitted with correlation including hyperspherical harmonics with angular momentum $l = 1$ for the two neutrons (cyan line). Right: Condition $0.2 < \epsilon_{fn} < 0.3$, fitted with $l = 2$.

with $l = 2$ [192] using Eq. 5 from Ref. [127]. If this difference is confirmed to be significant, it means that there exist indeed an additional state close to $205\,\mathrm{keV}$ and the three-body resonance at $1337\,\mathrm{keV}$ can be separated into two. The momentum analysis in Fig. 8.16a may supports this argumentation but deeper conclusions are not possible because of low statistics.

The main result of this thesis work is the proposed level scheme of ^{29}F. From the neutron-knockout reaction on ^{29}F$(p, pn)^{28}$F it is concluded that the neutron configuration of the ground-state is strongly mixed involving different angular momenta. The excited states in the continuum are probed by proton knockout on ^{30}Ne, where the strength of those states depends also on the ground-state configuration of ^{30}Ne. Comparing the momentum distribution of ^{29}F to theory calculations can give insight into the proton configuration of ^{30}Ne and the parities of the ^{29}F states. In the QFS reaction it is likely that not only the valence $d_{5/2}$ proton is knocked out but also deeper bound orbitals like the p-shell are probed. An analysis in QFS reaction theory is intended.

Finally, the level scheme is compared to theory predictions from a shell-model calculation using effective interactions and from an *ab-initio* theory in the SCGF framework. The comparison is shown in Fig. 8.22. Another prediction by Macchiavelli et al. [195] in a particle-rotor model associated with deformed Nilsson orbits is not in good agreement.

The shell-model calculation (left column Fig. 8.22) is provided by P. Doornenbal [81], it uses the SDPF-M interaction [79, 196] with an exact diagonalization calculation and shows states calculated up to $\sim 4\,\mathrm{MeV}$. The valence space includes the full sd-shell and the $f_{7/2}p_{3/2}$ orbitals on top of a ^{16}O core. The effective SDPF-M interaction combines the USD interaction for the sd-shell

part, the Kuo-Brown interaction for the fp-shell part, and a modified Millener-Kurath interaction for the cross-shell part, where the strength of the $d_{3/2} - f_{7/2}$ TBMEs ($T = 0, 1$) is adjusted [79]. This kind of interaction is known to be applicable to the island-of-inversion nuclei because it reproduces the impact of the tensor force in the monopole part. However, the USD monopole part is adjusted to reproduce the neutron drip line of the oxygen isotopes.

^{27}F has one excited bound state, ^{28}F is unbound, but the ground state of ^{29}F is bound again and bound excited states exist. This implies that binding energy is gained by adding two more neutrons to ^{27}F although there is no energy gain by the valence-neutron interaction in the $0p0h$ configuration itself. In Ref. [81] it is argued that only the SDPF-M compared to USDA/B SM calculations (residual interaction limited to sd shell) produces a realistic result for $S_{2n} = 1028\,\mathrm{keV}$ and thus the ground state of ^{29}F is already substantially influenced by neutron fp-contributions what is basically confirmed by the experiment in the ^{29}F(p, pn) reaction. Their calculation predicts a shell gap of $\lesssim 2.4\,\mathrm{MeV}$. The authors conclude that the structure of ^{29}F is correlated with that of ^{28}O. The bound-excited state might be formed as $|^{29}\mathrm{F}(1/2^+)\rangle = |^{28}\mathrm{O}(2^+)\rangle \otimes |\pi 1d_{5/2}\rangle$, thus involving mainly the same-parity neutron fp-levels. In an earlier calculation by the same authors in Ref. [197] the underlying mechanism is investigated in a bit more detail. Due to the narrowing of the $sd - fp$ shell gap, $2p2h$ and even $4p4h$ become accessible. Additional energy is gained by the cross-shell but also fp-shell interactions in the $T = 1$ channel. Another conclusion is that ^{29}F is only modestly deformed in its ground state.

The experimental work done here can for the first time compare the higher excited states to theory. The excited states in the theory up to $\sim 2.5\,\mathrm{MeV}$ are of positive parity and are the multiplet from the just-mentioned coupling. Given that the two-neutron separation energy is experimentally known only by $\pm 436\,\mathrm{keV}$, the experimental state at $1743\,\mathrm{keV}$ may correspond to the $9/2^+$ state at $1525\,\mathrm{keV}$, and the state at $2780\,\mathrm{keV}$ is in the energy region of the other positive-parity states. However, only one bound-excited state is predicted. Higher excited states seem to correspond to the negative-parity states that would originate from proton knockout from the p-shell with smaller cross section. It is also possible that additional binding is missing so that the $9/2^+$ state becomes bound and the spectrum is shifted, an uncertainty of a few hundred keV must be considered.

The second theory that is compared to is the *ab-initio* SCGF theory, cf. Sec. 2.1.2, provided by C. Barbieri [198]. It is performed as particle-attached calculation of a proton to ^{28}O applying the third-order algebraic diagrammatic construction (ADC(3)) scheme and the N^{2}LO$_{\mathrm{sat}}$ chiral interaction together with the N^{3}LO(lnl) interaction (local and nonlocal regulators) [199]. This particular interaction includes two- and three-nucleon interactions up to next-to-next-to leading order and reproduces empirical nuclear saturation properties like radius and binding energy of ^{16}O [200]. The N^{3}LO(lnl) interaction is added on top and produces additional binding such that the first three excited states are bound below $1\,\mathrm{MeV}$. Although the low-lying spectrum with and without N^{3}LO(lnl) predicts the same states, the difference in energy reflects the ambiguity

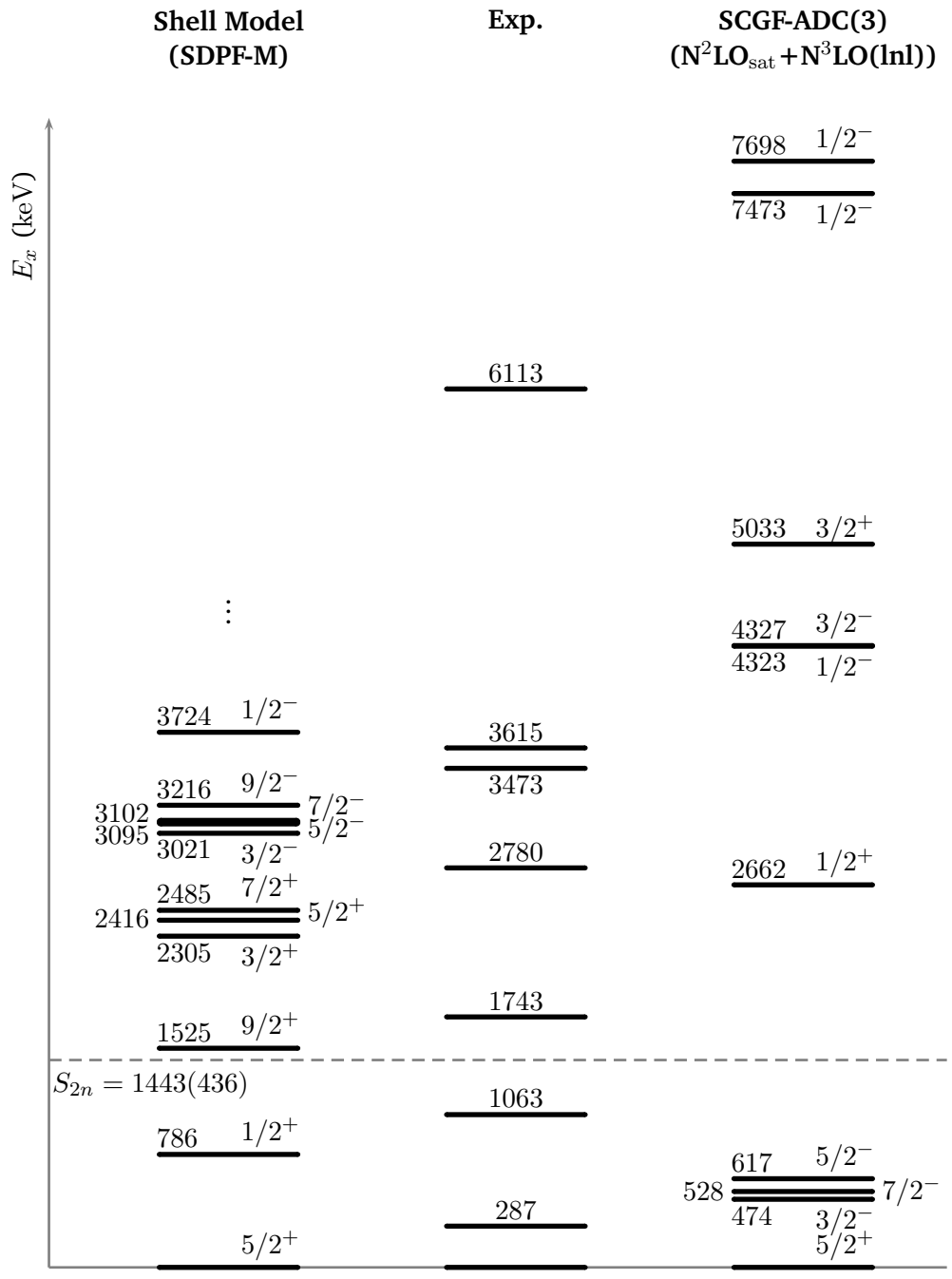

Figure 8.22: Experimental level scheme of ^{29}F compared to a shell-model calculation using the effective SDPF-M interaction [81] and to an *ab-initio* self-consistent Green's function theory calculation using the N^{2}LO$_{\rm sat}$+N^{3}LO(lnl) interaction [198].

Table 8.5: Weisskopf transition rate for possible γ-decays in ^{29}F, the transition character is assigned in comparison to theory.

Transition	E_γ (keV)	Weisskopf Rate λ	λ (1/s)	Lifetime τ
$E1$	1063	$1.0 \times 10^{14} \cdot A^{2/3} E_\gamma^3$	1.134×10^{15}	0.9 fs
$E2$	776	$7.3 \times 10^{7} \cdot A^{4/3} E_\gamma^5$	1.830×10^{9}	0.5 ns
$E1$	287	$1.0 \times 10^{14} \cdot A^{2/3} E_\gamma^3$	2.231×10^{13}	44.8 ps

in the knowledge of the nuclear forces of $\sim 1\,\mathrm{MeV}$. Only the spectrum with the two combined interactions (and for comparably large spectroscopic factor) is shown because it is supposed to agree better with experimental spectra for neutron-rich nuclei. The *ab-initio* calculation does not show satisfactory agreement with the experiment although the states at $\sim 3\,\mathrm{MeV}$ and $\sim 5.5\,\mathrm{MeV}$ seem to be rather stable while changing the interactions. In both theories, explicit continuum degrees of freedom are missing what is one factor leading to energy shifts.

The SCGF calculation predicts three bound excited states in ^{29}F while in this experiment at least one additional state is found compared to a previous experiment. Following the discussion in Sec. 8.2.1, experimentally there is no argument that the found decay energy of $287\,\mathrm{keV}$ either corresponds to a state at that energy or to a decay branch from $1063\,\mathrm{keV}$ via $776\,\mathrm{keV}$. However, the predicted spin-parity assignment is studied and whether the the given order can support the experimental results. Considering the first three states, there is the $E1$ transition from $7/2^-$ to $5/2^+$ with assumed $1063\,\mathrm{keV}$, the possible $E2$ transition is between $7/2^-$ and $3/2^-$, and another $E1$ transition for $3/2^-$ to $5/2^+$. The transition rates for these three decays are calculated in Table 8.5 according to the Weisskopf single-particle transition rates, whereas all transitions would be short lived and thus the decay chain cannot explain the observed experimental spectrum. The $287\,\mathrm{keV}$ transition energy is tentatively placed as separate low-lying state, although the $776\,\mathrm{keV}$ decay is not seen. Maybe, only the direct population is observed but the decay chain is too long lived.

The striking difference to the SM calculation is that the SCGF calculation predicts the negative-parity states first instead of the positive-parity states. The positive parity states in the SM calculation come from the $2p2h$ excitations that are coupled to the $\pi 1d_{5/2}$ or $\pi 2s_{1/2}$ proton. The negative-parity states in the SCGF theory would probably correspond to excitations involving the $1p$ shell also. Exclusive cross sections are not calculated, spectroscopic factors could be compared for proton-removal reactions on ^{30}Ne, where the ^{30}Ne structure is dominated by neutron pairs in the p and d (and f) orbitals [83].

The spectroscopy of ^{29}F and ^{28}F shows for both nuclei a rich excitation-energy spectrum. ^{29}F has two excited bound states, the additional binding can theoretically only be explained with a quenching of the $sd - fp$ shell gap and excitations across this spherical $N = 20$ shell closure. In the shell-model picture, many-particle many-hole excitations (even $4p4h$) become significant

admixtures to describe the level scheme (even in ground state) – intruder configurations are important. Similar is true for ^{28}F as demonstrated in the combined momentum analysis. It is concluded that ^{28}F, ^{29}F, and also ^{30}F show the characteristics that define the island of inversion. Thus, the island of inversion is extended including the neutron-rich $Z = 9$ isotopes, describing a shallow low-Z shore.

Chapter 9

Summary

The thesis focuses on the spectroscopy of the neutron-rich fluorine isotopes ^{30}F and ^{29}F that are found to show characteristics as particularly seen for nuclei in the island of inversion.

In order to perform the complete spectroscopy, the experiment was carried out at the SAMURAI setup at the RIBF (RIKEN, Tokyo). The secondary beam, produced from a ^{48}Ca beam, is provided by the BigRIPS fragment separator. Proton- and neutron-knockout reactions on a LH_2 target in inverse kinematics at beam energies of $\sim 220\,\mathrm{MeV/u}$ are employed to populate excited bound and neutron-unbound states in the nuclei of interest. The reactions under QFS conditions are tagged with the MINOS TPC. Prompt γ-decays are coincidentally measured with the detector array DALI2. Besides the incoming beam, and the charged scattered nucleons from the reaction, the heavy reaction fragment and its momentum is measured using the large-acceptance spectrometer SAMURAI to unambiguously identify the reaction channel. In addition, fast neutrons from decays flying in forward direction are measured with the NeuLAND demonstrator and NEBULA.

NeuLAND is the neutron ToF spectrometer of the R^{3}B experiment at GSI/FAIR (Germany). A part of the detector, the so-called NeuLAND demonstrator, was used for a two-year long campaign at SAMURAI. Another experiment during this campaign was the lifetime measurement of the two-neutron decay of the ^{26}O(g.s.). Therefore, a new experimental method has been developed and applied as part of this thesis work. The NeuLAND detector itself was commissioned in a particular experiment where the one-neutron detection efficiency was determined. The experiment and characterization of the detector is also discussed in this thesis. Quasi-monoenergetic neutrons are produced in the $p(^7\mathrm{Li},^7\mathrm{Be})n$ reaction at $110\,\mathrm{MeV}$ and $250\,\mathrm{MeV}$ and measured in NeuLAND. With the known cross section for this reaction, the one-neutron detection efficiency is determined to be $31.0(13)\,\%$ and $27.4(10)\,\%$ (for $\Delta E > 5\,\mathrm{MeV}$), respectively. The results agree well with the simulations.

The full capability of the setup is exploited in the spectroscopy of ^{30}F and ^{29}F. The neutron-unbound ^{30}F is investigated in the $^{31}\mathrm{Ne}(p,2p)^{30}\mathrm{F}\rightarrow^{29}\mathrm{F}+n$ reaction, where all particles are measured coincidentally. By measuring the neutron and fragment momenta, and applying the invariant-

mass method, the relative-energy spectrum is obtained. The first spectroscopic measurement done here identifies the ^{30}F ground state at $583(85)\,\mathrm{keV}$. The resonance width is $730(151)\,\mathrm{keV}$, although ambiguity is left due to low statistics. Following experiments with higher incoming-beam intensity can help to confirm the ground- and also excited-state properties. It is argued in the single-particle limit of the resonance width that the neutron $2p$-orbital configuration plays a significant role in the ground-state description. The intruder configuration, that is energetically favored compared to the $1f$ orbital, is a signature of the island of inversion.

The spectroscopy of ^{29}F is more complex, while bound and neutron-unbound states are investigated. The neutron decay is a three-body decay because ^{28}F is itself ground-state unbound. The excited states are populated in the ^{30}Ne$(p,2p)^{29}$F* reaction. A bound excited state at $1063(7)\,\mathrm{keV}$ is confirmed in this experiment and a new one with a transition energy of $287(4)\,\mathrm{keV}$ is found. Above the threshold, ^{29}F decays into ^{27}F$+n+n$. This channel is also measured and five other excited states are found. The Breit-Wigner line shapes for sequential decay are introduced for the neutron decay to determine the resonance properties. The correlation analysis of this three-body decay in Jacobi coordinates shows that ^{29}F* decays dominantly in sequential mode via resonances in ^{28}F. The nucleus ^{28}F is also investigated separately in the ^{29}F$(p,pn)^{27}$F$+n$ reaction in order to identify possible intermediate resonances in the two-neutron decay. The analysis of the ^{28}F momentum distributions after neutron knockout indicate that the ground state of ^{29}F also has a significant neutron $2p$-orbital contribution.

Eventually, the comparison to a shell-model calculation with the SDPF-M interaction and to an *ab-initio* Self-consistent Green's function theory using a N^{2}LO$_{\mathrm{sat}}$+N^{3}LO(lnl) interaction is made. Both theories encounter difficulties to describe the spectrum, even though continuum degrees of freedom are difficult to capture. The shell-model calculation reproduces only one bound excited state. Bound excited states are also found in the *ab-initio* calculation but involve large uncertainties. The conclusion is that the $N=20$ shell-gap quenching persists at the low-Z shore of the island of inversion and multi-particle multi-hole admixtures are crucial in the description. The island of inversion seem to exhibit a shallow low-Z boundary where the neutron-rich fluorine isotopes are included. Partial cross sections can help to determine the strength of the admixtures.

In a complementary experiment, namely the exclusive measurement of the Coulomb breakup reaction of ^{29}F, the $B(E1)$-strength distribution could be extracted and compared to models in order to obtain information about the ground-state configuration and the halo character of the Borromean nucleus ^{29}F.

Appendix A

Lifetime Measurement of the Two-Neutron Decay of ^{26}O(g. s.)

Nuclear Inst. and Methods in Physics Research, A 866 (2017) 265–271

Contents lists available at ScienceDirect

Nuclear Inst. and Methods in Physics Research, A

journal homepage: www.elsevier.com/locate/nima

Neutron radioactivity—Lifetime measurements of neutron-unbound states

J. Kahlbow [a,b,*], C. Caesar [a,b,*], T. Aumann [a,b], V. Panin [c], S. Paschalis [a,1], H. Scheit [a], H. Simon [b]

[a] Institut für Kernphysik, Technische Universität Darmstadt, 64289 Darmstadt, Germany
[b] GSI Helmholtzzentrum für Schwerionenforschung, Planckstraße 1, 64291 Darmstadt, Germany
[c] RIKEN Nishina Center for Accelerator-Based Science, 2-1 Hirosawa, 351-0198, Wako, Saitama, Japan

ARTICLE INFO

Keywords:
Neutron radioactivity
Neutron spectroscopy
Lifetime measurements
Neutron-rich nuclei
^{26}O

ABSTRACT

A new technique to measure the lifetime τ of a neutron-radioactive nucleus that decays in-flight via neutron emission is presented and demonstrated utilizing MonteCarlo simulations. The method is based on the production of the neutron-unbound nucleus in a target, which at the same time slows down the produced nucleus and the residual nucleus after (multi-) neutron emission. The spectrum of the velocity difference of neutron(s) and the residual nucleus has a characteristic shape, that allows to extract the lifetime. If the decay happens outside the target there will be a peak in the spectrum, while events where the decay is in the target show a broad flat distribution due to the continuous slowing down of the residual nucleus. The method itself and the analysis procedure are discussed in detail for the specific candidate ^{26}O. A stack of targets with decreasing target thicknesses can expand the measurable lifetime range and improve the sensitivity by increasing the ratio between decays outside and inside the target. The simulations indicate a lower limit of measurable lifetime $\tau \sim 0.2$ ps for the given conditions.

1. Introduction

The access to exotic nuclei opens the possibility to study new kinds of radioactive decays at the limits of nuclear stability (recent reviews, e. g., [1,2]). While for proton-unbound nuclei several cases of "proton radioactivity" have already been measured, no radioactive decay via neutron emission has been observed experimentally yet. This is mainly because the lifetime for proton-unbound nuclei can be rather long (~ ms) due to the presence of the large Coulomb barrier. For nuclei beyond the neutron drip line, which are candidates for neutron radioactivity, the predicted lifetimes are considerably shorter due to the missing Coulomb barrier. The lifetime is governed mainly by the decay energy and depends strongly on the angular momentum of the decay particles [3], thus reducing the number of possible candidates.

Several definitions of radioactivity are existing, giving different lower limits on the lifetime τ, which marks the boundary between the existence of a nucleus and a ground-state resonance in the continuum, see e. g. [1,4]. Here, $\tau > 10^{-14}$ s will be used as definition of radioactivity, following the guidelines for the discovery of a chemical element from the International Union of Pure and Applied Chemistry (IUPAC) [5].

Fig. 1 shows the different lifetime regimes for radioactivity and resonant phenomena. The new method fills a gap to measure directly lifetimes in the regime of neutron radioactive nuclei.

For the neutron-unbound nuclei with $Z \leq 10$, which can be investigated nowadays, ^{26}O is the most promising candidate. ^{26}O will serve in the following as illustrative example to describe the method. It has been speculated according to the estimates of Grigorenko et al. [3,8], that a very low-lying ground-state resonance of ^{26}O might be rather long-lived representing a case of neutron radioactivity.

Invariant mass measurements of the ^{26}O ground state via proton-removal reaction from ^{27}F have been reported recently by NSCL [9], GSI [6], and RIBF [10] groups. The NSCL and GSI experiments could only deduce upper limits for the energy of the ground state. The experiment performed at RIBF determined the position of the ground-state resonance at $18 \pm 3(\text{stat}) \pm 4(\text{syst})$ keV above neutron-separation threshold, see Fig. 2.

From the GSI data an upper limit of $\tau \leq 5.7$ ns (95% c. l.) for the ^{26}O ground-state lifetime was deduced by the time-of-flight between the target and the spectrometer magnet. The ^{26}O ground-state half-life value of $T_{1/2} = 4.5^{+1.1}_{-1.5}(\text{stat}) \pm 3(\text{sys})$ ps (corresponding to $\tau = 6.5$ ps) has been reported from an analysis of the NSCL measurement [7],

* Corresponding authors.
E-mail addresses: jkahlbow@ikp.tu-darmstadt.de (J. Kahlbow), c.caesar@gsi.de (C.Caesar), t.aumann@gsi.de (T. Aumann).
[1] Present address: Department of Physics, University of York, Heslington, York, YO10 5DD, United Kingdom.

http://dx.doi.org/10.1016/j.nima.2017.06.002
Received 14 March 2017; Received in revised form 31 May 2017; Accepted 3 June 2017
Available online 7 June 2017

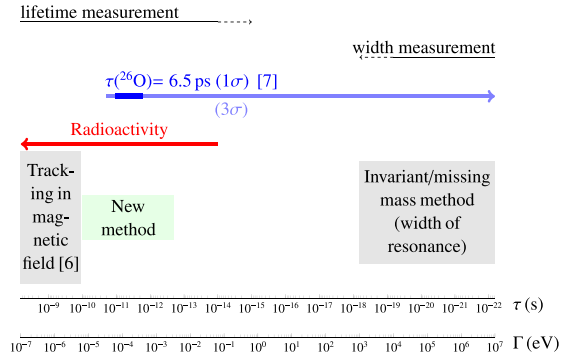

Fig. 1. (Colour online) Characteristic decay widths Γ and corresponding lifetime τ scales are shown. The regimes of radioactive and resonant phenomena are indicated as well as selected experimental techniques that are applicable to measure lifetimes for decays via neutron emission.

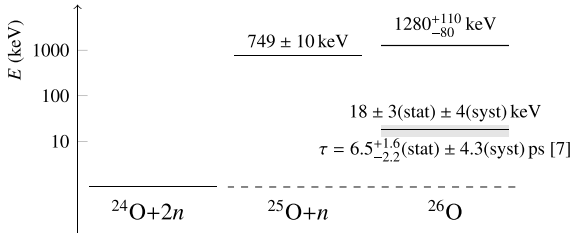

Fig. 2. Excitation energy spectrum of ^{26}O relative to the ^{24}O g. s. in non-linear scale. The values are taken from [10], uncertainty intervals are shown as grey shaded areas. The ground-state decay of ^{26}O via the intermediate ^{25}O resonance is energetically forbidden, the ^{26}O g. s. decays via $2n$ emission to the ^{24}O ground-state.

which, if corroborated, would constitute the first discovery of neutron radioactivity.[2]

Recent theoretical calculations predict that the ^{26}O ground state is dominated by two $d_{3/2}$ valence neutrons [12,13]. Grigorenko et al. [3] state that the influence of pairing and n-n final state interactions and core recoil actually increases the decay width while migrating to lower angular momenta. A precise method to measure lifetimes of neutron-radioactive decays will also help to conclude on the two experimental findings and the theoretical prediction for the ^{26}O ground state, in particular:

- The position of the ground-state resonance [10]; precisely measured to 18 ± 5 keV.
- The experimental lifetime of the ground state [7]; $\tau \leq 11.1$ ps.
- The theoretical relation between the decay energy and the lifetime [3,8], depending on used model interactions.

A direct measurement of the width of the state is impossible because it is much smaller than achievable energy resolutions, which typically are in $\sim$ 10 keV region (cf. Fig. 1), while the width predicted by Grigorenko et al. [3] would only be $\lesssim 10^{-1}$ keV, based on the energy of the experimental ground-state resonance as obtained by Kondo et al. [10].

The technique used by Kohley et al. at NSCL [7,14] is based on a lifetime measurement extracted from the velocity difference measurement of neutrons and the ^{24}O fragment. This velocity difference depends on the energy loss of the charged fragment in the target, causing a shift of the mean velocity difference for finite lifetimes. The method relies on absolute calibrations of the velocity measurements, which is rather difficult and thus introducing a large systematic uncertainty.

We propose a complementary method, which does not depend on an absolute calibration and is more sensitive. Thus, the method will be able to provide a more precise measurement.

2. Lifetime measurement method

Our method adapts the basic principle of the well known Doppler Shift Attenuation Method (DSAM). In the DSAM [15] nuclear lifetimes of nuclei are measured. The nucleus is formed in an excited state in-flight and slowed down in the target material. While being stopped in the target, the nucleus may emit a γ-ray. The γ-ray energy carries information on the velocity of the emitting nucleus due to the Doppler effect. Taking the stopping power into account allows to extract the decay time of the nucleus.

The new technique presented here to measure lifetimes of possible neutron-radioactive nuclei is based on this idea. The nucleus of interest is produced in-flight at point x_r with reaction cross section σ_r in the reaction target of thickness d, see Fig. 3. The energy loss, which the charged fragment undergoes in the target, depends on the point of decay, which in turn depends on the lifetime of the populated system. The lifetime τ of the nucleus under investigation defines the decay curve:

$$N(t) = N_0 \cdot e^{-t/(\gamma\tau)}\,, \tag{1}$$

where $N(t)$ is the number of residual nuclei after time t, and $N_0 - N(t)$ the number of products which have decayed already. The time t in the laboratory frame is a function of the travelled straight pathlength x_t and the exponent becomes

$$\frac{x_t}{\beta\gamma c\tau}, \tag{2}$$

let λ be

$$\lambda = \beta\gamma c\tau \tag{3}$$

the decay length with Lorentz factor γ and velocity βc where the velocity is assumed to be constant along the target thickness for the moment. Decays will occur inside and outside the target with amount D_i and D_o, respectively. Considering first the amount of decays inside the target: at the reaction point an amount of initial nuclei $\mathrm{d}N_0$ is produced. The number that decays from there until the end of the target on path $d - x_r$ is, cf. Fig. 3,

$$\mathrm{d}\tilde{D}_i = \mathrm{d}N_0 \left[1 - e^{-(d-x_r)/\lambda}\right]. \tag{4}$$

Taking into account all the reactions points in the target with cross section σ_r, incoming beam particles N_{in} and target particle-density ρ_t with area density $\left(\mathrm{d}N_0/A\right)_t = \rho_t \cdot \mathrm{d}x_r$ leads to

$$D_i = \int \mathrm{d}\tilde{D}_i = \int \mathrm{d}N_0 \left[1 - e^{-(d-x_r)/\lambda}\right] \tag{5}$$

$$= \sigma_r \rho_t N_{\mathrm{in}} \int_{x_0=0}^{d} \left[1 - e^{-(d-x_r)/\lambda}\right] \mathrm{d}x_r \tag{6}$$

$$= \sigma_r \rho_t N_{\mathrm{in}} \cdot \left[d - \lambda\left(1 - e^{-d/\lambda}\right)\right]. \tag{7}$$

The amount of decays outside the target D_o is simply the difference between produced nuclei-of-interest in the target and D_i,

$$D_o = \sigma_r \rho_t N_{\mathrm{in}} \cdot \lambda \cdot \left[1 - e^{-d/\lambda}\right]. \tag{8}$$

The ratio defined as

$$R(\lambda) = \frac{D_o}{D_i} \tag{9}$$

is

$$R(\lambda) = \frac{1}{\frac{d}{\lambda(1-e^{-d/\lambda})} - 1}, \tag{10}$$

[2] Kryger et al. [11] investigated already in 1996 the one-neutron radioactivity of ^{16}B and obtained an upper limit of 191 ps (68% c. l.)

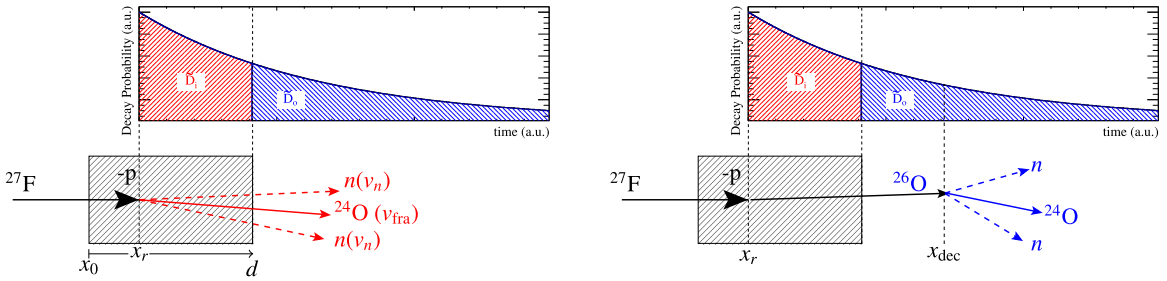

Fig. 3. (Colour online) Two event classes appear for an unbound system populated in-flight, which has an appreciable lifetime τ – decays inside and outside the target. An example is shown for proton removal from a ^{27}F beam on a target of thickness d at reaction point x_r and subsequent decay at x_{dec} of the populated ^{26}O into $^{24}\mathrm{O} + n + n$. Left: An immediate decay inside the target is shown. The amount of decays inside the target from x_r is depicted as $\tilde{D}_i$ (see text). Right: A late decay after the ^{26}O has left the target is displayed, their amount is $\tilde{D}_o$. The velocity difference $\Delta v = v_n - v_{fra}$ (see left Figure) is the parameter of interest.

and depends on the lifetime, $R(\tau)$ with $\tau = \lambda/(\beta\gamma c)$. The decays can be measured and could be disentangled to inside and outside contributions to deduce the lifetime τ. This analytical form of $R(\tau)$ does not include all the physics as, e. g., the stopping power and the resulting effect on β and γ and thus will not be used in the analysis here. It reproduces the behaviour of R as function of τ well for one target, see Fig. 7(b), but shows deviations for consecutive calculations and longer lifetimes as described later. This is one reason why the simulations are employed. The dependence on the experimental circumstances as target material or incoming energy on the fragment velocity is addressed later.

A major improvement of our proposed method is achieved by analysing the shape of the velocity-difference distribution Δv between neutron and fragment ($\Delta v = v_n - v_{fra}$), which is related to $R(\tau)$, instead of the shift of its mean.[3] The method can thus be used without the need of an absolute calibration of Δv to determine τ very accurately. The idea of using the ratio between delayed and prompt decays to determine the lifetime of an unbound nucleus has also been applied very recently to measure a two-proton decay lifetime [16], although the experimental technique differs from the one presented here.

To enhance the sensitivity, the target material should be chosen such that on one hand the energy loss is maximized and on the other hand the decays outside the target will happen at a considerable rate. To maximize the energy loss, target materials of large stopping power, i. e., with high density and large atomic number Z are used. This creates a box-like, broad neutron–fragment velocity difference distribution for the decays inside the target. A characteristic Δv spectrum is shown in Fig. 4. Furthermore, the target length needs to be optimized such that decays outside the target become also possible with sufficient amount. These events yield a sharp "peak" in the Δv spectrum since they as well as the neutrons do not suffer from a continuous slowing-down process in the material anymore.

2.1. Simulation for the ^{26}O case—An example

Simulation and experimental conditions are discussed in the next sections for a specific example, namely the ^{26}O ground-state decay, for which the method being developed is most sensitive to the quoted value of $\tau = 6.5$ ps [7] and well below that.

Here, the emphasis is put on illustrating the idea and describing the method. The details of the experimental realization are not described or are not even covered.

The simulations are MonteCarlo type. The code itself is tailor-made, the work flow is described in the following. With regard to Fig. 3, each ^{26}O event is produced by a one-proton removal reaction from ^{27}F in the target where the cross section and detection efficiencies are assumed to be constant as a function of reaction position as well as energy. Secondary break-up reactions with a thick target may have a contribution of $\approx$ 10% but are not further considered here since the focus is put on presenting the method and not the experimental implementation, the ratio $R(\tau)$ is anyhow not a function of the cross section. The cross section itself is scaled to Pt according to the nuclear cross section on a C target as used in an experiment at RIBF [10]. After the reaction, as a next step, the decay point of the three-body system $^{24}\mathrm{O} + 2n$ is sampled from a probability distribution which is described by an exponential-decay function with the state's proper lifetime τ as the decay constant, as given in Eq. (1). The decay itself is assumed to be a simple phase-space decay with decay energy $E_{dec} = 0$ as a good approximation [10].

The energy loss ΔE of the charged fragments and unreacted particles travelling a distance Δx in the material is calculated with JavaATIMA,[4] a program to calculate the energy loss of ions based on theory and experimental results. In addition to the used theory by Lindhard and Sørensen (applicable above 30 AMeV), it includes relevant corrections. In detail, the relation between stopping power and mean range P is defined as follows

$$\begin{aligned}\Delta x &= \int_{E_0-\Delta E}^{E_0} \left(\frac{\mathrm{d}E}{\mathrm{d}x}\right)^{-1} \mathrm{d}E \\ &= P(E_0, x_0) - P(E_0 - \Delta E, x_0 + \Delta x),\end{aligned} \tag{11}$$

and it is evaluated from a lookup table, while the energy loss from the reaction to the decay point is, in particular, sampled stepwise in order to cope with the γ dependence of the decay curve. The knowledge of the stopping power is as important as for the DSAM for extracting the lifetime. But the absolute range of the Δv spectrum and possible peak positions allow to evaluate the quality of the underlying stopping power and can be used for calibration. The energy-loss straggling is modelled according to the relativistic Bohr formula as described in [17], whereas the effect of the angular straggling on the energy loss is found to be negligible.

Beam energy, target material, and target thickness are optimized to provide the highest sensitivity in a certain region of τ. For the lifetime to be determined with high precision, a (natural) Pt target turned out to be a good choice. Both, high mass density and large charge Z result in a large energy loss on a sufficiently short distance.

A time-of-flight resolution σ_t, assumed to be of Gaussian shape, for the neutron (fragment) measurement of 260 ps (40 ps) for a flight-path length of 11 m (9 m) are realistic values as achievable at SAMURAI setup [18] at RIBF.[5] These values were used as an input of all following simulations.

Fig. 4 shows results from a simulation as proof of principle with a well fixed incoming energy of 220 AMeV and target thickness of 6 g/cm^2 optimized to be sensitive to lifetimes around $\tau = 6.5$ ps. One identifies

[3] Note, in Ref. [14], e. g., Fig. 4 it is visible that the shape of the velocity difference is sensitive to the lifetime, however, the idea on using this feature is not elaborated.

[4] https://web-docs.gsi.de/~weick/atima/

[5] With the R^{3}B setup and the neutron detector NeuLAND at FAIR the time resolution will improve significantly down to $\sigma_t \lesssim 150$ ps for neutrons and $\lesssim 28$ ps for fragments [19].

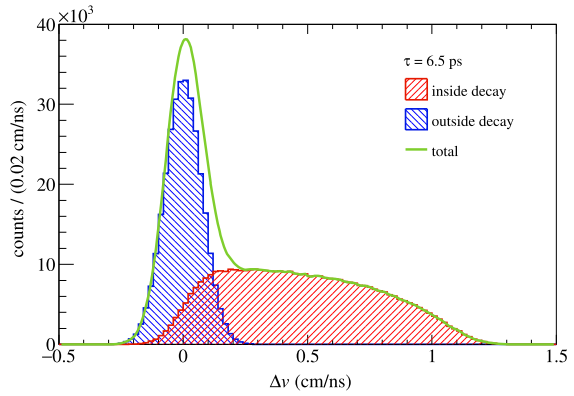

Fig. 4. (Colour online) Simulated velocity difference ($\Delta v = v_n - v_{\mathrm{fra}}$) between neutron and fragment for the ^{26}O(g.s.) decay with lifetime $\tau = 6.5$ ps; for one Pt target (6 g/cm^2) and incoming energy $E_{\mathrm{inc}} = 220$ AMeV. The "box shaped" contribution (red) stems from decays inside the target and the peak (blue) from outside decays.

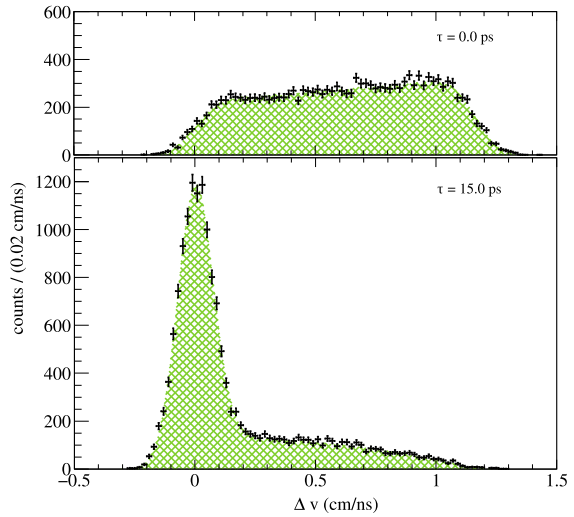

Fig. 5. (Colour online) Pseudo-experimental velocity spectra (black crosses) of 1.6×10^4 events fitted with the input-lifetime spectra (green cross-hatched) for Pt(6 g/cm^2) and $E_{\mathrm{inc}} = 220$ AMeV. Top: $\tau = 0$ ps; bottom: $\tau = 15$ ps.

clearly two structures in the Δv spectrum of neutrons and ^{24}O fragment: a broad "box-like" shape from ~ 0 to ~ 1 cm/ns and an adjacent peak around 0 cm/ns. For prompt decays the velocity difference becomes broadest and smears out the distribution with respect to the target thickness. Again, the velocity difference of neutrons and fragment depends only on the travelled distance from the point of decay in the target, thus on τ. The charged fragment suffers from the energy loss but neutrons are insensitive. The narrow component centred around zero appears for longer lifetimes, which arises from decays outside the target with no relative energy loss between neutrons and fragments any more. The width of the narrow component is dominated by the time-of-flight resolution σ_t of the neutron detection.

2.2. Analysis procedure—determining the lifetime

As discussed above, the ratio of outside-the-target to inside-the-target decays ("box-to-peak" ratio), cf. Eq. (10), translates into the lifetime, whereas the shape of the box itself depends also slightly on τ. In order to extract the lifetime from experimental data, where τ is

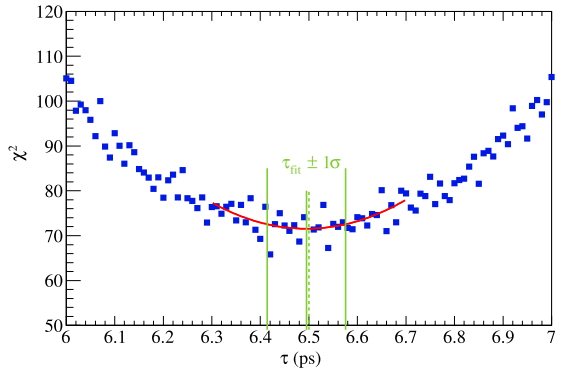

Fig. 6. (Colour online) Chi-square χ^2 distribution from the fit of trial spectra of the velocity difference Δv with lifetime τ to an assumed "experimental" spectrum, with exact lifetime $\tau = 6.5$ ps denoted by the dashed green line. The fitted minimum (red curve) indicates the deduced lifetime, depicted by the short green line, and the longer green lines confine the statistical uncertainty deduced from $\chi^2 = \chi^2_{\mathrm{min}} + 1$, $\tau_{\mathrm{fit}} = 6.49 \pm 0.08$ ps.

unknown, the data points are proposed to be fitted with trial spectra taken from simulations for several different lifetimes. The unnormalized chi-square χ^2 is a measure on how good the parent distribution describes the experimental data. In the following, "experimental" and simulated data are compared to test the analysis. For "experimental" spectra the simulated data are taken with reasonable but lower statistics, it is called pseudo-experimental data in the following. All the pseudo-experimental spectra are randomly filled with statistics that could be acquired within four or five days of beam time with a ^{27}F rate of 3×10^3 pps and the efficiency of triple coincidences as both is achievable at the RIBF, 1.6×10^4 events are analysed for Fig. 5.

The measured lifetime τ and the uncertainty is deduced from a second-order polynomial fit to the determined unnormalized χ^2 values around the minimum as shown in Fig. 6, where the minimum results in τ. The 1σ limit is calculated by finding the values of τ where $\chi^2 = \chi^2_{\mathrm{min}} + 1$ in the fit. The resulting value for the case discussed previously is $\tau = 6.49 \pm 0.08$ ps. In the following sections it is described how to increase the sensitivity.

2.3. Extended method

From known experimental results and theoretical predictions, described in Section 1, the lifetime of ^{26}O is expected to be of lower picosecond range, which is what our proposed method can measure, however the lifetime could even be smaller by orders of magnitude. In order to increase the sensitivity, the coverable lifetime range, and the luminosity within one experimental run, several targets in a row as "sandwich-like structure" are suggested in this work. Thinner targets and lower energies translate into shorter lifetimes for $R(\tau) = \mathrm{const.}$ Here, the single target thicknesses are decreasing in the direction of the beam and are chosen according to energy and lifetime-sensitivity following a constant difference of the fragment flight time through the material, given as follows

$$\frac{2E + 2m_0c^2}{\sqrt{\left(E^2 + 2Em_0c^2\right)^3}}\Delta E = \mathrm{const.}, \tag{12}$$

with the kinetic energy E and energy loss ΔE. The thickness of the initial target and incident energy are chosen such that high sensitivity is achieved for lifetimes longer than 3 ps. The target's thickness uniformity in general is of special importance. It was evaluated that deviations of ±5% smear out the Δv distributions so much that no result can be extracted lower than 0.5 ps that looks different than for 0 ps.

In the following, a setup of eight Pt targets with first target thickness of 3.63 g/cm^2 and ^{27}F beam at 200 AMeV energy on target is considered. In front and behind the target stack one and two silicon detectors are

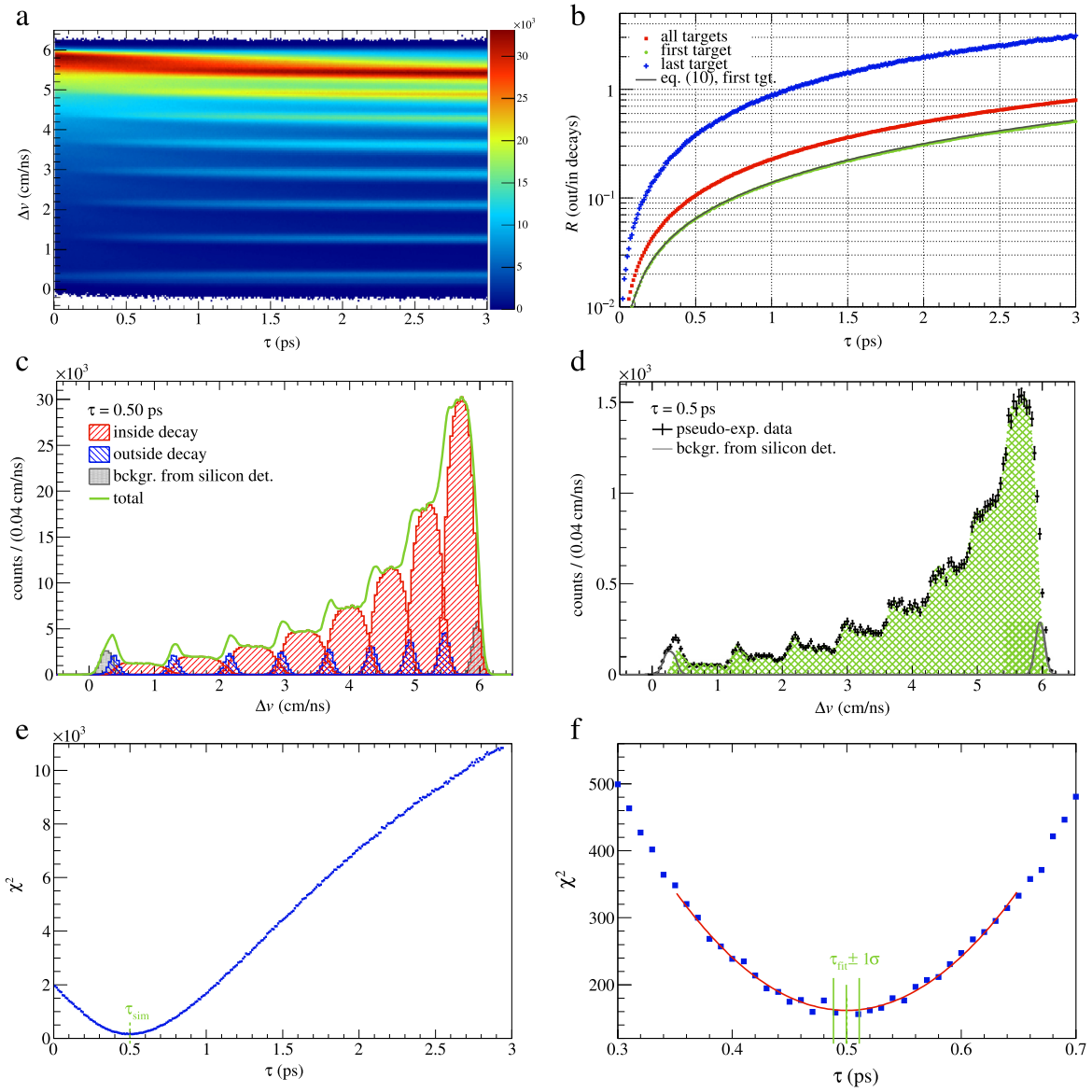

Fig. 7. (Colour online) Simulation for eight targets and optimized conditions for $\tau = 0.5$ ps and above (see text). 7(a) Velocity difference Δv as a function of the lifetime τ. The peak structure becomes more pronounced with larger lifetimes. 7(b) Inside-to-outside the target decay-ratio as function of the lifetime for only the first (green) and last target (blue) and all the simulated eight targets together (red). The "peak-to-box" ratio $R(\tau)$ increases with increasing lifetime. The simulation result is compared to the analytical Eq. (10) for the first target, for the following targets the deviation increases. 7(c) Velocity difference spectrum for $\tau = 0.5$ ps; the single components for inside (red) and outside (blue) the target decay, and the total spectrum (green) are shown. The background contribution (grey) after the ΔE cut for particle identification from the silicon detectors is included. 7(d) Fit of best trial spectrum ($\tau = 0.5$ ps, cross-hatched in green) with fixed background (grey) to pseudo-experimental data (black crosses; 6×10^4 events in total, the simulation has a factor ~ 30 more statistics) for exactly this case. 7(e) Chi-square χ^2 as function of the fit of the trial spectra with lifetime τ in steps of 0.01 ps. The green dashed lines indicates the "experimental" lifetime. 7(f) This graph shows a zoom of 7(e) in the region 0.3 ps to 0.7 ps. The fitted minimum (red curve) for $\tau_{sim} \pm 0.15$ ps indicates the deduced lifetime. The obtained lifetime $\tau_{fit} = 0.50 \pm 0.01$ ps and the 1σ uncertainty interval are denoted by the green lines.

inserted, respectively, in order to identify the proton removal reaction. In fact, these materials also act as target, see next Section 2.4. The simulation result for Δv is shown in Fig. 7(a) as function of τ in steps of 0.01 ps. For longer lifetimes the peaks of outside decays are getting more pronounced, which is also evident the ratio $R(\tau)$ in Fig. 7(b). The projection for a physical lifetime of 0.5 ps, one of the lowest reachable values, is shown in Fig. 7(c) where the sandwich-like arrangement of the targets can be recognized (cf. Fig. 3) in the repeating box-peak structure. The probed ratio of outside to inside decays is increasing from one target to another, while the targets are getting thinner and lowering the particle's energy from one to the other. In this way, a broad range and lower lifetimes are probed as well, where the last target is most sensitive to shorter lifetimes with a distinct ratio $R(\tau = 0.5\,\text{ps}) \approx 0.38$ and a pronounced box shape. The overall Δv spectrum shows several pronounced peaks, which improves accuracy and precision of the method, even when the number of outside decays is relatively small. The first targets could also be replaced by an upstream energy degrader but sensitivity to longer lifetimes would then be lost. The approach with only one target is better suited to probe a narrow lifetime region when

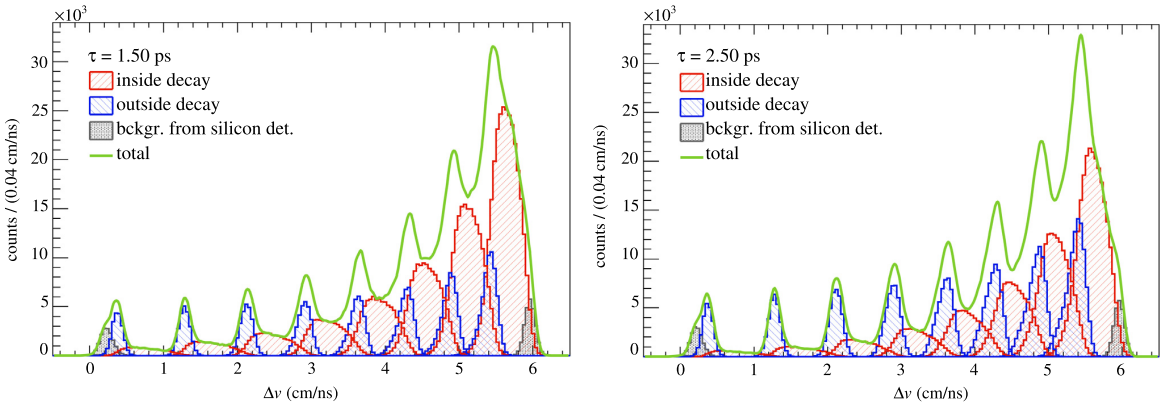

Fig. 8. (Colour online) Same as Fig. 7(c) but for τ = 1.5 ps (left) and 2.5 ps (right).

the lifetime to look at is known and the setup is optimized such that the ratio $R(\tau)$ does not saturate.

It turned out that a peak-to-box ratio (outside to inside the target decays) of $\sim$ 0.4–0.7 is optimal for deducing the lifetime with several targets. This includes a well pronounced peak and a "box" shape of the velocity-difference distribution for a certain lifetime, and for the analysis a small χ^2 value and a one-to-one relation between the extracted and simulated τ. Furthermore, the thickness is optimized such that a steep slope of the ratio $R(\tau)$ is achieved.

2.4. Contribution from auxiliary detectors

The method could be applied at one of the setups for spectroscopy of unbound neutron-rich nuclei, MoNA/NSCL [20], SAMURAI/RIBF [18], and R^{3}B at GSI or future FAIR [19].

To identify proton removal reactions from ^{27}F, energy-loss measurements need to be conducted in front of the target stack and behind. Three simple 300 µm thick single-area silicon detectors (one in front and two behind) are proposed to be installed. Actually, it is not necessary to identify explicitly in which target the reaction happens because this is already indicated in the Δv spectrum. The targets themselves are placed sufficiently apart with 1 cm distance between them to avoid reactions in one and the decay in the following target; this covers nearly 100% for $\tau \leq 20$ ps.

A selection on incoming charge Z is applied using the first detector and in the second and third detector the outgoing charge is fixed to $Z-1$. In the simulation, the energy-loss in the detectors is treated explicitly with a resolution of $\Delta E/E = 3.5\%$ and a selection on $(Z-1) = 8$ is applied. The silicon detectors themselves act as targets (cross section scaled with $A^{1/3}$ compared to Pt) contributing to the Δv distribution as peaks at both sides of the spectrum, Fig. 7(c). The main difficulty caused by this background is that an empty target measurement will not allow to subtract the background contribution. Due to the missing energy loss in the reaction target the background from one silicon detector will overlap with the background from another detector.

This challenge can be tackled by using the information from an empty target run as input to the simulation to improve the shape of the background contribution. Also, the total amount of events which contributes to the background can be determined from the experimental data. From the known integral and the relative amplitudes of the background components they can be uniquely identified and fixed. A second approach is to use in the here discussed ^{26}O example the ^{25}O [6,9,10] reference channel as "null measurement", where the desired contributions are measured all together in the Δv spectrum, but no lifetime is expected.

The full Δv distribution is then fitted using the shapes from the simulation for several different τ, where the amplitude of the simulated spectrum is the only free parameter and the background is fixed, Fig. 7(d). Here, the advantage of the target stack is that the background peaks from first and second silicon detector contribute only at the extreme edges of the Δv spectrum. Even though the last target is most sensitive to the shortest lifetimes, several peaks are present and one could also only fit the region where the silicon detectors do not contribute.

Table 1
Extracted lifetimes τ_{fit} from several analyses and their mean uncertainties in comparison with the simulated input data τ_{sim} for the examined test case with eight targets, cf. Fig. 7 & 8.

τ_{sim} (ps)	τ_{fit} (ps)	$\Delta\tau$ stat. (ps)
0.20	0.20	±0.01
0.50	0.51	±0.01
1.00	1.00	±0.01
1.50	1.52	±0.01
2.00	2.03	±0.01
2.50	2.50	±0.02

2.5. Sensitivity

The determined χ^2 is considered to be smallest in case of the real lifetime, cf. Fig. 7(e), which allows to determine the statistical uncertainty from the minimum of the χ^2 parabola as $\chi^2_{min} + 1$. The minimum number of reconstructed events in the experiment needed to determine a lifetime of 0.5 ps by a 5σ interval, only governed by the statistical uncertainty, is 5×10^3 events. In the case discussed above, the spectrum is clearly different from an instantaneous decay of a resonant ground state, see Fig. 5, which can be shown experimentally also with the one-neutron decay of ^{25}O. The method is proven to measure and confirm the neutron radioactive decay down to $\tau = 0.50 \pm 0.01(\text{stat})$ ps or even $\tau = 0.20 \pm 0.01(\text{stat})$ ps within at least a 5σ uncertainty interval under the examined conditions. Other systematic and experimental effects are not presented here. Further results from the same simulation, cf. Figs. 7 and 8, are summarized in Tab. 1.

3. Summary and outlook

We developed a method which will allow to directly measure the lifetime of neutron-unbound states from decays inside and outside the target. This method fills a gap for such decay studies and allows to measure lifetimes in the lower time regime of radioactive decays, the picosecond range. The method considers the velocity-difference spectrum between neutron(s) and fragment where the ratio of inside-to-outside decays translate into a characteristic spectrum, analysing the spectrum's

shape results in the lifetime. Thus, this method is independent of an absolute calibration of the velocity-difference spectrum.

The case of the $2n$ emitter ^{26}O was studied in detail. With a specific choice of target material and thickness according to the incoming energy we could show with simulations that the method is sensitive down to a lifetime of $\tau = 0.2$ ps within 5σ under the given conditions and statistics, especially in a target-stack arrangement. The method is however applicable to measure longer lifetimes even with one target. The systematics can be adapted for other possible candidate nuclei according to the lifetime.

Other possible candidates for neutron radioactive decays could be ^{16}B [14] or other *sd*-shell nuclei with a low ground-state energy and a sufficiently large angular momentum barrier.

Acknowledgements

This work was supported by the Deutsche Forschungsgemeinschaft through Grant No. SFB 1245 and by the Helmholtz International Center for FAIR within the framework of the LOEWE program launched by the state of Hesse.

References

[1] M. Pfützner, M. Karny, L.V. Grigorenko, K. Riisager, Radioactive decays at limits of nuclear stability, Rev. Modern Phys. 84 (2012) 567–619. http://dx.doi.org/10.1103/RevModPhys.84.567.

[2] M. Pfützner, Particle radioactivity of exotic nuclei, Physica Scripta Volume T 152 (1) (2013) 014014. http://dx.doi.org/10.1088/0031-8949/2013/T152/014014.

[3] L.V. Grigorenko, I.G. Mukha, M.V. Zhukov, Lifetime and Fragment Correlations for the Two-Neutron Decay of ^{26}O Ground State, Phys. Rev. Lett. 111 (4) (2013) 042501. http://dx.doi.org/10.1103/PhysRevLett.111.042501.

[4] M. Thoennessen, Reaching the limits of nuclear stability, Rep. Progr. Phys. 67 (2004) 1187–1232. http://dx.doi.org/10.1088/0034-4885/67/7/R04.

[5] A.H. Wapstra, IUPAC-IUPAP Transfermium Working Group, Criteria that must be satisfied for the discovery of a new chemical element to be recognized, Pure Appl. Chem. 63 (1991) 879–886. http://dx.doi.org/10.1351/pac199163060879.

[6] C. Caesar, J. Simonis, T. Adachi, Y. Aksyutina, J. Alcantara, S. Altstadt, H. Alvarez-Pol, N. Ashwood, T. Aumann, V. Avdeichikov, M. Barr, S. Beceiro, D. Bemmerer, J. Benlliure, C.A. Bertulani, K. Boretzky, M.J.G. Borge, G. Burgunder, M. Caamano, E. Casarejos, W. Catford, J. Cederkäll, S. Chakraborty, M. Chartier, L. Chulkov, D. Cortina-Gil, U. Datta Pramanik, P. Diaz Fernandez, I. Dillmann, Z. Elekes, J. Enders, O. Ershova, A. Estrade, F. Farinon, L.M. Fraile, M. Freer, M. Freudenberger, H.O.U. Fynbo, D. Galaviz, H. Geissel, R. Gernhäuser, P. Golubev, D. Gonzalez Diaz, J. Hagdahl, T. Heftrich, M. Heil, M. Heine, A. Heinz, A. Henriques, M. Holl, J.D. Holt, G. Ickert, A. Ignatov, B. Jakobsson, H.T. Johansson, B. Jonson, N. Kalantar-Nayestanaki, R. Kanungo, A. Kelic-Heil, R. Knöbel, T. Kröll, R. Krücken, J. Kurcewicz, M. Labiche, C. Langer, T. Le Bleis, R. Lemmon, O. Lepyoshkina, S. Lindberg, J. Machado, J. Marganiec, V. Maroussov, J. Menéndez, M. Mostazo, A. Movsesyan, A. Najafi, T. Nilsson, C. Nociforo, V. Panin, A. Perea, S. Pietri, R. Plag, A. Prochazka, A. Rahaman, G. Rastrepina, R. Reifarth, G. Ribeiro, M.V. Ricciardi, C. Rigollet, K. Riisager, M. Röder, D. Rossi, J. Sanchez del Rio, D. Savran, H. Scheit, A. Schwenk, H. Simon, O. Sorlin, V. Stoica, B. Streicher, J. Taylor, O. Tengblad, S. Terashima, R. Thies, Y. Togano, E. Uberseder, J. Van de Walle, P. Velho, V. Volkov, A. Wagner, F. Wamers, H. Weick, M. Weigand, C. Wheldon, G. Wilson, C. Wimmer, J.S. Winfield, P. Woods, D. Yakorev, M.V. Zhukov, A. Zilges, M. Zoric, K. Zuber, Beyond the neutron drip line: The unbound oxygen isotopes ^{25}O and ^{26}O, Phys. Rev. C 88 (3) (2013) 034313. http://dx.doi.org/10.1103/PhysRevC.88.034313.

[7] Z. Kohley, T. Baumann, D. Bazin, G. Christian, P.A. DeYoung, J.E. Finck, N. Frank, M. Jones, E. Lunderberg, B. Luther, S. Mosby, T. Nagi, J.K. Smith, J. Snyder, A. Spyrou, M. Thoennessen, Study of Two-Neutron Radioactivity in the Decay of ^{26}O, Phys. Rev. Lett. 110 (15) (2013) 152501. http://dx.doi.org/10.1103/PhysRevLett.110.152501.

[8] L.V. Grigorenko, I.G. Mukha, C. Scheidenberger, M.V. Zhukov, Two-neutron radioactivity and four-nucleon emission from exotic nuclei, Phys. Rev. C 84 (2) (2011) 021303. http://dx.doi.org/10.1103/PhysRevC.84.021303.

[9] E. Lunderberg, P.A. DeYoung, Z. Kohley, H. Attanayake, T. Baumann, D. Bazin, G. Christian, D. Divaratne, S.M. Grimes, A. Haagsma, J.E. Finck, N. Frank, B. Luther, S. Mosby, T. Nagi, G.F. Peaslee, A. Schiller, J. Snyder, A. Spyrou, M.J. Strongman, M. Thoennessen, Evidence for the Ground-State Resonance of ^{26}O, Phys. Rev. Lett. 108 (2012) 142503. http://dx.doi.org/10.1103/PhysRevLett.108.142503.

[10] Y. Kondo, T. Nakamura, R. Tanaka, R. Minakata, S. Ogoshi, N.A. Orr, N.L. Achouri, T. Aumann, H. Baba, F. Delaunay, P. Doornenbal, N. Fukuda, J. Gibelin, J.W. Hwang, N. Inabe, T. Isobe, D. Kameda, D. Kanno, S. Kim, N. Kobayashi, T. Kobayashi, T. Kubo, S. Leblond, J. Lee, F.M. Marqués, T. Motobayashi, D. Murai, T. Murakami, K. Muto, T. Nakashima, N. Nakatsuka, A. Navin, S. Nishi, H. Otsu, H. Sato, Y. Satou, Y. Shimizu, H. Suzuki, K. Takahashi, H. Takeda, S. Takeuchi, Y. Togano, A.G. Tuff, M. Vandebrouck, K. Yoneda, Nucleus ^{26}O: A Barely Unbound System beyond the Drip Line, Phys. Rev. Lett. 116 (2016) 102503. http://dx.doi.org/10.1103/PhysRevLett.116.102503.

[11] R.A. Kryger, A. Azhari, J. Brown, J. Caggiano, M. Hellström, J.H. Kelley, B.M. Sherrill, M. Steiner, M. Thoennessen, Upper limit of the lifetime of ^{16}B, Phys. Rev. C 53 (1996) 1971–1973. http://dx.doi.org/10.1103/PhysRevC.53.1971.

[12] K. Hagino, H. Sagawa, Decay dynamics of the unbound ^{25}O and ^{26}O nuclei, Phys. Rev. C 93 (2016) 034330. http://dx.doi.org/10.1103/PhysRevC.93.034330.

[13] L.V. Grigorenko, M.V. Zhukov, Continuum excitations of ^{26}O in a three-body model: 0^+ and 2^+ states, Phys. Rev. C 91 (2015) 064617. http://dx.doi.org/10.1103/PhysRevC.91.064617.

[14] M. Thoennessen, G. Christian, Z. Kohley, T. Baumann, M. Jones, J.K. Smith, J. Snyder, A. Spyrou, Novel techniques to search for neutron radioactivity, Nucl. Instrum. Methods Phys. Res. A 729 (2013) 207–211. http://dx.doi.org/10.1016/j.nima.2013.07.035.

[15] P.J. Nolan, J.F. Sharpey-Schafer, REVIEW: The measurement of the lifetimes of excited nuclear states, Rep. Progr. Phys. 42 (1979) 1–86. http://dx.doi.org/10.1088/0034-4885/42/1/001.

[16] P. Voss, T. Baumann, D. Bazin, A. Dewald, H. Iwasaki, D. Miller, A. Ratkiewicz, A. Spyrou, K. Starosta, M. Thoennessen, C. Vaman, J.A. Tostevin, ^{19}Mg two-proton decay lifetime, Phys. Rev. C 90 (2014) 014301. http://dx.doi.org/10.1103/PhysRevC.90.014301.

[17] C. Scheidenberger, H. Geissel, H.H. Mikkelsen, F. Nickel, S. Czajkowski, H. Folger, H. Irnich, G. Münzenberg, W. Schwab, T. Stöhlker, T. Suzuki, B. Voss, Energy-Loss-Straggling Experiments with Relativistic Heavy Ions in Solids, Phys. Rev. Lett. 77 (1996) 3987–3990. http://dx.doi.org/10.1103/PhysRevLett.77.3987.

[18] T. Kobayashi, N. Chiga, T. Isobe, Y. Kondo, T. Kubo, K. Kusaka, T. Motobayashi, T. Nakamura, J. Ohnishi, H. Okuno, H. Otsu, T. Sako, H. Sato, Y. Shimizu, K. Sekiguchi, K. Takahashi, R. Tanaka, K. Yoneda, SAMURAI spectrometer for RI beam experiments, Nucl. Instrum. Methods Phys. Res. B (ISSN: 0168-583X) 317 (Part B) (2013) 294–304. http://dx.doi.org/10.1016/j.nimb.2013.05.089.

[19] R^{3}B Collaboration, Technical Proposal for the Design, Construction, Commissioning and Operation of R^{3}B, 2005.

[20] T. Baumann, J. Boike, J. Brown, M. Bullinger, J.P. Bychoswki, S. Clark, K. Daum, P.A. Deyoung, J.V. Evans, J. Finck, N. Frank, A. Grant, J. Hinnefeld, G.W. Hitt, R.H. Howes, B. Isselhardt, K.W. Kemper, J. Longacre, Y. Lu, B. Luther, S.T. Marley, D. McCollum, E. McDonald, U. Onwuemene, P.V. Pancella, G.F. Peaslee, W.A. Peters, M. Rajabali, J. Robertson, W.F. Rogers, S.L. Tabor, M. Thoennessen, E. Tryggestad, R.E. Turner, P.J. Vanwylen, N. Walker, Construction of a modular large-area neutron detector for the NSCL, Nucl. Instrum. Methods A 543 (2005) 517–527. http://dx.doi.org/10.1016/j.nima.2004.12.020.

Appendix B

Analysis Methods

B.1 Breit-Wigner Line Shapes

In the following, the penetrability P_l and shift S_l functions are derived for different partial waves. In case of neutron scattering, the resonance solutions are superpositions of spherical Bessel functions. For charged particles the solutions are replaced by Coulomb functions [121].

The Breit-Wigner resonance line shape is characterized by the resonance energy E_r and the width Γ_l. They are functions of P_l and S_l, as shown in Eqs. 4.37 and 4.41,

$$P_l(E) = ka\frac{1}{F_l^2 + G_l^2}, \tag{B.1}$$

$$S_l(E) = ka\frac{\dot{F}_l F_l + \dot{G}_l G_l}{F_l^2 + G_l^2}. \tag{B.2}$$

F_l and G_l are expressed by the spherical Bessel functions of first kind j_l and of second kind n_l (or called Neumann functions), respectively, evaluated at $\rho = kr$ [53],

$$F_l(r) = kr \cdot j_l(\rho), \tag{B.3}$$

$$G_l(r) = kr \cdot n_l(\rho). \tag{B.4}$$

The used Bessel functions are listed in Table B.1. Following, P_l and S_l are calculated*, the derivative is

$$\dot{F} = \frac{\mathrm{d}}{\mathrm{d}\rho}F(\rho)\bigg|_{r=a}. \tag{B.5}$$

All functions are evaluated at the channel radius $r = a$, with $\rho = ka$ and $k = \sqrt{\frac{2\mu E}{\hbar c}}$. The resulting expressions are given in Table B.2.

*In Eq. (3F-38) in Ref. [53] a factor ka is missing for Δ_l.

Table B.1: Bessel functions of first j_l and second n_l kind for different orders (partial waves).

Order l	$j_l(\rho)$	$n_l(\rho)$
0	$\frac{\sin\rho}{\rho}$	$-\frac{\cos\rho}{\rho}$
1	$\frac{\sin\rho}{\rho^2}-\frac{\cos\rho}{\rho}$	$-\frac{\cos\rho}{\rho^2}-\frac{\sin\rho}{\rho}$
2	$\left(\frac{3}{\rho^2}-1\right)\frac{\sin\rho}{\rho}-\frac{3\cos\rho}{\rho^2}$	$\left(-\frac{3}{\rho^2}+1\right)\frac{\cos\rho}{\rho}-\frac{3\sin\rho}{\rho^2}$
3	$\left(\frac{15}{\rho^3}-\frac{6}{\rho}\right)\frac{\sin\rho}{\rho}-\left(\frac{15}{\rho^2}-1\right)\frac{\cos\rho}{\rho}$	$\left(-\frac{15}{\rho^3}+\frac{6}{\rho}\right)\frac{\cos\rho}{\rho}-\left(\frac{15}{\rho^2}-1\right)\frac{\sin\rho}{\rho}$

Table B.2: Penetrability P_l and shift S_l functions for different partial waves evaluated at $\rho = ka$.

Order l	$P_l(\rho)$	$S_l(\rho)$
0	ρ	0
1	$\frac{\rho^3}{\rho^2+1}$	$-\frac{1}{\rho^2+1}$
2	$\frac{\rho^5}{\rho^4+3\rho^2+9}$	$-\frac{3(6+\rho^2)}{\rho^4+3\rho^2+9}$
3	$\frac{\rho^7}{\rho^6+6\rho^4+45\rho^2+225}$	$-\frac{3(225+30\rho^2+2\rho^4)}{\rho^6+6\rho^4+45\rho^2+225}$

B.2 Least-Squares Fit to a Spectrum

Models are used to describe experimental spectra. In a fit procedure the model and data can be compared to each other.

Here, a minimization procedure according to the χ^2 is applied to find the best description of the data points. The χ^2 is defined as the weighted sum of the squared differences between the set of experimental data points $\{x_i, y_i\}$ and model function $f(x_i)$ [201],

$$\chi^2 = \sum_i \frac{1}{\sigma_i^2} \left[y_i - f(x_i)\right]^2 . \tag{B.6}$$

The uncertainty σ_i follows in a counting experiment Poisson statistics why $\sigma_i = \sqrt{y_i}$.

However, σ_i is only an estimate because the proper uncertainty comes from the parent distribution which is not known. Especially, it does not work for low-statistics experiment where Poisson statistics does not apply [201]. Here, the uncertainty from the fitted curve $\sigma_i^2 = f(x_i)$ is used which should be closer to the parent distribution.

When fitting relative-energy or γ-ray spectra the χ^2 formulation (Eq. B.6) with $\sigma_i^2 = f(x_i)$ ($\sigma_i^2 := 1$ for $f(x_i) = 0$) is embedded into the `Minuit` program [202] using the `Migrad` algorithm for function minimization and error analysis. In case of the relative-energy fitting, the Breit-Wigner functions are in each minimization step folded with the response matrix and the χ^2 is recalculated. After convergence is reached, the parameters' uncertainties are taken from the `HESSE` error matrix.

Another reason why the uncertainty from the function should be used is described in detail in Ref. [185]. It is derived that the fitted function has the same area as the data what is true for any test function and especially important for low-statistics analysis.

Appendix C

BigRIPS and SAMURAI Setup

C.1 BigRIPS Setup

BigRIPS setting for the production runs optimized for ^{29}F, see Table C.1.

C.2 SAMURAI Setup

C.2.1 MINOS Details

The technical details of MINOS and the parameters as applied in the experiment are listed in Table C.2, the general information are taken from Refs. [151, 153].

C.2.2 Material Budget in SAMURAI Beam Line

The material budget in the SAMURAI beam line is listed in Table C.3.

C.2.3 Photogrammetry Results

Positions of the detectors in the experimental hall relative to the center of the SAMURAI magnet and the zero-degree line are given in Fig. C.1. The coordinates have been obtained by a photogrammetry measurement which was analyzed by T. Ozaki [163].

*The KDC is a drift chamber that was only installed for test purposes.

Table C.1: BigRIPS setting for the ^{29}F production runs. The used detectors are included and the set-values of the dipole magnets D# are given.

Focus	Device	Setting
F0		
	Target	^{9}Be, 15 mm
	D1	8.6061 T m
F1		
	Slit	$\pm$119.0 mm
	Wedge Degrader	Al, 15 mm, 18.66 mrad
	D2	8.0673 T m
F2		
	Slit	$\pm$6.0 mm
F3		
	Plastic Sci.	3 mm
	D3	8.0053 T m
	D4	8.0053 T m
F5		
	PPAC	
	Wedge Degrader	Al, 7 mm, 5.969 mrad
	Slit	$\pm$120.0 mm
	PPAC	240 mm(X), 100 mm(Y)
	Plastic Sci.	3 mm
	D5	7.6896 T m
	D6	7.6896 T m
F7		
	Slit left	8.0 mm
	Slit right	4.0 mm
	Plastic Sci.	3 mm

Table C.2: MINOS parameters.

Parameter	
Target length	150 mm
Target radius	28 mm
Target density	0.0753 g/cm^3
TPC length	300 mm
TPC inner radius	45 mm
TPC outer radius	95 mm
Gas composition	Ar(82 %), CF_4(15 %), isobutane(3 %)
Micromegas readout	3604 pads
Shaping time	333 ns
Time sampling	50 MHz

Table C.3: Material budget in the beam line starting at the entrance of the SAMURAI cave.

Detector	Material	Area density ($\mathrm{mg/cm^2}$)	Length (mm)
SBT	Plastic	103	1
	Plastic	103	1
	Mylar	13	0.096
Drift	Vacuum	0	901.527
BDC1	Kapton	23	0.160
	Ibutane	2	120
	Kapton	11	0.08
Drift	Vacuum	0	382
KDC*	Aramid	3	0.024
	Ibutane	1	100
	Mylar	6	0.044
Drift	Vacuum	0	397.14
BDC2	Kapton	23	0.16
	Ibutane	2	120
	Kapton	11	0.080
Drift	Vacuum	0	114.0
	Kapton	18	0.125
	Air	45	381.9
MINOS	Kapton	18	0.125
	Vacuum	0	493.3
	Mylar	17	0.125
	LH_2	11.3552	151
	Mylar	21	0.15
Drift	Vacuum	0	236.8
	Kapton	18	0.129
	Air	20	169.2
	Kapton	18	0.129
	Vacuum	0	920
FDC1	Kapton	23	0.16
	Aramid	1	0.008
	Kapton	17	0.120
	Ibutane	5	336.0

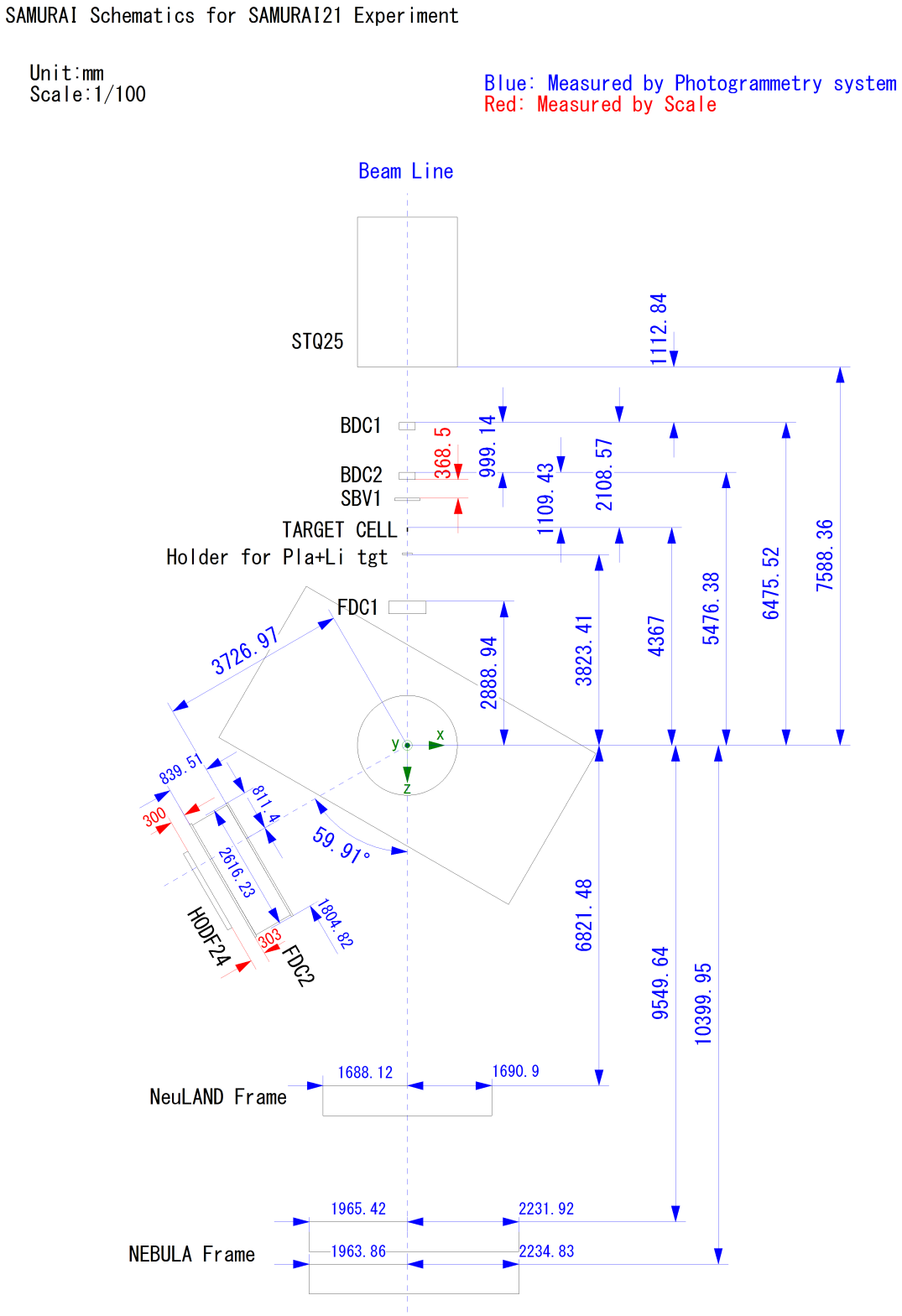

Figure C.1: Detector positions in the SAMURAI cave obtained in a photogrammetry measurement.

Appendix D

Calibration

D.1 Drift-Chamber Position Resolution

The BDCs have a simple structure. The x position of a particle track through the detector is determined from wires in vertical direction and accordingly, the y position is deduced from horizontal wires separately. There are $n = 4$ layers in x and 4 layers oriented in y direction.

The track is determined in a linear regression model from the single interactions of the passing particle. The x_k position at the kth layer with in-beam position z_k is

$$x_k = \alpha \cdot z_k + x_0. \tag{D.1}$$

The parameters α and x_0 need to be determined to describe the linear track. The parameters are obtained in a least-square approach [201] based on the linear model. The multiple linear regression can be formulated in a matrix representation,

$$\vec{b} = A \cdot \vec{a}. \tag{D.2}$$

The parameter vector $\vec{a}$ is thus

$$\vec{a} = A^{-1} \cdot \vec{b}. \tag{D.3}$$

In the linear case of Eq. D.1 this becomes

$$\begin{pmatrix} x_0 \\ \alpha \end{pmatrix} = \begin{pmatrix} n & \sum_{i=1}^{n} z_i \\ \sum_{i=1}^{n} z_i & \sum_{i=1}^{n} z_i^2 \end{pmatrix}^{-1} \cdot \begin{pmatrix} \sum_{i=1}^{n} x_i \\ \sum_{i=1}^{n} x_i z_i \end{pmatrix}. \tag{D.4}$$

The goal is to determine the position resolution of each layer from the resolution of the residual

r_k, that is defined as

$$\begin{aligned} r_k &= x_k^{\text{meas}} - x_k^{\text{track}} \\ &= x_k^{\text{meas}} - (\alpha z_k + x_0), \end{aligned} \tag{D.5}$$

with the measured position x_k^{meas} at layer k. In terms of the Gaussian error propagation the resolution is derived as

$$\sigma_{r_k}^2 = \sum_{i=1}^{n} \left(\frac{\partial r_k}{\partial x_i} \sigma_{x_i} \right)^2 . \tag{D.6}$$

It is assumed that the position resolution is the same for all layers $\sigma_{x_i} = \sigma_x$ and the z_i-position uncertainty is negligible. The derivation is

$$\sigma_{r_k}^2 = \sigma_x^2 \cdot \underbrace{\sum_{i=1}^{n} \left[\delta_{ik} - \frac{n z_i z_k - z_i \sum_{i=1}^{n} z_i - z_k \sum_{i=1}^{n} z_i + \sum_{i=1}^{n} z_i^2}{n \sum_{i=1}^{n} z_i^2 - \left(\sum_{i=1}^{n} z_i \right)^2} \right]^2}_{=\kappa} . \tag{D.7}$$

The position resolution is calculated with the conversion factor κ,

$$\sigma_x = \frac{\sigma_{r_k}}{\sqrt{\kappa}} . \tag{D.8}$$

The conversion factor for the BDCs is listed in Tab. D.1. In the same way the position resolution of the FDCs is determined. The expressions become more complex because wires are rotated in the x-y-plane, and the x and y position are deduced from one track. The residual relative to the local hit position is here

$$r_k = x_k^{\text{meas}} - \left[(\alpha z_k + x_0) \cdot \cos(\theta_k) + (\beta z_k + y_0) \cdot \sin(\theta_k) \right] , \tag{D.9}$$

with the wire's rotation angle θ_k. The least-square approach in matrix representation is

$$\begin{pmatrix} x_0 \\ \alpha \\ y_0 \\ \beta \end{pmatrix} = A^{-1} \cdot \begin{pmatrix} \sum_{i=1}^{n} x_i \cos(\theta_i) \\ \sum_{i=1}^{n} x_i z_i \cos(\theta_i) \\ \sum_{i=1}^{n} x_i \sin(\theta_i) \\ \sum_{i=1}^{n} x_i z_i \sin(\theta_i) \end{pmatrix} , \tag{D.10}$$

with

$$A^{-1} = \frac{1}{2} \cdot \begin{pmatrix} 2n\cos^2(\theta_i) & 2\sum_{i=1}^{n} z_i \cos^2(\theta_i) & n(\sin(2\theta_i)) & \sum_{i=1}^{n} z_i(\sin(2\theta_i)) \\ 2\sum_{i=1}^{n} z_i \cos^2(\theta_i) & 2\sum_{i=1}^{n} z_i^2 \cos^2(\theta_i) & \sum_{i=1}^{n} z_i(\sin(2\theta_i)) & \sum_{i=1}^{n} z_i^2(\sin(2\theta_i)) \\ n\sin(2\theta_i) & \sum_{i=1}^{n} z_i \sin(2\theta_i) & 2n\sin^2(\theta_i) & 2\sum_{i=1}^{n} z_i \sin^2(\theta_i) \\ \sum_{i=1}^{n} z_i \sin(2\theta_i) & \sum_{i=1}^{n} z_i^2 \sin(2\theta_i) & 2\sum_{i=1}^{n} z_i \sin^2(\theta_i) & 2\sum_{i=1}^{n} z_i^2 \sin^2(\theta_i) \end{pmatrix}^{-1} . \tag{D.11}$$

Starting with this expression, the position resolution is derived in the same way as in Eq. D.6. The expression becomes rather complex, it is evaluated in `Mathematica` [203]. It is also refrained from giving the resulting formula explicitly but the conversion factors κ, used in Eq. D.8, are given in Table D.1.

Table D.1: Conversion factor κ to determine the position resolution σ_x from the residual resolution σ_{r_k} for BDCs, FDC1, and FDC2.

Layer	κ		
k	BDC	FDC1	FDC2
1	0.382	0.702	0.720
2	0.618	0.762	0.741
3	0.382	0.562	0.597
4	0.618	0.674	0.637
5	0.618	0.651	0.681
6	0.382	0.738	0.711
7	0.618	0.911	0.912
8	0.382	0.911	0.912
9		0.738	0.711
10		0.651	0.681
11		0.674	0.637
12		0.562	0.597
13		0.762	0.741
14		0.702	0.720

D.2 DALI2 Calibration

The γ-ray sources used for the energy calibration of DALI2 are listed in Table D.2.

Table D.2: Used γ-ray sources for the energy calibration of DALI2.

Source	γ Energy (keV)	Activity (kBq)	at ref. day
^{137}Cs	661.657	8.23	2010/03/16
^{60}Co	1173.228	88.1	2010/03/16
	1332.501		
^{88}Y	898.042	852.0	2013/06/17
	1836.063		

List of NaI(Tl) crystals that show relatively small efficiency and low energy resolution in this experiment, and are thus not considered in the analysis. ID: $<$ 20, 24, 26, 28, 29, 32, 35, 36, 38, 45, 46, 47, 49, 54, 57, 58, 59, 60, 64, 66, 67, 88, 123

Appendix E

Three-Body Analysis in Jacobi Coordinates for ^{29}F

E.1 Fractional-Energy Spectra

Fitted fractional-energy spectra shown in Fig. E.1, for explanations see Sec. 8.2.3.

E.2 Three-Body Correlations in Jacobi Coordinates

Three-body correlation spectra in Jacobi coordinates shown in Figs. E.2, E.3, E.4, E.5 for different E_{fnn} regions.

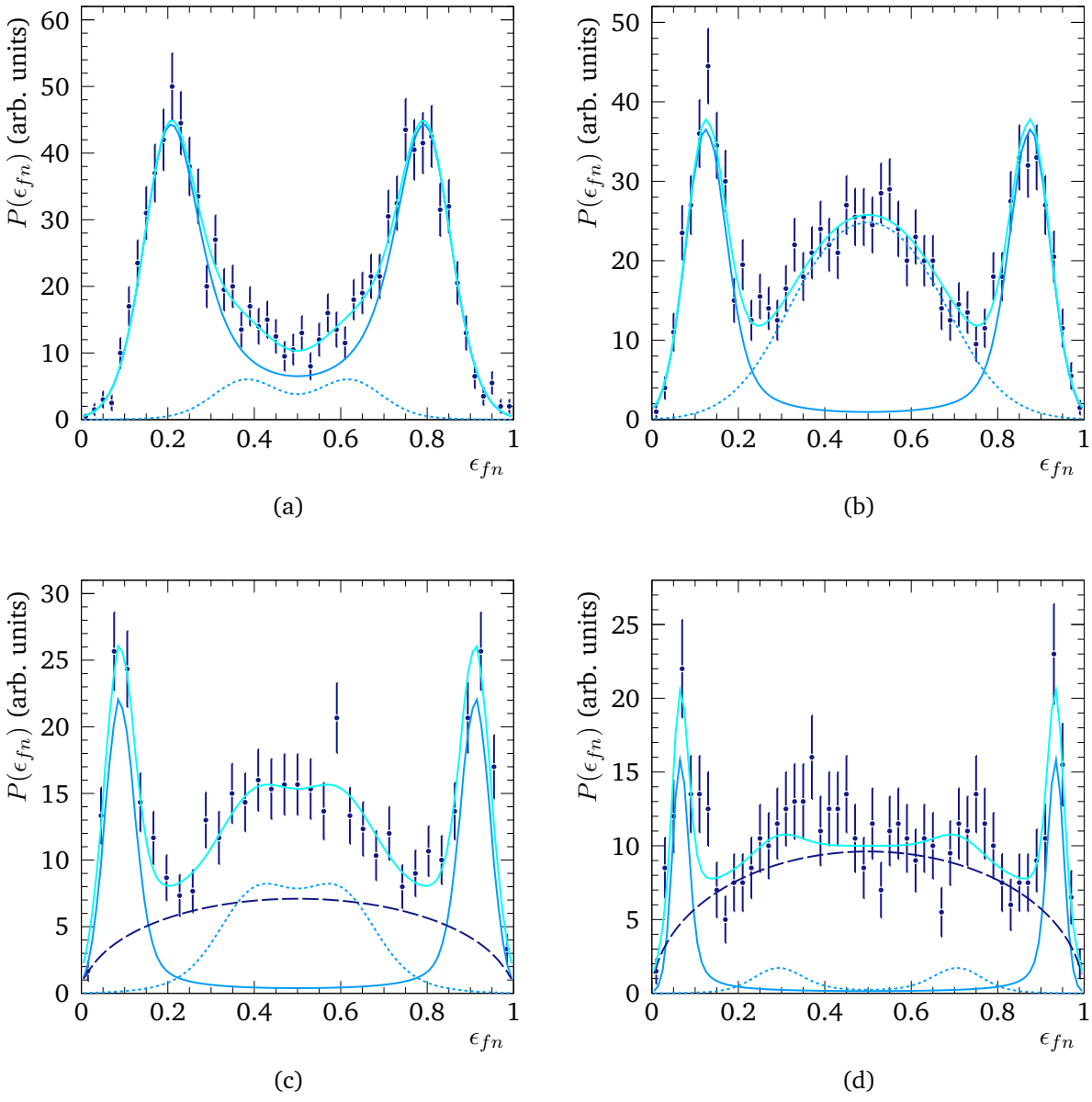

Figure E.1: Fractional-energy spectra ϵ_{fn} of ^{29}F in Y-system for different energies regions in E_{fnn}, see Sec. 8.2.3. The data (blue dots) are fit with a theory for sequential decay, the total fit is shown as cyan line.
(a) $0.9\,\mathrm{MeV} < E_{fnn} < 1.2\,\mathrm{MeV}$: $E^r_{fn} = 223(6)\,\mathrm{keV}$, $\Gamma_r = 114(16)\,\mathrm{keV}$ (blue line); $E^r_{fn} = 400(20)\,\mathrm{keV}$, $\Gamma^r < 50\,\mathrm{keV}$ (dashed blue line).
(b) $1.8\,\mathrm{MeV} < E_{fnn} < 2.3\,\mathrm{MeV}$: $E^r_{fn} = 241(5)\,\mathrm{keV}$, $\Gamma_r < 50\,\mathrm{keV}$; $E^r_{fn} = 914(62)\,\mathrm{keV}$, $\Gamma^r = 240(122)\,\mathrm{keV}$.
(c) $2.3\,\mathrm{MeV} < E_{fnn} < 3.0\,\mathrm{MeV}$: $E^r_{fn} = 223(7)\,\mathrm{keV}$, $\Gamma_r = 50\,\mathrm{keV}$ (fixed); $E^r_{fn} = 1053(36)\,\mathrm{keV}$, $\Gamma^r < 240\,\mathrm{keV}$ (fixed). Phase-space contributions become apparent (dashed dark blue line).
(d) $3.0\,\mathrm{MeV} < E_{fnn} < 4.0\,\mathrm{MeV}$: $E^r_{fn} = 219(8)\,\mathrm{keV}$, $\Gamma_r = 50\,\mathrm{keV}$ (fixed); $E^r_{fn} = 992(128)\,\mathrm{keV}$, $\Gamma^r = 250\,\mathrm{keV}$ (fixed). Phase-space contribution as dashed dark blue line.

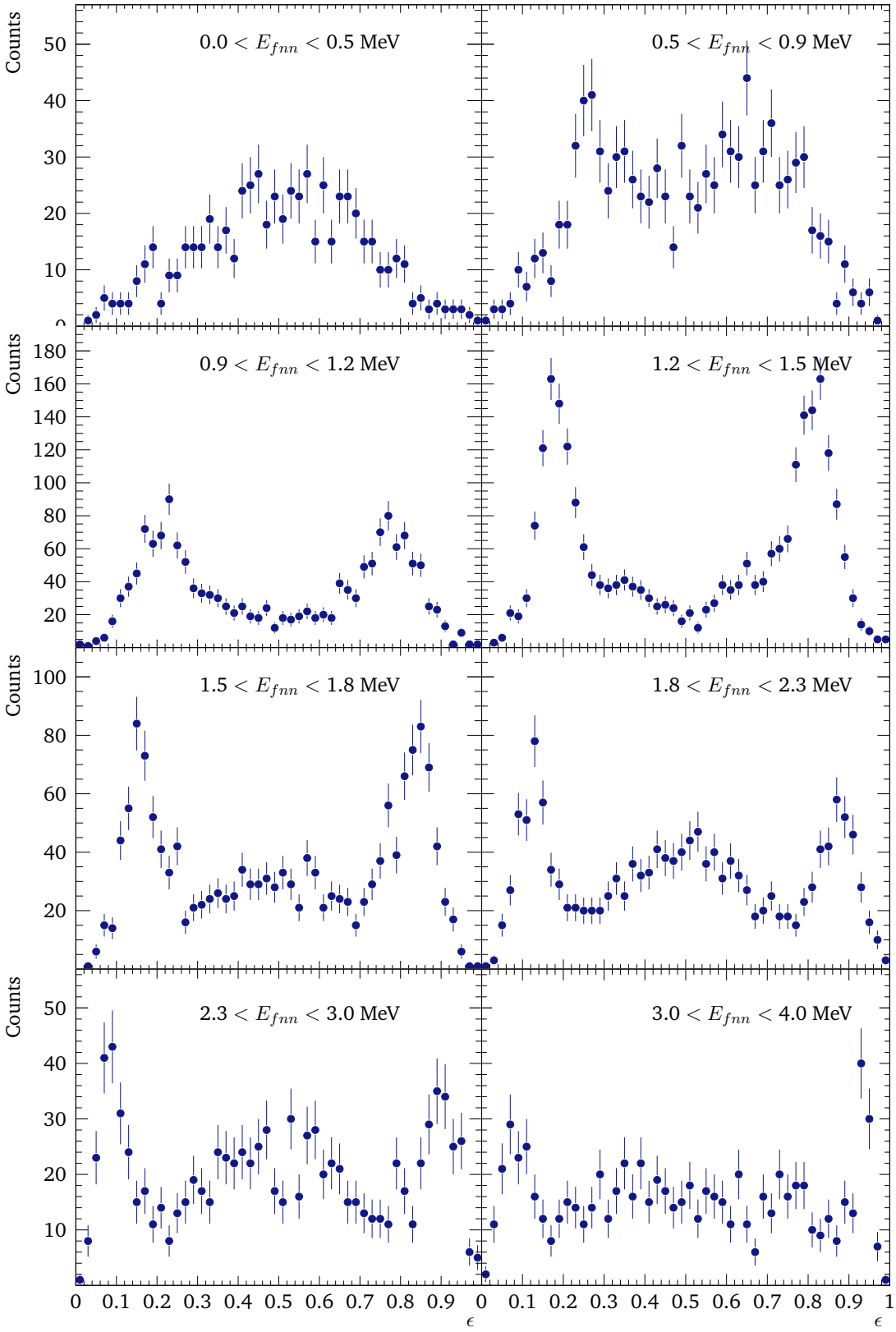

Figure E.2: Fractional energy in Y-system.

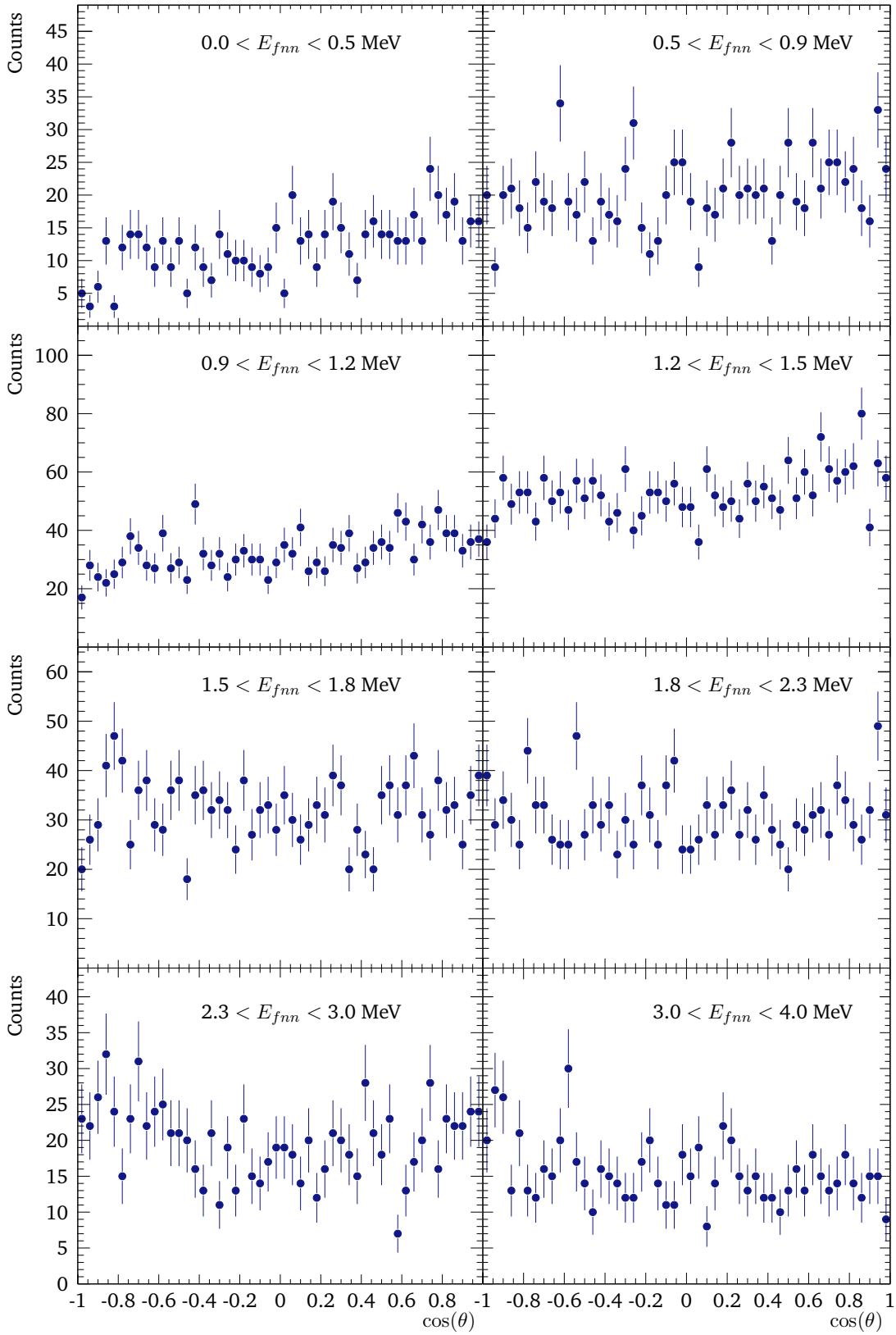

Figure E.3: Angular distribution in Y-system.

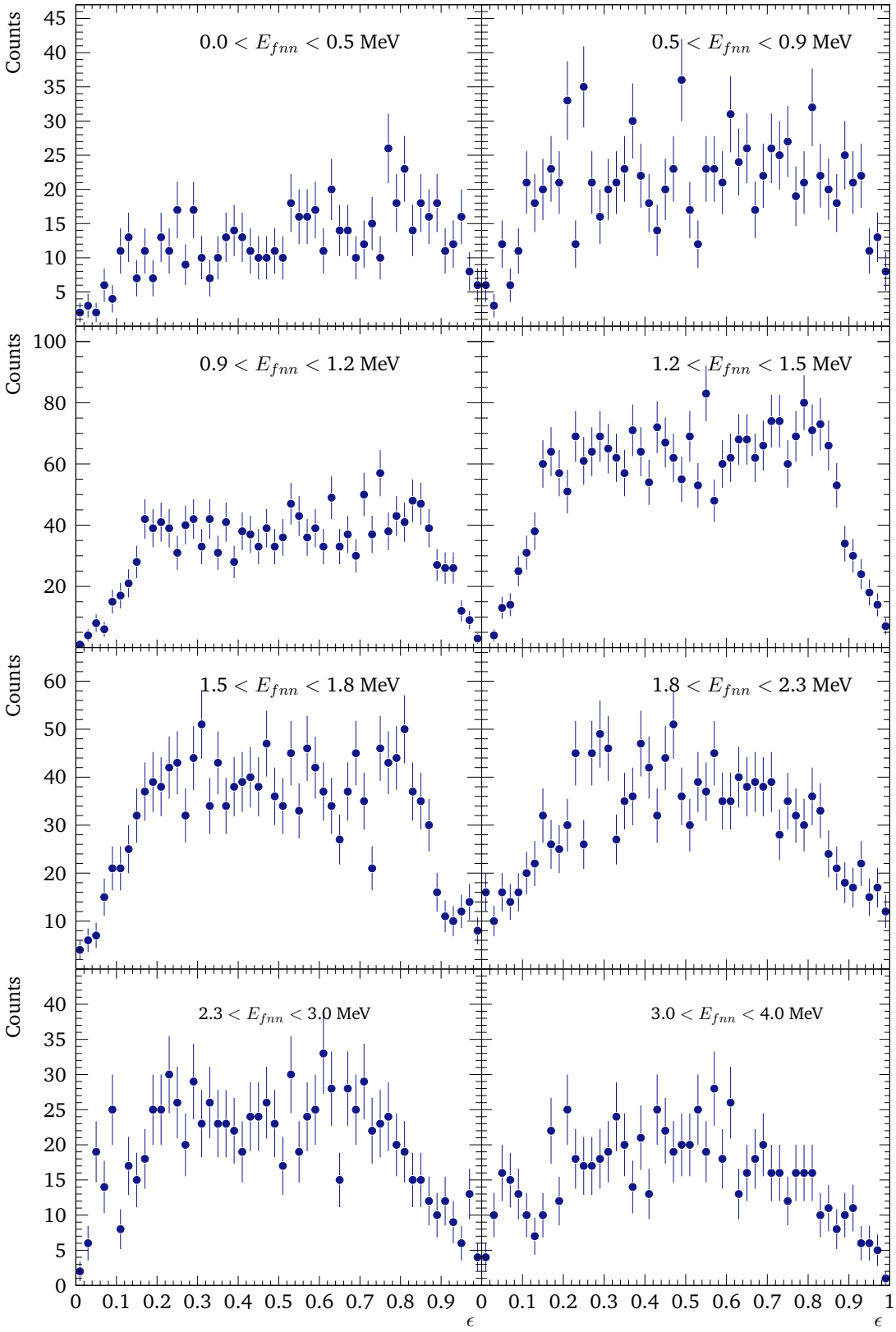

Figure E.4: Fractional energy in T-system.

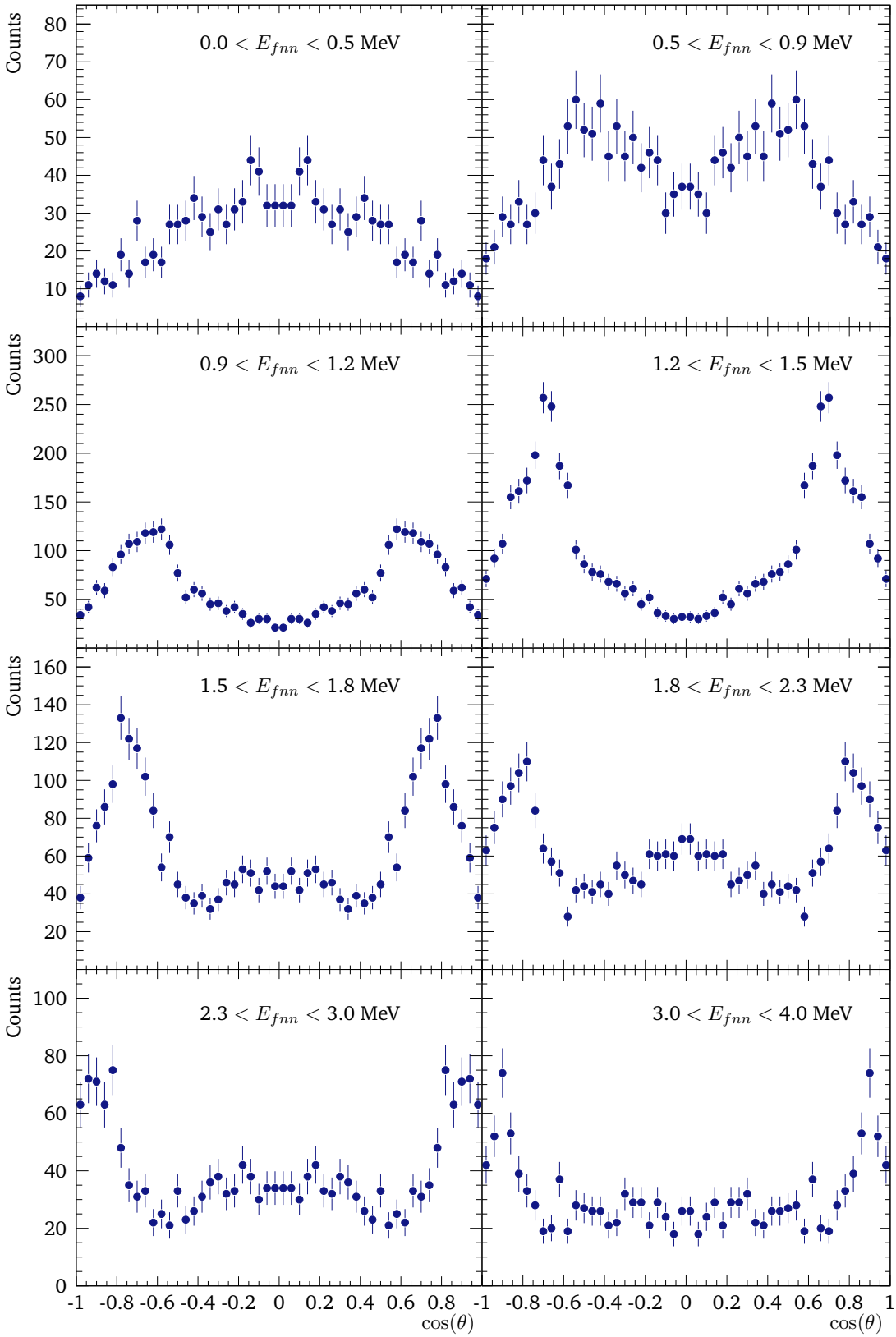

Figure E.5: Angular distribution in T-system.

E.3 Relative-energy Spectrum

^{29}F relative-energy spectrum fit with an additional resonance at $\sim$ 800 keV, see Fig. E.6, cf. Sec. 8.2.6.

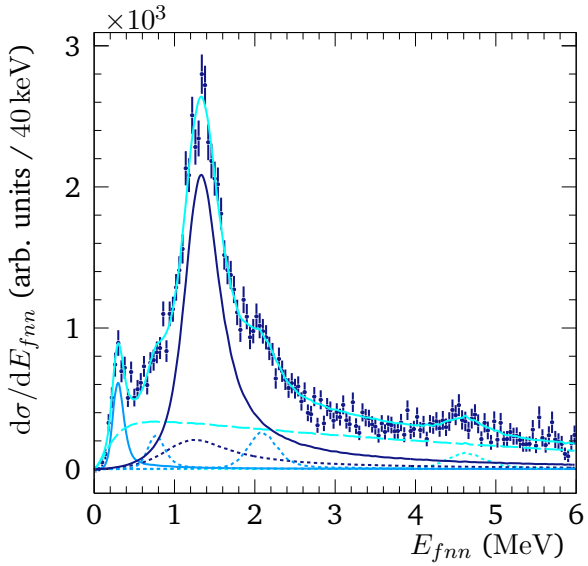

Figure E.6: Relative-energy spectrum of ^{29}F* fit with sequential Breit-Wigner line shapes and an additional resonance in comparison to the result in Fig. 8.19, $\chi^2_{\mathrm{red}} = 1.11$.

Bibliography

[1] The Nuclide Chart. URL http://people.physics.anu.edu.au/~ecs103/chart/. Accessed: 2019-04-18.

[2] A.H. Becquerel. On radioactivity, a new property of matter, Dec 1903. URL https://www.nobelprize.org/prizes/physics/1903/becquerel/lecture/. Nobel lecture.

[3] P. Radvanyi and J. Villain. The discovery of radioactivity. *Comptes Rendus Physique*, 18 (9):544 – 550, 2017. ISSN 1631-0705. doi: https://doi.org/10.1016/j.crhy.2017.10.008. URL http://www.sciencedirect.com/science/article/pii/S1631070517300786. Science in the making: The Comptes rendus de l'Académie des sciences throughout history.

[4] K. Heyde. Unveiling the many facets of the atomic nucleus: from Rutherford to exotic nuclei. *Physica Scripta*, T152:014006, Jan 2013. doi: 10.1088/0031-8949/2013/t152/014006. URL https://doi.org/10.1088%2F0031-8949%2F2013%2Ft152%2F014006.

[5] W.M. Elsasser. Sur le principe de Pauli dans les noyaux - II. *J. Phys. Radium*, 5(8):389–397, 1934. doi: https://doi.org/10.1051/jphysrad:0193400508038900. URL https://hal.archives-ouvertes.fr/jpa-00233250/document.

[6] M. Goeppert Mayer. On closed shells in nuclei. *Phys. Rev.*, 74:235–239, Aug 1948. doi: 10.1103/PhysRev.74.235. URL https://link.aps.org/doi/10.1103/PhysRev.74.235.

[7] M. Goeppert Mayer. On closed shells in nuclei. II. *Phys. Rev.*, 75:1969–1970, Jun 1949. doi: 10.1103/PhysRev.75.1969. URL https://link.aps.org/doi/10.1103/PhysRev.75.1969.

[8] M. Goeppert Mayer. Nuclear configurations in the spin-orbit coupling model. I. Empirical evidence. *Phys. Rev.*, 78:16–21, Apr 1950. doi: 10.1103/PhysRev.78.16. URL https://link.aps.org/doi/10.1103/PhysRev.78.16.

[9] O. Haxel, J.H.D. Jensen, and H.E. Suess. On the "magic numbers" in nuclear structure. *Phys. Rev.*, 75:1766–1766, Jun 1949. doi: 10.1103/PhysRev.75.1766.2. URL https://link.aps.org/doi/10.1103/PhysRev.75.1766.2.

[10] M.H.L. Pryce. Nuclear shell structure. *Reports on Progress in Physics*, 17(1):1–34, Jan 1954. doi: 10.1088/0034-4885/17/1/301. URL https://doi.org/10.1088%2F0034-4885%2F17%2F1%2F301.

[11] C. Thibault, R. Klapisch, C. Rigaud, A.M. Poskanzer, R. Prieels, L. Lessard, and W. Reisdorf. Direct measurement of the masses of ^{11}Li and $^{26-32}$Na with an on-line mass spectrometer. *Phys. Rev. C*, 12:644–657, Aug 1975. doi: 10.1103/PhysRevC.12.644. URL https://link.aps.org/doi/10.1103/PhysRevC.12.644.

[12] C. Détraz, D. Guillemaud, G. Huber, R. Klapisch, M. Langevin, F. Naulin, C. Thibault, L.C. Carraz, and F. Touchard. Beta decay of $^{27-32}$Na and their descendants. *Phys. Rev. C*, 19: 164–176, Jan 1979. doi: 10.1103/PhysRevC.19.164. URL https://link.aps.org/doi/10.1103/PhysRevC.19.164.

[13] C. Forssén, G. Hagen, M. Hjorth-Jensen, W. Nazarewicz, and J. Rotureau. Living on the edge of stability, the limits of the nuclear landscape. *Physica Scripta*, 2013(T152):014022, 2013. URL http://stacks.iop.org/1402-4896/2013/i=T152/a=014022.

[14] Y. Blumenfeld, T. Nilsson, and P. Van Duppen. Facilities and methods for radioactive ion beam production. *Physica Scripta*, T152:014023, Jan 2013. doi: 10.1088/0031-8949/2013/t152/014023. URL https://doi.org/10.1088%2F0031-8949%2F2013%2Ft152%2F014023.

[15] B.A. Brown. Islands of insight in the nuclear chart. *Physics*, 3:104, 2010. doi: 10.1103/Physics.3.104. URL http://link.aps.org/doi/10.1103/Physics.3.104.

[16] K. Riisager. Halos and related structures. *Physica Scripta*, T152:014001, Jan 2013. doi: 10.1088/0031-8949/2013/t152/014001. URL https://doi.org/10.1088%2F0031-8949%2F2013%2Ft152%2F014001.

[17] I. Tanihata, H. Hamagaki, O. Hashimoto, Y. Shida, N. Yoshikawa, K. Sugimoto, O. Yamakawa, T. Kobayashi, and N. Takahashi. Measurements of interaction cross sections and nuclear radii in the light p-shell region. *Phys. Rev. Lett.*, 55:2676–2679, Dec 1985. doi: 10.1103/PhysRevLett.55.2676. URL https://link.aps.org/doi/10.1103/PhysRevLett.55.2676.

[18] P.G. Hansen and B. Jonson. The neutron halo of extremely neutron-rich nuclei. *Europhysics Letters (EPL)*, 4(4):409–414, Aug 1987. doi: 10.1209/0295-5075/4/4/005. URL https://doi.org/10.1209%2F0295-5075%2F4%2F4%2F005.

[19] T. Kobayashi, O. Yamakawa, K. Omata, K. Sugimoto, T. Shimoda, N. Takahashi, and I. Tanihata. Projectile fragmentation of the extremely neutron-rich nucleus ^{11}Li at 0.79

GeV/nucleon. *Phys. Rev. Lett.*, 60:2599–2602, Jun 1988. doi: 10.1103/PhysRevLett.60.2599. URL https://link.aps.org/doi/10.1103/PhysRevLett.60.2599.

[20] T. Aumann and T. Nakamura. The electric dipole response of exotic nuclei. *Physica Scripta*, T152:014012, Jan 2013. doi: 10.1088/0031-8949/2013/t152/014012. URL https://doi.org/10.1088%2F0031-8949%2F2013%2Ft152%2F014012.

[21] M. Thoennessen. Reaching the limits of nuclear stability. *Reports on Progress in Physics*, 67 (7):1187–1232, jun 2004. doi: 10.1088/0034-4885/67/7/r04. URL https://doi.org/10.1088%2F0034-4885%2F67%2F7%2Fr04.

[22] P. Möller. The limits of the nuclear chart set by fission and alpha decay. *EPJ Web Conf.*, 131:03002, 2016. doi: 10.1051/epjconf/201613103002. URL https://doi.org/10.1051/epjconf/201613103002.

[23] M. Wang, G. Audi, F.G. Kondev, W.J. Huang, S. Naimi, and X. Xu. The AME2016 atomic mass evaluation (II). tables, graphs and references. *Chinese Physics C*, 41(3):030003, Mar 2017. doi: 10.1088/1674-1137/41/3/030003. URL https://doi.org/10.1088%2F1674-1137%2F41%2F3%2F030003.

[24] D. Lunney, J.M. Pearson, and C. Thibault. Recent trends in the determination of nuclear masses. *Rev. Mod. Phys.*, 75:1021–1082, Aug 2003. doi: 10.1103/RevModPhys.75.1021. URL https://link.aps.org/doi/10.1103/RevModPhys.75.1021.

[25] T. Otsuka, T. Suzuki, J.D. Holt, A. Schwenk, and Y. Akaishi. Three-body forces and the limit of oxygen isotopes. *Phys. Rev. Lett.*, 105:032501, Jul 2010. doi: 10.1103/PhysRevLett.105.032501. URL https://link.aps.org/doi/10.1103/PhysRevLett.105.032501.

[26] T. Kobayashi, N. Chiga, T. Isobe, Y. Kondo, T. Kubo, K. Kusaka, T. Motobayashi, T. Nakamura, J. Ohnishi, H. Okuno, H. Otsu, T. Sako, H. Sato, Y. Shimizu, K. Sekiguchi, K. Takahashi, R. Tanaka, and K. Yoneda. SAMURAI spectrometer for RI beam experiments. *Nuclear Instruments and Methods in Physics Research Section B: Beam Interactions with Materials and Atoms*, 317:294 – 304, 2013. ISSN 0168-583X. doi: https://doi.org/10.1016/j.nimb.2013.05.089. URL http://www.sciencedirect.com/science/article/pii/S0168583X13007118. XVIth International Conference on ElectroMagnetic Isotope Separators and Techniques Related to their Applications, December 2–7, 2012 at Matsue, Japan.

[27] FAIR – baseline technical report, March 2006. URL https://fair-center.eu/for-users/publications/fair-publications.html.

[28] J. Kahlbow, K. Boretzky, N.L. Achouri, D.S. Ahn, H. Al Falou, G. Alkhazov, M. Assie, L. Atar, T. Aumann, H. Baba, D. Beaumel, D. Bemmerer, M. Böhmer, M. Caamano, C. Caesar, D. Cal-

vet, H. Chae, S. Chen, M.I. Cherciu, N. Chiga, L. Chulkov, A. Corsi, M.L. Cortes, D. Cortina, T.E. Cowan, H.L. Crawford, F. de Oliveira Santos, F. Delaunay, A. Delbart, G. Dentinger, Q. Deshayes, Z. Dombradi, P. Doornenbal, C.A. Douma, F. Dufter, Z. Elekes, J. Enders, P. Fallon, J. Feng, B. Fernandez, F. Flavigny, U. Forsberg, N. Fukuda, Z. Fülöp, D. Galaviz Redondo, I. Gasparic, Z. Ge, R. Gernhäuser, J.-M. Gheller, J. Gibelin, A. Gilibert, K. Göbel, N. Gruzinsky, Z. Halasz, F. Hammache, M.N. Harakeh, T. Heftrich, M. Heil, A. Heinz, A. Hirayama, C.R. Hoffman, M. Holl, A. Horvat, A. Horvath, J.W. Hwang, N. Inabe, T. Isobe, H.T. Johansson, B. Jonson, N. Kalantar-Nayestanaki, S. Kawase, A. Kelic-Heil, S. Kim, D. Kim, K. Kisamori, R. Kissel, M. Knösel, T. Kobayashi, Y. Kondo, D. Körper, P. Koseoglou, S. Koyama, N.G. Kozlenko, D. Kresan, T. Kubo, Y.Kubota, I. Kuti, V. Kuznetsov, C. Langer, V. Lapoux, C.S. Lee, C. Lehr, P.J. Li, S. Lindberg, Y. Liu, B. Löher, Y. Maeda, F.M. Marques, S. Masuoka, Y. Matsuda, M. Matsumoto, A. Matta, J. Mayer, K. Miki, M. Miwa, B. Monteagudo, T. Murakami, I. Murray, M.A. Najafi, T. Nakamura, K. Nakano, N. Nakatsuka, T. Nilsson, G.H. Nyman, A. Obertelli, N.A. Orr, H. Otsu, T. Ozaki, V. Panin, S. Park, M. Parlog, S. Paschalis, N. Paul, M. Petri, S.G. Pickstone, M. Pohl, P.-M. Potlog, S. Reichert, R. Reifarth, S. Reinicke, A. Revel, C. Rigollet, D.M. Rossi, A.T. Saito, T. Saito, S. Sakaguchi, M. Sako, H. Sakurai, M. Sasano, H. Sato, Y. Satou, D. Savran, H. Scheit, F. Schindler, P. Schrock, M. Shikata, Y. Shimizu, S. Shimoura, H. Simon, D. Sohler, O. Sorlin, E. Stan, S. Storck, L. Stuhl, T. Sumikama, Y.L. Sun, H. Suzuki, D. Symochko, I. Syndikus, H. Takeda, S. Takeuchi, J. Tanaka, M. Tanaka, M. Thoennessen, Y. Togano, T. Tomai, H.T. Törnqvist, J. Tscheuschner, J. Tsubota, T. Uesaka, L. Uvarov, S. Volkov, V. Wagner, A. Wagner, H. Wang, K. Wimmer, H. Yamada, Z. Yang, B. Yang, L. Yang, M. Yasuda, K. Yoneda, L. Zanetti, J. Zenihiro, A. Zilges, and K. Zuber. Experimental campaign using the NeuLAND demonstrator at SAMURAI. *GSI-FAIR Scientific Report 2017*, 2018. doi: 10.15120/GSI-2017-01856. URL `http://repository.gsi.de/record/208542`.

[29] S.C. Pieper and R.B. Wiringa. Quantum Monte Carlo calculations of light nuclei. *Annual Review of Nuclear and Particle Science*, 51(1):53–90, 2001. doi: 10.1146/annurev.nucl.51.101701.132506. URL `https://doi.org/10.1146/annurev.nucl.51.101701.132506`.

[30] O. Sorlin and M.-G. Porquet. Nuclear magic numbers: New features far from stability. *Progress in Particle and Nuclear Physics*, 61(2):602 – 673, 2008. ISSN 0146-6410. doi: https://doi.org/10.1016/j.ppnp.2008.05.001. URL `http://www.sciencedirect.com/science/article/pii/S0146641008000380`.

[31] C.A. Bertulani. *Nuclear Physics in a Nutshell*. Princeton University Press, STU - student edition, 2007. ISBN 9780691125053. URL `http://www.jstor.org/stable/j.ctt7shsk`.

[32] B.A. Brown. The nuclear shell model towards the drip lines. *Progress in Particle and Nuclear Physics*, 47(2):517 – 599, 2001. ISSN 0146-6410. doi: https://doi.

org/10.1016/S0146-6410(01)00159-4. URL http://www.sciencedirect.com/science/article/pii/S0146641001001594.

[33] B.A. Brown and W.A. Richter. New "USD" Hamiltonians for the sd shell. *Phys. Rev. C*, 74:034315, Sep 2006. doi: 10.1103/PhysRevC.74.034315. URL https://link.aps.org/doi/10.1103/PhysRevC.74.034315.

[34] B.H. Wildenthal. Empirical strengths of spin operators in nuclei. *Progress in Particle and Nuclear Physics*, 11:5 – 51, 1984. ISSN 0146-6410. doi: https://doi.org/10.1016/0146-6410(84)90011-5. URL http://www.sciencedirect.com/science/article/pii/0146641084900115.

[35] B.A Brown, W.A Richter, R.E Julies, and B.H Wildenthal. Semi-empirical effective interactions for the $1s$-od shell. *Annals of Physics*, 182(2):191 – 236, 1988. ISSN 0003-4916. doi: https://doi.org/10.1016/0003-4916(88)90013-9. URL http://www.sciencedirect.com/science/article/pii/0003491688900139.

[36] N. Takigawa and K. Washiyama. *Fundamentals of Nuclear Physics*. Springer, Japan, 2017. ISBN 9784431553786.

[37] S. Weinberg. Nuclear forces from chiral Lagrangians. *Physics Letters B*, 251(2):288 – 292, 1990. ISSN 0370-2693. doi: https://doi.org/10.1016/0370-2693(90)90938-3. URL http://www.sciencedirect.com/science/article/pii/0370269390909383.

[38] E. Epelbaum, H.-W. Hammer, and U.-G. Meißner. Modern theory of nuclear forces. *Rev. Mod. Phys.*, 81:1773–1825, Dec 2009. doi: 10.1103/RevModPhys.81.1773. URL https://link.aps.org/doi/10.1103/RevModPhys.81.1773.

[39] R. Machleidt and D.R. Entem. Chiral effective field theory and nuclear forces. *Physics Reports*, 503(1):1 – 75, 2011. ISSN 0370-1573. doi: https://doi.org/10.1016/j.physrep.2011.02.001. URL http://www.sciencedirect.com/science/article/pii/S0370157311000457.

[40] B.R. Barrett, P. Navrátil, and J.P. Vary. *Ab initio* no core shell model. *Progress in Particle and Nuclear Physics*, 69:131 – 181, 2013. ISSN 0146-6410. doi: https://doi.org/10.1016/j.ppnp.2012.10.003. URL http://www.sciencedirect.com/science/article/pii/S0146641012001184.

[41] R.J. Furnstahl and K. Hebeler. New applications of renormalization group methods in nuclear physics. *Reports on Progress in Physics*, 76(12):126301, 2013. URL http://stacks.iop.org/0034-4885/76/i=12/a=126301.

[42] R.J. Furnstahl. The renormalization group in nuclear physics. *Nuclear Physics B - Proceedings Supplements*, 228:139 – 175, 2012. ISSN 0920-5632. doi: https://doi.org/10.1016/j.nuclphysbps.2012.06.005. URL http://www.sciencedirect.com/science/article/pii/S0920563212001624. "Physics at all scales: The Renormalization Group". Proceedings of the 49th Internationale Universitätswochen für Theoretische Physik.

[43] H. Hergert, S.K. Bogner, T.D. Morris, A. Schwenk, and K. Tsukiyama. The in-medium similarity renormalization group: A novel ab initio method for nuclei. *Physics Reports*, 621:165 – 222, 2016. ISSN 0370-1573. doi: https://doi.org/10.1016/j.physrep.2015.12.007. URL http://www.sciencedirect.com/science/article/pii/S0370157315005414. Memorial Volume in Honor of Gerald E. Brown.

[44] A. Cipollone, C. Barbieri, and P. Navrátil. Chiral three-nucleon forces and the evolution of correlations along the oxygen isotopic chain. *Phys. Rev. C*, 92:014306, Jul 2015. doi: 10.1103/PhysRevC.92.014306. URL https://link.aps.org/doi/10.1103/PhysRevC.92.014306.

[45] A. Cipollone, C. Barbieri, and P. Navrátil. Isotopic chains around oxygen from evolved chiral two- and three-nucleon interactions. *Phys. Rev. Lett.*, 111:062501, Aug 2013. doi: 10.1103/PhysRevLett.111.062501. URL https://link.aps.org/doi/10.1103/PhysRevLett.111.062501.

[46] J. Dobaczewski, N. Michel, W. Nazarewicz, M. Płoszajczak, and J. Rotureau. Shell structure of exotic nuclei. *Progress in Particle and Nuclear Physics*, 59(1):432 – 445, 2007. ISSN 0146-6410. doi: https://doi.org/10.1016/j.ppnp.2007.01.022. URL http://www.sciencedirect.com/science/article/pii/S0146641007000233. International Workshop on Nuclear Physics 28th Course.

[47] C. Mahaux and H.A. Weidenmüller. *Shell-model approach to nuclear reactions*. North-Holland Publishing Company, 1969.

[48] C. Mahaux and H.A. Weidenmüller. Comparison between R-matrix and shell-model approaches to nuclear reactions. *Nuclear Physics A*, 97(2):378 – 404, 1967. ISSN 0375-9474. doi: https://doi.org/10.1016/0375-9474(67)90494-0. URL http://www.sciencedirect.com/science/article/pii/0375947467904940".

[49] P. Descouvemont and D. Baye. The R-matrix theory. *Reports on Progress in Physics*, 73(3):036301, Feb 2010. doi: 10.1088/0034-4885/73/3/036301. URL https://doi.org/10.1088%2F0034-4885%2F73%2F3%2F036301.

[50] G. Breit and E. Wigner. Capture of slow neutrons. *Phys. Rev.*, 49:519–531, Apr 1936. doi: 10.1103/PhysRev.49.519. URL https://link.aps.org/doi/10.1103/PhysRev.49.519.

[51] F. Nunes. Scattering theory, Sep 2014. URL https://www.asc.ohio-state.edu/physics/ntg/8805/notes/section_3_Scattering_1.pdf. Lecture Notes.

[52] Yu. Aksyutina. *Light Unbound Nuclear Systems beyond the Dripline*. PhD thesis, Johann Wolfgang Goethe Universität, Frankfurt am Main, 2009.

[53] A. Bohr and B.R. Mottelson. *Nuclear Structure*, volume 1 (Single-Particle Motion). World Scientific, 1998.

[54] W.H. Dickhoff and C. Barbieri. Self-consistent Green's function method for nuclei and nuclear matter. *Progress in Particle and Nuclear Physics*, 52(2):377 – 496, 2004. ISSN 0146-6410. doi: https://doi.org/10.1016/j.ppnp.2004.02.038. URL http://www.sciencedirect.com/science/article/pii/S0146641004000535.

[55] A. Gade, P. Adrich, D. Bazin, M.D. Bowen, B.A. Brown, C.M. Campbell, J.M. Cook, T. Glasmacher, P.G. Hansen, K. Hosier, S. McDaniel, D. McGlinchery, A. Obertelli, K. Siwek, L.A. Riley, J.A. Tostevin, and D. Weisshaar. Reduction of spectroscopic strength: Weakly-bound and strongly-bound single-particle states studied using one-nucleon knockout reactions. *Phys. Rev. C*, 77:044306, Apr 2008. doi: 10.1103/PhysRevC.77.044306. URL https://link.aps.org/doi/10.1103/PhysRevC.77.044306.

[56] Yu. Aksyutina, H.T. Johansson, T. Aumann, K. Boretzky, M.J.G. Borge, A. Chatillon, L.V. Chulkov, D. Cortina-Gil, U. Datta Pramanik, H. Emling, C. Forssén, H.O.U. Fynbo, H. Geissel, G. Ickert, B. Jonson, R. Kulessa, C. Langer, M. Lantz, T. LeBleis, A.O. Lindahl, K. Mahata, M. Meister, G. Münzenberg, T. Nilsson, G. Nyman, R. Palit, S. Paschalis, W. Prokopowicz, R. Reifarth, A. Richter, K. Riisager, G. Schrieder, H. Simon, K. Sümmerer, O. Tengblad, H. Weick, and M.V. Zhukov. Properties of the ^{7}He ground state from ^{8}He neutron knockout. *Physics Letters B*, 679(3):191 – 196, 2009. ISSN 0370-2693. doi: https://doi.org/10.1016/j.physletb.2009.07.044. URL http://www.sciencedirect.com/science/article/pii/S0370269309008788.

[57] T.A. Golubkova, X.-D. Xu, L.V. Grigorenko, I.G. Mukha, C. Scheidenberger, and M.V. Zhukov. Transition from direct to sequential two-proton decay in s-d shell nuclei. *Physics Letters B*, 762:263 – 270, 2016. ISSN 0370-2693. doi: https://doi.org/10.1016/j.physletb.2016.09.034. URL http://www.sciencedirect.com/science/article/pii/S0370269316305299.

[58] F.E. James. Monte Carlo phase space. Geneva, 1968. CERN. URL https://cds.cern.ch/record/275743.

[59] L.V. Grigorenko, J.S. Vaagen, and M.V. Zhukov. Exploring the manifestation and nature of a dineutron in two-neutron emission using a dynamical dineutron model. *Phys. Rev. C*,

97:034605, Mar 2018. doi: 10.1103/PhysRevC.97.034605. URL https://link.aps.org/doi/10.1103/PhysRevC.97.034605.

[60] A. Revel. *Nuclear forces at the extremes*. PhD thesis, Normandie Université, 2018. URL http://www.theses.fr/2018NORMC227/document.

[61] A. Spyrou, Z. Kohley, T. Baumann, D. Bazin, B.A. Brown, G. Christian, P.A. DeYoung, J.E. Finck, N. Frank, E. Lunderberg, S. Mosby, W.A. Peters, A. Schiller, J.K. Smith, J. Snyder, M.J. Strongman, M. Thoennessen, and A. Volya. First observation of ground state dineutron decay: ^{16}Be. *Phys. Rev. Lett.*, 108:102501, Mar 2012. doi: 10.1103/PhysRevLett.108.102501. URL https://link.aps.org/doi/10.1103/PhysRevLett.108.102501.

[62] K. Hagino and H. Sagawa. Are there good probes for the di-neutron correlation in light neutron-rich nuclei? *Few-Body Systems*, 57(3):185–193, Mar 2016. ISSN 1432-5411. doi: 10.1007/s00601-015-1027-3. URL https://doi.org/10.1007/s00601-015-1027-3.

[63] R. Machleidt and I. Slaus. The nucleon-nucleon interaction. *Journal of Physics G: Nuclear and Particle Physics*, 27(5):R69–R108, mar 2001. doi: 10.1088/0954-3899/27/5/201. URL https://doi.org/10.1088%2F0954-3899%2F27%2F5%2F201.

[64] K.M. Watson. The effect of final state interactions on reaction cross sections. *Phys. Rev.*, 88:1163–1171, Dec 1952. doi: 10.1103/PhysRev.88.1163. URL https://link.aps.org/doi/10.1103/PhysRev.88.1163.

[65] A.B. Migdal. The theory of nuclear reactions with production of slow particles. *J. Exper. Theoret. Phys. USSR*, 28:3–9, Jan 1955. URL http://www.jetp.ac.ru/cgi-bin/dn/e_001_01_0002.pdf.

[66] Z. Kohley, E. Lunderberg, P.A. DeYoung, A. Volya, T. Baumann, D. Bazin, G. Christian, N.L. Cooper, N. Frank, A. Gade, C. Hall, J. Hinnefeld, B. Luther, S. Mosby, W.A. Peters, J.K. Smith, J. Snyder, A. Spyrou, and M. Thoennessen. First observation of the ^{13}Li ground state. *Phys. Rev. C*, 87:011304, Jan 2013. doi: 10.1103/PhysRevC.87.011304. URL https://link.aps.org/doi/10.1103/PhysRevC.87.011304.

[67] A. Volya and V. Zelevinsky. Continuum shell model. *Phys. Rev. C*, 74:064314, Dec 2006. doi: 10.1103/PhysRevC.74.064314. URL https://link.aps.org/doi/10.1103/PhysRevC.74.064314.

[68] M. Pfützner, M. Karny, L.V. Grigorenko, and K. Riisager. Radioactive decays at limits of nuclear stability. *Rev. Mod. Phys.*, 84:567–619, Apr 2012. doi: 10.1103/RevModPhys.84.567. URL https://link.aps.org/doi/10.1103/RevModPhys.84.567.

[69] F.C. Barker. R-matrix formulas for three-body decay widths. *Phys. Rev. C*, 68:054602, Nov 2003. doi: 10.1103/PhysRevC.68.054602. URL https://link.aps.org/doi/10.1103/PhysRevC.68.054602.

[70] X. Campi, H. Flocard, A.K. Kerman, and S. Koonin. Shape transition in the neutron rich sodium isotopes. *Nuclear Physics A*, 251(2):193 – 205, 1975. ISSN 0375-9474. doi: https://doi.org/10.1016/0375-9474(75)90065-2. URL http://www.sciencedirect.com/science/article/pii/0375947475900652.

[71] B.H. Wildenthal and W. Chung. Collapse of the conventional shell-model ordering in the very-neutron-rich isotopes of Na and Mg. *Phys. Rev. C*, 22:2260–2262, Nov 1980. doi: 10.1103/PhysRevC.22.2260. URL https://link.aps.org/doi/10.1103/PhysRevC.22.2260.

[72] T. Motobayashi, Y. Ikeda, K. Ieki, M. Inoue, N. Iwasa, T. Kikuchi, M. Kurokawa, S. Moriya, S. Ogawa, H. Murakami, S. Shimoura, Y. Yanagisawa, T. Nakamura, Y. Watanabe, M. Ishihara, T. Teranishi, H. Okuno, and R.F. Casten. Large deformation of the very neutron-rich nucleus $^{32}\mathrm{Mg}$ from intermediate-energy Coulomb excitation. *Physics Letters B*, 346(1):9 – 14, 1995. ISSN 0370-2693. doi: https://doi.org/10.1016/0370-2693(95)00012-A. URL http://www.sciencedirect.com/science/article/pii/037026939500012A.

[73] A. Poves and J. Retamosa. The onset of deformation at the $N = 20$ neutron shell closure far from stability. *Physics Letters B*, 184(4):311 – 315, 1987. ISSN 0370-2693. doi: https://doi.org/10.1016/0370-2693(87)90171-7. URL http://www.sciencedirect.com/science/article/pii/0370269387901717.

[74] E.K. Warburton, J.A. Becker, and B.A. Brown. Mass systematics for $A = 29 - 44$ nuclei: The deformed $A \sim 32$ region. *Phys. Rev. C*, 41:1147–1166, Mar 1990. doi: 10.1103/PhysRevC.41.1147. URL https://link.aps.org/doi/10.1103/PhysRevC.41.1147.

[75] M. Vandebrouck, A. Lepailleur, O. Sorlin, T. Aumann, C. Caesar, M. Holl, V. Panin, F. Wamers, S.R. Stroberg, J.D. Holt, F. de Oliveira Santos, H. Alvarez-Pol, L. Atar, V. Avdeichikov, S. Beceiro-Novo, D. Bemmerer, J. Benlliure, C.A. Bertulani, S.K. Bogner, J.M. Boillos, K. Boretzky, M.J.G. Borge, M. Caamaño, E. Casarejos, W. Catford, J. Cederkäll, M. Chartier, L. Chulkov, D. Cortina-Gil, E. Cravo, R. Crespo, U. Datta Pramanik, P. Díaz Fernández, I. Dillmann, Z. Elekes, J. Enders, O. Ershova, A. Estradé, F. Farinon, L.M. Fraile, M. Freer, D. Galaviz, H. Geissel, R. Gernhäuser, J. Gibelin, P. Golubev, K. Göbel, J. Hagdahl, T. Heftrich, M. Heil, M. Heine, A. Heinz, A. Henriques, H. Hergert, A. Hufnagel, A. Ignatov, H.T. Johansson, B. Jonson, J. Kahlbow, N. Kalantar-Nayestanaki, R. Kanungo, A. Kelic-Heil, A. Knyazev, T. Kröll, N. Kurz, M. Labiche, C. Langer, T. Le Bleis, R. Lemmon, S. Lindberg, J. Machado, J. Marganiec, F.M. Marqués, A. Movsesyan, E. Nacher, M. Najafi, E. Nikolskii, T. Nilsson, C. Nociforo, S. Paschalis, A. Perea,

M. Petri, S. Pietri, R. Plag, R. Reifarth, G. Ribeiro, C. Rigollet, M. Röder, D. Rossi, D. Savran, H. Scheit, A. Schwenk, H. Simon, I. Syndikus, J.T. Taylor, O. Tengblad, R. Thies, Y. Togano, P. Velho, V. Volkov, A. Wagner, H. Weick, C. Wheldon, G. Wilson, J.S. Winfield, P. Woods, D. Yakorev, M. Zhukov, A. Zilges, and K. Zuber. Effective proton-neutron interaction near the drip line from unbound states in ^{25,26}F. *Phys. Rev. C*, 96:054305, Nov 2017. doi: 10.1103/PhysRevC.96.054305. URL https://link.aps.org/doi/10.1103/PhysRevC.96.054305.

[76] E. Caurier, F. Nowacki, and A. Poves. Merging of the islands of inversion at $N = 20$ and $N = 28$. *Phys. Rev. C*, 90:014302, Jul 2014. doi: 10.1103/PhysRevC.90.014302. URL https://link.aps.org/doi/10.1103/PhysRevC.90.014302.

[77] T. Otsuka and D. Abe. Mean field properties of exotic nuclei and the tensor force. *Progress in Particle and Nuclear Physics*, 59(1):425 – 431, 2007. ISSN 0146-6410. doi: https://doi.org/10.1016/j.ppnp.2007.01.016. URL http://www.sciencedirect.com/science/article/pii/S0146641007000117. International Workshop on Nuclear Physics 28th Course.

[78] T. Otsuka, T. Suzuki, M. Honma, Y. Utsuno, N. Tsunoda, K. Tsukiyama, and M. Hjorth-Jensen. Novel features of nuclear forces and shell evolution in exotic nuclei. *Phys. Rev. Lett.*, 104:012501, Jan 2010. doi: 10.1103/PhysRevLett.104.012501. URL https://link.aps.org/doi/10.1103/PhysRevLett.104.012501.

[79] Y. Utsuno, T. Otsuka, T. Mizusaki, and M. Honma. Varying shell gap and deformation in $N \sim 20$ unstable nuclei studied by the Monte Carlo shell model. *Phys. Rev. C*, 60: 054315, Oct 1999. doi: 10.1103/PhysRevC.60.054315. URL https://link.aps.org/doi/10.1103/PhysRevC.60.054315.

[80] K. Wimmer, T. Kröll, R. Krücken, V. Bildstein, R. Gernhäuser, B. Bastin, N. Bree, J. Diriken, P. Van Duppen, M. Huyse, N. Patronis, P. Vermaelen, D. Voulot, J. Van de Walle, F. Wenander, L.M. Fraile, R. Chapman, B. Hadinia, R. Orlandi, J.F. Smith, R. Lutter, P.G. Thirolf, M. Labiche, A. Blazhev, M. Kalkühler, P. Reiter, M. Seidlitz, N. Warr, A.O. Macchiavelli, H.B. Jeppesen, E. Fiori, G. Georgiev, G. Schrieder, S. Das Gupta, G. Lo Bianco, S. Nardelli, J. Butterworth, J. Johansen, and K. Riisager. Discovery of the shape coexisting 0^+ state in ^{32}Mg by a two neutron transfer reaction. *Phys. Rev. Lett.*, 105:252501, Dec 2010. doi: 10.1103/PhysRevLett.105.252501. URL https://link.aps.org/doi/10.1103/PhysRevLett.105.252501.

[81] P. Doornenbal, H. Scheit, S. Takeuchi, Y. Utsuno, N. Aoi, K. Li, M. Matsushita, D. Steppenbeck, H. Wang, H. Baba, E. Ideguchi, N. Kobayashi, Y. Kondo, J. Lee, S. Michimasa, T. Motobayashi, T. Otsuka, H. Sakurai, M. Takechi, Y. Togano, and K. Yoneda. Low-Z shore of the "island of inversion" and the reduced neutron magicity toward ^{28}O. *Phys. Rev. C*,

95:041301, Apr 2017. doi: 10.1103/PhysRevC.95.041301. URL https://link.aps.org/doi/10.1103/PhysRevC.95.041301.

[82] L. Gaudefroy, W. Mittig, N.A. Orr, S. Varet, M. Chartier, P. Roussel-Chomaz, J. P. Ebran, B. Fernández-Domínguez, G. Frémont, P. Gangnant, A. Gillibert, S. Grévy, J.F. Libin, V.A. Maslov, S. Paschalis, B. Pietras, Yu.-E. Penionzhkevich, C. Spitaels, and A.C.C. Villari. Direct mass measurements of ^{19}B, ^{22}C, ^{29}F, ^{31}Ne, ^{34}Na and other light exotic nuclei. *Phys. Rev. Lett.*, 109:202503, Nov 2012. doi: 10.1103/PhysRevLett.109.202503. URL https://link.aps.org/doi/10.1103/PhysRevLett.109.202503.

[83] H.N. Liu, J. Lee, P. Doornenbal, H. Scheit, S. Takeuchi, N. Aoi, K.A. Li, M. Matsushita, D. Steppenbeck, H. Wang, H. Baba, E. Ideguchi, N. Kobayashi, Y. Kondo, G. Lee, S. Michimasa, T. Motobayashi, A. Poves, H. Sakurai, M. Takechi, Y. Togano, J.A. Tostevin, and Y. Utsuno. Intruder configurations in the ground state of ^{30}Ne. *Physics Letters B*, 767:58 – 62, 2017. ISSN 0370-269. doi: https://doi.org/10.1016/j.physletb.2017.01.052. URL http://www.sciencedirect.com/science/article/pii/S0370269317300709.

[84] P. Doornenbal, H. Scheit, S. Takeuchi, N. Aoi, K. Li, M. Matsushita, D. Steppenbeck, H. Wang, H. Baba, E. Ideguchi, N. Kobayashi, Y. Kondo, J. Lee, S. Michimasa, T. Motobayashi, A. Poves, H. Sakurai, M. Takechi, Y. Togano, and K. Yoneda. Mapping the deformation in the "island of inversion": Inelastic scattering of ^{30}Ne and ^{36}Mg at intermediate energies. *Phys. Rev. C*, 93:044306, Apr 2016. doi: 10.1103/PhysRevC.93.044306. URL https://link.aps.org/doi/10.1103/PhysRevC.93.044306.

[85] S. Lindberg. *Exciting Neutron-rich Nuclei – Radioactive beam experiments in complete kinematics*. PhD thesis, Chalmers University of Technology, Göteburg, Sweden, August 2018. URL https://research.chalmers.se/publication/503837.

[86] G. Christian, N. Frank, S. Ash, T. Baumann, D. Bazin, J. Brown, P.A. DeYoung, J.E. Finck, A. Gade, G.F. Grinyer, A. Grovom, J.D. Hinnefeld, E.M. Lunderberg, B. Luther, M. Mosby, S. Mosby, T. Nagi, G.F. Peaslee, W.F. Rogers, J.K. Smith, J. Snyder, A. Spyrou, M.J. Strongman, M. Thoennessen, M. Warren, D. Weisshaar, and A. Wersal. Exploring the low-Z shore of the island of inversion at $N = 19$. *Phys. Rev. Lett.*, 108:032501, Jan 2012. doi: 10.1103/PhysRevLett.108.032501. URL https://link.aps.org/doi/10.1103/PhysRevLett.108.032501.

[87] G. Christian, N. Frank, S. Ash, T. Baumann, P.A. DeYoung, J.E. Finck, A. Gade, G.F. Grinyer, B. Luther, M. Mosby, S. Mosby, J.K. Smith, J. Snyder, A. Spyrou, M.J. Strongman, M. Thoennessen, M. Warren, D. Weisshaar, and A. Wersal. Spectroscopy of neutron-unbound ^{27,28}F. *Phys. Rev. C*, 85:034327, Mar 2012. doi: 10.1103/PhysRevC.85.034327. URL https://link.aps.org/doi/10.1103/PhysRevC.85.034327.

[88] Z. Elekes, Zs. Dombrádi, A. Saito, N. Aoi, H. Baba, K. Demichi, Zs. Fülöp, J. Gibelin, T. Gomi, H. Hasegawa, N. Imai, M. Ishihara, H. Iwasaki, S. Kanno, S. Kawai, T. Kishida, T. Kubo, K. Kurita, Y. Matsuyama, S. Michimasa, T. Minemura, T. Motobayashi, M. Notani, T. Ohnishi, H.J. Ong, S. Ota, A. Ozawa, H.K. Sakai, H. Sakurai, S. Shimoura, E. Takeshita, S. Takeuchi, M. Tamaki, Y. Togano, K. Yamada, Y. Yanagisawa, and K. Yoneda. Bound excited states in ^{27}F. *Physics Letters B*, 599(1):17 – 22, 2004. ISSN 0370-2693. doi: https://doi.org/10.1016/j.physletb.2004.08.028. URL http://www.sciencedirect.com/science/article/pii/S0370269304011785.

[89] H. Sakurai, S.M. Lukyanov, M. Notani, N. Aoi, D. Beaumel, N. Fukuda, M. Hirai, E. Ideguchi, N. Imai, M. Ishihara, H. Iwasaki, T. Kubo, K. Kusaka, H. Kumagai, T. Nakamura, H. Ogawa, Yu.E. Penionzhkevich, T. Teranishi, Y.X. Watanabe, K. Yoneda, and A. Yoshida. Evidence for particle stability of ^{31}F and particle instability of ^{25}N and ^{28}O. *Physics Letters B*, 448(3):180 – 184, 1999. ISSN 0370-2693. doi: https://doi.org/10.1016/S0370-2693(99)00015-5. URL http://www.sciencedirect.com/science/article/pii/S0370269399000155.

[90] A. Poves and J. Retamosa. Theoretical study of the very neutron-rich nuclei around $N = 20$. *Nuclear Physics A*, 571(2):221 – 241, 1994. ISSN 0375-9474. doi: https://doi.org/10.1016/0375-9474(94)90058-2. URL http://www.sciencedirect.com/science/article/pii/0375947494900582.

[91] P. Fallon, E. Rodriguez-Vieitez, A.O. Macchiavelli, A. Gade, J.A. Tostevin, P. Adrich, D. Bazin, M. Bowen, C.M. Campbell, R.M. Clark, J.M. Cook, M. Cromaz, D.C. Dinca, T. Glasmacher, I.Y. Lee, S. McDaniel, W.F. Mueller, S.G. Prussin, A. Ratkiewicz, K. Siwek, J.R. Terry, D. Weisshaar, M. Wiedeking, K. Yoneda, B.A. Brown, T. Otsuka, and Y. Utsuno. Two-proton knockout from ^{32}Mg: Intruder amplitudes in ^{30}Ne and implications for the binding of ^{29,31}F. *Phys. Rev. C*, 81:041302, Apr 2010. doi: 10.1103/PhysRevC.81.041302. URL https://link.aps.org/doi/10.1103/PhysRevC.81.041302.

[92] E. Gebrerufael, K. Vobig, H. Hergert, and R. Roth. Ab initio description of open-shell nuclei: Merging no-core shell model and in-medium similarity renormalization group. *Phys. Rev. Lett.*, 118:152503, Apr 2017. doi: 10.1103/PhysRevLett.118.152503. URL https://link.aps.org/doi/10.1103/PhysRevLett.118.152503.

[93] A. Tichai, E. Gebrerufael, K. Vobig, and R. Roth. Open-shell nuclei from no-core shell model with perturbative improvement. *Physics Letters B*, 786:448 – 452, 2018. ISSN 0370-2693. doi: https://doi.org/10.1016/j.physletb.2018.10.029. URL http://www.sciencedirect.com/science/article/pii/S0370269318307986.

[94] A. Gade and T. Glasmacher. In-beam nuclear spectroscopy of bound states with fast exotic ion beams. *Progress in Particle and Nuclear Physics*, 60(1):161 – 224, 2008.

ISSN 0146-6410. doi: https://doi.org/10.1016/j.ppnp.2007.08.001. URL http://www.sciencedirect.com/science/article/pii/S014664100700066X.

[95] T. Otsuka, A. Gade, O. Sorlin, T. Suzuki, and Y. Utsuno. Evolution of nuclear structure in exotic nuclei driven by nuclear forces, 2018. URL https://arxiv.org/abs/1805.06501.

[96] Yu. Aksyutina, T. Aumann, K. Boretzky, M.J.G. Borge, C. Caesar, A. Chatillon, L.V. Chulkov, D. Cortina-Gil, U. Datta Pramanik, H. Emling, H.O.U. Fynbo, H. Geissel, G. Ickert, H.T. Johansson, B. Jonson, R. Kulessa, C. Langer, T. LeBleis, K. Mahata, G. Münzenberg, T. Nilsson, G. Nyman, R. Palit, S. Paschalis, W. Prokopowicz, R. Reifarth, D. Rossi, A. Richter, K. Riisager, G. Schrieder, H. Simon, K. Sümmerer, O. Tengblad, H. Weick, and M.V. Zhukov. Momentum profile analysis in one-neutron knockout from Borromean nuclei. *Physics Letters B*, 718(4):1309 – 1313, 2013. ISSN 0370-2693. doi: https://doi.org/10.1016/j.physletb.2012.12.028. URL http://www.sciencedirect.com/science/article/pii/S0370269312012816.

[97] J. Marganiec, F. Wamers, F. Aksouh, Yu. Aksyutina, H. Álvarez Pol, T. Aumann, S. Beceiro-Novo, C.A. Bertulani, K. Boretzky, M.J.G. Borge, M. Chartier, A. Chatillon, L.V. Chulkov, D. Cortina-Gil, H. Emling, O. Ershova, L.M. Fraile, H.O.U. Fynbo, D. Galaviz, H. Geissel, M. Heil, D.H.H. Hoffmann, J. Hoffmann, H.T. Johansson, B. Jonson, C. Karagiannis, O.A. Kiselev, J.V. Kratz, R. Kulessa, N. Kurz, C. Langer, M. Lantz, T. Le Bleis, R. Lemmon, Yu.A. Litvinov, K. Mahata, C. Müntz, T. Nilsson, C. Nociforo, G. Nyman, W. Ott, V. Panin, S. Paschalis, A. Perea, R. Plag, R. Reifarth, A. Richter, C. Rodriguez-Tajes, D. Rossi, K. Riisager, D. Savran, G. Schrieder, H. Simon, J. Stroth, K. Sümmerer, O. Tengblad, S. Typel, H. Weick, M. Wiescher, and C. Wimmer. Coulomb and nuclear excitations of narrow resonances in ^{17}Ne. *Physics Letters B*, 759:200 – 205, 2016. ISSN 0370-2693. doi: https://doi.org/10.1016/j.physletb.2016.05.073. URL http://www.sciencedirect.com/science/article/pii/S0370269316302209.

[98] K. Ikeda, N. Takigawa, and H. Horiuchi. The systematic structure-change into the molecule-like structures in the self-conjugate $4n$ nuclei. *Progress of Theoretical Physics Supplement*, E68:464–475, 07 1968. doi: 10.1143/PTPS.E68.464. URL https://doi.org/10.1143/PTPS.E68.464.

[99] A. Revel, F.M. Marqués, O. Sorlin, T. Aumann, C. Caesar, M. Holl, V. Panin, M. Vandebrouck, F. Wamers, H. Alvarez-Pol, L. Atar, V. Avdeichikov, S. Beceiro-Novo, D. Bemmerer, J. Benlliure, C.A. Bertulani, J.M. Boillos, K. Boretzky, M.J.G. Borge, M. Caamaño, E. Casarejos, W.N. Catford, J. Cederkäll, M. Chartier, L. Chulkov, D. Cortina-Gil, E. Cravo, R. Crespo, U. Datta Pramanik, P. Díaz Fernández, I. Dillmann, Z. Elekes, J. Enders, O. Ershova, A. Estradé, F. Farinon, L.M. Fraile, M. Freer, D. Galaviz, H. Geissel, R. Gernhäuser,

P. Golubev, K. Göbel, J. Hagdahl, T. Heftrich, M. Heil, M. Heine, A. Heinz, A. Henriques, A. Ignatov, H.T. Johansson, B. Jonson, J. Kahlbow, N. Kalantar-Nayestanaki, R. Kanungo, A. Kelic-Heil, A. Knyazev, T. Kröll, N. Kurz, M. Labiche, C. Langer, T. Le Bleis, R. Lemmon, S. Lindberg, J. Machado, J. Marganiec, A. Movsesyan, E. Nacher, M. Najafi, T. Nilsson, C. Nociforo, S. Paschalis, A. Perea, M. Petri, S. Pietri, R. Plag, R. Reifarth, G. Ribeiro, C. Rigollet, M. Röder, D. Rossi, D. Savran, H. Scheit, H. Simon, I. Syndikus, J.T. Taylor, O. Tengblad, R. Thies, Y. Togano, P. Velho, V. Volkov, A. Wagner, H. Weick, C. Wheldon, G. Wilson, J.S. Winfield, P. Woods, D. Yakorev, M. Zhukov, A. Zilges, and K. Zuber. Strong neutron pairing in core + $4n$ nuclei. *Phys. Rev. Lett.*, 120:152504, Apr 2018. doi: 10.1103/PhysRevLett.120.152504. URL `https://link.aps.org/doi/10.1103/PhysRevLett.120.152504`.

[100] Y. Kondo, T. Nakamura, R. Tanaka, R. Minakata, S. Ogoshi, N.A. Orr, N.L. Achouri, T. Aumann, H. Baba, F. Delaunay, P. Doornenbal, N. Fukuda, J. Gibelin, J.W. Hwang, N. Inabe, T. Isobe, D. Kameda, D. Kanno, S. Kim, N. Kobayashi, T. Kobayashi, T. Kubo, S. Leblond, J. Lee, F.M. Marqués, T. Motobayashi, D. Murai, T. Murakami, K. Muto, T. Nakashima, N. Nakatsuka, A. Navin, S. Nishi, H. Otsu, H. Sato, Y. Satou, Y. Shimizu, H. Suzuki, K. Takahashi, H. Takeda, S. Takeuchi, Y. Togano, A.G. Tuff, M. Vandebrouck, and K. Yoneda. Nucleus ^{26}O: A barely unbound system beyond the drip line. *Phys. Rev. Lett.*, 116:102503, Mar 2016. doi: 10.1103/PhysRevLett.116.102503. URL `https://link.aps.org/doi/10.1103/PhysRevLett.116.102503`.

[101] L.V. Grigorenko, I.G. Mukha, C. Scheidenberger, and M.V. Zhukov. Two-neutron radioactivity and four-nucleon emission from exotic nuclei. *Phys. Rev. C*, 84:021303, Aug 2011. doi: 10.1103/PhysRevC.84.021303. URL `https://link.aps.org/doi/10.1103/PhysRevC.84.021303`.

[102] L.V. Grigorenko, I.G. Mukha, and M.V. Zhukov. Lifetime and fragment correlations for the two-neutron decay of ^{26}O ground state. *Phys. Rev. Lett.*, 111:042501, Jul 2013. doi: 10.1103/PhysRevLett.111.042501. URL `https://link.aps.org/doi/10.1103/PhysRevLett.111.042501`.

[103] Z. Kohley, T. Baumann, D. Bazin, G. Christian, P.A. DeYoung, J.E. Finck, N. Frank, M. Jones, E. Lunderberg, B. Luther, S. Mosby, T. Nagi, J.K. Smith, J. Snyder, A. Spyrou, and M. Thoennessen. Study of two-neutron radioactivity in the decay of ^{26}O. *Phys. Rev. Lett.*, 110: 152501, Apr 2013. doi: 10.1103/PhysRevLett.110.152501. URL `https://link.aps.org/doi/10.1103/PhysRevLett.110.152501`.

[104] J. Kahlbow, C. Caesar, T. Aumann, V. Panin, S. Paschalis, H. Scheit, and H. Simon. Neutron radioactivity—lifetime measurements of neutron-unbound states. *Nuclear Instruments and Methods in Physics Research Section A: Accelerators, Spectrometers, Detec-*

tors and Associated Equipment, 866:265 – 271, 2017. ISSN 0168-9002. doi: https://doi.org/10.1016/j.nima.2017.06.002. URL http://www.sciencedirect.com/science/article/pii/S0168900217306460.

[105] J.-J. Gaimard and K.-H. Schmidt. A reexamination of the abrasion-ablation model for the description of the nuclear fragmentation reaction. *Nuclear Physics A*, 531(3):709 – 745, 1991. ISSN 0375-9474. doi: https://doi.org/10.1016/0375-9474(91)90748-U. URL http://www.sciencedirect.com/science/article/pii/037594749190748U.

[106] A.S. Goldhaber. Statistical models of fragmentation processes. *Physics Letters B*, 53(4):306 – 308, 1974. ISSN 0370-2693. doi: https://doi.org/10.1016/0370-2693(74)90388-8. URL http://www.sciencedirect.com/science/article/pii/0370269374903888.

[107] P.G. Hansen and J.A. Tostevin. Direct reactions with exotic nuclei. *Annual Review of Nuclear and Particle Science*, 53(1):219–261, 2003. doi: 10.1146/annurev.nucl.53.041002.110406. URL https://doi.org/10.1146/annurev.nucl.53.041002.110406.

[108] G. Jacob and Th.A.J. Maris. Quasi-free scattering and nuclear structure. *Rev. Mod. Phys.*, 38:121–142, Jan 1966. doi: 10.1103/RevModPhys.38.121. URL https://link.aps.org/doi/10.1103/RevModPhys.38.121.

[109] R. Serber. Nuclear reactions at high energies. *Phys. Rev.*, 72:1114–1115, Dec 1947. doi: 10.1103/PhysRev.72.1114. URL https://link.aps.org/doi/10.1103/PhysRev.72.1114.

[110] O. Chamberlain and E. Segrè. Proton-proton collisions within lithium nuclei. *Phys. Rev.*, 87:81–83, Jul 1952. doi: 10.1103/PhysRev.87.81. URL https://link.aps.org/doi/10.1103/PhysRev.87.81.

[111] L. Lapikás. Quasi-elastic electron scattering off nuclei. *Nuclear Physics A*, 553:297 – 308, 1993. ISSN 0375-9474. doi: https://doi.org/10.1016/0375-9474(93)90630-G. URL http://www.sciencedirect.com/science/article/pii/037594749390630G.

[112] V. Panin, J.T. Taylor, S. Paschalis, F. Wamers, Y. Aksyutina, H. Alvarez-Pol, T. Aumann, C.A. Bertulani, K. Boretzky, C. Caesar, M. Chartier, L.V. Chulkov, D. Cortina-Gil, J. Enders, O. Ershova, H. Geissel, R. Gernhäuser, M. Heil, H.T. Johansson, B. Jonson, A. Kelić-Heil, C. Langer, T. Le Bleis, R. Lemmon, T. Nilsson, M. Petri, R. Plag, R. Reifarth, D. Rossi, H. Scheit, H. Simon, H. Weick, and C. Wimmer. Exclusive measurements of quasi-free proton scattering reactions in inverse and complete kinematics. *Physics Letters B*, 753:204 – 210, 2016. ISSN 0370-2693. doi: https://doi.org/10.1016/j.physletb.2015.11.082. URL http://www.sciencedirect.com/science/article/pii/S0370269315009612.

[113] V. Panin. *Fully exclusive measurements of quasi-free single-nucleon knockout reactions in inverse kinematics.* PhD thesis, Technische Universität, Darmstadt, Nov 2012. URL http://tuprints.ulb.tu-darmstadt.de/3170/.

[114] G. Jacob and Th.A.J. Maris. Quasi-free scattering and nuclear structure. II. *Rev. Mod. Phys.*, 45:6–21, Jan 1973. doi: 10.1103/RevModPhys.45.6. URL https://link.aps.org/doi/10.1103/RevModPhys.45.6.

[115] T. Aumann, C.A. Bertulani, and J. Ryckebusch. Quasifree (p,$2p$) and (p,pn) reactions with unstable nuclei. *Phys. Rev. C*, 88:064610, Dec 2013. doi: 10.1103/PhysRevC.88.064610. URL https://link.aps.org/doi/10.1103/PhysRevC.88.064610.

[116] R. Palit, P. Adrich, T. Aumann, K. Boretzky, B.V. Carlson, D. Cortina, U. Datta Pramanik, Th.W. Elze, H. Emling, H. Geissel, M. Hellström, K.L. Jones, J.V. Kratz, R. Kulessa, Y. Leifels, A. Leistenschneider, G. Münzenberg, C. Nociforo, P. Reiter, H. Simon, K. Sümmerer, and W. Walus. Exclusive measurement of breakup reactions with the one-neutron halo nucleus ^{11}Be. *Phys. Rev. C*, 68:034318, Sep 2003. doi: 10.1103/PhysRevC.68.034318. URL https://link.aps.org/doi/10.1103/PhysRevC.68.034318.

[117] P.G. Hansen. Momentum content of single-nucleon halos. *Phys. Rev. Lett.*, 77:1016–1019, Aug 1996. doi: 10.1103/PhysRevLett.77.1016. URL https://link.aps.org/doi/10.1103/PhysRevLett.77.1016.

[118] C.A. Bertulani and P.G. Hansen. Momentum distributions in stripping reactions of radioactive projectiles at intermediate energies. *Phys. Rev. C*, 70:034609, Sep 2004. doi: 10.1103/PhysRevC.70.034609. URL https://link.aps.org/doi/10.1103/PhysRevC.70.034609.

[119] I.J. Thompson. Introduction to R-matrix theory. In *The 2016 R-Matrix Workshop on Methods and Applications*. Lawrence Livermore National Laboratory, June 2016. URL https://e-reports-ext.llnl.gov/pdf/825367.pdf.

[120] E.P. Wigner and L. Eisenbud. Higher angular momenta and long range interaction in resonance reactions. *Phys. Rev.*, 72:29–41, Jul 1947. doi: 10.1103/PhysRev.72.29. URL https://link.aps.org/doi/10.1103/PhysRev.72.29.

[121] A.M. Lane and R.G. Thomas. R-matrix theory of nuclear reactions. *Rev. Mod. Phys.*, 30:257–353, Apr 1958. doi: 10.1103/RevModPhys.30.257. URL https://link.aps.org/doi/10.1103/RevModPhys.30.257.

[122] J.K. Smith. *Unbound States in the lightest Island of Inversion: Neutron Decay Measurements of* ^{11}Li, ^{10}Li, *and* ^{12}Be. PhD thesis, Michigan State University, 2014. URL http://www.theses.fr/2015PA112153.

[123] C.B. Dover, C. Mahaux, and H.A. Weidenmüller. The single-particle limit for partial widths. *Nuclear Physics A*, 39(3):593 – 604, 1969. ISSN 0375-9474. doi: https://doi.org/10.1016/0375-9474(69)90281-4. URL http://www.sciencedirect.com/science/article/pii/0375947469902814.

[124] T. Teichmann and E.P. Wigner. Sum rules in the dispersion theory of nuclear reactions. *Phys. Rev.*, 87:123–135, Jul 1952. doi: 10.1103/PhysRev.87.123. URL https://link.aps.org/doi/10.1103/PhysRev.87.123.

[125] R.A. Kryger, A. Azhari, M. Hellström, J.H. Kelley, T. Kubo, R. Pfaff, E. Ramakrishnan, B.M. Sherrill, M. Thoennessen, S. Yokoyama, R.J. Charity, J. Dempsey, A. Kirov, N. Robertson, D.G. Sarantites, L.G. Sobotka, and J.A. Winger. Two-proton emission from the ground state of ^{12}O. *Phys. Rev. Lett.*, 74:860–863, Feb 1995. doi: 10.1103/PhysRevLett.74.860. URL https://link.aps.org/doi/10.1103/PhysRevLett.74.860.

[126] F.C. Barker. Width of the ^{12}O ground state. *Phys. Rev. C*, 59:535–538, Jan 1999. doi: 10.1103/PhysRevC.59.535. URL https://link.aps.org/doi/10.1103/PhysRevC.59.535.

[127] J. Marganiec, F. Wamers, F. Aksouh, Yu. Aksyutina, H. Álvarez-Pol, T. Aumann, S. Beceiro-Novo, K. Boretzky, M.J.G. Borge, M. Chartier, A. Chatillon, L.V. Chulkov, D. Cortina-Gil, H. Emling, O. Ershova, L.M. Fraile, H.O.U. Fynbo, D. Galaviz, H. Geissel, M. Heil, D.H.H. Hoffmann, J. Hoffmann, H.T. Johansson, B. Jonson, C. Karagiannis, O.A. Kiselev, J.V. Kratz, R. Kulessa, N. Kurz, C. Langer, M. Lantz, T. Le Bleis, R. Lemmon, Yu. A. Litvinov, K. Mahata, C. Müntz, T. Nilsson, C. Nociforo, G. Nyman, W. Ott, V. Panin, S. Paschalis, A. Perea, R. Plag, R. Reifarth, A. Richter, C. Rodriguez-Tajes, D. Rossi, K. Riisager, D. Savran, G. Schrieder, H. Simon, J. Stroth, K. Sümmerer, O. Tengblad, H. Weick, M. Wiescher, C. Wimmer, and M.V. Zhukov. Studies of continuum states in ^{16}Ne using three-body correlation techniques. *The European Physical Journal A*, 51(1):9, Jan 2015. ISSN 1434-601X. doi: 10.1140/epja/i2015-15009-0. URL https://doi.org/10.1140/epja/i2015-15009-0.

[128] H. Simon. Masses of unbound nuclear systems. *International Journal of Mass Spectrometry*, 349-350:172 – 180, 2013. ISSN 1387-3806. doi: https://doi.org/10.1016/j.ijms.2013.05.013. URL http://www.sciencedirect.com/science/article/pii/S1387380613001826.

[129] Y. Kondo. Spectroscopy of unbound oxygen isotopes II. Proposal NP1312-SAMURAI21 to the NP-PAC at the RIBF, 2013. (unpublished).

[130] Y. Yano. The RIKEN RI beam factory project: A status report. *Nuclear Instruments and Methods in Physics Research Section B: Beam Interactions with Materials and Atoms*, 261(1):1009 – 1013, 2007. ISSN 0168-583X. doi: https://doi.org/10.1016/j.nimb.2007.04.174. URL http://www.sciencedirect.com/science/article/pii/S0168583X07009792. The Application of Accelerators in Research and Industry.

[131] H. Sakurai. RI beam factory project at RIKEN. *Nuclear Physics A*, 805(1):526c – 532c, 2008. ISSN 0375-9474. doi: https://doi.org/10.1016/j.nuclphysa.2008.02.291. URL http://www.sciencedirect.com/science/article/pii/S0375947408003862. INPC 2007.

[132] RIBF schematic view. URL http://ribf.riken.jp/intds2014/location/images/CG_bird.jpg. Accessed: 2018-05-05.

[133] RIBF technical information – beam intensity. URL http://www.nishina.riken.jp/RIBF/accelerator/tecinfo.html. Accessed: 2018-05-05.

[134] RIKEN facilities. URL https://www.nishina.riken.jp/facility/RIBFfacility_e.html. Accessed: 2019-06-04.

[135] H. Okuno, J. Ohnishi, K. Yamada, N. Fukunishi, K. Ikegami, T. Maie, H. Hasebe, M. Hamanaka, M. Kase, A. Goto, and Y. Yano. The superconducting ring cyclotron in RIKEN. *IEEE Transactions on Applied Superconductivity*, 17(2):1063–1068, June 2007. ISSN 1051-8223. doi: 10.1109/TASC.2007.899864.

[136] M. Thoennessen. 2017 update of the discoveries of nuclides. *International Journal of Modern Physics E*, 27(1830002), Feb 2018. doi: https://doi.org/10.1142/S0218301318300023.

[137] T. Kubo. In-flight RI beam separator BigRIPS at RIKEN and elsewhere in Japan. *Nuclear Instruments and Methods in Physics Research Section B: Beam Interactions with Materials and Atoms*, 204:97 – 113, 2003. ISSN 0168-583X. doi: https://doi.org/10.1016/S0168-583X(02)01896-7. URL http://www.sciencedirect.com/science/article/pii/S0168583X02018967. 14th International Conference on Electromagnetic Isotope Separators and Techniques Related to their Applications.

[138] T. Kubo, K. Kusaka, K. Yoshida, A. Yoshida, T. Ohnishi, M. Ohtake, Y. Yanagisawa, N. Fukuda, T. Haseyama, Y. Yano, N. Kakutani, T. Tsuchihashi, and K. Sato. Status and overview of superconducting radioactive isotope beam separator BigRIPS at RIKEN. *IEEE Transactions on Applied Superconductivity*, 17(2):1069–1077, June 2007. ISSN 1051-8223. doi: 10.1109/TASC.2007.897203.

[139] BigRIPS Information. URL http://ribf.riken.jp/BigRIPSInfo/. Accessed: 2018-05-07.

[140] Decay radiation of NNDC. URL http://www.nndc.bnl.gov/. Accessed: 2018-05-05.

[141] J.P. Dufour, R. Del Moral, H. Emmermann, F. Hubert, D. Jean, C. Poinot, M.S. Pravikoff, A. Fleury, H. Delagrange, and K.-H. Schmidt. Projectile fragments isotopic separation: Application to the LISE spectrometer at GANIL. *Nuclear Instruments and Methods in Physics Research Section A: Accelerators, Spectrometers, Detectors and Associated Equipment*, 248(2):

267 – 281, 1986. ISSN 0168-9002. doi: https://doi.org/10.1016/0168-9002(86)91008-9. URL http://www.sciencedirect.com/science/article/pii/0168900286910089.

[142] K.-H. Schmidt, E. Hanelt, H. Geissel, G. Münzenberg, and J.P. Dufour. The momentum-loss achromat – a new method for the isotopical separation of relativistic heavy ions. *Nuclear Instruments and Methods in Physics Research Section A: Accelerators, Spectrometers, Detectors and Associated Equipment*, 260(2):287 – 303, 1987. ISSN 0168-9002. doi: https://doi.org/10.1016/0168-9002(87)90092-1. URL http://www.sciencedirect.com/science/article/pii/0168900287900921.

[143] H. Kumagai, T. Ohnishi, N. Fukuda, H. Takeda, D. Kameda, N. Inabe, K. Yoshida, and T. Kubo. Development of parallel plate avalanche counter (PPAC) for BigRIPS fragment separator. *Nuclear Instruments and Methods in Physics Research Section B: Beam Interactions with Materials and Atoms*, 317:717 – 727, 2013. ISSN 0168-583X. doi: https://doi.org/10.1016/j.nimb.2013.08.050. URL http://www.sciencedirect.com/science/article/pii/S0168583X13009932. XVIth International Conference on ElectroMagnetic Isotope Separators and Techniques Related to their Applications, December 2–7, 2012 at Matsue, Japan.

[144] Large-acceptance multi-particle spectrometer SAMURAI – construction proposal. URL http://ribf.riken.jp/SAMURAI/120425_SAMURAIConstProp.pdf. Accessed: 2019-06-04.

[145] Y. Shimizu, T. Kobayashi, T. Kubo, N. Chiga, T. Isobe, T. Kawabata, Y. Kondo, K. Kusaka, Y. Matsuda, T. Motobayashi, T. Murakami, T. Nakamura, J. Ohnishi, T. Ohnishi, H. Okuno, H. Otsu, H. Sakurai, H. Sato, Y. Satou, K. Sekiguchi, Y. Togano, and K. Yoneda. SAMURAI project at RIBF. *Journal of Physics: Conference Series*, 312(5):052022, 2011. URL http://stacks.iop.org/1742-6596/312/i=5/a=052022.

[146] Technical report for the design, construction and commissioning of NeuLAND: The high-resolution neutron time-of-flight spectrometer for R^3B, Nov 2011. URL https://edms.cern.ch/document/1865739/1.

[147] SAMURAI21 Wiki. URL http://be.nucl.ap.titech.ac.jp/~samurai21/moin/moin.cgi/FrontPage. Accessed: 2019-05-14.

[148] G.F. Knoll. *Radiation detection and measurement; 4th Ed.* Wiley, New York, NY, 2010.

[149] C. Patrignani and others (Particle Data Group). Review of Particle Physics. *Chin. Phys.*, C40(10):100001, 2016. doi: 10.1088/1674-1137/40/10/100001. URL http://pdg.lbl.gov/.

[150] W.R. Leo. *Techniques for Nuclear and Particle Physics Experiments*. Springer-Verlag, 1994.

[151] C. Santamaria. *Quest for new nuclear magic numbers with MINOS*. PhD thesis, Université Paris-Sud XI, Paris, 2015. URL http://www.theses.fr/2015PA112153. 2015PA112153.

[152] L. Atar, S. Paschalis, C. Barbieri, C. A. Bertulani, P. Díaz Fernández, M. Holl, M. A. Najafi, V. Panin, H. Alvarez-Pol, T. Aumann, V. Avdeichikov, S. Beceiro-Novo, D. Bemmerer, J. Benlliure, J. M. Boillos, K. Boretzky, M. J. G. Borge, M. Caamaño, C. Caesar, E. Casarejos, W. Catford, J. Cederkall, M. Chartier, L. Chulkov, D. Cortina-Gil, E. Cravo, R. Crespo, I. Dillmann, Z. Elekes, J. Enders, O. Ershova, A. Estrade, F. Farinon, L. M. Fraile, M. Freer, D. Galaviz Redondo, H. Geissel, R. Gernhäuser, P. Golubev, K. Göbel, J. Hagdahl, T. Heftrich, M. Heil, M. Heine, A. Heinz, A. Henriques, A. Hufnagel, A. Ignatov, H. T. Johansson, B. Jonson, J. Kahlbow, N. Kalantar-Nayestanaki, R. Kanungo, A. Kelic-Heil, A. Knyazev, T. Kröll, N. Kurz, M. Labiche, C. Langer, T. Le Bleis, R. Lemmon, S. Lindberg, J. Machado, J. Marganiec-Galazka, A. Movsesyan, E. Nacher, E. Y. Nikolskii, T. Nilsson, C. Nociforo, A. Perea, M. Petri, S. Pietri, R. Plag, R. Reifarth, G. Ribeiro, C. Rigollet, D. M. Rossi, M. Röder, D. Savran, H. Scheit, H. Simon, O. Sorlin, I. Syndikus, J. T. Taylor, O. Tengblad, R. Thies, Y. Togano, M. Vandebrouck, P. Velho, V. Volkov, A. Wagner, F. Wamers, H. Weick, C. Wheldon, G. L. Wilson, J. S. Winfield, P. Woods, D. Yakorev, M. Zhukov, A. Zilges, and K. Zuber. Quasifree (p,$2p$) reactions on oxygen isotopes: Observation of isospin independence of the reduced single-particle strength. *Phys. Rev. Lett.*, 120:052501, Jan 2018. doi: 10.1103/PhysRevLett.120.052501. URL https://link.aps.org/doi/10.1103/PhysRevLett.120.052501.

[153] A. Obertelli, A. Delbart, S. Anvar, L. Audirac, G. Authelet, H. Baba, B. Bruyneel, D. Calvet, F. Château, A. Corsi, P. Doornenbal, J.-M. Gheller, A. Giganon, C. Lahonde-Hamdoun, D. Leboeuf, D. Loiseau, A. Mohamed, J.-Ph. Mols, H. Otsu, C. Péron, A. Peyaud, E.C. Pollacco, G. Prono, J.-Y. Rousse, C. Santamaria, and T. Uesaka. MINOS: A vertex tracker coupled to a thick liquid-hydrogen target for in-beam spectroscopy of exotic nuclei. *Eur. Phys. J. A*, 50(1):8, 2014. doi: 10.1140/epja/i2014-14008-y. URL https://doi.org/10.1140/epja/i2014-14008-y.

[154] A. Obertelli, P. Doornenbal, A. Corsi, Y. Kondo, Y. Kubota, J. Lee, T. Nakamura, N. Orr, H. Sakurai, M. Sasano, T. Uesaka, the MINOS collaboration, and the SEASTAR collaboration. *Physics Program at the RIBF with MINOS*. Proceedings of the Conference on Advances in Radioactive Isotope Science (ARIS2014). doi: 10.7566/JPSCP.6.010014. URL https://journals.jps.jp/doi/abs/10.7566/JPSCP.6.010014.

[155] R. Taniuchi, C. Santamaria, P. Doornenbal, A. Obertelli, K. Yoneda, G. Authelet, D. Baba, H.and Calvet, F. Château, A. Corsi, A. Delbart, J.-M. Gheller, A. Gillibert, J.D. Holt, T. Isobe, V. Lapoux, M. Matsushita, J. Menéndez, S. Momiyama, T. Motobayashi, M. Nikura, F. Nowacki, K. Ogata, H. Otsu, T. Otsuka, C. Péron, S. Péru, A. Peyaud, E.C. Pollacco, A. Poves, J.-Y. Roussé, H. Sakurai, A. Schwenk, Y. Shiga, J. Simonis, S.R. Stroberg,

S. Takeuchi, Y. Tsunoda, T. Uesaka, H. Wang, F. Browne, L.X. Chung, Z. Dombradi, S. Franchoo, F. Giacoppo, A. Gottardo, K. Hadynska-Klek, Z. Korkulu, S. Koyama, Y. Kubota, J. Lee, M. Lettmann, C. Louchart, R. Lozeva, K. Matsui, T. Miyazaki, S. Nishimura, L. Olivier, S. Ota, Z. Patel, E. Sahin, C. Shand, P.-A. Söderström, I. Stefan, D. Steppenbeck, T. Sumikama, D. Suzuki, Z. Vajta, V. Werner, J. Wu, and Z.Y. Xu. ^{78}Ni revealed as a doubly magic stronghold against nuclear deformation. *Nature*, 569(7754):53–58, 2019. ISSN 1476-4687. doi: 10.1038/s41586-019-1155-x. URL https://doi.org/10.1038/s41586-019-1155-x.

[156] N. Paul, A. Corsi, A. Obertelli, P. Doornenbal, G. Authelet, H. Baba, B. Bally, M. Bender, D. Calvet, F. Château, S. Chen, J.-P. Delaroche, A. Delbart, J.-M. Gheller, A. Giganon, A. Gillibert, M. Girod, P.-H. Heenen, V. Lapoux, J. Libert, T. Motobayashi, M. Niikura, T. Otsuka, T.R. Rodríguez, J.-Y. Roussé, H. Sakurai, C. Santamaria, N. Shimizu, D. Steppenbeck, R. Taniuchi, T. Togashi, Y. Tsunoda, T. Uesaka, T. Ando, T. Arici, A. Blazhev, F. Browne, A.M. Bruce, R. Carroll, L.X. Chung, M.L. Cortés, M. Dewald, B. Ding, F. Flavigny, S. Franchoo, M. Górska, A. Gottardo, A. Jungclaus, J. Lee, M. Lettmann, B.D. Linh, J. Liu, Z. Liu, C. Lizarazo, S. Momiyama, K. Moschner, S. Nagamine, N. Nakatsuka, C. Nita, C.R. Nobs, L. Olivier, Z. Patel, Zs. Podolyák, M. Rudigier, T. Saito, C. Shand, P.-A. Söderström, I. Stefan, R. Orlandi, V. Vaquero, V. Werner, K. Wimmer, and Z. Xu. Are there signatures of harmonic oscillator shells far from stability? First spectroscopy of ^{110}Zr. *Phys. Rev. Lett.*, 118:032501, Jan 2017. doi: 10.1103/PhysRevLett.118.032501. URL https://link.aps.org/doi/10.1103/PhysRevLett.118.032501.

[157] S. Takeuchi, T. Motobayashi, Y. Togano, M. Matsushita, N. Aoi, K. Demichi, H. Hasegawa, and H. Murakami. DALI2: A NaI(Tl) detector array for measurements of γ rays from fast nuclei. *Nuclear Instruments and Methods in Physics Research Section A: Accelerators, Spectrometers, Detectors and Associated Equipment*, 763:596 – 603, 2014. ISSN 0168-9002. doi: https://doi.org/10.1016/j.nima.2014.06.087. URL http://www.sciencedirect.com/science/article/pii/S0168900214008419.

[158] Y. Kondo, T. Tomai, and T. Nakamura. Recent progress and developments for experimental studies with the SAMURAI spectrometer. 2019. Proceedings of the XVIIIth International Conference on Electromagnetic Isotope Separators and Related Topics (EMIS2018), to be published.

[159] K. Koch, H. Hardel, R. Schulze, E. Badura, and J. Hoffmann. A new TAC based multi channel front-end electronics for TOF experiments with very high time resolution. In *IEEE Symposium Conference Record Nuclear Science 2004.*, volume 3, pages 1357–1359 Vol. 3, Oct 2004. doi: 10.1109/NSSMIC.2004.1462493.

[160] SAMURAI-NeuLAND Wiki. URL http://be.nucl.ap.titech.ac.jp/~samurai-neuland/moin.cgi/FrontPage. Accessed: 2019-06-04.

[161] C. Caesar. *Beyond the Neutron Drip-Line: Superheavy Oxygen Isotopes*. PhD thesis, Technische Universität, Darmstadt, Oct 2012. URL http://tuprints.ulb.tu-darmstadt.de/3224/.

[162] V-STARS Geodetic Systems. URL https://www.geodetic.com/products/systems/v-stars-n/. Accessed: 2019-04-22.

[163] T. Ozaki. Photogrammetry analysis, Jan 2016. URL http://be.nucl.ap.titech.ac.jp/~samurai21/moin/moin.cgi/Offline/Materials. Private communication.

[164] H. Baba, T. Ichihara, T. Ohnishi, S. Takeuchi, K. Yoshida, Y. Watanabe, S. Ota, and S. Shimoura. New data acquisition system for the RIKEN Radioactive Isotope Beam Factory. *Nuclear Instruments and Methods in Physics Research Section A: Accelerators, Spectrometers, Detectors and Associated Equipment*, 616(1):65 – 68, 2010. ISSN 0168-9002. doi: https://doi.org/10.1016/j.nima.2010.02.120. URL http://www.sciencedirect.com/science/article/pii/S0168900210003761.

[165] T. Isobe and the RIBF DAQ group. ANAROOT: online/offline framework for RIBF data analysis based on ROOT. URL https://ribf.riken.jp/RIBFDAQ/index.php?Tools%2FAnalysis%2FInformation. Accessed: 2019-05-14.

[166] H. Baba, T. Ichihara, T. Ohnishi, S. Takeuchi, K. Yoshida, Y. Watanabe, S. Ota, and S. Shimoura. Development of the GTO module. In *RIKEN Accelerator Progress Report 2012*, volume 46. 2013. URL http://www.nishina.riken.jp/researcher/APR/APR050/APR050.html.

[167] R. Brun and F. Rademakers. ROOT – an object oriented data analysis framework. *Nuclear Instruments and Methods in Physics Research Section A: Accelerators, Spectrometers, Detectors and Associated Equipment*, 389:81 – 86, Sep 1996. URL http://root.cern.ch/. Proceedings AIHENP'96 Workshop, Lausanne.

[168] I. Gasparic. NeuLAND calibration parameters, Dec 2015. Private communication.

[169] Y. Kondo. Time-of-flight analysis of the neutron detectors at SAMURAI, Jan 2018. Private communication.

[170] T. Sako. Development of the large neutron detector NEBULA for RI-beam experiments, 2012. Master's Thesis, Tokyo Institute of Technology.

[171] J. Lindhard and A.H. Sørensen. Relativistic theory of stopping for heavy ions. *Phys. Rev. A*, 53:2443–2456, Apr 1996. doi: 10.1103/PhysRevA.53.2443. URL https://link.aps.org/doi/10.1103/PhysRevA.53.2443.

[172] ATIMA – slowing down of protons and heavy ions in matter. URL https://web-docs.gsi.de/~weick/atima/. Accessed: 2018-06-09.

[173] O.B. Tarasov and D. Bazin. LISE++: Radioactive beam production with in-flight separators. *Nuclear Instruments and Methods in Physics Research Section B: Beam Interactions with Materials and Atoms*, 266(19):4657 – 4664, 2008. ISSN 0168-583X. doi: https://doi.org/10.1016/j.nimb.2008.05.110. URL http://www.sciencedirect.com/science/article/pii/S0168583X08007969. Proceedings of the XVth International Conference on Electromagnetic Isotope Separators and Techniques Related to their Applications.

[174] SAMURAI Simulator. URL http://be.nucl.ap.titech.ac.jp/~nebula/simulator.php. Accessed: 2018-06-21.

[175] S. Agostinelli, J. Allison, K. Amako, J. Apostolakis, H. Araujo, P. Arce, M. Asai, D. Axen, S. Banerjee, G. Barrand, F. Behner, L. Bellagamba, J. Boudreau, L. Broglia, A. Brunengo, H. Burkhardt, S. Chauvie, J. Chuma, R. Chytracek, G. Cooperman, G. Cosmo, P. Degtyarenko, A. Dell'Acqua, G. Depaola, D. Dietrich, R. Enami, A. Feliciello, C. Ferguson, H. Fesefeldt, G. Folger, F. Foppiano, A. Forti, S. Garelli, S. Giani, R. Giannitrapani, D. Gibin, J.J. Gómez Cadenas, I. González, G. Gracia Abril, G. Greeniaus, W. Greiner, V. Grichine, A. Grossheim, S. Guatelli, P. Gumplinger, R. Hamatsu, K. Hashimoto, H. Hasui, A. Heikkinen, A. Howard, V. Ivanchenko, A. Johnson, F.W. Jones, J. Kallenbach, N. Kanaya, M. Kawabata, Y. Kawabata, M. Kawaguti, S. Kelner, P. Kent, A. Kimura, T. Kodama, R. Kokoulin, M. Kossov, H. Kurashige, E. Lamanna, T. Lampén, V. Lara, V. Lefebure, F. Lei, M. Liendl, W. Lockman, F. Longo, S. Magni, M. Maire, E. Medernach, K. Minamimoto, P. Mora de Freitas, Y. Morita, K. Murakami, M. Nagamatu, R. Nartallo, P. Nieminen, T. Nishimura, K. Ohtsubo, M. Okamura, S. O'Neale, Y. Oohata, K. Paech, J. Perl, A. Pfeiffer, M.G. Pia, F. Ranjard, A. Rybin, S. Sadilov, E. Di Salvo, G. Santin, T. Sasaki, N. Savvas, Y. Sawada, S. Scherer, S. Sei, V. Sirotenko, D. Smith, N. Starkov, H. Stoecker, J. Sulkimo, M. Takahata, S. Tanaka, E. Tcherniaev, E. Safai Tehrani, M. Tropeano, P. Truscott, H. Uno, L. Urban, P. Urban, M. Verderi, A. Walkden, W. Wander, H. Weber, J.P. Wellisch, T. Wenaus, D.C. Williams, D. Wright, T. Yamada, H. Yoshida, and D. Zschiesche. Geant4—a simulation toolkit. *Nuclear Instruments and Methods in Physics Research Section A: Accelerators, Spectrometers, Detectors and Associated Equipment*, 506(3):250 – 303, 2003. ISSN 0168-9002. doi: https://doi.org/10.1016/S0168-9002(03)01368-8. URL http://www.sciencedirect.com/science/article/pii/S0168900203013688.

[176] GEANT4 a simulation toolkit. URL https://geant4.web.cern.ch/. Accessed: 2018-06-21.

[177] A. Boudard, J. Cugnon, J.-C. David, S. Leray, and D. Mancusi. New potentialities of the Liège intranuclear cascade model for reactions induced by nucleons and light charged particles. *Phys. Rev. C*, 87:014606, Jan 2013. doi: 10.1103/PhysRevC.87.014606. URL https://link.aps.org/doi/10.1103/PhysRevC.87.014606.

[178] *Charting NeuLAND: Towards multi-neutron reconstruction with the New Large Area Neutron Detector and The virtual γ-ray spectrometer G4Horus*. PhD thesis, 2018.

[179] T. Nakamura and Y. Kondo. Large acceptance spectrometers for invariant mass spectroscopy of exotic nuclei and future developments. *Nuclear Instruments and Methods in Physics Research Section B: Beam Interactions with Materials and Atoms*, 376:156 – 161, 2016. ISSN 0168-583X. doi: https://doi.org/10.1016/j.nimb.2016.01.003. URL http://www.sciencedirect.com/science/article/pii/S0168583X1600029X. Proceedings of the XVIIth International Conference on Electromagnetic Isotope Separators and Related Topics (EMIS2015), Grand Rapids, MI, U.S.A., 11-15 May 2015.

[180] Kanzo Nakayama, Elizabeth Farrelly Pessoa, and Ross Alan Douglas. A modified version of the Monte Carlo computer code for calculating neutron detection efficiencies. *Nuclear Instruments and Methods in Physics Research*, 190(3):555 – 563, 1981. ISSN 0167-5087. doi: https://doi.org/10.1016/0029-554X(81)90956-3. URL http://www.sciencedirect.com/science/article/pii/0029554X81909563.

[181] Y. Iwamoto, M. Hagiwara, D. Satoh, S. Araki, H. Yashima, T. Sato, A. Masuda, T. Matsumoto, N. Nakao, T. Shima, T. Kin, Y. Watanabe, H. Iwase, and T. Nakamura. Characterization of high-energy quasi-monoenergetic neutron energy spectra and ambient dose equivalents of 80–389 MeV $^{7}\mathrm{Li}(p,n)$ reactions using a time-of-flight method. *Nuclear Instruments and Methods in Physics Research Section A: Accelerators, Spectrometers, Detectors and Associated Equipment*, 804:50 – 58, 2015. ISSN 0168-9002. doi: https://doi.org/10.1016/j.nima.2015.09.045. URL http://www.sciencedirect.com/science/article/pii/S0168900215011006.

[182] T.N. Taddeucci, W.P. Alford, M. Barlett, R.C. Byrd, T.A. Carey, D.E. Ciskowski, C.C. Foster, C. Gaarde, C.D. Goodman, C.A. Goulding, E. Gülmez, W. Huang, D.J. Horen, J. Larsen, D. Marchlenski, J.B. McClelland, D. Prout, J. Rapaport, L.J. Rybarcyk, W.C. Sailor, E. Sugarbaker, and C.A. Whitten. Zero-degree cross sections for the $^{7}\mathrm{Li}(p,n)^{7}\mathrm{Be}$(g.s.+0.43-MeV) reaction in the energy range 80–795 MeV. *Phys. Rev. C*, 41:2548–2555, Jun 1990. doi: 10.1103/PhysRevC.41.2548. URL https://link.aps.org/doi/10.1103/PhysRevC.41.2548.

[183] Y. Iwamoto, M. Hagiwara, D. Satoh, H. Iwase, H. Yashima, T. Itoga, T. Sato, Y. Nakane, H. Nakashima, Y. Sakamoto, T. Matsumoto, A. Masuda, J. Nishiyama, A. Tamii, K. Hatanaka, C. Theis, E. Feldbaumer, L. Jaegerhofer, C. Pioch, V. Mares, and T. Nakamura. Quasi-monoenergetic neutron energy spectra for 246 and 389 MeV $^{7}\mathrm{Li}(p,n)$ reactions at angles from 0° to 30°. *Nuclear Instruments and Methods in Physics Research Section A: Accelerators, Spectrometers, Detectors and Associated Equipment*, 629(1):43 – 49, 2011. ISSN 0168-9002. doi: https://doi.org/10.1016/j.nima.2010.12.022. URL http://www.sciencedirect.com/science/article/pii/S0168900210027609.

[184] J.W. Watson, B.D. Anderson, A.R. Baldwin, C. Lebo, B. Flanders, W. Pairsuwan, R. Madey, and C.C. Foster. A comparison of methods for determining neutron detector efficiencies at medium energies. *Nuclear Instruments and Methods in Physics Research*, 215(3):413 – 421, 1983. ISSN 0167-5087. doi: https://doi.org/10.1016/0167-5087(83)90472-6. URL http://www.sciencedirect.com/science/article/pii/0167508783904726.

[185] H. Scheit. *Low-Lying Collective Excitations in Neutron-Rich Even-Even Sulfur and Argon Isotopes Studied via Intermediate-Energy Coulomb Excitation and Proton Scattering*. PhD thesis, Michigan State University, 1998. URL https://groups.nscl.msu.edu/nscl_library/Thesis/Scheit,%20Heiko.pdf.

[186] J. Davidson, N. Jarmie, and A. Niethammer. RELKIN: A two-body relativistic kinematics code, Jan 1969. URL https://www.osti.gov/biblio/4108993-relkin-two-body-relativistic-kinematics-code.

[187] Y. Iwamoto. Data points of neutron-energy spectra, Apr 2016. Private communication.

[188] H.T. Fortune and R. Sherr. Widths and spectroscopic factors in ^{21}O. *Phys. Rev. C*, 85: 027305, Feb 2012. doi: 10.1103/PhysRevC.85.027305. URL https://link.aps.org/doi/10.1103/PhysRevC.85.027305.

[189] H.T. Fortune. Decays of $^{15}\mathrm{Be}(5/2^{+})$. *Phys. Rev. C*, 98:054317, Nov 2018. doi: 10.1103/PhysRevC.98.054317. URL https://link.aps.org/doi/10.1103/PhysRevC.98.054317.

[190] C. Caesar, J. Simonis, T. Adachi, Y. Aksyutina, J. Alcantara, S. Altstadt, H. Alvarez-Pol, N. Ashwood, T. Aumann, V. Avdeichikov, M. Barr, S. Beceiro, D. Bemmerer, J. Benlliure, C.A. Bertulani, K. Boretzky, M.J.G. Borge, G. Burgunder, M. Caamano, E. Casarejos, W. Catford, J. Cederkäll, S. Chakraborty, M. Chartier, L. Chulkov, D. Cortina-Gil, U. Datta Pramanik, P. Diaz Fernandez, I. Dillmann, Z. Elekes, J. Enders, O. Ershova, A. Estrade, F. Farinon, L.M. Fraile, M. Freer, M. Freudenberger, H.O.U. Fynbo, D. Galaviz, H. Geissel, R. Gernhäuser, P. Golubev, D. Gonzalez Diaz, J. Hagdahl, T. Heftrich, M. Heil, M. Heine, A. Heinz, A. Henriques, M. Holl, J.D. Holt, G. Ickert, A. Ignatov, B. Jakobsson, H.T. Johansson, B. Jonson, N. Kalantar-Nayestanaki, R. Kanungo, A. Kelic-Heil, R. Knöbel, T. Kröll,

R. Krücken, J. Kurcewicz, M. Labiche, C. Langer, T. Le Bleis, R. Lemmon, O. Lepyoshkina, S. Lindberg, J. Machado, J. Marganiec, V. Maroussov, J. Menéndez, M. Mostazo, A. Movsesyan, A. Najafi, T. Nilsson, C. Nociforo, V. Panin, A. Perea, S. Pietri, R. Plag, A. Prochazka, A. Rahaman, G. Rastrepina, R. Reifarth, G. Ribeiro, M.V. Ricciardi, C. Rigollet, K. Riisager, M. Röder, D. Rossi, J. Sanchez del Rio, D. Savran, H. Scheit, A. Schwenk, H. Simon, O. Sorlin, V. Stoica, B. Streicher, J. Taylor, O. Tengblad, S. Terashima, R. Thies, Y. Togano, E. Uberseder, J. Van de Walle, P. Velho, V. Volkov, A. Wagner, F. Wamers, H. Weick, M. Weigand, C. Wheldon, G. Wilson, C. Wimmer, J.S. Winfield, P. Woods, D. Yakorev, M.V. Zhukov, A. Zilges, M. Zoric, and K. Zuber. Beyond the neutron drip line: The unbound oxygen isotopes ^{25}O and ^{26}O. *Phys. Rev. C*, 88:034313, Sep 2013. doi: 10.1103/PhysRevC.88.034313. URL `https://link.aps.org/doi/10.1103/PhysRevC.88.034313`.

[191] T. Nakamura, N. Kobayashi, Y. Kondo, Y. Satou, J.A. Tostevin, Y. Utsuno, N. Aoi, H. Baba, N. Fukuda, J. Gibelin, N. Inabe, M. Ishihara, D. Kameda, T. Kubo, T. Motobayashi, T. Ohnishi, N.A. Orr, H. Otsu, T. Otsuka, H. Sakurai, T. Sumikama, H. Takeda, E. Takeshita, M. Takechi, S. Takeuchi, Y. Togano, and K. Yoneda. Deformation-driven p-wave halos at the drip line: ^{31}Ne. *Phys. Rev. Lett.*, 112:142501, Apr 2014. doi: 10.1103/PhysRevLett.112.142501. URL `https://link.aps.org/doi/10.1103/PhysRevLett.112.142501`.

[192] L. Chulkov. Sequential-decay analysis for three-body fractional energy, May 2019. Private communication.

[193] C.A. Bertulani. Momentum distributions in QFS theory for ^{29}F, May 2019. Private communication.

[194] F. Deák, A. Kiss, Z. Seres, G. Caskey, A. Galonsky, and B. Remington. Method for the study of neutron emission from light fragments in intermediate energy heavy-ion collisions. *Nuclear Instruments and Methods in Physics Research Section A: Accelerators, Spectrometers, Detectors and Associated Equipment*, 258(1):67 – 74, 1987. ISSN 0168-9002. doi: https://doi.org/10.1016/0168-9002(87)90080-5. URL `http://www.sciencedirect.com/science/article/pii/0168900287900805`.

[195] A.O. Macchiavelli, H.L. Crawford, P. Fallon, C.M. Campbell, R.M. Clark, M. Cromaz, M.D. Jones, I.Y. Lee, and M. Salathe. Structure of ^{29}F in the rotation-aligned coupling scheme of the particle-rotor model. *Physics Letters B*, 775:160 – 162, 2017. ISSN 0370-2693. doi: https://doi.org/10.1016/j.physletb.2017.10.041. URL `http://www.sciencedirect.com/science/article/pii/S0370269317308535`.

[196] Y. Utsuno, T. Otsuka, T. Glasmacher, T. Mizusaki, and M. Honma. Onset of intruder ground state in exotic Na isotopes and evolution of the $N = 20$ shell gap. *Phys. Rev. C*, 70:

044307, Oct 2004. doi: 10.1103/PhysRevC.70.044307. URL https://link.aps.org/doi/10.1103/PhysRevC.70.044307.

[197] Y. Utsuno, T. Otsuka, T. Mizusaki, and M. Honma. Extreme location of F drip line and disappearance of the $N = 20$ magic structure. *Phys. Rev. C*, 64:011301, Jun 2001. doi: 10.1103/PhysRevC.64.011301. URL https://link.aps.org/doi/10.1103/PhysRevC.64.011301.

[198] C. Barbieri. Gorkov calculation in SCGF theory for ^{29}F, Apr 2019. Private communication.

[199] V. Somà, P. Navrátil, F. Raimondi, C. Barbieri, and T. Duguet. Novel chiral Hamiltonian and observables in light and medium-mass nuclei, 2019.

[200] A. Idini, C. Barbieri, and P. Navrátil. Ab initio optical potentials and nucleon scattering on medium mass nuclei. *Phys. Rev. Lett.*, 123:092501, Aug 2019. doi: 10.1103/PhysRevLett.123.092501. URL https://link.aps.org/doi/10.1103/PhysRevLett.123.092501.

[201] P.R. Bevington and D.K. Robinson. *Data reduction and error analysis for the physical sciences*. Boston [u.a.], 3. edition, 2003. ISBN 0072472278.

[202] F. James. MINUIT: Function minimization and error analysis reference manual. 1998. URL http://cds.cern.ch/record/2296388. CERN Program Library Long Writeups.

[203] Wolfram Research, Inc. Mathematica, Version 11.2.0.0. Champaign, IL, 2018.

List of Notations

ADC	Analog-to-Digital Converter.
BDC	Beam Drift Chamber.
BigRIPS	Big RIKEN Projectile Fragment Separator.
c. m.	Center-of-Mass.
CC	Coupled Cluster.
CERN	Conseil Européen pour la Recherche Nucléaire.
CFD	Constant-Fraction Discriminator.
DALI2	Detector Array for Low Intensity radiation 2.
DAQ	Data Acquisition.
DWIA	Distorted Wave Impulse Approximation.
ECR	Electron Cyclotron Resonance.
EFT	Effective Field Theory.
EoS	Equation of State.
ESPE	Effective Single Particle Energy.
FAIR	Facility for Antiproton and Ion Research.
FDC	Forward Drift Chamber.
FEC	Front End Computer.
FPGA	Field-Programmable Gate Array.
fRC	Fixed Frequency Ring Cyclotron.
FRIB	Facility for Rare Isotope Beams.
FRS	Fragment Separator.
FSI	Final State Interactions.
FWHM	Full Width at Half Maximum.

GANIL	Grand Accélérateur National d'Ions Lourds.
GSI	GSI Helmholtz Centre for Heavy-Ion Research.
GSM	Gamow Shell Model.
GTO	Generic Trigger Operator.
HO	Harmonic Oscillator.
HODF24	Hodoscope for Fragment-24.
IM-SRG	In-Medium Similarity Renormalization Group.
IPM	Independent Particle Model.
IRC	Intermediate-stage Ring Cyclotron.
ISOL	Isotope Separation On-Line.
ISOLDE	Isotope Separator On-Line Detector.
IT-NCSM	Importance-Truncated No-Core Shell Model.
iThemba LABS	iThemba Laboratory for Accelerator-Based Sciences.
LH_2 target	Liquid Hydrogen Target.
LINAC	Linear Accelerator.
LUPO	Logic Unit for Programmable Operation.
MBPT	Many-Body Perturbation Theory.
MBS	Multi Branch System.
MINOS	MagIc Numbers Off Stability.
MWDC	Multi Wire Drift Chamber.
NCSM	No-Core Shell Model.
NEBULA	NEutron Detection System for Breakup of Unstable Nuclei with Large Acceptance.
NeuLAND	New Large-Area Neutron Detector.
NNDC	National Nuclear Data Center.
NSCL	National Superconducting Cyclotron Laboratory.
PMT	Photo Multiplier Tube.
PPAC	Parallel Plate Avalanche Counter.
QCD	Quantum Chromodynamics.
QDC	Charge-to-Digital Converter.
QFS	Quasi-Free Scattering.

QMC	Quantum Monte Carlo.
R^3B	Reactions with Relativistic Radioactive Beams.
RCNP	Research Center for Nuclear Physics.
RF	Radio Frequency.
RI	Radioactive Isotope.
RIBF	Radioactive Ion Beam Factory.
RIKEN	Rikagaku Kenkyūjyo, Designated National Research and Development Institute.
RILAC	RIKEN LINAC.
RIPS	RIKEN Projectile Fragment Separator.
RMS	Root Mean Square.
RRC	RIKEN Ring Cyclotron.
SAMURAI	Superconducting Analyzer for MUlti-particles from RAdioIsotope beams.
SBT	SBT Start Timer.
SCGF	Self-Consistent Green's Function.
SEASTAR	Shell Evolution And Search for Two-plus energies in neutron-rich nuclei At the RIBF.
SM	Shell Model.
SPE	Single Particle Energy.
SRC	Superconducting Ring Cyclotron.
SRG	Similarity Renormalization Group.
Super-FRS	Superconducting Fragment Separator.
TacQuila	TacQuila Electronics.
TBME	Two-Body Matrix Element.
TDC	Time-to-Digital Converter.
TIARA	Takasaki Ion Accelerators for Advanced Radiation Application.
ToF	Time-of-Flight.
ToT	Time-over-Threshold.
TPC	Time-Projection Chamber.
TRIUMF	Canada's Particle Accelerator Centre.
ZDS	ZeroDegree Spectrometer.

Erklärung zur Dissertation

gemäß §9 der Promotionsordnung

Hiermit versichere ich, dass ich die vorliegende Dissertation selbstständig angefertigt und keine anderen als die angegebenen Quellen und Hilfsmittel verwendet habe. Alle wörtlichen und paraphrasierten Zitate wurden angemessen kenntlich gemacht. Die Arbeit hat bisher noch nicht zu Prüfungszwecken gedient.

Darmstadt, den 11. Juni 2019

Julian Kahlbow